Study on the Electrodynamic Interaction Between a Tethered Satellite System and Space Plasma

by

Hideyuki USUI

December 1993

Study on the Electrodynamic Interaction Between a Tethered Satellite System and Space Plasma

by

Hideyuki USUI

December 1993

ACKNOWLEDGMENTS

ABSTRACT

In the last decade, space has become the most hopeful frontier for human beings owing especially to the practical use of the Space Shuttle. In the next century, large-scale space structures such as a space station are planned and will be constructed. Prior to the increased human activity in space, it is very important to understand the space environment in the vicinity of space structures. Since space is filled with conductive medium called a plasma which consists of mobile charged particles, an electrodynamic interaction will occur between the space structure and the plasma.

To investigate the details of this interaction, a Tethered Satellite System (TSS) has been utilized in active experiments in space. This system consists of an orbiter and a satellite which are physically as well as electrically connected to each other via a long conducting tether wire. Since the system is longer in one dimension, motion across the geomagnetic field develops a high potential in the system. This development enables us to study the details of electrodynamic interaction such as ambient plasma response to the high potential, current-voltage characteristics and current collection of the system as well as plasma wave excitation. Since the 1960's, theoretical studies have been done regarding the electrical behavior of a conducting body in a magnetized plasma. Further, in the last decade, the interaction of the TSS with a space plasma has been investigated theoretically in terms of wave radiation and current collection. By analyzing the results of these past experimental and theoretical studies, we can obtain some basic knowledge about the electrodynamic environment in the vicinity of a space structure.

To proceed in a more detailed analysis and obtain better understanding of the TSS-plasma interaction in space, we devoted ourselves to computer experiments in the present study. In these computer experiments, we construct a model which includes the space structure and the ambient plasma environment on the memory space of computer. The electrodynamic phenomena which will be observed in the vicinity of the structure are numerically solved in time and space. Since our concern is in the microscopic interaction, which is mainly governed by the electron dynamics near the space structure, we have utilized a two-dimensional fully electromagnetic particle code. We have modified the code to be able to handle the interaction of conducting bodies within a magnetized plasma. To see the interactions in a three-dimensional aspect, we have developed a three-dimensional electrostatic particle code.

Using these codes, we have first investigated the electrodynamic interaction of the TSS with the ambient plasma by introducing two conducting bodies, representing a satellite and an orbiter, into the model space. The electron beam emission from the orbiter is also carried out in the computer experiments. The

results obtained from the experiments could reveal the electrical properties of the TSS such as the charging, the potential variation, and the current collection of the system. These are examined both in two-dimensional and three-dimensional space and some of the results regarding the current collection of the TSS are compared with the data obtained from the TSS-1 mission. We can also clarify the ambient plasma response to the TSS and the electron beam dynamics in terms of density and current. From the interaction between the electron beam emission and the ambient plasma, a lower hybrid mode wave is excited and its generation mechanism is also discussed.

Secondly, we considered the high potential satellite which is one of the tethered ends in the TSS. We performed computer experiments to investigate the electrodynamic interaction of the satellite with the surrounding plasma. The process of the sheath formation and the spatial profiles of the current flow around the satellite are examined in both two-dimensional and three-dimensional space. The current-voltage characteristics of the satellite are quantitatively studied by comparing them with the classical theories. An estimate of the peak current obtained in the transient stage is also performed and compared with the results from the computer experiments.

Thirdly, we investigated the field response to potential change in the TSS. The results obtained in the set of computer experiments show that the electrostatic field is strongly perturbed at the tether ends at the characteristic frequencies of the plasma. We show that the low frequency perturbation is reduced by the electron beam emission which is used to remove negative charge from the TSS. In response to the transient current in the tether wire, it is also found that a whistler mode wave packet is induced which propagates along B_0. In terms of plasma instability, it is found that the ion-electron two-stream instability occurs in the presheath region due to the relative motion of electrons and ions. Along B_0 the Buneman instability, which is driven by electron acceleration toward the satellite, is responsible for the electrostatic perturbation. Across B_0 the beam cyclotron instability occurs and is associated with the electron beam $E \times B$ drift velocity. In both of these instabilities, the frequency range of the field perturbation corresponds approximately to the ω_{LHR} in the ion rest frame of reference.

Contents

List of Figures

Chapter 1

General Introduction

1.1 Electrodynamic Tethered Satellite System in Space Plasma

The concept of Tethered Satellite System (TSS) was originally proposed by Prof. Giuseppe Colombo of Smithonian Institution Astrophysical Observatory in 1974 [Colombo et al., 1974]. It was introduced to sound the low ionosphere below 120 km of altitude with use of a satellite tethered by a wire of 100 km long from Space Shuttle. Since then, many applications using tether system have been proposed by scientists such as a momentum transfer system for space [Woodies and VanPelt, 1986], a tether elevator [Merlina et al., 1986], and tether-assisted microgravity laboratory [Kroll, 1986]. Besides those technological applications, TSS can be applied to study the space plasma physics.

Electrodynamic tether system, consisting of tethered satellite, conducting tether wire, and orbiter will provide capabilities for many new scientific investigation. Since the system is longer in one dimension than any previous space structure, motion across the geomagnetic field causes high potential of the order of kilovolts in the system. These characteristics enable us to study current-voltage characteristics and charge collection at high potential in space plasma, the generation, propagation and interaction of low frequency waves in the ULF-ELF-VLF range, the interaction of large vehicles with the space environment, and beam plasma interaction.

From the view point of scale and conductivity of the system, the electrodynamic tether system can be assumed as a large structure in space such as a future space station. In this aspect, studies on electrodynamic interaction of the tether system with the surrounding plasma will provide us significant knowledge for the construction of large-scale space structure in the near future.

1

1.2   Shuttle Electrodynamic Tether System

In the past decade, several active experiments utilizing electrodynamic tether system have been carried out in space.

The first mother-daughter tethered rocket experiment was conducted in 1980 by the Institute of Space and Astronautical Science(ISAS) and Utah State University using a Japanese sounding rocket. The experiment was repeated in 1981 and 1983. The last experiment was called CHARGE-1 (Cooperative High Altitude Rocket Gun Experiment). A reflight of the CHARGE payload called CHARGE-2 was successfully carried out in December of 1985. In the CHARGE-2, an electron beam from 0.5 to 48 mA at 1 keV was injected from the mother payload, moreover a voltage up to 500 V was applied between the two payloads with and without the beam injection [Sasaki et al., 1988].

The first mission of Tethered Satellite System (TSS-1) was carried out in 1992 as a joint project between NASA and Italian Space Agency (ASI). Space Shuttle Atlantis carried the TSS-1 in its payload bay to be a circular orbit at an altitude of 296 km. The schematic illustration of the configuration of the TSS-1 is depicted in Figure 1.1. The TSS-1 consisting of a tethered satellite, conducting tether wire, and shuttle orbiter provides capabilities not only for many new scientific investigation but also for technological applications. Since the system is longer in one dimension than any previous space structure, motion across the geomagnetic field can cause high potential of the order of kilovolts in the system due to the Lorentz $V \times B$ effect. Taking advantage of this feature, 13 experiments were planned to be conducted together in the TSS-1 mission in order to determine and understand the electrodynamic interaction of the satellite, the tether and the shuttle orbiter with electric and magnetic fields in the ionosphere. The Shuttle Electrodynamic Tether System (SETS) experiment [Banks et al., 1993; Banks, 1989; Banks et al., 1981] is one of those experiments and we will focus on this in the present study.

The SETS experiments utilizing the tethered satellite system can offer the opportunity to provide important, new, basic, knowledge about fundamental plasma electrodynamics and the interactions of rapidly moving objects through the magnetized plasma of the earth's ionosphere. The primary objectives of the SETS investigation includes several different aspects of the primary objectives as described below.

Primary objectives include scientific studies of the following topics.

1. Current-voltage characteristics for a Satellite at potentials up to 5 kV.

   This is required for planning future missions. Yet, no reliable theory exists for the high voltage. At the voltage up to 10 V, classical prove theory can
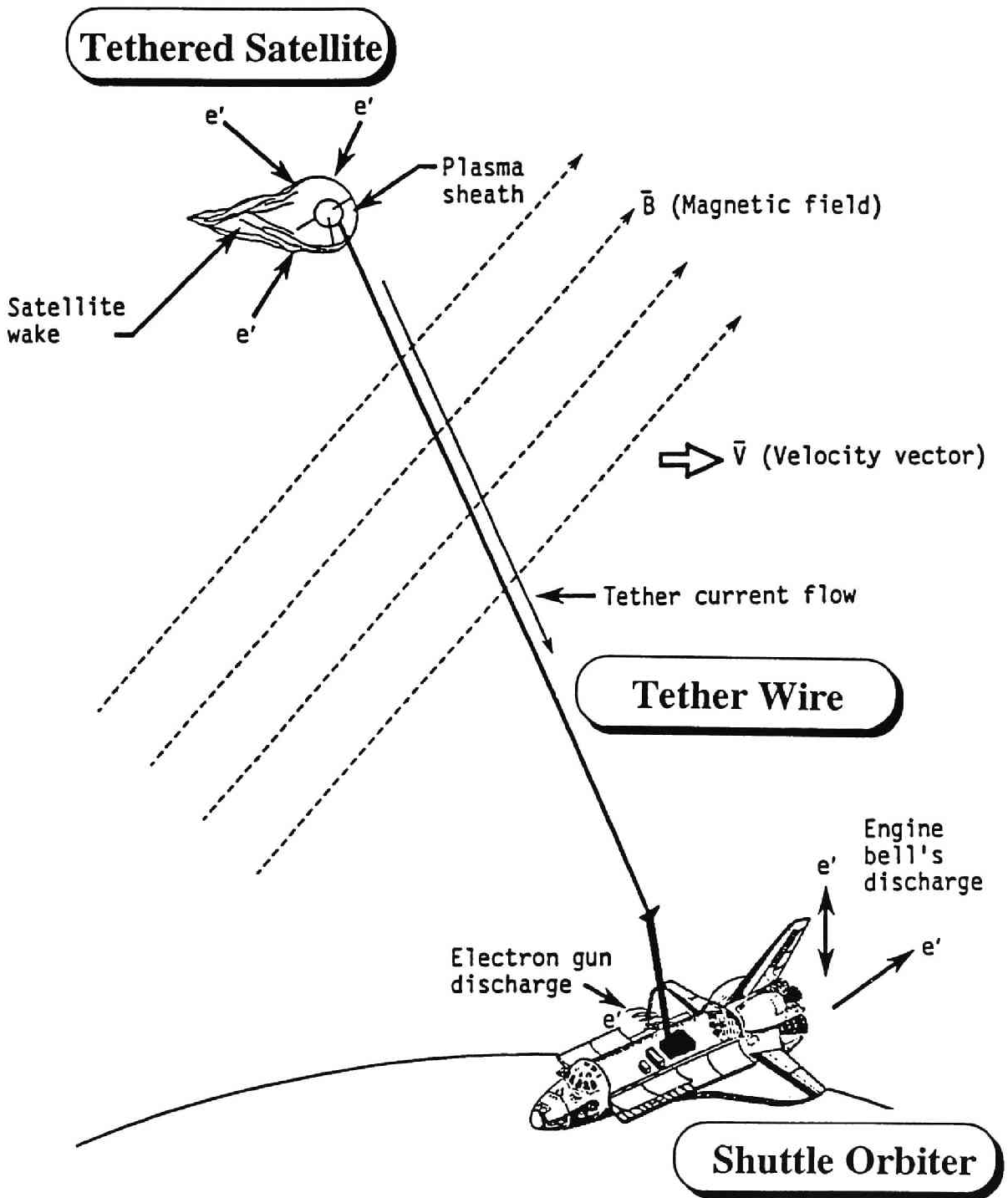
Figure 1.1: Schematic illustration of the TSS-1.

apply. At some larger voltage, 100, 1000 V, the plasma around the Satellite may become unstable. According to Linson [1982], the current should be proportional to $(voltage)^{6/7}$. Due to $E \times B$ electron drift and field aligned electron current, instability may occur and the unstable waves are expected to modulate the characteristics.

2. Measurement of the tether impedance characteristics.

   The TSS can be modeled as a transmission line in series with a high voltage source arising from the $V \times B$ emf, the satellite plasma interface, orbiter-plasma interface, and a short circuit through the surrounding plasma. Small pulses in the tether current induced by the SETS instrument will be used to study impedances of the tether system. By sending a square pulse, we can determine the dispersion characteristics of the tether system over the frequency band determined by the pulse width.

3. Spacecraft charging characteristics.

   An accurate, high time resolution potential reference has been available for observing the variation of vehicle potential during electron beam operation on the Space Shuttle. Results from these measurements will provide a means of controlling and emitting electrons from the tether end and will provide insight into the results from previous sounding rocket flight and Space Shuttle based experiments.

4. Wave generation and propagation (ULF/ELF/VLF)

   TSS is utilized for generation of ULF/ELF/VLF waves in a pulsed current driven mode to carry out active wave generation/reception experiments. Tether lengths in the range 20km are comparable to, or longer than, the longest antennas currently in use for long wave generation on the surface. In the ionospheric and magnetospheric plasma, the wave length of 1 Hz wave varies from about 200 km at 300 km to about 1000 km at an altitude of 2000 km.

5. Beam-plasma interaction.

   The generation of ULF/ELF/VLF/HF via the use of modulated electron beams and the interaction between these waves and the plasma have been hot topics in recent years. Collected charges due to the high voltage generated by the $V \times B$ emf are emitted from the Fast Pulse Electron Gun(FPEG) at the Orbiter.

To meet the scientific objectives described above, the SETS flight equipment includes five scientific instruments, its flight computer (DEP), and power inter-

SETS on TSS-1

Approximate MAX CURRENT

SHUNT - 15 Ω	(200 mA)	
R_1 - 24.94 kΩ	200 mA	
R_2 - 293.84 kΩ	20 mA	
R_3 - 2.473 MΩ	2 mA	

Acronym Table

AMAG	- Aspect Magnetometer
CCP	- Charge Current Probe
CMM	- Current Mode Monitor
CMS	- Current Mode Switch
DMS	- Deployer Master Switch
FPEG	- Fast Pulsed Electron Gun
MMS	- Mechanical Mode Switch
PROT	- Protection
SRPA/LP	- Spherical Retarding Potential Analyzer/Lamgmuir Probe
TCM	- Tether Current Monitor
TCVM	- SETS Subsystem
TVM	- Tether Voltage Monitor

TSS-1 Satellite

Martin-Marietta Tether Reel

DMS

TCVM

TVM

TCM (Hall Effect Current Sensor)

To DCORE Experiment

AMAG

CMS

MMS

PROT

SHUNT R_1 R_2 R_3 CMM

200 nF

CCP

SRPA/LP

Main Engine Housings (Primary Contact to Space Plasma)

QTY 2 1 keV, 100 mA E-Beam sources

FPEG

ORBITER ELECTRICAL GROUND

Figure 1.2: Schematic illustration of the SETS instrument and its interconnection with the tether system.

face box (SPIB) [Banks et al., 1993]. Figure 1.2 shows a schematic illustration of the SETS instrument and its interconnection with the tether system. Control and measurements of tether current and voltage by SETS is made through its Tether Current Voltage Monitor (TCVM). Excess negative charge in the system is removed through a Fast Pulsed Electron Gun (FPEG). The Charge Current Probe (CCP) measures the differential changes in the vehicle potential and return current from the ionosphere to the orbiter. The thermal plasma characteristics are determined by the Spherical Retarding Potential Analyzer and Langmuir Probe (SRPA/LP). The magnetic field in the orbiter's payload bay is measured with a Aspect Magnetometer (AMAG). Tether current is controlled by placing one of four load resistors in series between the tether end and the orbiter electrical ground. Ion current can flow to the orbiter primarily through the orbiter's engine bells. The FPEG, which is also connected to the orbiter

electrical ground, emits a 100 mA electron beam.

Unfortunately, due to a mechanical trouble in reeling the tether wire, the tether wire which was originally planned to be releases up to 20Km could not be fully extended. However, many significant data associated with the electrodynamic interaction were obtained during the TSS-1 mission [Aguero, 1993; Gilchrist, 1993; Thompson et al., 1993]. In order to investigate the more detail, NASA has decided to refly TSS-1 in 1995.

1.3   Significance of Computer Experiments

In the past ten years, as stated in the previous section, several active experiments utilizing the TSS have been carried out. Although very significant data regarding the electrodynamic interaction with the space plasma were obtained in those experiments, the amount of the data is not sufficient enough for the full understanding of the process of the electrodynamic interaction of the TSS with the ambient space plasma. This is due to the limited observation in terms of space and time.

Meanwhile, theoretical works regarding the electrical behavior of a conducting structure in a magnetized plasma have been done since 1960's. In the decade, electrodynamics in TSS have also been studied theoretically. However, the analytical studies based on the simplified linear model cannot sufficiently explain the phenomena resulting from the electrodynamic interaction of the space structure with its surrounding plasma. This is partly because the region of our interest is non-uniform space including both the space structure and the space plasma, and partly because the plasma kinetic effects which show high nonlinearity play an important role in the interaction.

To compensate the weak points in the observations and the theories and obtain quantitative understanding of the electrodynamic interactions between the TSS and the space plasma, we perform computer experiment which has advantages such as low cost, multi-points observation, and capability of nonlinear analysis in phenomena compared with the theoretical and space experimental approaches. Moreover, remarkable progress in supercomputer makes the computer experiments practical in terms of cost and time. These situations allow us to plunge oneself into the phase that the computer experiments come first of all and we predict phenomena which will be observed in space experiments. In this respect, in order to investigate the scientific items stated in the previous section and give some physical and technical suggestions for the future experiments utilizing electrodynamic tether, we have devoted the present thesis to the computer experiments on electrodynamic interaction of tether system with space plasma.

1.4 Contribution of the Present Work

In Chapter 2, we first give a concept of computer experiment and basic equations to be solved in electromagnetic particle model. The detailed explanation of how to solve the basic equations is not given because it is found in the existing literature [e.g., Hockney and Eastwood, 1981; Birdsall and Langdon, 1984]. Conventionally, periodic boundary condition is used for simulation codes because the numerical treatment is quite simple. This boundary condition is useful when one deals with plasma phenomenon which occurs uniformly in space. However, when an energy source is localized in a model region, the periodic boundary condition cannot be adopted because locally induced phenomena such as plasma wave can propagate away from the source but cannot escape from the system. To avoid such a situation, we have to introduce an isolated system for computer experiments. In order to realize an isolated system in terms of electrostatic field, we also adopted the Dirichlet condition $\phi = 0$ on the boundaries for the solution of Poisson's equation. The numerical treatment of the boundary is described in detail in this chapter. For a problem on interactions between space vehicles such as TSS and its surrounding plasma, we need to bring in internal conducting bodies into the model region. The numerical method for an equipotential solution on the internal bodies is also introduced. To examine three-dimensional effects of the phenomena, we newly developed a three-dimensional electrostatic particle code in which Poisson's equation and the equation of motion are solved for field and particles, respectively.

In Chapter 3, we describe the computer experiments on the electrodynamic interaction between the TSS and the ambient space plasma. First we briefly introduce the theoretical and experimental works related to the tether system. Then we move to description of the computer experiments. We used two types of code for the computer experiments; one is a two-dimensional electromagnetic particle code, and the other is a three-dimensional electrostatic code which is newly developed for the present study. As previously stated, the TSS is a unique structure in space in terms of its dimension. Since a conducting satellite is connected to an orbiter with a conducting wire, this system can be assumed as one conductor which has a long dimension in one direction. To deal with this system in the computer experiments, we introduce two conducting bodies electrically connected to each other in a model region by taking account of the charge separation due to the $V \times B$ effects. To avoid the charge accumulation due to the electron collection of the TSS, we emit electron beam from the orbiter. To clarify the beam effects in the computer experiments, we also used non-beam model in the TSS. We examined the plasma response to the TSS in terms of density distribution, current path, and field perturbation. The electrical properties of

the TSS such as potential variation and current collection at the tether ends are also investigated. The results obtained in the computer experiments are compared between the two-dimensional cases and the three-dimensional cases. The beam-plasma interaction is also studied in terms of the beam dynamics and the wave excitation. In particular in the two-dimensional case, the enhancement of local LHR mode wave is observed at the plasma cloud which is created due to the electron rotation by the $E \times B$ drift effects in the direction perpendicular to B_0. The physical interpretation of the mechanism of the wave excitation is described in the discussion.

In Chapter 4, we focus on the plasma environment in the vicinity of the high potential tethered satellite. As well as in Chapter 3, we perform the computer experiment by utilizing two- and three-dimensional models which include one conducting body representing a satellite in a magnetized plasma. Through the results obtained in these computer experiments, we examine the plasma response to the high potential satellite such as density modulation in its vicinity and current collection of the satellite. The transient process in the plasma density variation and current collection is quantitatively studied. In general, charged particles have high mobility along B_0 so that electrons are attracted to the satellite and form a dense sheath. Ions, on the contrary, are evacuated by the satellite and eventually form an ion cavity. In the presheath region, low density region is created along B_0 due to the ion acceleration away from the satellite region. To keep the local charge neutrality, electron density there is also low. In the direction perpendicular to B_0, electrons are hard to move and the electron sheath becomes thick because of they are frozen to B_0. In this situation, electron sheath is formed with a donut-like structure stuck by B_0. This is clearly observed in the three-dimensional case. In the downstream region, a rarefactional wake is created due to the presence of the satellite. The density profile in the plane perpendicular to B_0 shows asymmetry with respect to the plasma flow direction. One of the main concern in this chapter is the current-voltage characteristics of the satellite at steady state. The existing classical theories such as the Langmuir theory are used to be compared with the results obtained in the computer experiments.

In Chapter 5, we describe the two-dimensional computer experiments associated with the field perturbation induced by the tether current and the plasma instability due to the relative motion of electrons and ions in the vicinity of the high potential satellite. The potential difference generated by the electromotive force of the TSS causes the current circuit through the TSS and the ambient space plasma. In such a situation, the long tether can be assumed as a cross-field antenna which can radiate plasma waves. By assuming the satellite current due to the electron collection in the initial stage is equivalent to the transient current

flow in the tether wire, we performed computer experiments and examined the field response to the tether current in a magnetized plasma. It is found that a wave packet of whistler mode is enhanced and propagates mostly along B_0 when the modulated frequency is below the electron cyclotron frequency. The characteristics of the whistler wave packet such as the direction of the propagation and frequency are studied by one-dimensional computer experiments. We also examine the wave activity around the high potential satellite. As basic physics, the high potential satellite attracts and excludes electrons and ions in its vicinity, respectively. During its process, electrons and ions make a relative motion, which can drive the two-stream instability. By performing the two-dimensional computer experiments, we study the possibility of a plasma instability along and across B_0. The detail is described in this chapter.

In Chapter 6, we summarize the present study and give conclusions obtained in the computer experiments regarding the electrodynamic interaction of the TSS with the space plasma. Finally, we give suggestions for future works.

Chapter 2

Numerical Technique in Computer Experiment

2.1 Introduction

Computer experiment enables us to numerically simulate the electrodynamic interaction between the TSS and its surrounding plasma. To perform computer experiment, we need a simulation code which solves the basic equations governing the time and space evolution of all the possible phenomena to occur in a given system. Prior to the description of the computer experiment, we will present an introductory guide for the simulation codes used in the present study. Since the basic concept and the numerical scheme of the code have been described in the existing literatures [Omura, 1985; Hockney and Eastwood, 1981; Birdsall and Langdon, 1984], their details are not stated in the present paper.

In the present study, the model region used in the computer experiments is non-uniform one which includes a stationary conducting structure and ambient plasma flow, not the conventional one which treats uniform plasma with periodic boundary condition. In order to realize such a unique model, we adopt a several new numerical technique in the simulation codes such as open boundary condition for an isolated system and capacity matrix method for equipotential conductive multi-bodies.

In the present study, we primarily utilize a two-dimensional full electromagnetic particle code, KEMPO (Kyoto University Electromagnetic Particle Code) [Matsumoto and Omura, 1985; Omura, 1985] which has been developed in the space plasma study group at Radio Atmospheric Science Center of Kyoto University. Generally, plasma in simulation codes can be treated as a bulk of fluid or a group of particle depending on a phenomenon to be focused on with computer experiment. For example, a magnetohydrodynamic code treats the plasma

as fluid, which is suitable for solving the problems associated with macroscopic phenomena such as solar flow plasma interaction with the magnetosphere. In order to investigate the phenomena in which ion dynamics plays an important role, a hybrid code is appropriate in which electron and ion are treated as fluid and particle, respectively. In the present study, the electron kinetic effects in the vicinity of the tether system are considered as an important factor to determine the plasma response and field environment. In this sense, KEMPO which can tread all the species of plasma as particle is most suitable for the present computer experiments. For the analysis in the three-dimensional space, we newly developed an electrostatic particle code in which we adopted an electrostatic approximation in solving the fields in a given system.

In Section 2.2 we will give general features of KEMPO such as the basic equations, the boundary conditions and the numerical treatment of a space vehicle and TSS. Section 2.3 is devoted to the numerical scheme for solving the Poisson equation in a three-dimensional isolated system. In Section 2.4 numerical treatment of conducting bodies is described in terms of the capacity matrix method. The treatment of tethered satellite system in computer experiment is also stated in Section 2.5.

2.2   Two-Dimensional Electromagnetic Particle Code

In the present study, one of our interests is the kinetic effect which significantly affects the microscopic plasma interaction in the vicinity of the vehicle surface. In addition, to quantitatively determine the electrical properties of a space vehicle such as the charging and the current collection, we need to take the electron dynamics into consideration because they can control the plasma environment in the vicinity of the TSS. From a view point of field variation, we are interested in not only the electrostatic response to the TSS but also the electromagnetic field environment around the system. In order to satisfy those demands stated above, we will utilize KEMPO in the present computer experiments. This section is devoted to the description of the general features of KEMPO.

2.2.1   Basic Equations

For the last decade, much efforts have been dedicated to revise our KEMPO code. In conjunction with the rapid progress in computer in terms of its speed and working area of memory, KEMPO has become a very powerful tool in investigating nonlinear phenomena in space plasmas. In KEMPO, the equations

of motion with no collision terms and Maxwell's equations are simultaneously solved in self consistent manner. Assuming a non-relativistic effect, equations of motion are given by

$$\frac{d\boldsymbol{r_s}}{dt} = \boldsymbol{v_s} \tag{2.1}$$

$$\frac{d\boldsymbol{v_s}}{dt} = \frac{q_s}{m_s}(\boldsymbol{E} + \boldsymbol{v_s} \times \boldsymbol{B}), \tag{2.2}$$

where the subscript s denotes the s- th species of particles and v_s, r_s, q_s, m_s, E, and B denote particle position, velocity, charge, mass, electric field and magnetic field, respectively. Maxwell's equations in the MKS unit are

$$\boldsymbol{\nabla} \times \boldsymbol{E} = -\frac{\partial \boldsymbol{B}}{\partial t} \tag{2.3}$$

$$\boldsymbol{\nabla} \times \boldsymbol{B} = \frac{1}{c^2}\frac{\partial \boldsymbol{E}}{\partial t} + \mu_0 \boldsymbol{J} \tag{2.4}$$

$$\boldsymbol{\nabla} \cdot \boldsymbol{E} = \frac{\rho}{\epsilon_0} \tag{2.5}$$

$$\boldsymbol{\nabla} \cdot \boldsymbol{B} = 0, \tag{2.6}$$

where c, ϵ_0, and μ_0 denote the speed of light, dielectric constant and magnetic permeability, respectively. The quantities ρ and J denote the charge and current density, respectively and they are calculated by using PIC (Particle In Cell) method which distributes the current and charge of particles to the adjacent four grids points with an area weighting.

The basic equations stated above are replaced by the finite-difference equations to be solved. The detailed description is shown in Omura, [1985], Hockney and Eastwood, [1981], and Birdsall and Langdon, [1984]. Analytically, we do not need to solve (2.5), (2.6) if they are satisfied at $t = 0$. With a help of the continuity equation, one can find that the two equations are satisfied all the time. Since the continuity equation is not solved explicitly in KEMPO, there is no guarantee that it is satisfied all the time. In order to satisfy the continuity equation, we need to solve Poisson's equation and correct the electrostatic component at each time step.

Mainly because of shortage of the memories for a working area on our computer, we reduce the dimension in phase space, i.e., we do treat all the six components but only five components, If we take the z axis orthogonal to the model plane, for example, five components (x, y, V_x, V_y, V_z) are solved. We neglect the dependence on z of all quantities and assume $\partial/\partial z = 0$ in the basic equations. Three components are calculated for the electric and magnetic fields, and current density.

2.2.2 Boundary Conditions

In computer experiment, the basic equations are solved as an initial value problem. Therefore, as long as the time integration is concerned, all we have to give is an initial solution at $t = 0$. In integration of space, however, we have to determine boundary conditions at each time step.

Boundary conditions which have to be determined are summarized as follows.

(1) Maxwell's equation

(2) Poisson's equation (for electrostatic components)

(3) Particle position r

So far, a periodic boundary condition has been widely used. One boundary is connected to the other boundary, giving no ending point in the simulation region. This is suitable for a case which treats a uniform space. In this case, the total energy should be exactly conserved because it is a closed system.

On the other hand, in an inhomogeneous space including a spacecraft, a local beam, the gradient in charge density, etc., the periodic boundary condition fails. By the periodic condition, fields and particles are perturbed non physically through the fields and particles reentering to the simulation region. In order to neglect the artifact, it is necessary to invent an isolated system by hiring an open boundary condition [Usui, 1989].

In the following, we present the boundary conditions for full-open system. General features of the open boundary version of KEMPO are stated below.

1. We revised the Poisson solver from the conventional FFT to the Sine FFT method. This is done based on the following consideration. In a large isolated system, the solution to the potential at the boundaries can be set to zero allowing the Dirichlet condition $\phi = 0$ on the boundaries.

2. Numerical damping region is placed at each boundary of the x and y direction. Outgoing perturbed fields are absorbed in the damping region and never reflected back to the simulation region through the boundaries.

3. An outgoing particle is no more traced. Instead a new particle is injected with a newly given position and velocity on the occasion of the outgoing particle.

2.3 Three-Dimensional Electrostatic Particle Code

Basic physics associated with the interaction between the TSS and the ambient space plasma can be investigated by performing two-dimensional computer experiments. By combining the results obtained in different model planes, we can analyze the plasma phenomena in three dimensional aspect. However, to quantitatively examine the plasma dynamics in a realistic situation, we definitely need to carry out computer experiments in a three-dimensional space.

In the present studies, the electrostatic component originated from the potential difference between the two tether ends governs the plasma dynamics and field perturbation in its vicinity. In this sense, the electrostatic component obtained by solving Poisson's equation can represent the field variations in a model region. For this reason, we have newly developed a three-dimensional electrostatic particle code.

As stated above, the electrostatic field is calculated by solving Poisson's equation with the data of the charge density at each grid point. The obtained electric field is used to push the particles according to the equation of motion. Then, the value of charge density is renewed at each grid point. The time variation of the magnetic field is not solved. The boundary condition for particles are the same as that adopted in the two-dimensional KEMPO. As for the boundary condition of the electrostatic field, we use the Dirichlet condition $\phi = 0$ as adopted in the KEMPO. In order to realize this condition, we introduce the sine transform method for Poisson's equation [*Press et al.*, 1987]. This method is also applied in KEMPO full-open boundary version stated in the previous section. The brief formulation is stated in the following.

Instead of expanding a potential ϕ as the usual Fourier transform given by

$$\phi_{hjk} = \frac{1}{NX}\frac{1}{NY}\frac{1}{NZ} \sum_{l=0}^{NX-1}\sum_{m=0}^{NY-1}\sum_{n=0}^{NZ-1} \hat{\phi}_{lmn} e^{-2\pi ihl/NX} e^{-2\pi ijm/NY} e^{-2\pi ikn/NY} \quad (2.7)$$

we expand ϕ in sine waves.

$$\phi_{hjk} = \frac{2}{NX}\frac{2}{NY}\frac{2}{NZ} \sum_{l=1}^{NX-1}\sum_{m=1}^{NY-1}\sum_{n=1}^{NZ-1} \hat{\phi}_{lmn} \sin\frac{\pi hl}{NX} \sin\frac{\pi jm}{NY} \sin\frac{\pi kn}{NZ} \quad (2.8)$$

where ϕ_{hjk} denotes the potential value at grid point (h, j, k) and $\hat{\phi}$ indicates the potential value Fourier transformed with respect to space. In the above equations, NX, NY, and NZ are the numbers of the grid point in the x, y, and z directions, respectively.
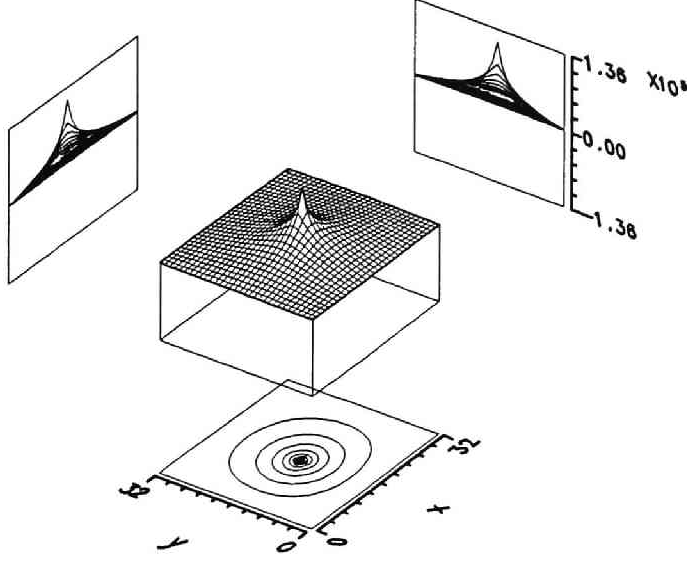
Figure 2.1: Spatial profile of the solution of Poisson's equation in a two-dimensional space including a unit charge at the center.

(2.8) satisfies the Dirichlet conditions at the boundaries. Using this expansion, we find that the solution procedure parallels that for periodic boundary conditions as follows.

We have Poisson's equation

$$\nabla^2 \phi = \frac{\partial^2 \phi}{\partial x^2} + \frac{\partial^2 \phi}{\partial y^2} + \frac{\partial^2 \phi}{\partial z^2} = -\frac{\rho}{\epsilon_0} \qquad (2.9)$$

First of all, we compute the Fourier component of the charge density $\hat{\rho}_{lmn}$ by the sine transform.

$$\hat{\rho}_{lmn} = \sum_{h=1}^{NX-1} \sum_{j=1}^{NY-1} \sum_{k=1}^{NZ-1} \rho_{hjk} \sin\frac{\pi hl}{NX} \sin\frac{\pi jm}{NY} \sin\frac{\pi kn}{NZ}. \qquad (2.10)$$

Next we calculate $\hat{\phi}_{lmn}$ by

$$\hat{\phi}_{lmn} = \frac{\hat{\rho}_{lmn}}{(\frac{\pi l}{NX})^2 + (\frac{\pi m}{NY})^2 + (\frac{\pi n}{NZ})^2} \frac{1}{\epsilon_0} \qquad (2.11)$$

Then ϕ_{hjk} can be computed by the inverse sine transform (2.7).

In the two-dimensional KEMPO of full-open boundary version described in the previous section, the sine transform method is also adopted for Poisson's equation. Because a model region is two-dimensional $x - y$ plane, the spatial variation with respect to z direction is neglected in the above formulation.

In Figure 2.1, we have a three-dimensional spatial profile of potential solution owing to a single charge. Since the Dirichlet conditions are adopted for the boundary conditions, it is shown that potential solutions at boundaries are all zero. This is solved with the sine transform method described above.

There is one thing we have to be careful with when we use the sine transform method. If we take the simulation region smaller than the depth of debye shielding, we can not neglect the effect on the field inside the model region by the fixed zero potential at boundary. We have to use such a large simulation plane that we can assume far field solution ($\phi = 0$) at boundaries. For an isolated system in a strict sense, potential solutions of Laplace's equation has to be connected at the boundaries of the model region. The method to realize this isolated system is described in Appendix [Hockney, 1970; Eastwood and Brownrigg, 1979].

2.4   Numerical Treatment of Conducting Bodies

In solving problems about the interaction between a space vehicle and space plasma, we need to bring in an internal conducting body representing the vehicle into the model region. In a real situation, space vehicle is not necessarily made of conducting materials. Space Shuttle, for example, is mostly covered with non-metal materials to avoid the melt of body surface owing to the heat in reentering the atmosphere. Only the part of engine thruster is conductive. From a view point of electrodynamic interaction, the charging and potential variations of the space vehicle are affected by the interaction of the conducting parts of the vehicle with its surrounding plasma. Since our main concern is the process of the electrodynamic interaction, we just take account of and treat numerically the conducting parts of the space vehicle in the present computer experiments. To do this in KEMPO in self-consistent manner, we utilize a numerical method which realizes equipotential solution on the vehicle surface. In this section, we describe the way for equipotential solution on internal conducting bodies through the use of the capacity matrix method [*Hockney and Eastwood*, 1981].

In the following we first describe the basic concept of the capacity matrix method to obtain an equipotential solution for one conducting body. The capacity matrix method can be applied to multi-bodies case, which will be stated next. Finally the application to the TSS model will be presented.

2.4.1 Equipotential Solution on One Internal Body

In treating the interaction of one conducting body with the surrounding plasma, we need to obtain the equipotential solution of the body surface at each time step in self-consistent manner. We summarize the treatment of potential and surface charge on one conducting body.

The potential value ϕ_j and charge density ρ_i on the grid points are related to each other by a quantity of 'capacity matrix C_{ij} '. The relation is given by

$$\rho_i = \sum_j C_{ij}\phi_j. \tag{2.12}$$

where i and j are varied from 1 to the total grid number in the simulation box. ϕ_i is calculated as

$$\phi_i = \sum_j B_{ij}\rho_j \tag{2.13}$$

where $B = C^{-1}$.

Before correcting the surface charge on the body to realize an equipotential, (2.13) gives the relation between the charge density ρ and the potential value ϕ in the simulation box as

$$\begin{bmatrix} \phi_1 \\ \vdots \\ \phi_{NBODY} \\ \phi_{NBODY+1} \\ \vdots \\ \phi_{NALL} \end{bmatrix} = \begin{bmatrix} B \end{bmatrix} \begin{bmatrix} \rho_1 \\ \vdots \\ \rho_{NBODY} \\ \rho_{NBODY+1} \\ \vdots \\ \rho_{NALL} \end{bmatrix} \tag{2.14}$$

where NALL and NBODY are the total number of grid points in the simulation box and in the body, respectively.

For the corrected charge density ρ' and potential value ϕ', we have the same relation as expressed above

$$\begin{bmatrix} \phi_C \\ \vdots \\ \phi_C \\ \phi'_{NBODY+1} \\ \vdots \\ \phi'_{NALL} \end{bmatrix} = \begin{bmatrix} B \end{bmatrix} \begin{bmatrix} \rho'_1 \\ \vdots \\ \rho'_{NBODY} \\ \rho'_{NBODY+1} \\ \vdots \\ \rho'_{NALL} \end{bmatrix} \tag{2.15}$$

where ϕ_C is an equipotential value in the body. We do not change the charge density outside the body, then $\rho'_i = \rho_i$ (NBODY+1 $\leq$ i $\leq$ NALL).

By subtracting (2.14) from (2.15), we obtain

$$
\begin{bmatrix}
\phi_C - \phi_1 \\
\vdots \\
\phi_C - \phi_{NBODY} \\
\phi'_{NBODY+1} - \phi_{NBODY+1} \\
\vdots \\
\phi'_{NALL} - \phi_{NALL}
\end{bmatrix}
= \begin{bmatrix} B \end{bmatrix}
\begin{bmatrix}
\rho'_1 - \rho_1 \\
\vdots \\
\rho'_{NBODY} - \rho_{NBODY} \\
0 \\
\vdots \\
0
\end{bmatrix}.
\qquad (2.16)
$$

Writing each component of the column vector in the both sides of (2.16) as $\Delta\phi_i$ and $\Delta\rho_i$ and dividing the matrix B into four sections, B^b, B^{bp}, B^{pb}, and B^p, (2.16) is rewritten as

$$
\begin{bmatrix}
\Delta\phi_1 \\
\vdots \\
\Delta\phi_{NBODY} \\
\Delta\phi_{NBODY+1} \\
\vdots \\
\Delta\phi_{NALL}
\end{bmatrix}
= \begin{bmatrix} B^b & B^{bp} \\ B^{pb} & B^p \end{bmatrix}
\begin{bmatrix}
\Delta\rho_1 \\
\vdots \\
\Delta\rho_{NBODY} \\
0 \\
\vdots \\
0
\end{bmatrix}.
\qquad (2.17)
$$

B^b contributes to the values of the body only while B^p to the values in the surrounding plasma outside the body only. B^{bp} contributes to the ϕ in the body and the ρ in the plasma and B^{pb} connects the ρ in the body to the ϕ in the plasma.

Since we focus on the charge density and the potential values only in the body, we use a subset of (2.17) as

$$
\begin{bmatrix}
\Delta\phi_1 \\
\vdots \\
\Delta\phi_{NBODY}
\end{bmatrix}
= \begin{bmatrix} B^b \end{bmatrix}
\begin{bmatrix}
\Delta\rho_1 \\
\vdots \\
\Delta\rho_{NBODY}
\end{bmatrix}.
\qquad (2.18)
$$

The correction of the surface charge for an equipotential solution is calculated by a matrix inversion of B^b

$$
\begin{bmatrix}
\Delta\rho_1 \\
\vdots \\
\Delta\rho_{NBODY}
\end{bmatrix}
= \begin{bmatrix} B^b \end{bmatrix}^{-1}
\begin{bmatrix}
\Delta\phi_1 \\
\vdots \\
\Delta\phi_{NBODY}
\end{bmatrix}.
\qquad (2.19)
$$

which is expressed in a form as

$$
\Delta\rho_i = \sum_j B^{b^{-1}}_{ij} \Delta\phi_j = \sum_j D_{ij}\Delta\phi_j \qquad (2.20)
$$
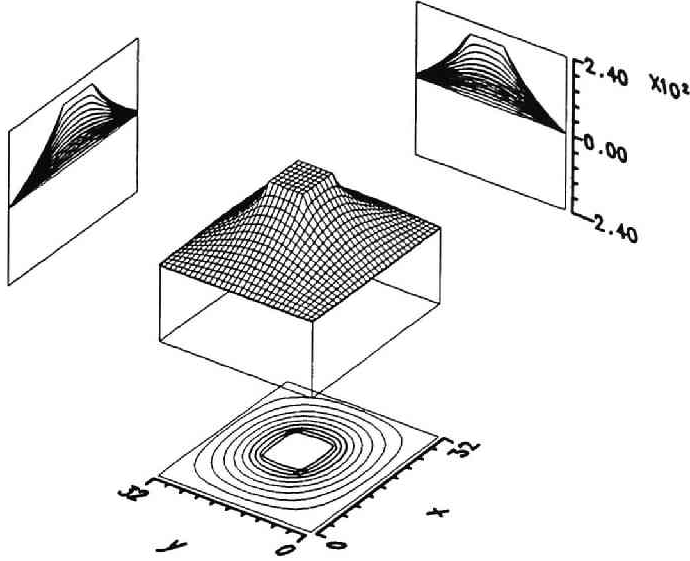
Figure 2.2: Potential profile of a two-dimensional system with one conducting body with a square shape

where D represents the inverse matrix of B^b and i and j are varied from 1 to NBODY. ϕ_i is given by

$$\Delta\phi_i = \sum_j D_{ij}^{-1}\Delta\rho_j \qquad (2.21)$$

When we calculate the capacity matrix D for the body, we give a unit charge density to $\Delta\rho_j$ and give zero charge to all other grid points, then solve Poisson's equation and obtain $\Delta\phi_i$ ($1 \leq i \leq$ NBODY). The solutions $\Delta\phi_i$ ($1 \leq i \leq$ NBODY) are equivalent to D_{ij}^{-1}. Repeating this process from 1 to NBODY with respect to j, all elements of D^{-1} are determined. D is calculated by a matrix inversion of D^{-1}. D is unique for the shape of a given internal body, so the calculation stated above is needed only once before the simulation run.

When we calculate $\Delta\rho$ at each grid point in the body, we need to obtain the equipotential solution ϕ_C in advance. From (2.20),

$$\Delta\rho_i = \sum_j D_{ij}(\phi_C - \phi_j) \qquad (2.22)$$

where ϕ_j ($1 \leq i \leq$ NBODY) are the potential values before correction. The

total charge in the body should be conserved, then

$$\sum_i \Delta\rho_i = 0 \tag{2.23}$$

This gives us ϕ_C as

$$\phi_C = \frac{\sum_{ij} D_{ij}\phi_j}{\sum_{ij} D_{ij}} \tag{2.24}$$

We calculate the correction of the charge density $\Delta\rho_i$ by solving (2.22) again with the determined ϕ_C. The correction $\Delta\rho_i$ ($1 \leq i \leq$ NBODY) gives us the corrected charge density ρ'_i ($1 \leq i \leq$ NBODY) and from (2.15), the equipotential ϕ_C is guaranteed in the body.

In order to demonstrate the results with use of the method stated above, we conducted a test analysis with a model region including a conducting body. Figure 2.2 shows the potential profile of a two-dimensional system in which the conducting body with a square shape is put at the center. We provide some positive potential to the body. As clearly shown, equipotential is realized on the surface of the body, which assures that the numerical scheme with use of the capacity matrix works with no trouble.

2.4.2   Equipotential Solutions on Multi-Bodies

We can apply this method to not only two bodies' case but also as many bodies as we desire. For simplicity, we introduce the method for two internal bodies. One might think that we have to have two capacity matrix for each internal body. This is wrong. The charge correction for one equipotential solution changes the potential of the other body. Two equipotential solutions have to be obtained simultaneously. That means all we need is one capacity matrix including two internal bodies just like one body.

As well as the one body case, the relation between the potential and the charge density is given by (2.12). However, for two bodies case, i and j vary from 1 to $NCPMX1 + NCPMX2$ where $NCPMX1$ and $NCPMX2$ denote the numbers of grid points of the body1 and body2, respectively.

The capacity matrix C is obtained easily by the same procedure as stated in the last section, and this calculation is also needed only once before the simulation run. Assuming the two bodies have different equipotential each other, ϕ_{ref1} and ϕ_{ref2}, we have two equations involving the capacity matrix.

$$\Delta\rho_i = \sum_j C_{ij}(\phi_{ref1} - \phi_{0j}) \tag{2.25}$$

for $1 \leq i \leq NCPMX1$, and

$$\Delta \rho_i = \sum_j C_{ij}(\phi_{ref2} - \phi_{0j}) \tag{2.26}$$

for $NCPMX1 + 1 \leq i \leq NCPMX1 + NCPMX2$, where ϕ_{oj} is the potential before correcting the charge density. The conservation of the total charge gives two equations independently

$$\sum_i \Delta \rho_i = 0 \tag{2.27}$$

for $1 \leq i \leq NCPMX1$,

$$\sum_i \Delta \rho_i = 0 \tag{2.28}$$

for $NCPMX1 + 1 \leq i \leq NCPMX1 + NCPMX2$,

By solving these two equations together with respect to ϕ_{ref1} and ϕ_{ref2}, equipotential solutions are determined. $\Delta \rho_i$ is recalculated with (2.25) and (2.26).

2.4.3   Potential Treatment of Tethered Satellite System

In the TSS, high potential is generated by the $V \times B$ emf between the tether ends due to the cross-field motion of the system. If the system's speed V_b is constant, $V_b \times B_0$ is also kept constant. The potential difference between the satellite and the orbiter, $\Delta \phi_c = L \cdot V_b \times B_0$ has no change where L is the tether length. We present here how to apply the capacity matrix method to the TSS model. In the previous section, we seek equipotential solutions for independent two bodies. In the computer experiment of TSS, however, two conducting bodies corresponding to the satellite and orbiter are electrically connected and therefore are not independent in terms of potential. The following relation should be maintained if L and V_b are constant.

$$\phi_{sat} - \phi_{orb} = L \cdot V \times B = \Delta \phi_c = const. \tag{2.29}$$

where ϕ_{sat} and ϕ_{orb} represent the potential of the satellite and orbiter, respectively.

The capacity matrix C is obtained in the same way as we have done in the last section. From (2.25) and (2.26),

$$\Delta \rho_i = \sum_j C_{ij}(\phi_{sat} - \phi_{0j}) \tag{2.30}$$

for $1 \leq i \leq NCPMX1$,
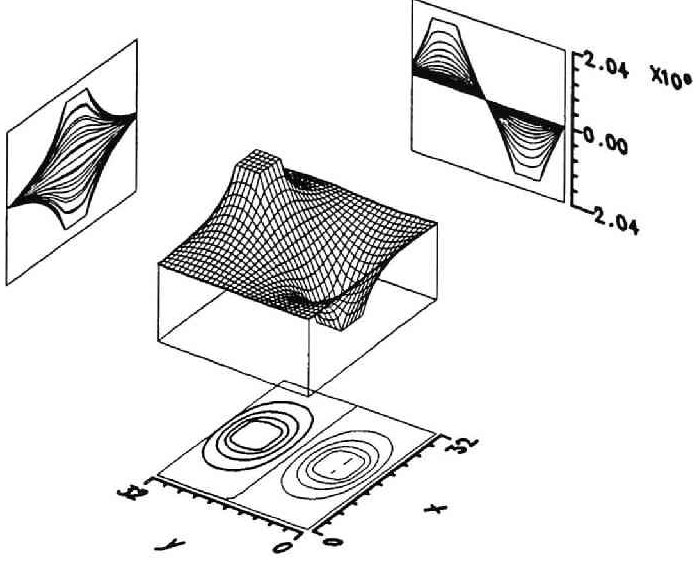
Figure 2.3: Potential profile in a two-dimensional space which includes two bodies representing the TSS. Owing to the charge separation by the $V \times B$ effect the satellite potential and the orbiter potential become positive and negative with respect to the space potential, respectively.

$$\Delta \rho_i = \sum_j C_{ij}(\phi_{sat} - \Delta\phi_c - \phi_{0j}) \qquad (2.31)$$

for $NCPMX1 + 1 \leq i \leq NCPMX1 + NCPMX2$.

Since the two bodies are connected with a conducting tether, the total charge of them, not each body, should be constant. Therefore we have

$$\sum_i \Delta\rho_i = 0 \qquad (2.32)$$

for $1 \leq i \leq NCPMX1 + NCPMX2$,

$$\sum_i \Delta\rho_i = -\sum_{ij} C_{ij}\phi_{0j} + \phi_{sat}\sum_{ij} C_{ij} - \Delta\phi_c \sum_{ij} C_{ij} \qquad (2.33)$$

By solving the equation above, we get ϕ_{sat} and with (2.29) ϕ_{orb} is obtained. The correction of the charge density $(\Delta\rho_i)$ is accomplished with use of the equation (2.30) and (2.31). To test the numerical treatment, we solve Poisson's

equation in a two-dimensional space including two conducting bodies which represent the tether ends. We set $\Delta\phi_c$ and provide no net charge on the bodies. In this situation, positive and negative $\Delta\phi_c/2$ should be provided to each body, respectively. Figure 2.3 shows the potential profile in the same manner as Figure 2.2. Two bodies representing the TSS have square shapes. As clearly seen, equipotentials are realized on each body with $\pm\Delta\phi_c/2$ as expected. During the runtime of the computer experiments, the TSS may accumulate the charged particles which will affect the net potential of the system. In this situation, the right hand side of (2.32) becomes non-zero. Therefore, we need to take account of the charge amount accumulated to the tether system to obtain its potential distribution in self-consistent way.

2.5 Model of Tethered Satellite System in Computer Experiments

In this section, we will describe the TSS model used in the computer experiments. The configuration of TSS in a magnetized plasma is rather complicated because it is primarily three-dimensional. Namely, The directions of the tether, TSS speed, and B_0 intersect to each other as illustrated in Figure 1.1. As for a reference frame of the model region, We have two choices; one is a moving vehicle frame and the other is an ambient plasma frame. In the present study, we use the vehicle frame of reference. due to the following reason.

In order to obtain an equipotential solution on the tether system, we use the capacity matrix as stated above. In the vehicle frame, the grid points occupied by the vehicle never changes and the calculation of the capacity matrix needs only once before the computer experiment.

In the vehicle frame, the ambient plasma should have drift velocity whose intensity is the same as the vehicle's. Assuming the vehicle moves parallel to B_0, it is easy to give the plasma drift velocity because the direction of the plasma flow is along B_0 and there is no need to consider the effect of the gyromotion of plasma.

Difficulty arises when the direction of relative motion between the vehicle and the ambient plasma is not parallel to B_0. In the vehicle frame of reference, we show this situation in Figure 2.4(a). Even if we initially set the plasma drift velocity across B_0, the gyromotion of charged particle occurs and eventually every particle moves along B_0. We would like to realize the cross-field plasma drift across B_0 at any time which is illustrated in Figure 2.4(b).

Figure 2.5 shows the detail of this situation. From the plasma rest frame, the vehicle moves oblique to B_0. Then the electromotive force, $V_b \times B_0$, causes

(a)   **(b)**
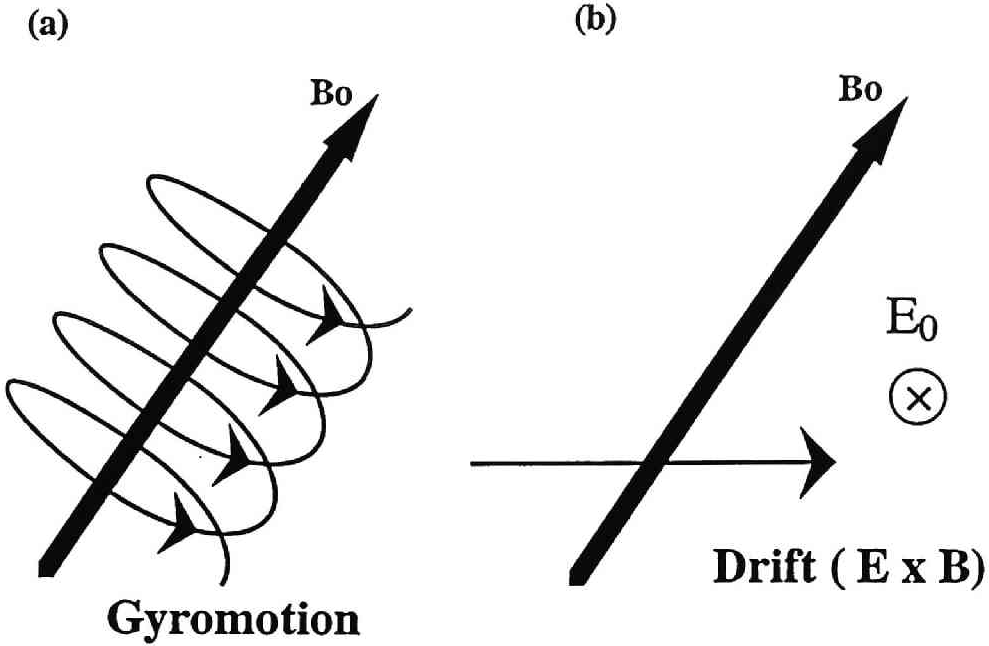
Figure 2.4: Schematic illustration of a particle motion oblique to B_0. (a) gyromotion, (b) drift motion across B_0.

the electric field perpendicular to both the direction of V_b and B_0.

$$E_0 = -V_b \times B_0 = V_b B_0 \sin\theta \hat{z} \tag{2.34}$$

where $\hat{z}$ direction is orthogonal to the plane.

Taking the vehicle as a reference frame, no electric field is allowed inside since it is assumed to be made of conducting material. Instead, E_0 obtained in (2.34) exists in the ambient plasma pointing to the opposite direction as shown in Figure 2.4. With B_0, this electric field gives a $E \times B$ drift velocity to the charged particles perpendicular to both E_0 and B_0 as shown in Figure 2.5. Adding another drift velocity $V_{drift}\cos\theta$ parallel to B_0, we can realize the plasma drift motion oblique to B_0.

Since the two bodies, satellite and orbiter, are connected with a conducting wire, no potential difference is allowed inside the system in the vehicle frame of reference. However this does not imply that we can ignore the charge separation between the tether ends. The charge separation caused by the cross-field motion exists which frame of reference we take. Therefore all we have to do is evaluate the amount of the charge separation. In Section 2.4.3, we take the plasma frame and evaluate the charge separation by seeking the potential solutions of the

(a)

B_0

θ

Vehicle

E_0

V_{body}

(b) $V_{body} = -V_{drift}$

$V_{drift} \cos \theta$

B_0

θ

V_{drift}

Vehicle

$\otimes$
E_0

$V_{drift} \sin \theta = \dfrac{|E_0 \times B_0|}{B_0^2}$
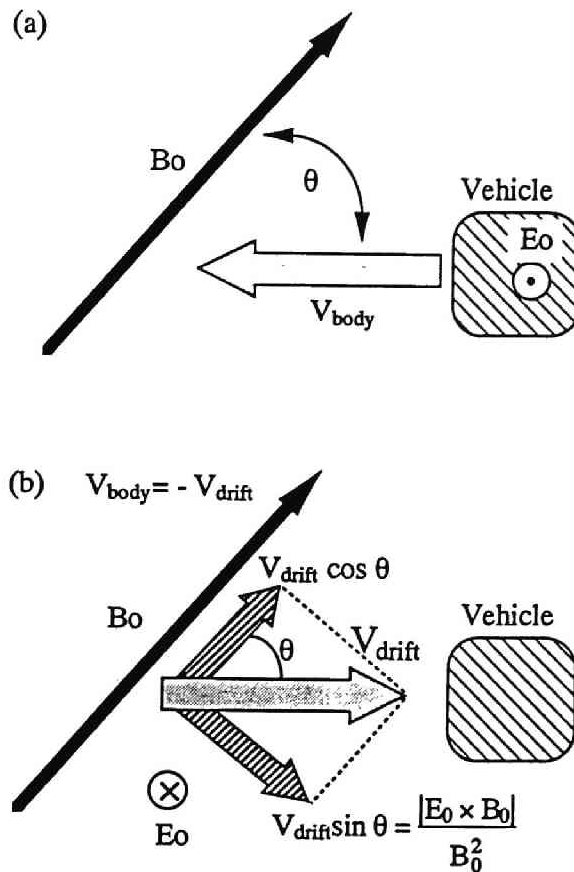
Figure 2.5: Schematic diagram of a moving body across B_0. (a) plasma rest frame of reference, (b) vehicle frame of reference.

tether ends. The obtained quantity on the charge separation never changes even if we take the vehicle frame of reference.

The tether wire which electrically connect the satellite and the orbiter is not treated as an internal conductive body in the present computer experiments because it is primarily insulated and therefore the direct contact with the plasma surrounding it is assumed to be neglected compared with the plasma contact at the tether ends. Instead, taking account of the rate of charge accumulation to the tether ends, we provide current flow on the grid points which corresponding to the location of the tether wire between the tether ends.

In the next chapter, we will present the computer experiments of the TSS by using the numerical treatment described in this chapter.

Chapter 3

Computer Experiments of Electrodynamic Tether System

3.1 Introduction

As a part of the first mission of the Tethered Satellite System (TSS-1) launched 31 July, 1992 aboard the space shuttle Atlantis, the SETS experiment was carried out [Banks and Byers, 1986]. The tether wire connecting the orbiter to the satellite experiences the Lorentz electric field, $V \times B$, due to its motion across the geomagnetic field, which causes large potential difference between the tether ends. To control the system charging, the electron beam is emitted from the orbiter [Banks et al., 1981; Gilchrist, 1990]. The primary objectives of the SETS investigation are to study space plasma physics associated with the interaction of the satellite, tether and orbiter with each other and with their environment. The scientific objectives are itemized in Chapter 1.

Since 1970's, theoretical works regarding the electrodynamics of the TSS have been conducted. Dobrowolny [1978], and Arnold and Dobrowolny [1980] investigated the current and potential distribution along the tether taking account of its internal resistance. From the view point of electromagnetic radiation, Hastings and Wang [1987], and Estes [1988], assuming a dumbbell-like current system for tether system, calculated the wave impedance which determined the power of the Alfvén wings. As well as the theoretical works, CHARGE experiments using a tethered rocket have been carried out since 1980 with collaboration between Japan and the United States. The initial results obtained in the latest experiment, called CHARGE-2, were described in Sasaki et al. [1988]. Laboratory experiments have also been conducted by Stenzel and Urrutia [1990] in which a field-aligned electron beam was emitted from a cathode and return electrons were collected by a plane electrode. They showed the behavior of a current system,

which modeled some aspects of the TSS-1. In numerical studies, two-dimensional computer simulations of the electron beam injection from an isolated conducting spacecraft have been performed [Winglee and Pritchett, 1988; Okuda and Berchem, 1988; Winglee and Kellogg, 1990]. However, computer experiments of TSS including two conducting bodies representing a satellite and an orbiter have never been reported. For the first time, we performed computer experiments of the TSS [Usui et al. 1991].

In this chapter, we describe the obtained results in the computer experiments of the TSS and analyze them quantitatively. Since we deal with the non-uniform space including the TSS in a magnetized plasma, it is difficult to examine the electrostatic and electromagnetic environment in the vicinity of the conducting system in the analytic way. Moreover, the electron beam is emitted from the orbiter, which makes the plasma environment complex around the TSS. To quantitatively investigate the TSS - plasma interaction such as the plasma response to the TSS, electron beam dynamics, and wave emission, we utilized two types of simulation codes in the computer experiments; a two-dimensional electromagnetic and a three-dimensional electrostatic codes.

3.2 Two-Dimensional Electromagnetic Particle Model

3.2.1 Model and Parameters

Since the electron kinetic effects are significant in the analysis of the electromagnetic perturbations and plasma behaviors around the TSS, we use the two-dimensional full electromagnetic particle code called KEMPO which can treat electrons as particles as well as ions. The numerical technique used in KEMPO was described in Chapter 2.

The model for the computer experiments is shown in Figure 3.1. We take a vehicle frame of reference. Namely, the ambient plasma flows across the static magnetic field B_0. We adopt two models; one is Model-1 where the simulation plane includes the plasma flow V_p along the x axis. B_0 is orthogonal to the plane. The other is Model-2 which contains B_0 in the y direction. The plasma flow is perpendicular to the plane of Model-2. As for the outer edge boundary conditions of the simulation box, we use open-boundaries conditions by adding wave-absorbing regions to the simulation system.

In each model plane, we have two conducting bodies representing a satellite and an orbiter, respectively, whose dimensions are $6\lambda_D \times 6\lambda_D$ where λ_D denotes the Debye length for the background plasma. Although the actual size of the
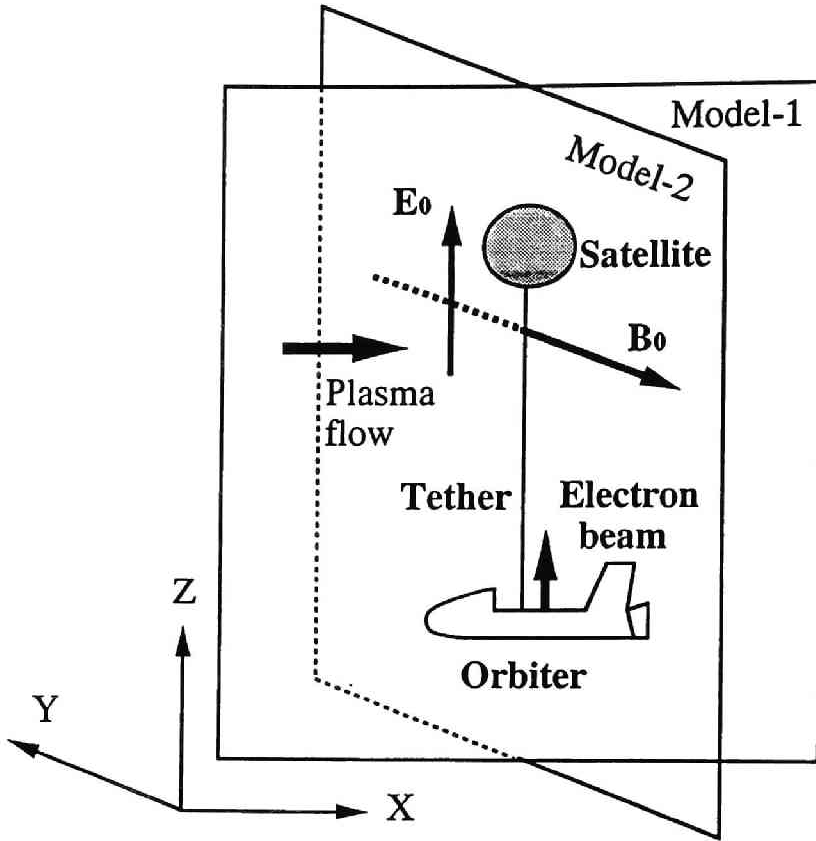
Figure 3.1: Schematic illustration of the model plane for the computer experiments. Model-1 and Model-2 has a plasma flow parallel and perpendicular to the model plane, respectively.

satellite (1 ∼ 2 m) is much smaller than that of the shuttle orbiter (10 ∼ 20 m), we choose the same size for the two conducting bodies for simplicity. They are located with a distance of approximately $40\lambda_D$ each other. For numerical brevity, we assume that both of the bodies are conductive. In the plasma rest frame of reference, the potential difference $\Delta\phi$ between the tether ends is calculated by taking account of the $V \times B$ effect, i.e., $\Delta\phi = L \cdot |V_v \times B_0|$ where L and V_v denote the tether length and the vehicle velocity. This $\Delta\phi$ is caused by the charge separation due to the $V \times B$ electromotive force of the TSS. As described in Chapter 2, this effect always exists whichever frame of reference we take in the computer experiments and all we should know is the quantity of the charge separation. In order to evaluate this, we solve Poisson's equation using the capacity matrix method [Hockney and Eastwood, 1981] under the assumption

that the tether ends have a potential difference $\Delta\phi$ which should be observed from the plasma rest frame. The detail was described in the previous chapter.

In the SETS experiment, the charge collection of the TSS affects its potential. Since the electron thermal velocity is much larger than the ion's in the ionosphere, electrons are collected to the conductive system much more than ions. This causes the negative charging of the TSS. To avoid the excess charging of the system, electron beam is injected from the orbiter into the ambient plasma. For simplicity, in the computer experiment, we emit the same number of beam electrons as that of incoming electrons at each time step from the orbiter in order to keep the amount of the total charge in the TSS conserved during the simulation. Since it is one of our interests to see the influence of the electron beam to the electrodynamics of the TSS. we perform several cases of computer experiment by changing the manner of the electron beam emission from the orbiter. In each model plane, we change the location of the electron gun and the initial pitch angle of the electron beam. Three cases stated below are commonly adopted for the computer experiment in Model-1 and Model-2. In Case (a) and Case (b), electrons are emitted from the top and the bottom of the orbiter with 90 degrees of the initial pitch angle, respectively. In Case (c), no electrons are emitted. To see the dependence of the beam dynamics on the initial pitch angle, Case (d) and Case (e) are additionally introduced in Model-2, in which electrons are emitted from the top and the side of the orbiter with the initial pitch angle of 45 and zero degrees, respectively.

The parameters used in the computer experiments are the followings. The ratio of the tether potential energy to the electron thermal energy, $e\Delta\phi/k_B T_e$, is set equal to 10, where e, T_e and k_B denote the electron charge, temperature, and Boltzmann's constant, respectively. The grid spacing and the time step are taken as $\Delta r = \lambda_D$ and $\Delta t = 0.005/\Omega_e$, respectively, where Ω_e denotes the electron gyrofrequency, respectively. The dimension of simulation plane is $128\Delta r \times 256\Delta r$. We take $16\Delta r$ from each boundary for numerical damping of the outgoing wave fields. The number of the superparticles is 131,072 for each species of plasma particles at the initial state. For ambient electrons, $\Pi_e/\Omega_e = 2$, and $v_{te}/V_p = 8$, where Π_e and v_{te} denote the electron plasma frequency and thermal velocity, respectively. For ambient ions, $\Pi_i/\Omega_e = 0.2$, $\Omega_i/\Omega_e = 0.01$, and $v_{ti}/V_p = 0.8$, where Π_i, Ω_i, and v_{ti} denote the ion plasma frequency, gyrofrequency, and thermal velocity, respectively. We carried out the simulation run up to $\Omega_e t = 327$ for both Model-1 and Model-2 with the same parameters.

3.2.2 Ambient Plasma Response and Beam Dynamics

In this section, the ambient plasma response to the TSS and the electron
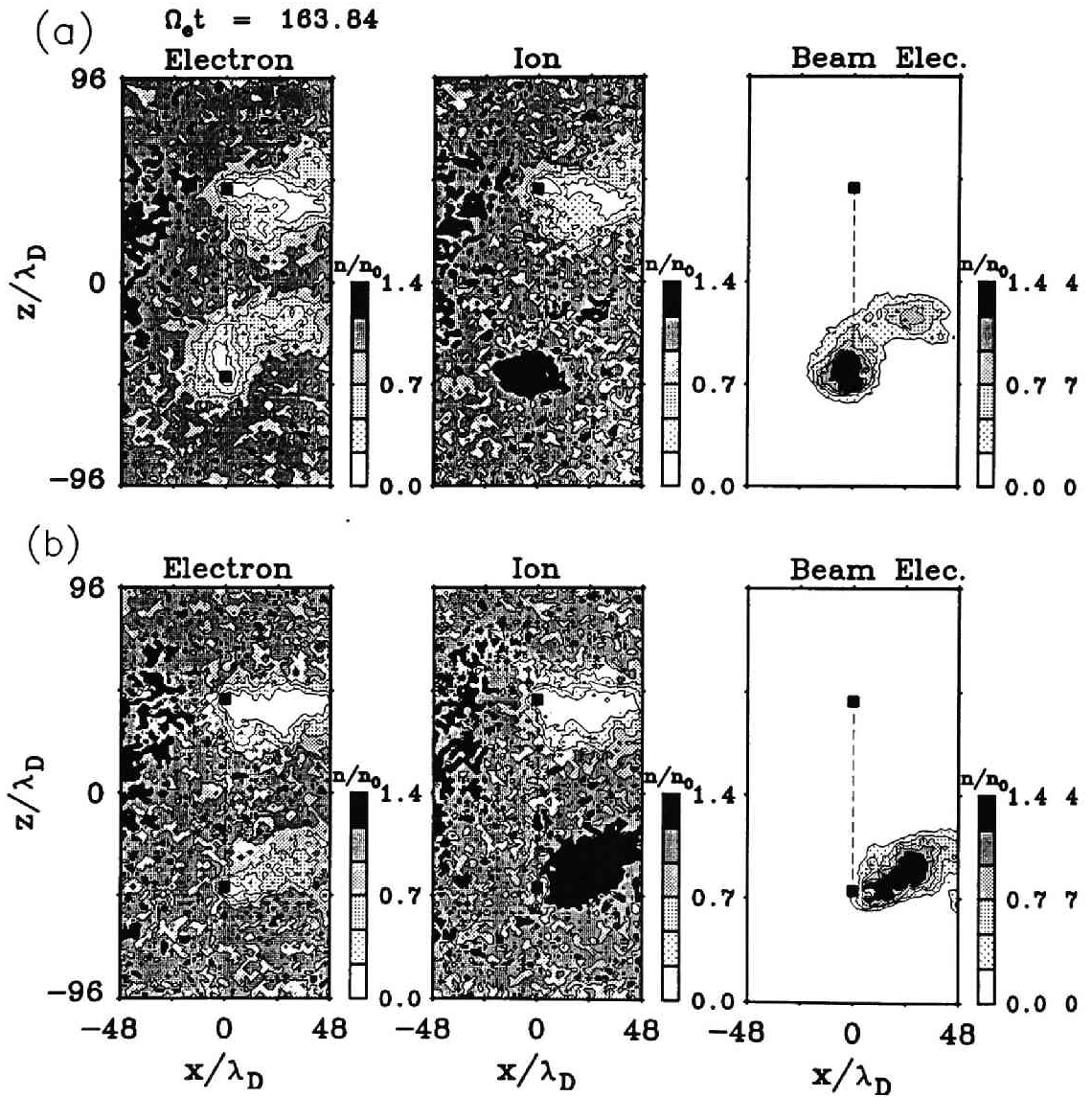
Figure 3.2: Contour maps of the number densities for the background electrons, ions, and beam electrons for Case (a) and (b) in Model-1.
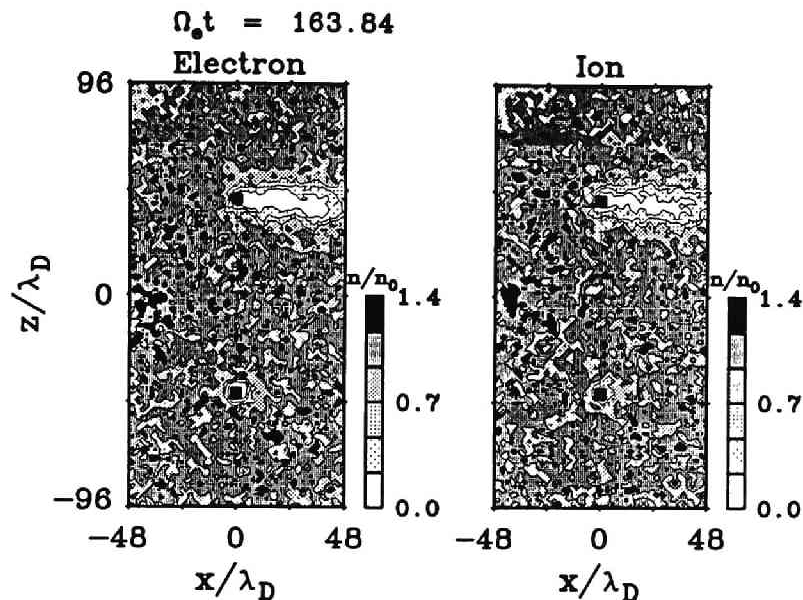
Figure 3.3: Contour maps of the number densities for the background electrons and ions for Case (c) in Model-1.

beam dynamics are described in terms of number density and current path. As stated previously, the satellite and orbiter have initially higher and lower potential than the space potential, respectively. This can modify the plasma distribution around the TSS in such a way that electrons and ions are attractive and repulsive to and from the satellite, respectively. The beam electrons emitted from the orbiter can also affect the plasma environment in the vicinity of the TSS. In particular, the electrostatic and electromagnetic environment of the orbiter will be greatly affected by the beam-plasma interaction.

First, we examine the spatial variation of the plasma density in Model-1. Figure 3.2 depicts the contour maps of the number densities for the background electrons, ions, and beam electrons. The upper and lower sets of the contour maps show the density variation in Case (a) and Case (b), respectively. The density profile in Case (c) is shown in Figure 3.3. The density values are averaged in time at the steady state. In each panel, the upper and lower squares indicate the satellite and orbiter, respectively. In Model-1, we have a plasma flow from the left to the right in the model plane. Then a rarefactional wake region is created in the downstream region of the satellite. The size of plasma void at the wake region is about $30 \sim 40\lambda_D$. The shape of the wake is almost identical for

the background electrons and ions. In the computer experiments, v_{te} is much greater than v_{ti}, and λ_D is smaller than the size of the body. In this situation, the dynamics of ions determines the wake formation. The ions blocked by the body cannot penetrate the wake region because of their small thermal velocity, which elongates a wake region behind the body. To maintain the local quasi-neutrality, the shape of the electron wake becomes very similar to that of the ion wake. The shapes of the wake in Case (a) and (b) are obviously asymmetric with respect to the direction of the ambient plasma flow. Although faintly observed in Case (c), this may be associated with the interaction between the local $E \times B$ rotation of electrons and the ambient plasma flow, which will be examined in detail in next chapter.

At the orbiter region, the electron beam injection completely changes the spatial profile of the ambient plasma. In the electron beam cases, i.e., Case (a) and Case (b), the emitted electrons from the orbiter, making gyromotion in the counterclockwise direction, hardly escape from the orbiter region and eventually form a high density electron cloud in the vicinity of the emission gate. The electron cloud causes the local intense electric field and rotate in the counterclockwise direction due to the $E \times B$ drift motion of the beam electrons. The beam electrons, however, are frozen in the ambient magnetic field and move to the downward region. For this reason, in Case (a), the electron cloud is carried downstream. The cloud in Case (b), however, is decelerated and cannot escape from the orbiter region because it tends to move to the upstream direction against the ambient plasma flow. Some of the beam electrons located at the edge of the cloud can be trapped by the ambient magnetic field and move in the downstream direction. Because of the electron cloud, the background electrons are expelled away from the cloud region. The ambient ions also form a cloud around the electron beam cloud to keep the local charge neutrality. As for Case (c) shown in Figure 3.3, in which no electron emission is performed, the rarefactional wake is observed at the orbiter region. The wake tail is much shorter than that at the satellite region. This is because the ions which can determine the shape of the wake as stated above are attracted by the orbiter which is negatively charged with respect to the ambient plasma.

Next, we present the plasma response in Model-2 contains B_0 in the y direction and the plasma flow in the $-x$ direction. Figure 3.4 shows the contour maps of the number density for each plasma species in Case (a) and Case(c). In Case (a) which is the electron beam mode, the low density region in the vicinity of the satellite has a shape elongated in the y direction for both of the background species. This is due to a large amount of electron collection and to ion scattering by the high potential satellite along B_0. As observed in Model-1, the density structure is almost identical for both of the background ions and
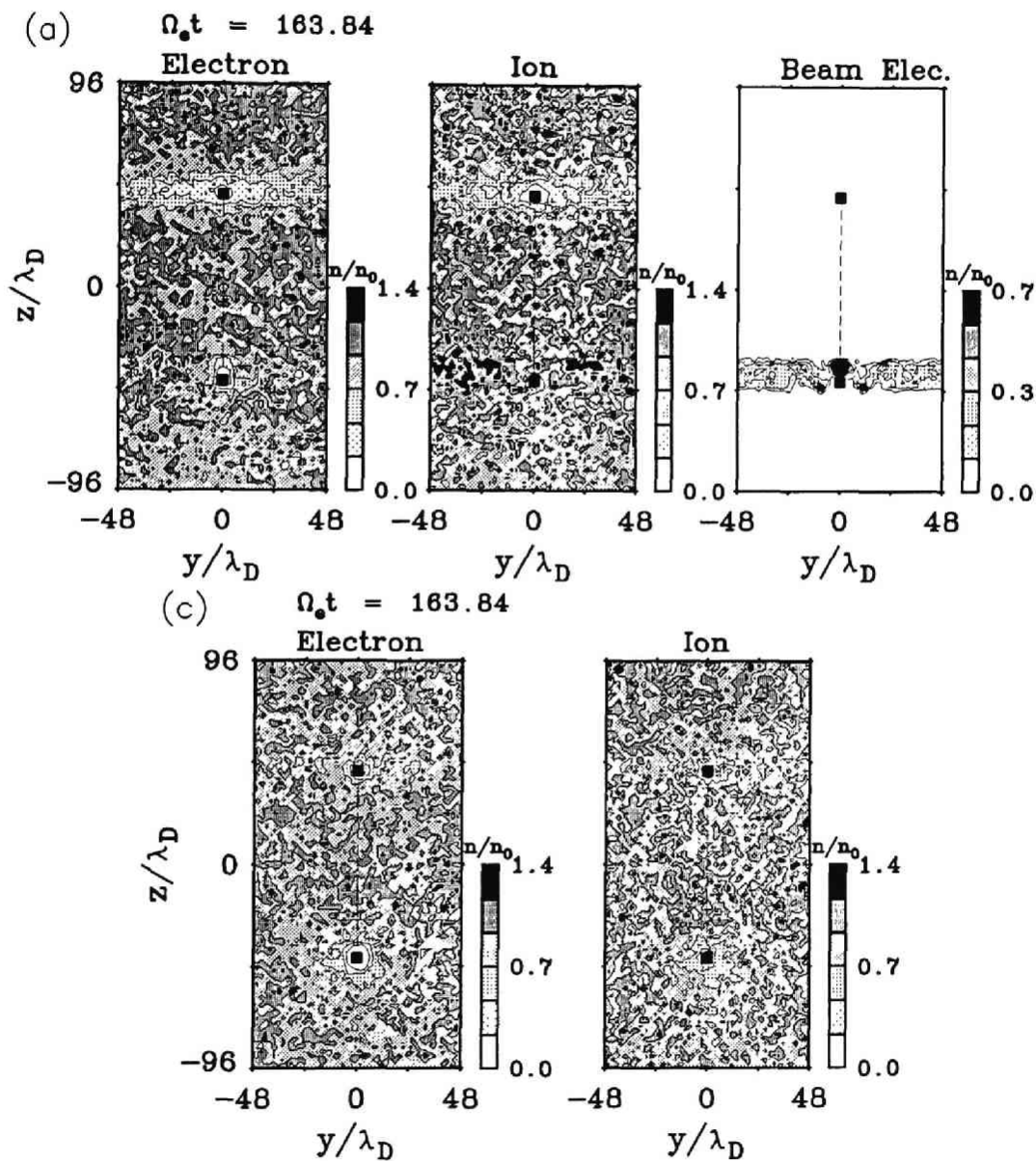
Figure 3.4: Contour maps of the number densities for the background electrons, ions, and beam electrons for Case (a) and the background electrons and ions for Case (c) in Model-2.

electrons keeping the local charge neutrality.

At the orbiter, the electron beam keeps its density maximum at the gate of the electron emission in Case (a) because the beam has the initial pitch angle of 90 degrees. In the both sides of the orbiter, some of the beam electrons escape and form wing-like orbit around B_0. The gyromotion of the beam electrons causes their bending orbits. The background electrons in the vicinity of the gate of the beam emitter are expelled by the beam electrons. In order to cancel the negative charge, the ions gather there. However, they are absorbed by the orbiter of negative potential. As the result, the beam electrons are rich and they can induce the electric field. This field causes the pitch angle modification and acceleration of the beam electrons along the wing-like orbit. Although faintly seen in the figure, the background electrons along the the wing-like orbit of the beam are scattered away while the ions gather to compensate the negative charge of the beam electron.

. We also performed the computer experiments including the electron beam emission with the pitch angle of 45 and zero degrees, which correspond to Case (d) and Case (e) in Model-2, respectively. The contour maps of the plasma number density are depicted in Figure 3.5 for both cases. The density profiles around the satellite are almost identical to those in Case (a) and Case (b). The plasma density is low along B_0 in the y direction due to the attraction and evacuation of electrons and ions to and from the satellite, respectively.

Since the pitch angle of the beam electron is not a right angel, the electrons can escape from the orbiter region along B_0. The beam trajectory in Case (d) bends due to the cyclotron motion of the electrons as shown in Case (a) and (b) in Model-2. In Case (e), the profile shows the beam electrons escape away along B_0.

Next, we examine the current profile in the vicinity of the TSS. Since electrons, which are light enough compared with ions, quickly response to the change of the field environment, they will play a major role to determine the current path associated with the TSS, As shown in the density profiles, electrons are primarily attracted by the high potential satellite. At the orbiter region, on the other hand, they are repulsive because the orbiter is negatively charged. In the beam mode, particularly, this repulsion is apparently seen and the beam electrons escape away along B_0. Figure 3.6 shows the vector plots of current density at each grid point in the model plane of Case (a) and Case (b) in Model-1. The squares in each panel represent the tether ends. In the direction perpendicular to B_0, as shown in the panel for Case (a), cross-field rotating current is observed at both satellite and orbiter region. Primarily, as stated above, the electron motion can determine the current flow. In this aspect, it is speculated that the cross-field current is due to the electron motion across B_0. Taking account of
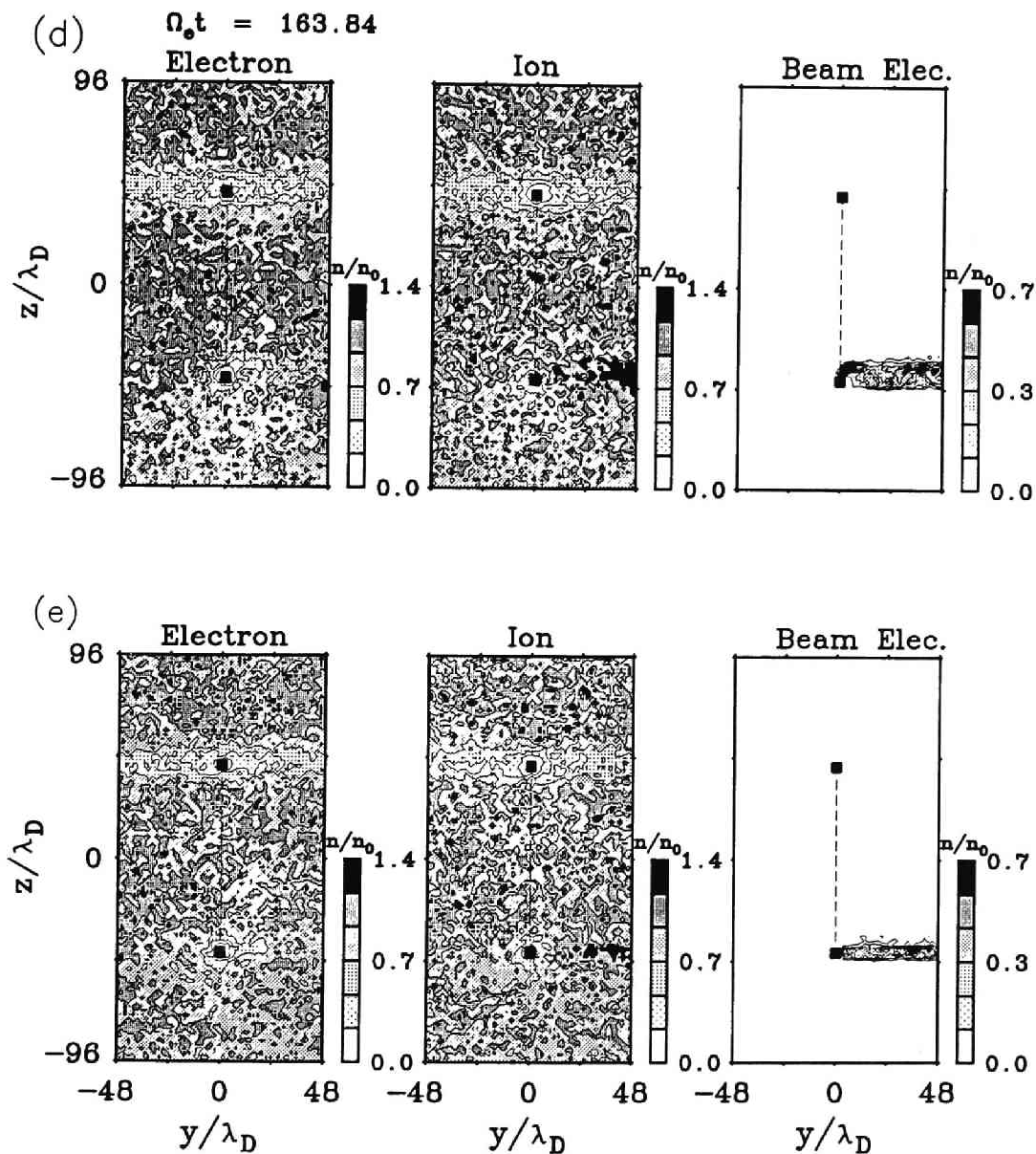
Figure 3.5: Contour maps of the number densities for the background electrons, ions, and beam electrons for Case (d) and (e) in Model-2.
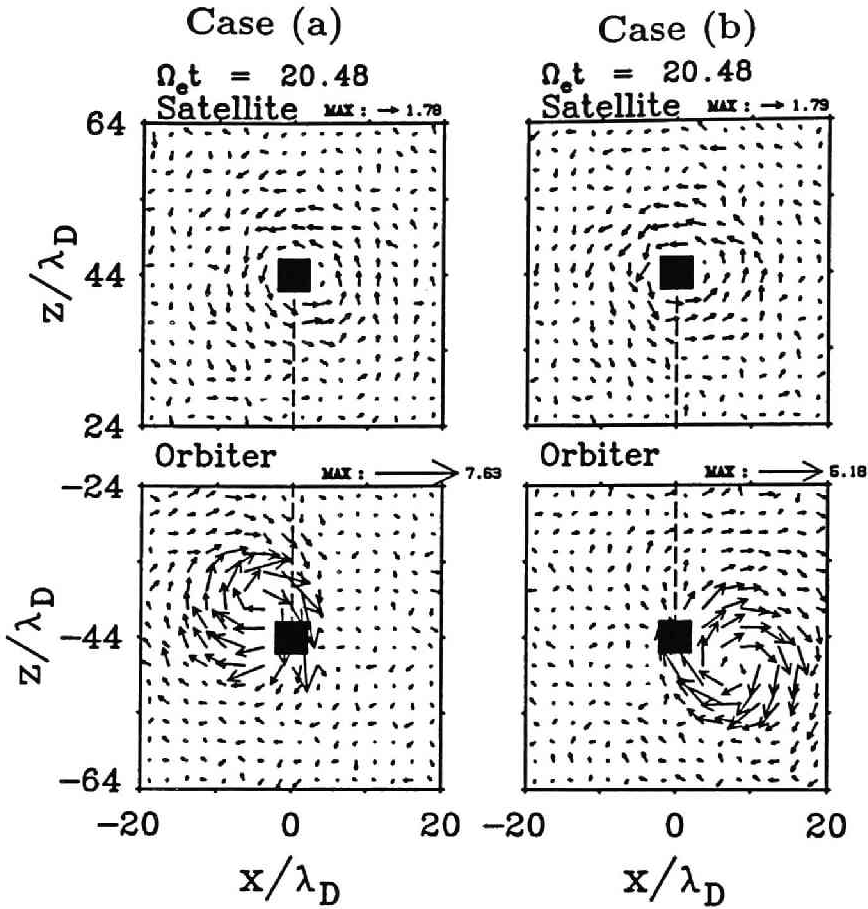
Figure 3.6: Vector plots of the current density in the model plane of Case (a) and (b) for Model-1.

the presence of the intense electric field of the satellite in the radial direction, the electrons in the vicinity of the satellite make cross-field motion with $E \times B$ velocity. In the present configuration of B_0, the direction of the electron cross-field motion around the satellite is clockwise. Hence, the current due to those electron drift is observed in the counterclockwise direction as shown in the figure. At the orbiter region, it is speculated that the beam electrons are mainly responsible for the current flow. In comparison with the density profile shown in Figure 3.2, it is found that the current rotates around the electron beam cloud. This implies that the cross-field current is owing to the cross-field drift motion of the beam electrons. In the later section, we will examine the potential profile at the orbiter region, and will clarify this point.
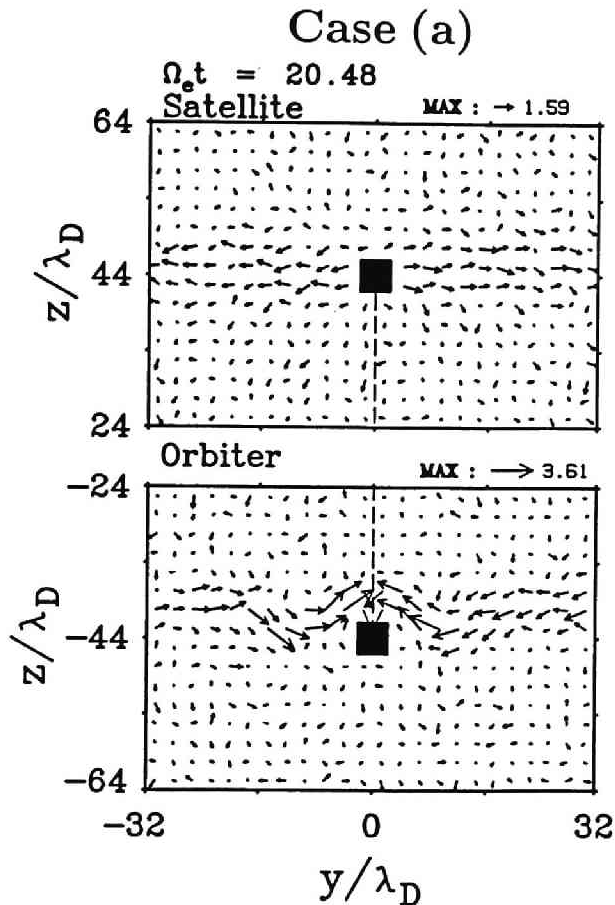
Figure 3.7: Vector plots of the current density in the model plane of Case (a) for Model-2.

We also depict the current profile for Case (a) of Model-2 in Figure 3.7. Primarily, the current path is obviously observed along the y direction, i.e., the B_0 direction, is dominantly observed at both the satellite and orbiter regions. At the satellite region, the electron collection of the high potential satellite is responsible for the intense current along B_0. At the orbiter region, the field-aligned current due to the beam electrons emitted from the orbiter is dominant. The profile of the current path is almost identical to the bending orbits of the beam electrons which is shown in Figure 3.4. Thus the modulation of the current path is caused by the gyromotion of the beam electrons. Although not shown in the figure, the field-aligned current at the tether ends are connected to each other by the tether current. For the completion of the current closure from

a macroscopic point of view, it is speculated that the field-aligned current in the ionosphere can be connected at low altitude around E region owing to the collisional diffusion of electrons and neutral particles. The detail of the current system including the ambient space plasma, the tethered satellite, tether wire, orbiter, and the electron beam will be discussed in the later section.

3.2.3   Electrical Property of Tethered Satellite System

In this section, we pay our attention to the electrical properties of the TSS such as charging and current collection. In the SETS experiment, a long conductive system of 20 km experiences the electromotive force, $V \times B$, between the tether ends, which makes the electrical properties of the TSS different from those of a single space vehicle. Since the satellite and the orbiter are electrically connected to each other by the conducting tether wire, the potential of the TSS and the current collection at each tether end cannot be determined independently. Moreover, as described in the previous section, the dynamics of the ambient plasma and the electron beam emitted from the orbiter have great influence on the charging and current collection of the TSS. Here, we focus on the following three points from a quantitative point of view;

1. Electron and ion current at the tether ends

2. Emissivity of the electron beam injection from the orbiter

3. Potential variations of the tether system

The current-voltage characteristics of the high potential satellite are one of the significant issues to be examined in the electrodynamic tether. In the next chapter we will present the computer experiment on the electrodynamics of the high potential satellite. The detailed current-voltage characteristics of the satellite will be described there.

First we examine the electron and ion current collected at each tether end at the steady state. Figure 3.8 shows the average amount of current collection to the tether ends for each case in Model-1 and Model-2. The current value is normalized to the average current of electron. Namely, the positive and negative values represent the current due to the electron and ion collection, respectively. In the figure we first pay our attention to the beam emission mode such as Case (a) and Case (b) in Model-1 and Case (a), (d), (e) in Model-2. Primarily, the amount of the electron collection of the satellite is much less in Model-1 because no field-aligned current is taken into consideration. The difference in the amount of the current collection is qualitatively seen in comparison of the satellite current between Model-1 and Model-2. The amount of the satellite
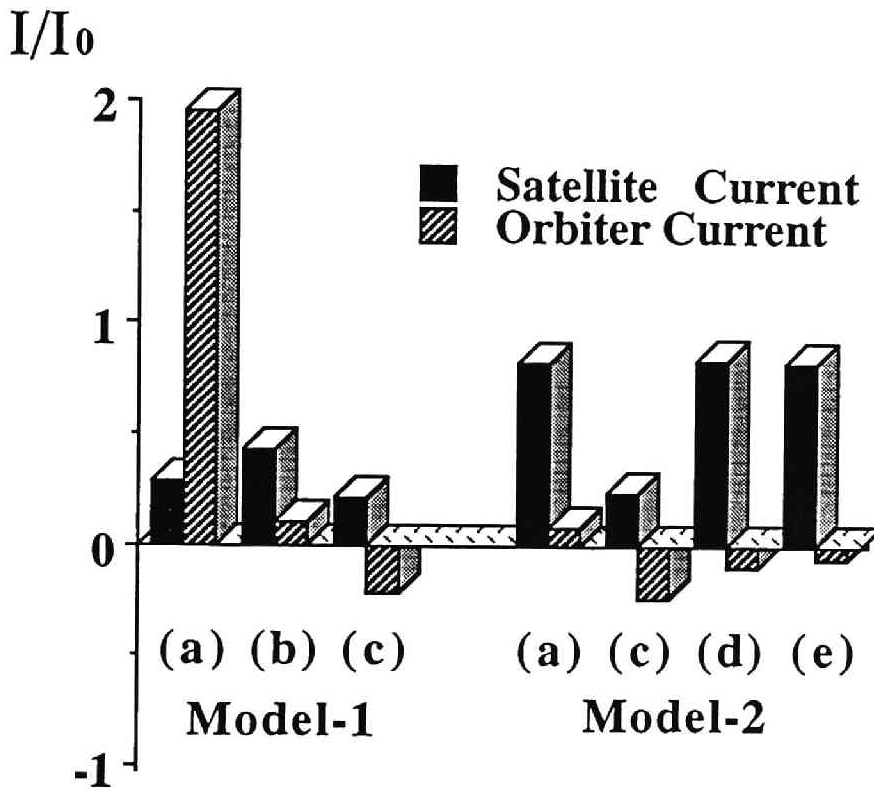
Figure 3.8: Amount of current collection to the tether ends at the steady state for Model-1 and Model-2.

current in Case (a) and (b) of Model-1 is approximately half of that in Case (a), (d), and (e) in Model-2. As examined in the previous section, the field-aligned electron attraction to the satellite in Model-2 contributes the large amount of the electron current.

In Case (a) and (b) of Model-1 and Case (a) of Model-2, the orbiter also obtains the electron current, although it is negatively charged in the present system. The common condition in all the cases above is the electron beam emission with 90 degrees of the beam pitch angle. In such a situation, the electron current at the orbiter can be return current due to the reentry of the beam electron to the orbiter. In particular, the orbiter current of Case (a) in Model-1 is approximately six times larger than the satellite current. This is due to the low emissivity of the electron beam. When the emissivity is low, most of the electrons emitted from the orbiter at each time step are collected again by the orbiter as the return current. At next time step, the electrons which are due to the return current and the collection to the satellite are emitted again

from the orbiter. Assuming the amount of the satellite current is constant at each time, eventually the electron beam current and the resulting return current increases. In Case (b) of Model-1, the orbiter current is much reduced compared with that in Case (a). This implies the decrease of the return current.

The orbiter current in Case (d) and Case(e) of Model-2 are ion current. This implies no returning electron beam to the orbiter because the pitch angle of the electron beam are 45 and zero degrees in Case (d) and Case(e), respectively, which enables the beam escape from the orbiter region along B_0.

As for Case (c) in which no electron beam is emitted, the satellite and orbiter current balance each other. Since the ion thermal velocity is approximately ten times lower than the electron's, the ions incoming to the orbiter eventually determine the current balance in the tether system.

We could qualitatively understand the current collection of the tether ends by the above discussion. In the following we estimate it quantitatively in terms of beam emissivity, i.e., the ratio of how much percentage of the total electron beam can escape from the orbiter region. Assuming that the beam current is equivalent to the sum of the satellite current and the return current at the orbiter, we can evaluate the beam emissivity for each case. The emissivity is defined as $1 - i_{rtn}/i_{beam}$ where i_{beam} and i_{rtn} denote the electron beam current and the return current at the orbiter, respectively. For the cases in which the beam pitch angle is 90 degrees, the emissivity is approximately 90 % except for Case (a) in Model-1. As shown in the density plot for Case (a) in Figure 3.2, the electron beam cloud is created in the vicinity of the orbiter rather at the upstream side with respect to the portion of the TSS. Since the most part of the cloud remains in the vicinity of the orbiter, the return current increases and the emissivity eventually becomes low around 13 %. When the initial pitch angle of the electron beam is not a right angle, such as Case (d) and Case (e) in Model-2, no electron return current is observed because the beam electrons can escape from the orbiter region. Hence, the beam emissivity for those cases are 100 %.

Next, we investigate the potential variation of the tether ends. Figure 3.9 shows the time evolution of the electric potential of the tether ends observed in Model-1. The potential value is plotted in terms of energy which is normalized to the electron thermal energy. The upper and lower panels indicate the potential variations for Case (a) and Case (c), respectively. In each figure, ϕ_{stlt} and ϕ_{obt} respectively denote the satellite and orbiter potential with respect to the space potential which is set as zero potential in the present case. The potential difference between the tether ends, $\Delta\phi = \phi_{obt} - \phi_{stlt}$ is kept constant self-consistently. In all the cases, we set ϕ_{stlt} and ϕ_{obt} as $+\Delta\phi/2$ and $-\Delta\phi/2$ at $t = 0$, respectively. As shown in the both panels, the time variation of the potential seems similar, i.e., the potential changes with a high frequency while the net potential varies
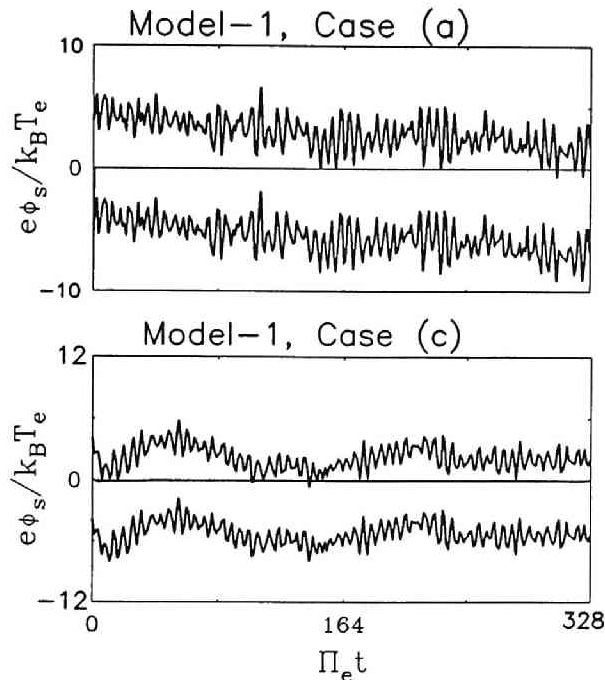
Figure 3.9: Time evolution of the potential at the tether ends for Case (a) and Case (c) of Model-1.

rather slowly. The main difference is found in the variation of the net potential. In Case (a), it simply decreases as time elapses. Owing to the bad emissivity of the electron beam, the continuous accumulation of the negative charges by the return current is responsible for the negative net potential. In Case (c) which represents the non-beam mode, the net potential also becomes below zero eventually because of the accumulation of electrons. However, contrary to the Case (a), the net potential drops abruptly to the negative value at the beginning of the simulation run and it starts to oscillate with a larger amplitude than that in Case (a). Since no beam is emitted in Case (c), the negative charges collected to the TSS in the initial phase are all accumulated in the system. This can lead to the abrupt drop of the net potential which triggers the potential oscillation later on. The oscillation has a frequency approximately at ω_{LHR} which is $0.1\Omega_e$ in the present parameters. Meanwhile, the oscillation with much shorter time period, which is overlapped on the main envelope of the potential profiles in the both cases, has a frequency of ω_{UHR}. This implies the electron oscillation around the tether ends perpendicular to B_0 in Model-1.
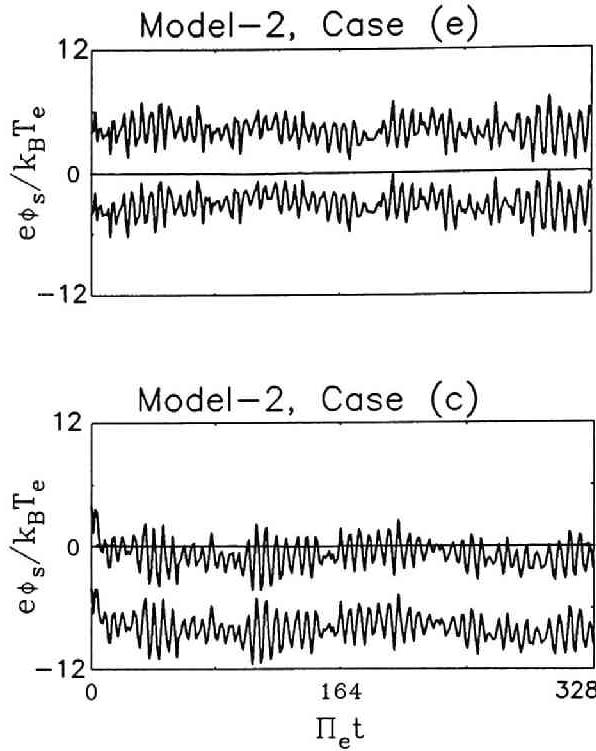
Figure 3.10: Time evolution of the potential at the tether ends for Case (e) and Case (c) of Model-2.

In the same fashion as in Figure 3.9, Figure 3.10 shows the time evolution of the electric potential of the tether ends observed in Model-2. The upper and lower panels indicate the potential variations for Case (e) and Case (c), respectively. Contrary to the potential variation in Model-1, the upper panel for the beam emission case along B_0 shows the ϕ_{stlt} and ϕ_{obt} are maintained as almost their initial values. Namely, the net potential of the TSS is kept almost as the space potential. The beam emissivity can account for the reason. In Model-1 where the system has low emissivity of the beam, negative charges are kept accumulated in the TSS. Hence, the net potential decreases in time as described previously. In Model-2, on the contrary, extra negative charge which is mainly collected to the satellite are almost emitted out with emissivity of 100 %. Then, the potential is not affected by the charge accumulation so that the potential decrease can be hardly observed. In the lower panel for the non-beam case, however, the net potential abruptly drops to the negative value in the

$$e\Delta\phi/k_B T_e$$
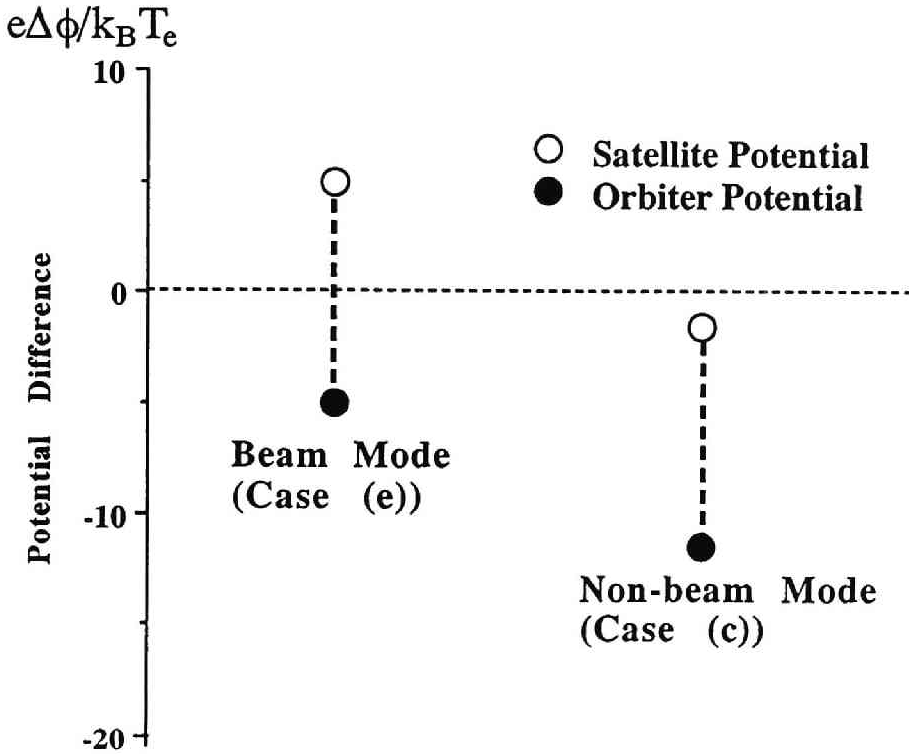
Figure 3.11: Potential values of the tether ends at the steady state for the different cases.

initial phase, which is also shown in Case (c) of Model-1. This is also due to the electron accumulation to the TSS. Regarding the high frequency oscillation in the profile, the frequency is slightly different from that observed in Model-1. In Model-2 which contains B_0 in the model plane, the frequency of the oscillation corresponds to Π_e. This is reasonable because the electrons oscillation along B_0 is stressed during the collection to the satellite. The envelope of the high frequency oscillation also suffers from modulation in the initial phase. The time interval is approximately $70/\Pi_e$, which corresponds to the frequency of $0.18\Omega_e$. This frequency is in between the beat frequency of ω_{UHR} and Π_e, and ω_{LHR}.

To summarize the dependence of the potential variation on the beam emissivity, we present Figure 3.11 which shows the potential values of the tether ends at the steady state for Case (c) and Case (e) in Model-2. The potential values are normalized in the same fashion as those in the previous figure. For Case (e) in which the electron emissivity is almost 100 %, the potential at each tether end keeps its initial value because no excess charge is accumulated in the tether

system. However, as for Case (c) in which no electron beam is emitted the net potential of the TSS becomes negative with respect to the space potential. It is due to the accumulation of the negative charges collected by the TSS.

3.2.4   Field Perturbation

In this section, we investigate the field environment of the TSS. When the $V \times B$ electromotive force is active in the TSS, the current closure is created through the TSS and the ambient plasma because the TSS works as a dynamo in the space plasma. Along the current path, the impedance between the tether ends and the ambient plasma is the largest because the tether ends are the contact surfaces to the ambient plasma. As the result, the field around the tether ends are perturbed as well as the plasma dynamics. During the transient period for the system to approach to the steady state, in particular, the field perturbation will be obvious. In this aspect, this section is devoted to the study on the field response near the tether ends against the change of the TSS potential, which is equivalent to a switch-on of the current system of the TSS. We also compare the results obtained in the beam mode and in the non-beam mode. In the current path associated with the TSS, the tether current is another important factor for the field perturbation. This topic will be discussed in Chapter 5.

In the vicinity of the tether ends which have large cross section to the ambient plasma, the plasma dynamics are greatly modulated due to the potential difference between the tether ends and the ambient plasma. In conjunction with the modulation of the plasma dynamics, the field environment is also affected near the tether ends. We first examine the electrostatic field perturbation by comparing the results in the case of the beam mode and the non-beam mode. Figure 3.12 shows frequency spectra of the perturbations in electrostatic potential in Model-1, Case (b), i.e., the case of the electron beam emission from the orbiter in the plane perpendicular to B_0. The electrostatic fields are measured along two lines in the y axis. One crosses the portion of the TSS at $x/\lambda_D = 0$ and the other does at $x/\lambda_D = 30$ which corresponds to the downstream region. The potential values and the frequency are normalized to $k_B T_e/e$ and Ω_e, respectively. In Figure 3.13, for the comparison, the spectra contour maps are depicted for Case (c) of Model-1 which is the non-beam emission mode. As shown in Figure 3.12 and Figure 3.13, potential perturbation around $\omega/\Omega_e \sim 2.3$ is intense, which corresponds to the oscillation at the upper hybrid resonance frequency $\omega_{UHR}/\Omega_e \sim 2.3$. At the lower frequency range around the lower hybrid resonance frequency ($\omega_{LHR}/\Omega_e = 0.1$), the field enhancement is also found near the region of the tether ends. However, it should be noted that the field profiles for the low frequency range are different between Figure 3.12 and Figure 3.13.
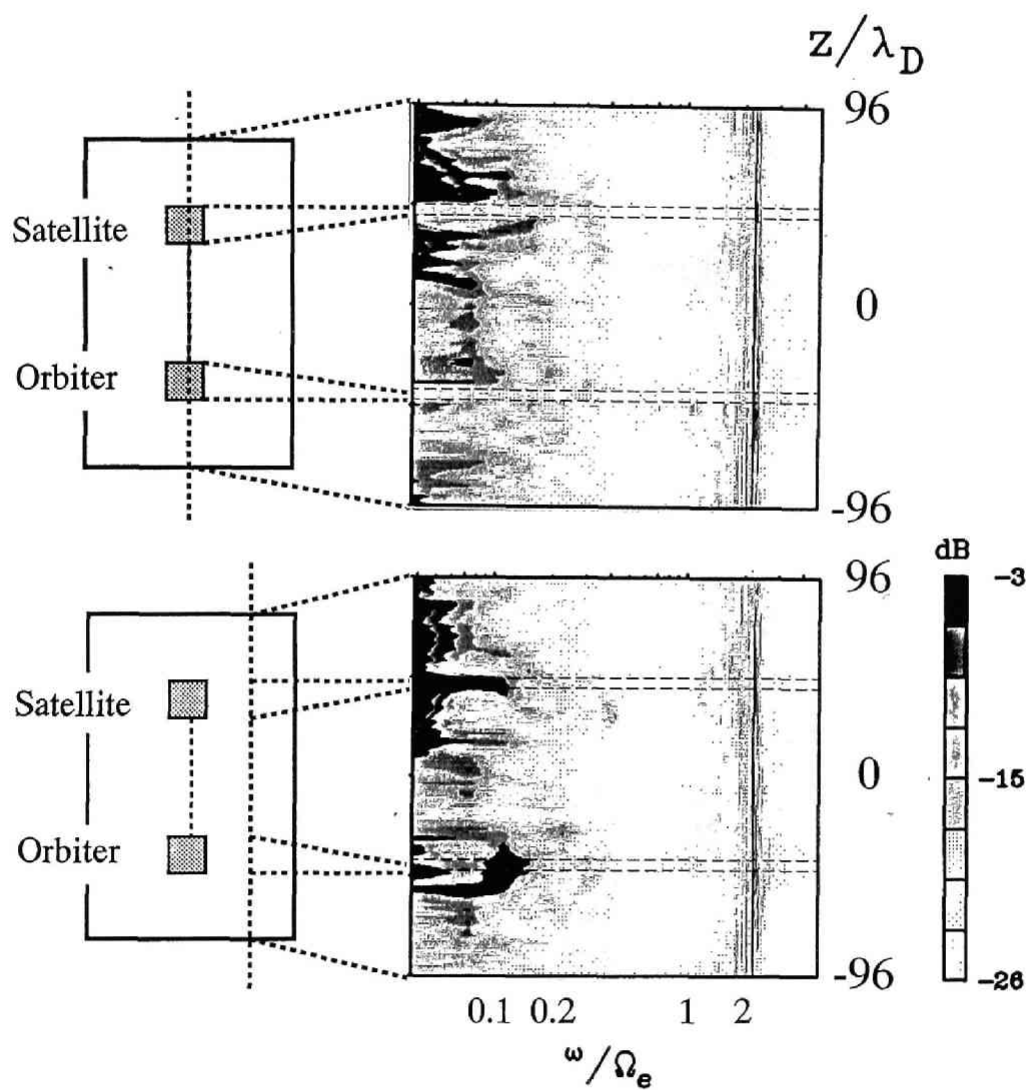
Figure 3.12: Frequency spectra of the electrostatic potential in Case (b) of Model-1 in which the electron beam is emitted downward from the orbiter.
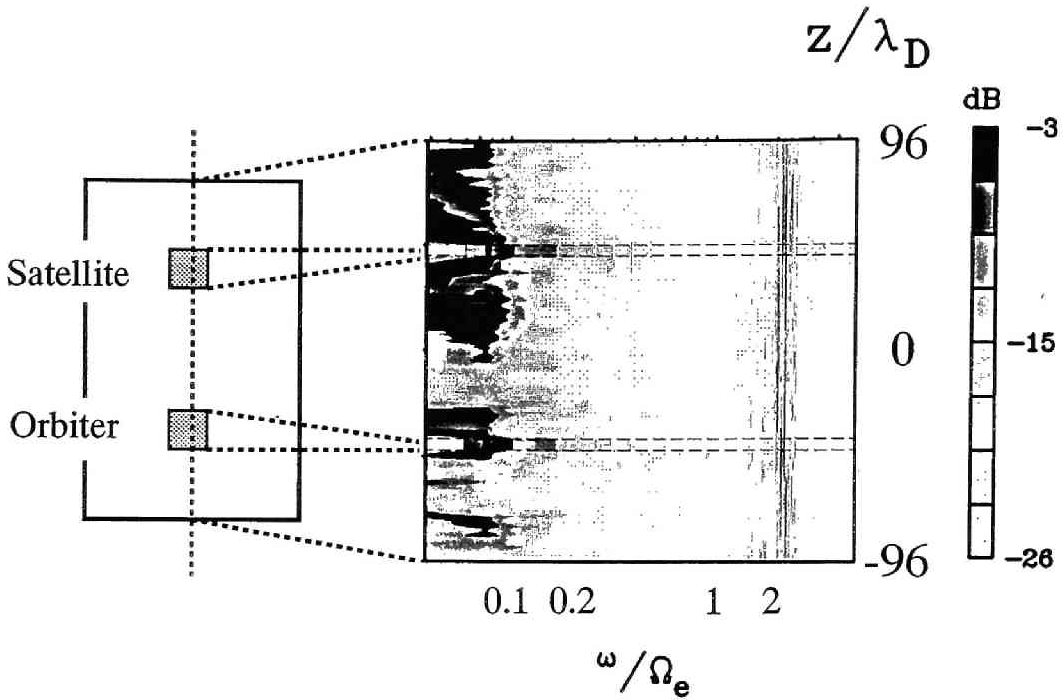
Figure 3.13: Frequency spectra of the electrostatic potential in Case (c) of Model-1 in which no electron beam is emitted from the orbiter.

In the non-beam model, as shown in Figure 3.13, the potential perturbation at the tether ends is the most intense while it is rather quiet at the same region in Figure 3.12 which displays the case of the beam model. The reason for this difference is speculated as follows. In the beam emission model, the extra negative charges collected by the high potential satellite are emitted as beam electrons from the orbiter. Owing to this function, the floating potential of the TSS is maintained not to become much below the space potential. In the non-beam model, on the contrary, the collected charges are accumulated in the TSS, then, the potential of the TSS eventually becomes much negative with respect to the space potential. Because of this difference in potential variation, the oscillation at the low frequency around ω_{LHR} is stressed in the case of the non-beam model as shown in Figure 3.13. In fact, as shown in Figure 3.9 which depicts the time variation of the potential at the tether ends, the oscillation with low frequency is obviously observed in the non-beam model during the transient phase.

Figure 3.14 depicts frequency spectra of the perturbations in the B_y field which contains the electromagnetic component observed in the Case (b) of Model-1. The field intensity is measured in the same fashion as in Figure 3.12.
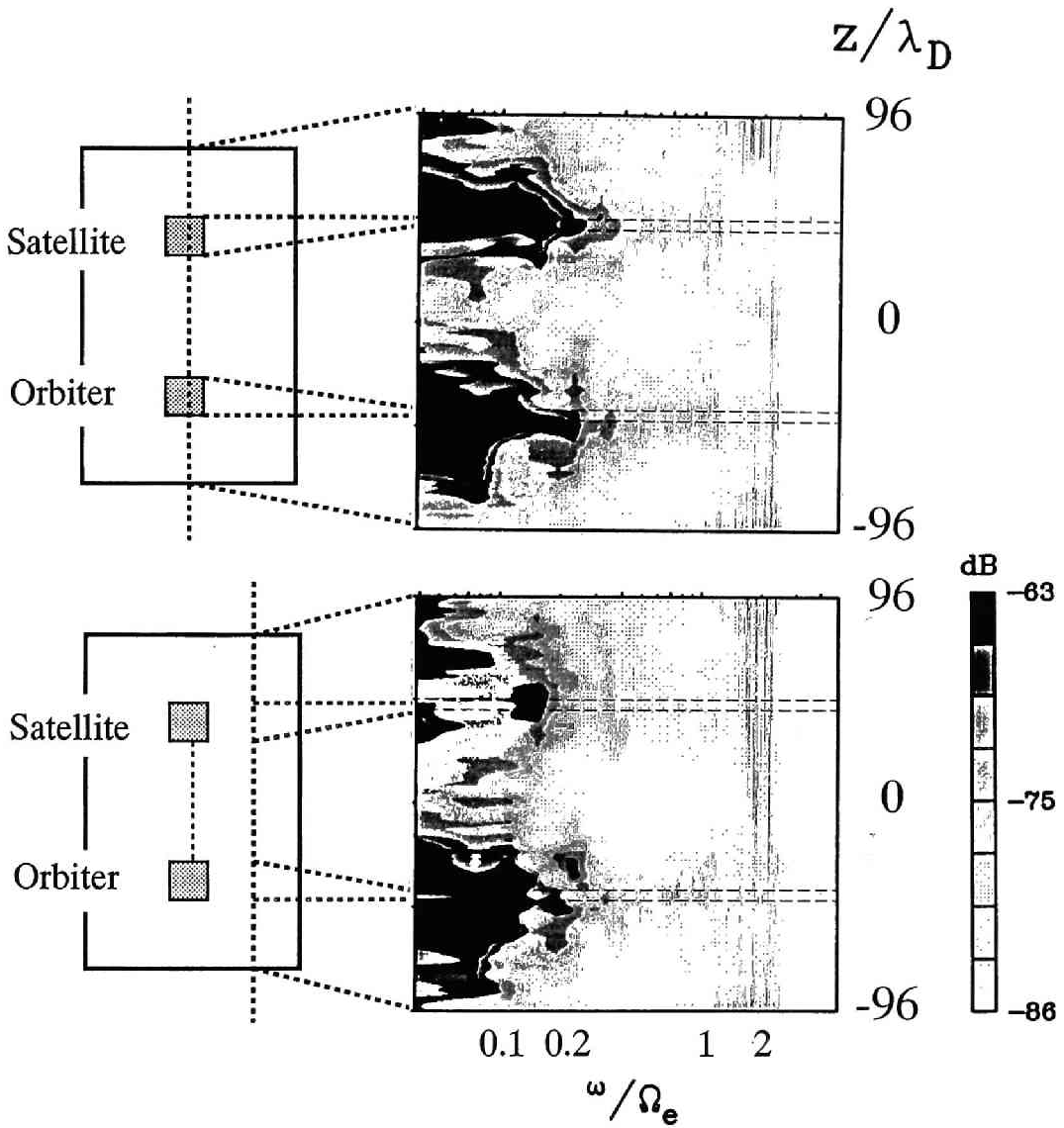
Figure 3.14: Frequency spectra of the B_y field in Case (b) of Model-1 in which the electron beam is emitted downward from the orbiter.

As shown in the upper panel, the field enhancement is observed at the tether ends with low frequency range up to $\omega/\Omega_e \sim 0.3$, which is approximately three times as high as ω_{LHR}. At the downstream region, the low frequency mode remains near the orbiter region while it is damped at the satellite region. Taking account of the location of the electron beam cloud which is shown in Figure 3.2, the frequency spectra suggests the strong correlation between the electron beam cloud and the local field enhancement at the frequency near ω_{LHR}. As shown in Figure 3.12, electrostatic perturbation is also intense at the downstream region which corresponds to the beam electron location.

According to the above analysis, we found the intense perturbations at frequencies of ω_{UHR} and ω_{LHR} around the tether ends and the electron beam cloud. To study the detail, we focus on the spatial distribution of those intense fields in the beam mode. Figure 3.15 displays the spatial profile of the potential perturbation for the LHR mode range in the model plane. In the figure, two squares connected by a dashed line represents the tether ends in the TSS. Primarily, as we examined above, the field activity is high around the tether ends as a transient response to the change of the TSS potential. It is also apparently shown that the field variation at the tether ends, particularly at the satellite, is less active compared with that in the surrounding ambient plasma. An important thing to be noted here is that the low frequency LHR mode is intensively enhanced at the downstream region where the electron beam creats the cloud. Figure 3.16 shows the spatial distribution of the electromagnetic component, i.e., the B_y field in the LHR mode range. The panel (a) and (b) correspond to the field perturbation of Case (a) and Case (b) which deal with the upward and downward beam emission from the orbiter, respectively. Basically, the field perturbation is intense at the tether ends as examined in the electrostatic field. The major difference of the field distribution between the two panels is found around the orbiter region. In the panel (b), the intense field is localized at the downstream region while it sticks to the orbiter region in the panel (a). Taking it into account that the electron beam location as shown in Figure 3.2 corresponds to the region of the intense field perturbation, it is straightforward to conclude that the local field enhancement at the frequency around ω_{LHR} is strongly correlated with the beam-plasma interaction. In the next section, we will examine and discuss the mechanism of the LHR mode wave excitation associated with the electron beam cloud.

Next we analyze the field environment in Model-2 in which B_0 lies along the y direction. Figure 3.17 depicts the frequency spectra of potential in Case (e) in which we emit the electron beam in the direction parallel to B_0. The field intensity is measured in the same manner as in Figure 3.12. Since B_0 lies in the model plane, the electron plasma oscillation is obviously observed at

$$\omega/\omega_{LHR} \text{ (max)} = 3.45$$
$$\omega/\omega_{LHR} \text{ (min)} = 0.38$$
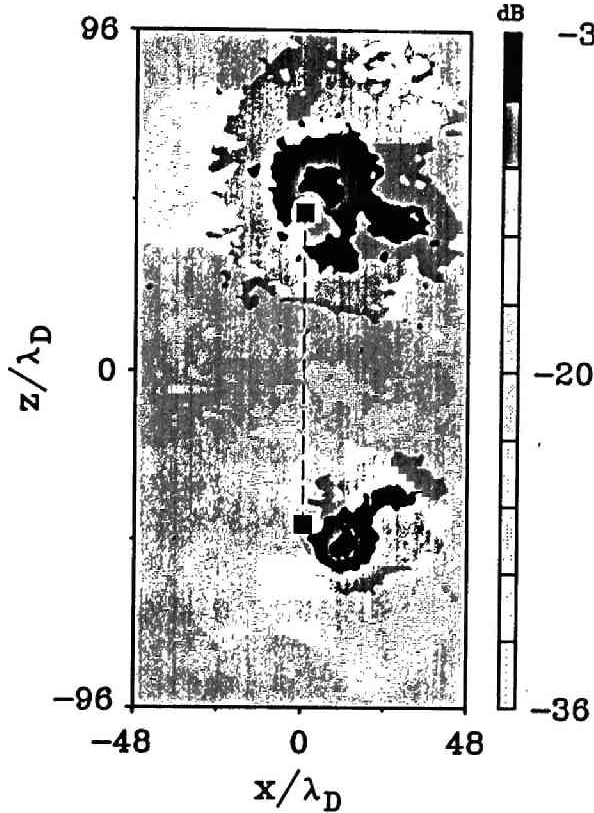
Figure 3.15: Spatial profile of the potential perturbation in the frequency ranges of LHR mode.

frequency of $\Pi_e/\Omega_e = 2$. The electrostatic perturbation is mainly due to the plasma oscillation in the process of the plasma response to the change of the tether potential and the electron beam emission. Namely, electrons which are much lighter than ions are responsible for the enhancement of the oscillation at high frequency of Π_e. Regarding the oscillation at low frequency around ω_{LHR}, ion dynamics which also should be affected by the potential change in the TSS play a role. At the low frequency region, as observed in Model-1, the electrostatic field is strongly perturbed at the region of the tether ends below the frequency of $\omega/\Omega_e = 0.1$ which corresponds to ω_{LHR}. In particular, at the beam electron region which is shown in the orbiter portion in the panel (b), the field enhancement is the most intense. In the panel (a), it is shown that the field activity at the low frequency range is quiet at the tether ends, which is also observed in Model-1. This is owing to the electron beam emission which can

$$\omega/\omega_{LHR} \text{ (max)} = 3.45$$
$$\omega/\omega_{LHR} \text{ (min)} = 0.38$$
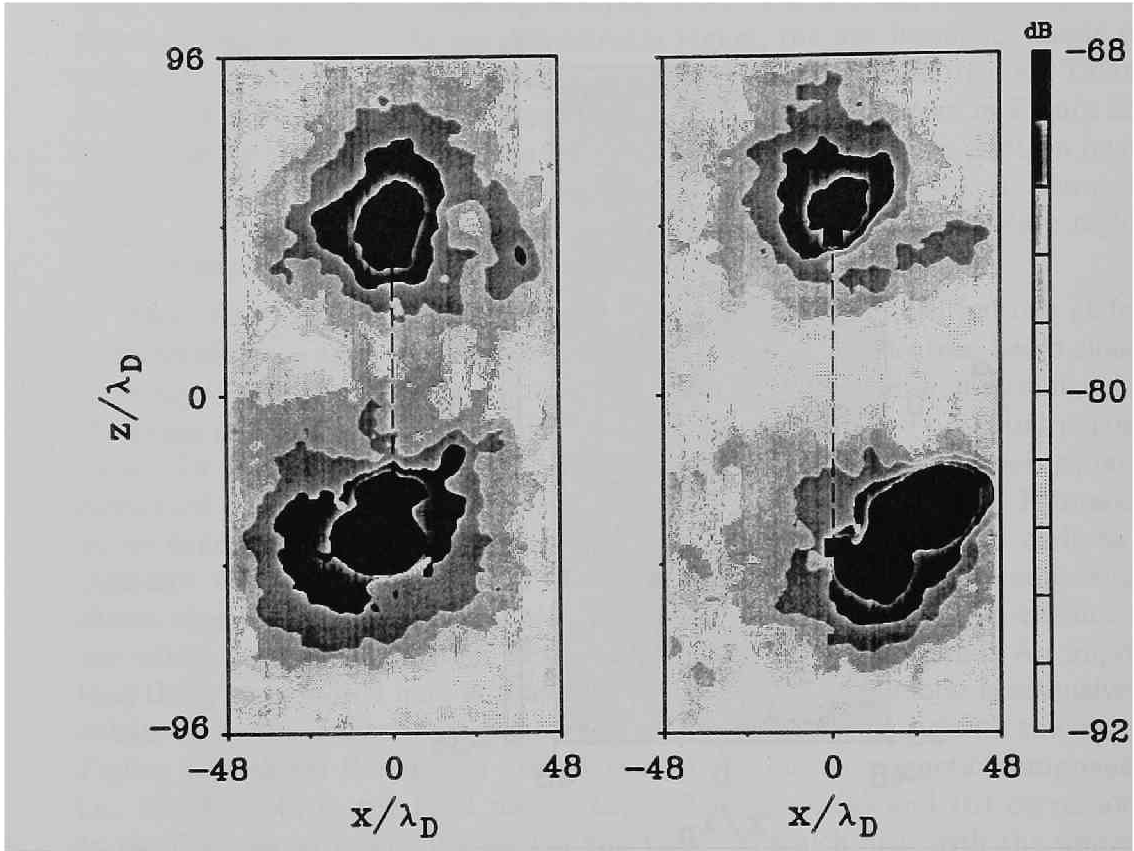
Figure 3.16: Spatial profile of the B_y field in the frequency ranges of LHR mode for (a) the upward beam mode (Case (a)) and (b) the downward beam mode (Case (b)).

get rid of the negative charges from the system and can contribute to stabilize the potential variation of the TSS. The field profile for ω_{LHR} range is shown in Figure 3.18. The region of the intense field spreads along the y direction around the tether ends. In the model plane, the electron beam is emitted from the right side of the orbiter along the y direction with a pitch angle of zero degree. Hence, the most intensive field is observed along the beam orbit.

In terms of electromagnetic field environment, we also analyze the magnetic field perturbation. The panel (a) of Figure 3.19 shows the frequency spectra of the B_y field observed along the line of $y/\lambda_D = 0$. As clearly seen, the magnetic field around ω_{LHR} is dominantly perturbed at the regions of the tether ends. To study the detail of the wave field distribution, we present the spatial profile of the B_y field at frequency range around ω_{LHR} in the panel (b) of Figure 3.19. It is
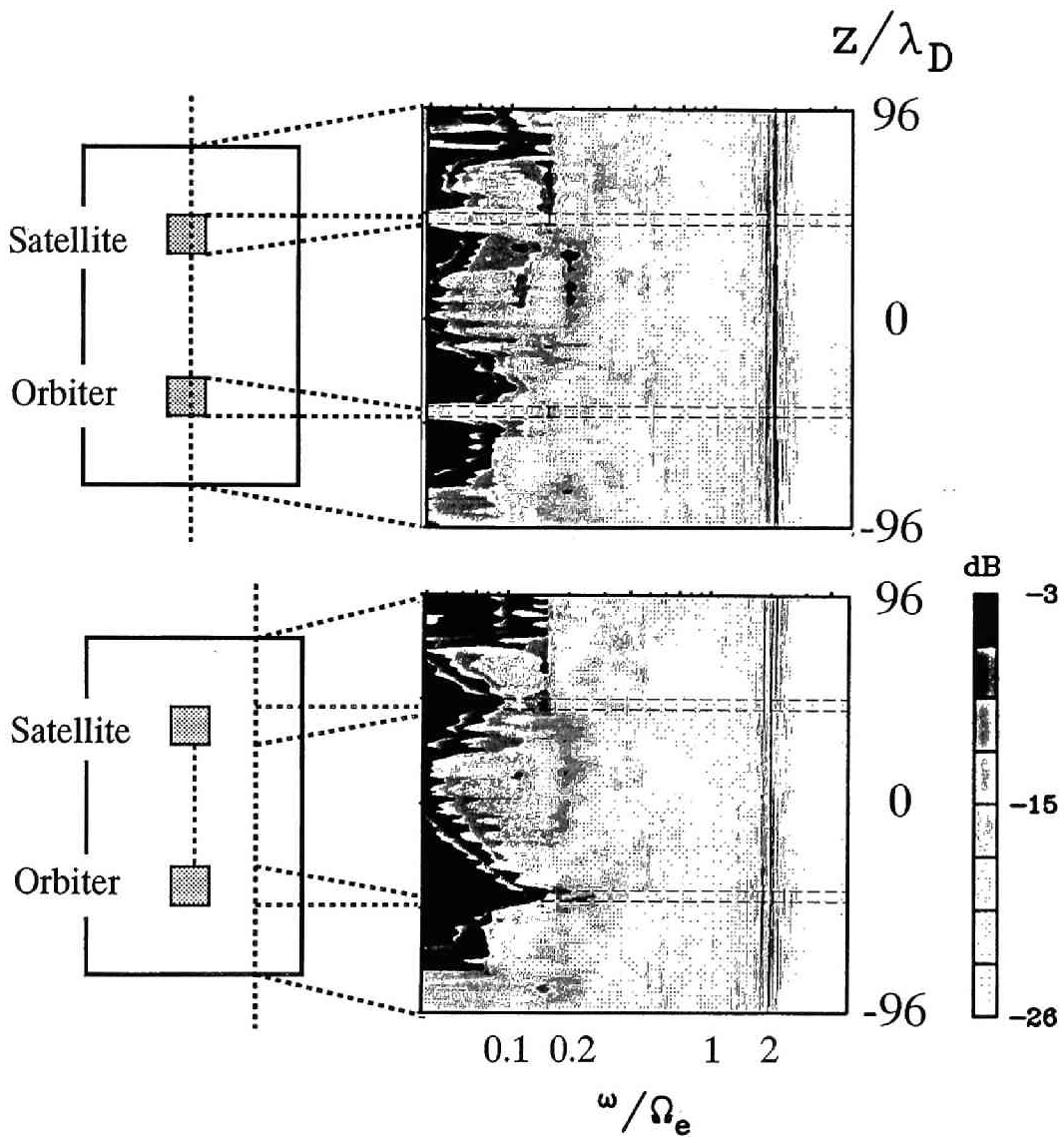
Figure 3.17: Frequency spectra of the electrostatic potential in Case (e) of Model-2 in which the electron beam is emitted along B_0.

$$\omega/\omega_{LHR} \ (\text{max}) \ = \ 3.45$$
$$\omega/\omega_{LHR} \ (\text{min}) \ = \ 0.38$$
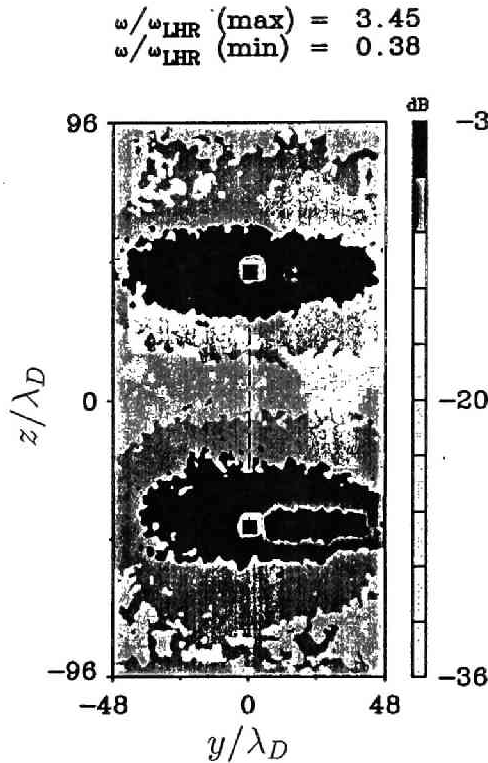
Figure 3.18: Spatial profile of the electrostatic potential perturbation in the frequency ranges of LHR mode.

shown that the region of the intense field perturbation spreads along the direction of the static magnetic field, i.e., the y direction. Particularly, the perturbation of the magnetic field is most intense at the electron beam region as well as the enhancement of the electrostatic field. In general, current variation causes the perturbation in the magnetic field. In the transient stage, the electromagnetic field environment near the TSS can be greatly perturbed as a response to the initial current variation near to the TSS. Regarding the perturbation on the static magnetic field as presented above, the time variation of cross-field current can be responsible. The relation between the current and the magnetic field perturbation will be discussed in the next section. We will also focus on the field perturbation associated with the high potential tethered satellite in Chapter 5.

3.2.5   Discussion

As described in the previous series of sections, the two-dimensional computer experiments could reveal some of the basic physics associated with the electrodynamic interactions between the TSS and its surrounding plasma. One significant

(a)

z/λ_D
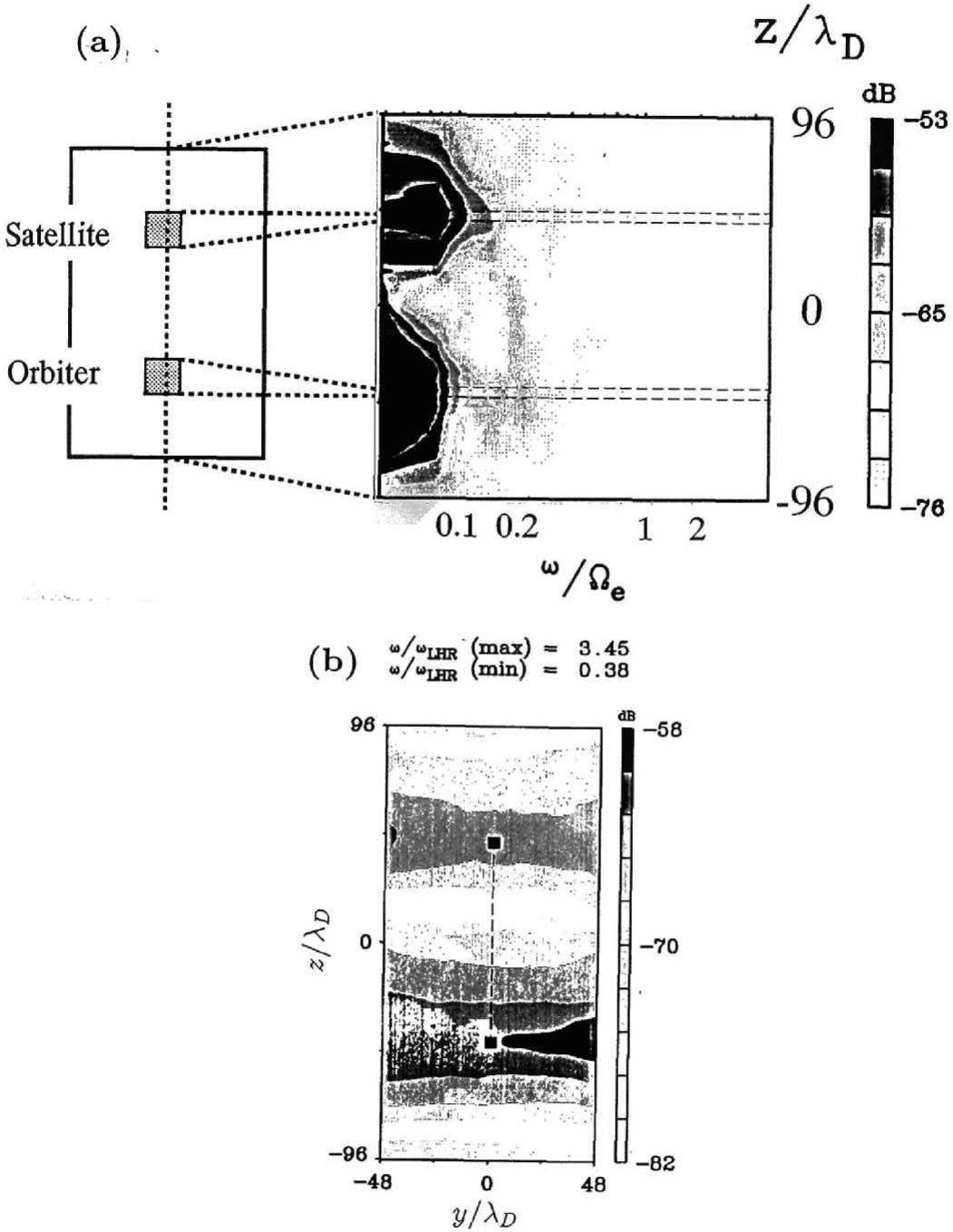
Figure 3.19: (a) Frequency spectra of the B_y field in Case (e) of Model-2 in which the electron beam is emitted along B_0. (b) Spatial profile of the B_y field perturbation in the frequency ranges of LHR mode.
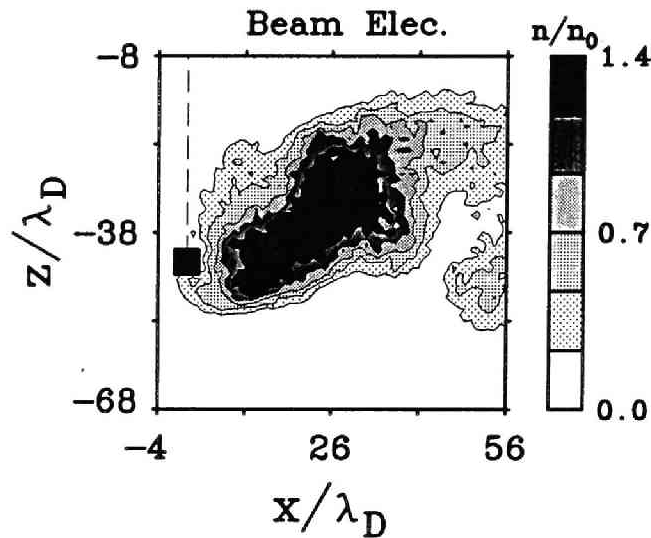
Figure 3.20: The magnified contour map of the number density for the electron beam cloud in Model-1.

issue to be discussed is the mechanism of the local LHR mode excitation associated with the electron beam emission from the orbiter. Here we seek a possible mechanism of the local LHR mode excitation.

First, we pay our attention to the energy source for the wave excitation. Since the wave is excited at the beam cloud region, we examine the properties of the cloud. As a reference, Figure 3.20 depicts the magnified contour map of the electron beam cloud. The profiles of the electrical potential and the current density in the vicinity of the orbiter is also shown in Figure 3.21. The rectangle in the figure indicates the orbiter. The potential values are obtained by solving Poisson's equation with use of the charge density at each grid point. It is found that a potential well due to the electron beam is clearly created at the beam cloud region. This implies inward electric field toward the center of the cloud. In particular, at the lower side of the cloud, the electric field is the most intense because of the steepest gradient of the potential. Since B_0 is perpendicular to the simulation plane, this electric field causes the cross-field vortex-like motion of electrons around the cloud with $E \times B$ velocity. Ions, which are weakly magnetized due to its large mass, move along the radial electric field. This difference of motion leads to a relative velocity between electrons and ions in the azimuthal direction, which causes cross-field current flow around the cloud as shown in the panel (b) of Figure 3.21. The cross-field current due to the electron $E \times B$ drift is obviously seen in the clockwise direction around the beam cloud.

This current can be the energy source for the perturbation of the LHR mode as shown in Figure 3.22.

To account for the LHR mode enhancement by the cross-field current, the theories of the modified two-stream instability and the lower-hybrid drift instability have been proposed. The characteristic frequency and growth rate enhanced by the instabilities are both comparable to the lower-hybrid frequency. At the plasma cloud such as observed in the present computer experiments, the relative electron-ion motion in the azimuthal direction can be generally written in the fluid approximation as

$$v_d = |E \times B|/B^2 + v_{ne} = V_g + |v_{ni}| + v_{ne} \tag{3.1}$$

Here $V_E = |E \times B|/B^2$, the density gradient drift $v_{nj} = \epsilon_{nj} T_j / m_j \Omega_j$, and $V_g = dV_i/dt\Omega_i$ where T_j, m_j, n_j, Ω_j, V_i and ϵ_{nj} denote the temperature, mass, density, gyrofrequency, velocity and the inverse density gradient length $|\nabla n_j/n_j|$ of the j-*th* species, respectively. When the term of the plasma density gradient is negligible in (3.1), the instability is categorized in the modified two-stream instability. When the plasma density gradient is apparent such as in the present case, the lower-hybrid drift instability can become dominant.

The theory of the lower-hybrid drift instability has been intensively studied in recent years. The local dispersion relation for the lower-hybrid drift instability was driven in a fully self-consistent manner including the finite electron temperature T_e, ∇B_0 electron orbit modifications [Davidson et al., 1977], electron temperature gradients, and finite $k_\parallel$ which is the component of wave vector parallel to B_0 [Zhou et al., 1983; Hsia et al., 1979]. However, when the electron temperature is finite, the problem becomes complicated and it is not our purpose to handle it in this paper. In fact, the beam electron emitted from the orbiter in the present computer experiment is cold. Therefore we just allow the finite temperature for ions but $T_e = 0$.

Here we show the linear dispersion relation obtained by Winske [1989]. The geometry used in the derivation is shown in Fig. 3.23. The density n and external magnetic field B_z are assumed as slow varying functions with respect to x; $n = n_0(x)$, $B_z = B_0(x)$. The wave vector k is pointed to the y direction. Under the assumption that electrons are magnetized while massive ions are unmagnetized, the linear dispersion relation is derived in the conventional way from the fluid equations for electrons and ions and Maxwell's equations. For simplicity, we first assume that both electrons and ions are cold and later include the effects of the finite ion temperature.

The cold dispersion relation is given;

$$1 + \frac{\Pi_e^2}{\Omega_e^2}(1 + \frac{\Pi_e^2}{c^2 k^2}) - \frac{\Pi_e^2}{k\Omega_e}(\frac{n_0'}{n_0} - \frac{B_0'}{B_0})\frac{1}{\omega - kV_E} - \frac{\Pi_i^2}{\omega^2} = 0 \tag{3.2}$$
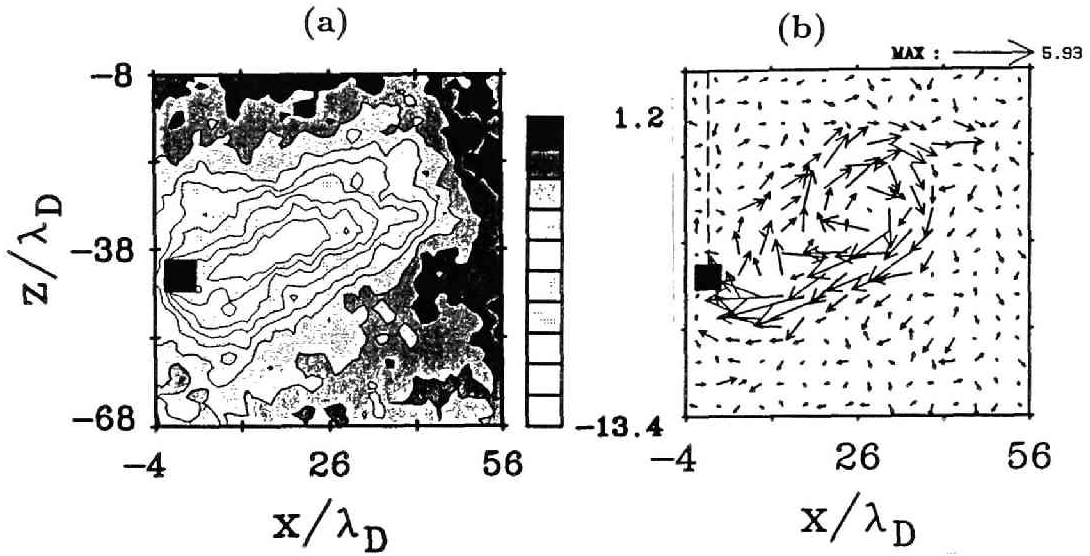
Figure 3.21: (a) Spatial profile of the potential and (b) vector plots of the current density at the beam cloud region in Model-1.
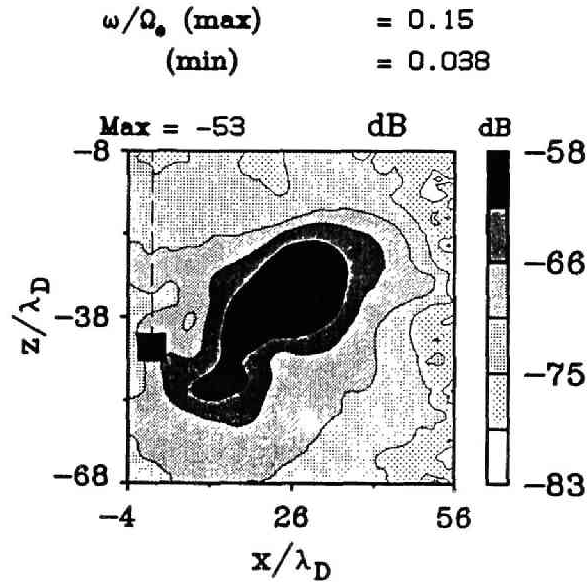
Figure 3.22: Spatial profile of the B_y field in the vicinity of the orbiter in Case (b) of Model-1.
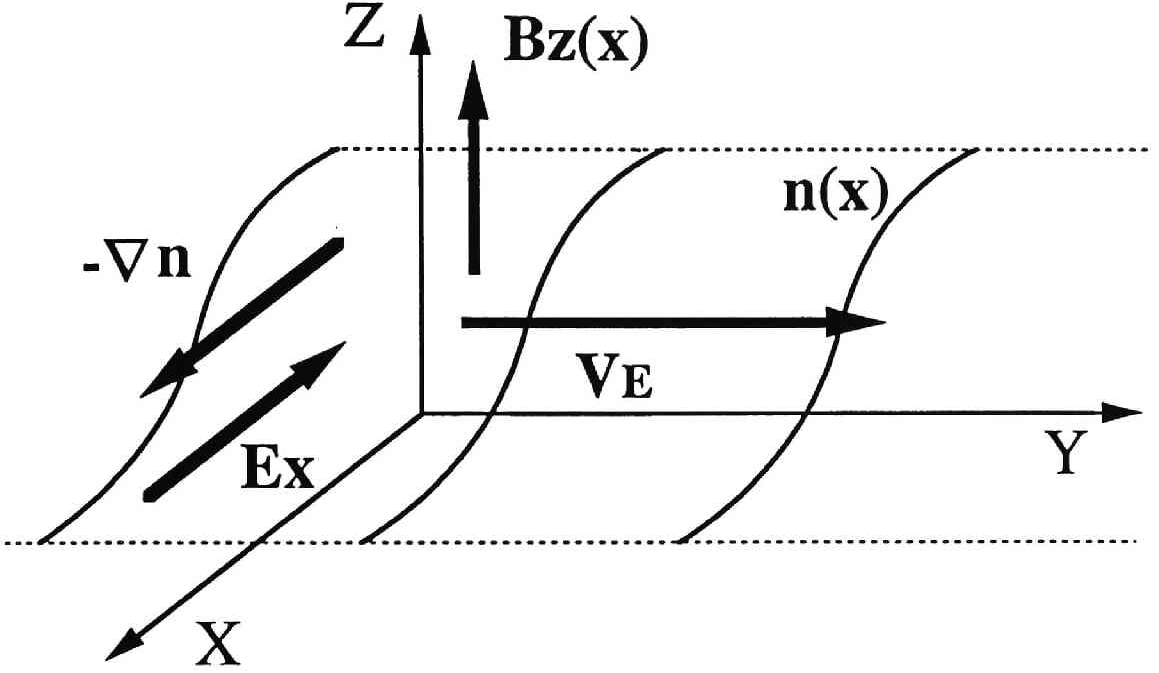
Figure 3.23: Schematic illustration of the geometry used in the calculations of the linear dispersion relation.

where c, ω, and k denote the light speed, frequency, and wavenumber, respectively. The prime in the above equation denotes d/dx. The Π_e^2/c^2k^2 in the second term of (3.2) is the electromagnetic component. The gradient effects is represented in the third term, and the last term is due to the ion contribution.

As for the magnetic field gradient, Ampere's law gives

$$\frac{B_0'}{B_0} = \frac{1}{B_0}\frac{dB_0}{dx} = \frac{\Pi_i^2}{\Omega_i}\frac{V_E}{c^2}. \tag{3.3}$$

By defining $L_i = c/\Pi_i$, and multiplying (3.2) by $v_A^2/c^2 (= \Omega_i^2/\Pi_i^2)$, (3.2) is rewritten as;

$$\frac{v_A^2}{c^2} + \frac{m_e}{m_i} + \frac{1}{k^2L_i^2} + \frac{\epsilon_{n_i}/k}{\omega/\Omega_i - kV_E/\Omega_i} + \frac{(V_E/v_A)/kL_i}{\omega/\Omega_i - kV_E/\Omega_i} - \frac{\Omega_i^2}{\omega^2} = 0 \tag{3.4}$$

where v_A is the Alfvén velocity.
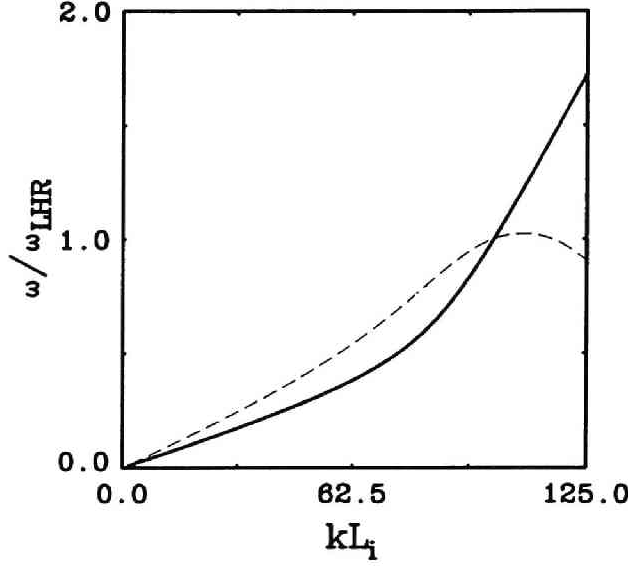
Figure 3.24: The $\omega - k$ diagram for the lower-hybrid drift instability obtained with the parameters used in the computer experiments.

Now we include the finite T_i in the equation above. The last term representing the ion effect is modified with the plasma dispersion function Z.

$$\frac{v_A^2}{c^2} + \frac{m_e}{m_i} + \frac{1}{k^2 L_i^2} + \frac{\epsilon_{n_i}/k}{\omega/\Omega_i - kV_E/\Omega_i} + \frac{(V_E/v_A)/kL_i}{\omega/\Omega_i - kV_E/\Omega_i} - \frac{1}{k^2 L_i^2 \beta_i} Z'\left(\frac{\omega/\Omega_i}{kL_i\beta_i^{1/2}}\right) = 0$$

(3.5)

where we define the ion beta as $\beta_i = 2\mu_0 n_i T_i / B_0^2$. If the quantities such as V_E/v_A, β_i, and $\epsilon_{n_i} L_i$ are known, the dispersion equation (3.5) gives us the complex frequency $\omega = \omega_r + i\gamma$ at each k value.

We now apply those quantities obtained in the computer experiment to the dispersion equation. At the equilibrium state when the beam cloud formation is completed, the maximum value of $|\epsilon_{n_i}|$ is approximately 0.1 at the steepest gradient of the cloud. β_i is a bit increased to approximately 0.01 owing to the effect of ion attraction to the beam electrons. Taking account of the intensity of the electric field at the edge of the cloud, V_E/v_A is obtained as approximately 0.4. Using the parameters stated above, Figure 3.24 is obtained which presents the complex frequency $\omega = \omega_r + i\gamma$ at each k value. The real part ω_r and imaginary part γ are indicated with solid and dashed lines, respectively. The frequency is normalized to the local lower hybrid frequency $\omega_{LHR} \simeq \sqrt{|\Omega_e|\Omega_i}$. As shown

clearly, γ which represents the growth rate has the peak at $kL_i \simeq 110$, i.e., $k = 0.22$, where the real part of the frequency is $\omega/\omega_{LHR} \simeq 1$. This implies that the most unstable mode in the simulation have the frequency around ω_{LHR}, which shows good agreement with the simulation result. Regarding the wavelength, it is approximately 28.6 according to the wave number at the maximum growth rate. Owing to the continuous beam injection to the plasma, the beam cloud in not symmetrically created in the azimuthal direction. Thus the mode number which is supposed to be confirmed at the edge of the cloud cannot be determined in this computer experiment. To discuss the details of the LHR mode wave including the wavelength, we need to perform a computer experiment focusing on the plasma cloud only, which is left as a future work.

It is clarified that the excited LHR mode wave is a drift mode owing to the nonuniform cloud caused by the beam-plasma interaction, not the Cherenkov or cyclotron radiation such as Alfvén wings due to a current source moving across B_0. In Model-1, the wave field is most intense at the edge of the cloud where the density gradient is large. In Model-2, although the intensity is much less than that observed in Model-1, the LHR mode is also enhanced along the beam orbits, in particular, at the edge of the beam. These facts suggest that the density gradient at the beam region, which induces the $E \times B$ cross-field drift of electrons, can cause the enhancement of the LHR mode wave. When the initial pitch angle of the electron beam differs from a right angle, most of the emitted electrons escape from the orbiter region along B_0 leading to less steep beam density gradient. Therefore the enhancement of the LHR mode waves owing to the density gradient in the realistic case is not as intense as observed in the present computer experiments. Instead, whistlers and plasma waves become dominant emission due to field-aligned injection of the electron beams [Omura and Matsumoto, 1988; Winglee and Kellogg, 1990].

Although not as intense as observed at the beam cloud region, the field is also perturbed at the frequency of ω_{LHR} at the satellite region. it also can be enhanced by the plasma instability driven by the density gradient at the edge of the sheath or the rarefactional region at the downstream region. However, taking account of the abrupt change of the TSS potential, the field oscillation at the tether ends is due to the transient response to the plasma oscillation. This is speculated by the fact that the activity of the low frequency field at the tether ends is much lower in the beam-emission mode in which the initial TSS potential is maintained in time than in the non-beam mode where the TSS potential drops abruptly because of the charge accumulation.

Besides the LHR mode excitation, the essential phenomena are well studied with the present model such as the electron absorption to the satellite, electrostatic oscillation at the tether ends, and electron beam dynamics. Regarding
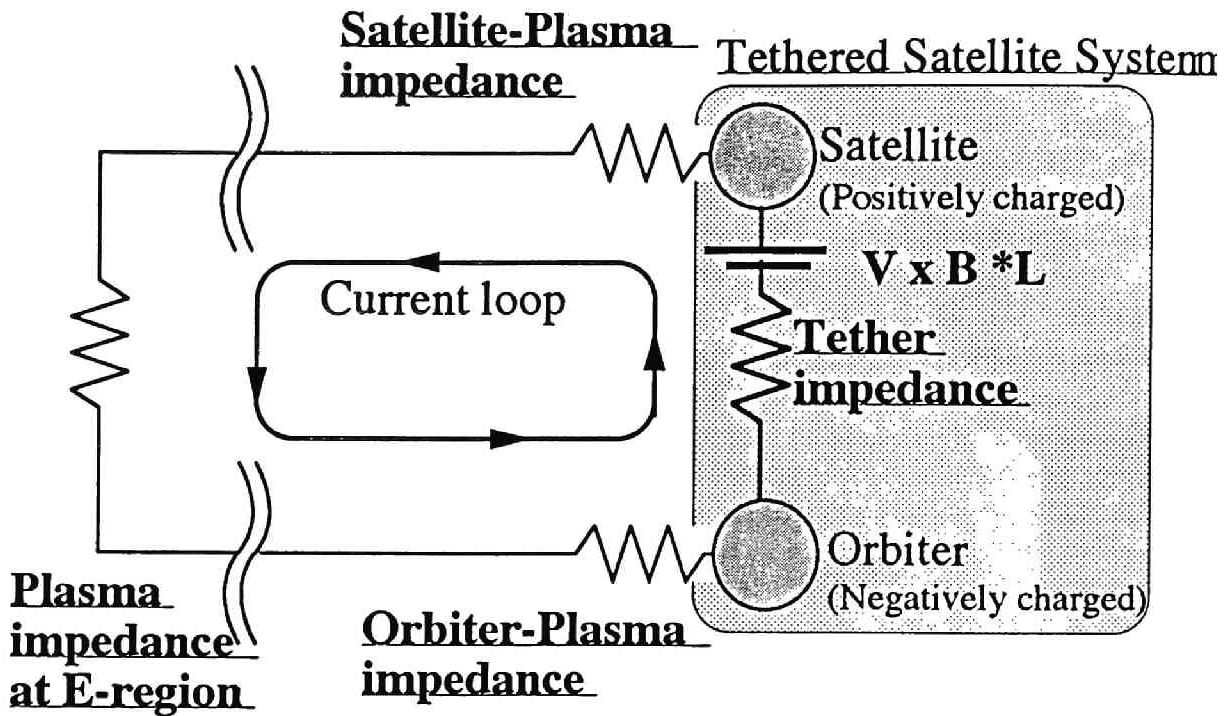
Figure 3.25: Schematic illustration of the current system through the ambient plasma and the TSS.

current path, we have clarified the field-aligned structure formed from the tether ends caused by the electron absorption to the satellite and electron emission from the orbiter in the steady state. Owing to the motion of the electrodynamic tether system across B_0, potential difference due to the electromotive force is generated between the tether ends. This dynamo can form a current system including the TSS and the ambient plasma surrounding it. Figure 3.25 shows a schematic illustration of the current system. As observed in the computer experiments, the currents are mainly carried by electrons along B_0. In the real situation, the current path is believed to be closed in the E-region of the ionosphere where the transverse electrical resistivity is small [Banks et al., 1981]. Qualitatively, the current path is predicted by the present computer experiments. However, it is difficult to answer the question of how much current can be drawn in such a current system. This is mainly because of unknown impedance in the current loop such as the satellite-plasma impedance and the orbiter-plasma impedance.

Assuming that the resistance of space plasma is low enough because the plasma is a conductive media, the major impedance is loaded at the contact surface between the conducting parts of the TSS and the space plasma. In this aspect, the satellite-plasma and orbiter-plasma impedances are important in determining the intensity of the current flow in the current loop. In particular, the latter impedance depends on the ways of the electron beam emission from the orbiter. As examined in the previous section, the beam emissivity is dependent on the initial pitch angle of the beam electron. It is noted that the total current in the current loop is maximized when the initial pitch angle of the beam is equal to zero. In terms of the satellite-plasma impedance, the plasma depletion by the positively biased satellite [Thompson, 1989] and the electron sheath formation are the major factors to control the current collection of the satellite. We will examine the current-voltage characteristics of the satellite in detail in the next chapter.

Regarding the electrostatic environment of the orbiter, it differs from that of an isolated single vehicle and it also causes the difference of the electron beam dynamics. In the case of beam emission from an isolated vehicle, the beam emissivity can be determined by the balance between the kinetic energy of the beam electrons escaping from the orbiter region and the potential energy due to the positively charged orbiter which causes the return current. In the present model, however, the orbiter, as one of the tether ends, keeps negative potential even if it emits electron beam. Then the electrons emitted from the orbiter are repulsively accelerated away due to the negative potential of the orbiter as well as the repulsion of the beam cloud itself. In this sense, the beam emissivity at the orbiter in the TSS may be larger than that of the isolated single vehicle.

Because of the restriction of the available memory and speed of the computer, the model in the present computer experiments does not give the same configuration as that of SETS in terms of dimension, the shape of vehicle, the way of electron beam injection, $e\Delta\phi/k_B T_e$, etc. Since we adopt the small $e\Delta\phi/k_B T_e$, the current-voltage characteristics, which is one of the crucial questions in electrodynamic tethers, is not obtained in the present computer experiments. In the next Chapter, we will focus on the satellite-plasma interaction such as the plasma response in terms of density variation and current path. We will also examine the current-voltage characteristics of the satellite.

3.3 Three-Dimensional Electrostatic Particle Model

3.3.1 Model and Parameters

The TSS with relative motion to the ambient plasma is unique in terms of its geometric configuration. The directions of the plasma flow, B_0, and the TSS are orthogonal to each other. In the previous sections, taking account of this configuration, we studied the basic physics of the electrodynamic interaction between the TSS and the ambient plasma by the two-dimensional computer experiments. In the actual three-dimensional space, however, it is not confirmed whether the results obtained in the two-dimensional computer experiments can be observed or not. In addition, there might be possibility to find phenomena which are peculiar to the three-dimensional configuration and cannot be seen in the two-dimensional space. Fortunately, owing to the rapid growth of the hardware of computers which provides us enough memories and speed of CPU, three-dimensional computer experiments becomes available. This situation enables us to perform three-dimensional computer experiments of the electrodynamic tether system with the three-dimensional configuration stated above for the first time. As shown in the plasma density profiles and the current path, the interaction between the TSS and the ambient plasma is mostly electrostatic. This is because that the energy source driving those plasma response is the electrostatic potential difference between the tether ends. Taking account of this, we put an emphasis on the electrostatic responses of the ambient plasma and the electron beam and use the three-dimensional electrostatic particle code which was described in Chapter 2.

The configuration of the model space is displayed in Figure 3.26 which is primarily the same as the one used in the two-dimensional computer experiments. The directions of the plasma flow V_p and the external magnetic field B_0 are along the x and the y axes, respectively. The potential values at the outer boundaries surrounding the model space are set to be zero. In the model space, the TSS is set along the z axis. Two conducting bodies representing a satellite and an orbiter have the same dimensions as $3\lambda_D \times 3\lambda_D \times 3\lambda_D$. They are located with a distance of approximately $30\lambda_D$ each other. For numerical brevity, as applied in the two-dimensional cases, the charge separation at the tether ends due to the electromotive force is calculated by the Capacity Matrix Method. The detail of this method is described in the previous chapter. Regarding the potential difference between the two tether ends $e\Delta\phi/k_B T_e$, we adopt two cases; one is $e\Delta\phi/k_B T_e = 10$ which is the same as previously used in the two-dimensional model for the comparison with the results obtained in the
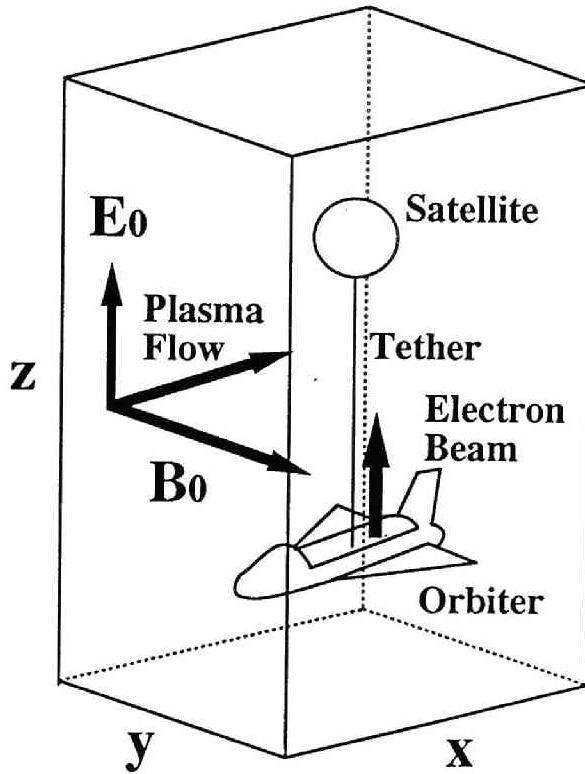
Figure 3.26: Schematic illustration of the model space for the three-dimensional computer experiments of the TSS.

two-dimensional computer experiments. The other is $e\Delta\phi/k_B T_e = 100$, which is utilized to emphasize the plasma response to the TSS. This large potential difference enable us to examine the detail of the plasma response such as the formation of sheath and rarefactional wake.

To avoid the excess charging of the TSS, an electron beam is injected from the orbiter into the ambient plasma. The way of the electron beam emission is the same as that in the two-dimensional computer experiment. For simplicity, we emit the same number of beam electrons as that of incoming electrons at each time step from the orbiter upward with a right angle of the initial pitch angle. No-beam emission model is also adopted to the computer experiments.

The physical parameters used in the computer experiments are almost the same as we used in the two-dimensional cases stated in the previous sections. Because of the limitation to the speed and memories of the computer, we reduced
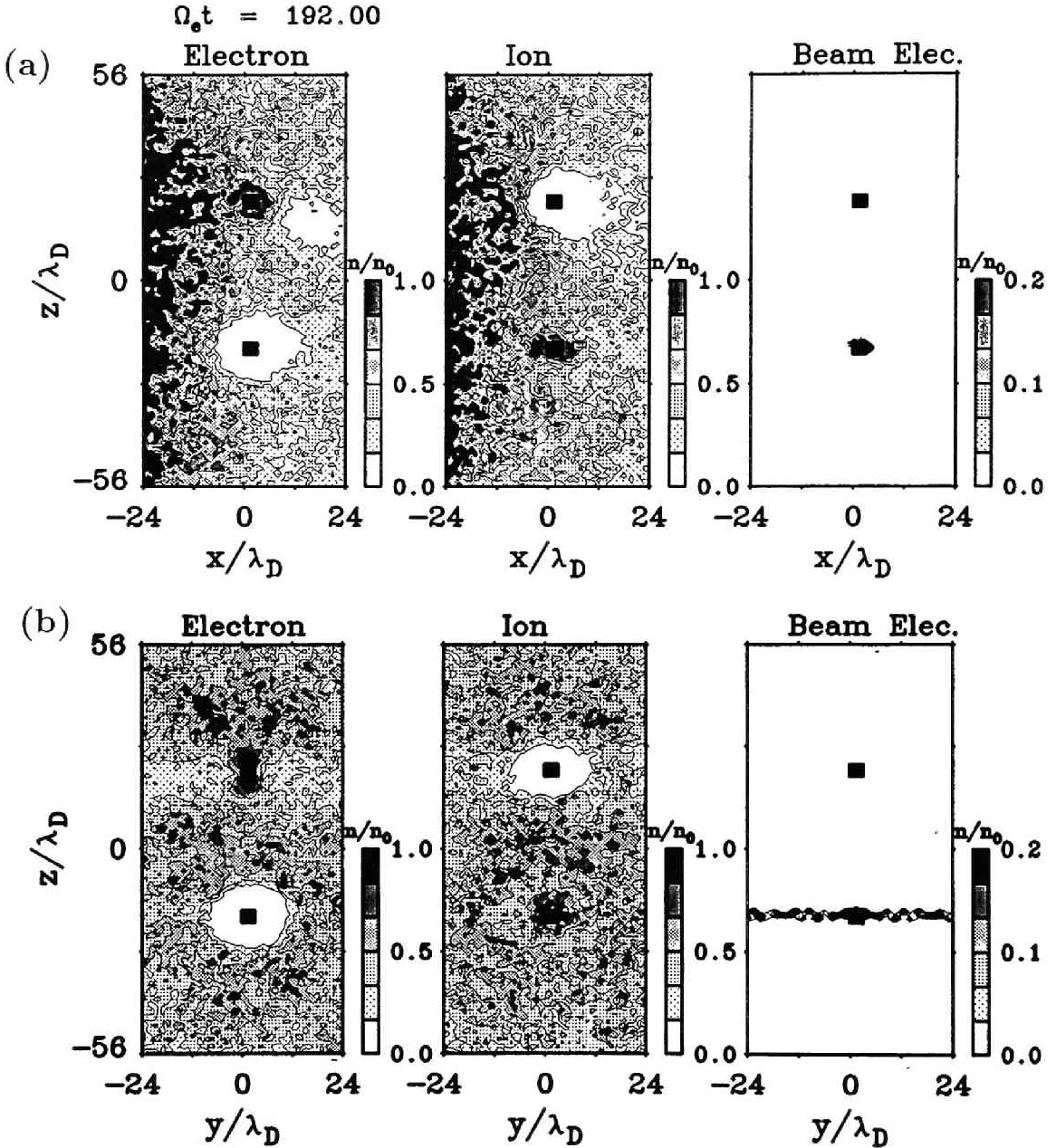
Figure 3.27: Contour maps of the number densities for the background electrons, ions, and beam electrons in (a) $x - z$ plane and (b) $y - z$ plane, respectively. The results obtained in the three-dimensional computer experiments with $e\Delta\phi_s/k_B T_e = 100$.

the size of a model space in this three-dimensional study. The dimensions of the model space are $64 \times 64 \times 128$ in the x, y, and z directions, respectively. The grid spacing is taken as $\Delta r = \lambda_D$. In electrostatic model, the Courant-Fredericks-Lewy (CFL) condition which provides the limitation of Δt is no more valid because of no need to consider the propagation of the speed of light. Then we can choose much larger Δt than the one we used in the electromagnetic model. In the present study, $\Delta t = 0.1/\Omega_e$ is selected which is still small enough for us to trace the plasma dynamics correctly. The number of the superparticles is 2,097,152 for each species of plasma particles at the initial state. The outgoing particles which have crossed the boundary planes are no more traced. To compensate the particles in the model box, the thermal plasma is injected from the $y - z$ planes at the edge of the x axis. For ambient electrons, $\Pi_e/\Omega_e = 2$, and $v_{te}/V_p = 8$. For ambient ions, $\Pi_i/\Omega_e = 0.2, \Omega_i/\Omega_e = 0.01$, and $v_{ti}/V_p = 0.8$. We carried out the simulation run up to $\Omega_e t = 327$. In the following section, we describe the results obtained in the three-dimensional computer experiments with the configuration and the parameters stated above.

3.3.2 Ambient Plasma Response and Beam Dynamics

The plasma response to the TSS is examined in terms of plasma number density in the three-dimensional space. In the three-dimensional model, Coulomb's force between charges is proportional to r^{-2} while it is r^{-1} in the two-dimensional model where r denotes the distance between the charges. This implies that the force in the three-dimensional space becomes weak more drastically than that in the two-dimensional space as the distance r increases. This difference of the basic physics will greatly affect the plasma response to the TSS. In addition the plasma dynamics itself differ from that of two-dimensional case because the spatial variation of the plasma dynamics is allowed in the direction of the third dimension in the three-dimensional case. Qualitatively, however, the plasma response to the TSS such as electron attraction and ion repulsion to and from the satellite will be the same as that observed in the two-dimensional cases, respectively. In the aspects stated above, we will describe the density variation in the vicinity of the TSS observed in the three-dimensional computer experiments in this section.

To obtain a clear profile of the plasma response to the TSS, $e\Delta\phi_s/k_B T_e$ adopted in the three-dimensional cases is 20 times as high as that used in the two-dimensional cases. The plasma density is obtained at each grid point in the three-dimensional space. To obtain better comprehension of the density variation, we cut two planes out of the model box; the $x - z$ and $y - z$ planes corresponding to Model-1 and Model-2 used in the two-dimensional computer

experiments in the previous sections. The $x - z$ and $y - z$ planes are parallel and perpendicular to the plasma flow, respectively. Figure 3.27a and Figure 3.27b show the contour maps of the number densities for the background electrons, ions, and the beam electrons in the $x - z$ plane and $y - z$ plane, respectively. In each panel, the upper and the lower squares indicate the satellite and the orbiter, respectively.

Around the tether ends the plasma distribution is greatly modulated by their potentials. At the satellite region, an electron sheath is clearly formed while ions in the vicinity of the orbiter are evacuated due to the repulsion from the positive potential of the satellite. The sheath structure shows directional dependence with respect to B_0. As shown in Figure 3.27a, the sheath is uniformly formed around the satellite in the $x - z$ plane. In the $y - z$ plane as shown in Figure 3.27b, however, the sheath is much thicker in the direction perpendicular to B_0, i.e., along the z direction, than parallel to it. This is because of the directional dependency of the electron mobility; the electrons attracted by the satellite are hard to move across B_0 while they are mobile along it. Low density region of electrons along B_0 in the satellite region is due to the electrons attraction to the positive potential of the satellite. In result, the electron sheath forms a donut-like structure around the satellite as speculated from the density profile in the both planes. At the downstream region of the satellite, a rarefactional region with a wake structure is clearly shown in Figure 3.27a particularly for the background ion. This is also observed in the two-dimensional computer experiments and will be examined in the next chapter.

From the top of the orbiter, an electron beam is emitted upward into the ambient plasma. Since the initial pitch angle of the electron beam is a right angle with respect to B_0, the maximum density of the beam is found near the gate of the electron emission at the orbiter. Owing to the local electric field which directs toward the high density of electrons, the beam electrons are accelerated and escape along B_0 in the y direction. Those processes are consistent with the results obtained in the two-dimensional computer experiments described in Section 3.2.2. As shown in the panel for the beam electrons in Figure 3.27b, the distortion of the beam trajectory due to the gyromotion around B_0 is also observed in the three-dimensional case. Compared to the two-dimensional case, however, the distortion is much less in the three-dimensional case, which will be discussed in the later section.

The main difference of the beam dynamics between the two- and three-dimensional cases is the formation of the electron beam cloud. As shown in Figure 3.2 obtained by the two-dimensional computer experiment, the electron beam cloud is spatially distributed in larger area near the orbiter. In the three-dimensional case, however, the beam cloud region is spatially limited in the
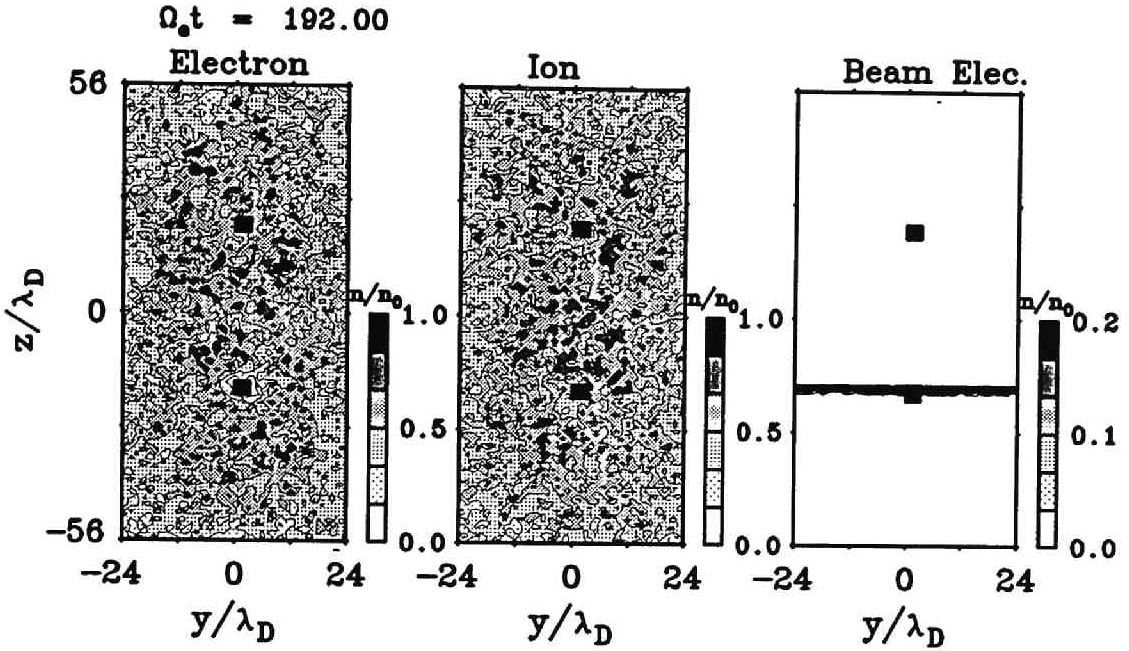
Figure 3.28: Contour maps of the number densities for the background electrons, ions, and beam electrons in the $y-z$ plane. The results obtained in the three-dimensional computer experiments with $e\Delta\phi_s/k_B T_e = 10$.

vicinity of the gate of the beam emitter at the orbiter. Besides, its density is much smaller than that observed in the two-dimensional case. This beam profile accounts for the little influence on the ambient plasma distribution. The reason for this difference is also discussed in the later section.

As a response to the negative potential of the orbiter, the ambient electrons are evacuated and an electron cavity is created around the orbiter. Ions are attracted to the orbiter and an ion sheath is eventually formed around the orbiter. Since the ion gyroradius is much larger than the size of the satellite in the computer experiments, the sheath is uniformly formed and shows little dependence on the direction of B_0 as shown in Figure 3.27.

To quantitatively compare the density structure between the two- and three-dimensional cases, we also performed the three-dimensional computer experiments with the same potential difference $e\Delta\phi_s/k_B T_e = 10$ as used in the previous two-dimensional computer experiments. Contour maps of the number densities for the background electrons, ions, and the beam electrons measured in the $y-z$ plane are depicted in the Figure 3.28 As in the figure, no evident structure is

shown in the ambient plasma such as sheath formation at the tether ends, although the density variation is apparently seen in the two-dimensional case. At the orbiter region, the trajectories of the beam electrons are clearly seen along the y direction, namely, B_0 direction. The electrons emitted from the orbiter are accelerated along B_0 due to the repulsion to the negative potential of the orbiter. The difference from the results obtained in the two-dimensional case is found the structure of the beam trajectories. In the two-dimensional case, as described in the previous sections, the electrons emitted form an electron cloud in the vicinity of the orbiter rotating itself owing to the local $E \times B$ drift motion in the direction perpendicular to B_0. Along B_0, the beam electrons are accelerated away from the orbiter, making gyromotion around B_0. In the three-dimensional case, the dynamics of the electron beam is primarily the same as observed in the two-dimensional case. However, the gyromotion of the electrons is not evident even though the initial pitch angle of the beam electron is the same as that of the two-dimensional model. Taking account of the quiet structure of the background plasma density around the satellite, the electron collection to the satellite is much less than that in the two-dimensional model. This implies that the amount of the electron beam emission is much reduced in the present case. Hence, the beam density in the vicinity of the orbiter becomes lower than that observed in the two-dimensional cases. In such a situation, the electric field induced by the beam electrons themselves becomes weak and the resulting pitch angle modulation of the beam electrons is hardly seen as shown in Figure 3.28. The essential reason for the difference in the plasma dynamics will be discussed in the later section.

3.3.3 Electrical Properties of Tethered Satellite System

In this section, the electrical properties of the TSS such as the potential variation and the current collection to the tether ends are studied with the three-dimensional model. As discussed in the previous section, the spatial variations of the charge density in the vicinity of the tether ends quantitatively differ from those observed in the two-dimensional case. This can also cause the difference in terms of the electrical properties of the TSS because they are strongly affected by the plasma environment in its vicinity.

According to the items concerning the electrical properties raised in the two-dimensional model, we will proceed in the analysis for the three-dimensional case. First, we focus on the current collection to the tether ends at the steady state. Figure 3.29 shows the current values normalized to the ambient electron current for the cases of $e\Delta\phi/k_B T_e = 100$. The positive values implies the electron current due to the electron collection. The electron current at the orbiter is
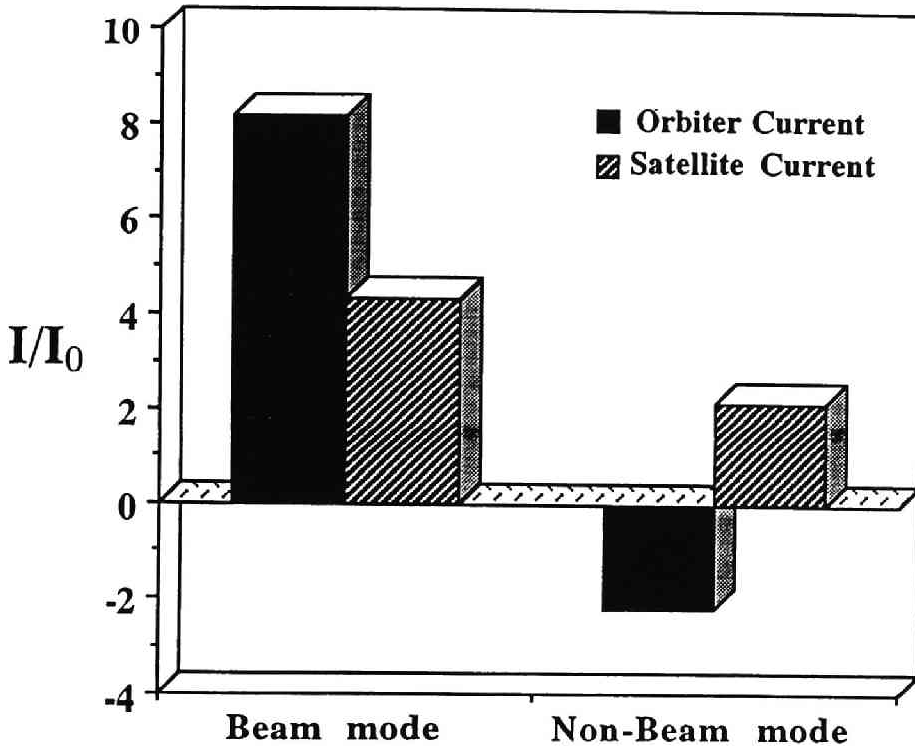
Figure 3.29: Amount of current collection to the tether ends at the steady state for the beam mode and the non-beam mode.

approximately twice as much as that at the satellite. This is due to the return current of the beam electrons to the orbiter. The beam emissivity is obtained from the current values at the tether ends as $1 - i_{rtn}/i_{beam}$. In this case it is estimated as approximately 35%. This emissivity is lower than that obtained in the two-dimensional model such as Model-2. This is because that the electric force which can accelerate the beam electrons away from the orbiter is reduced in the three-dimensional model. In the case where no beam is emitted from the orbiter, the electron current outgoing from the satellite and the ion current incoming to the orbiter are balancing each other. In this model, the negative charges are accumulated in the tether system. Then the average potential of the system should be negative, where ions, which are attracted to the tether system will play a roll to determine the current value to the TSS. Since the ions in the vicinity of the orbiter are accelerated due to its negative potential, the ion current at the orbiter becomes approximately 20 times as much as that of the ambient ion current. This is equivalent to twice of the ambient electron current. At the satellite, electrons are also collected to compensate the charges owing to the ion collection by the orbiter.
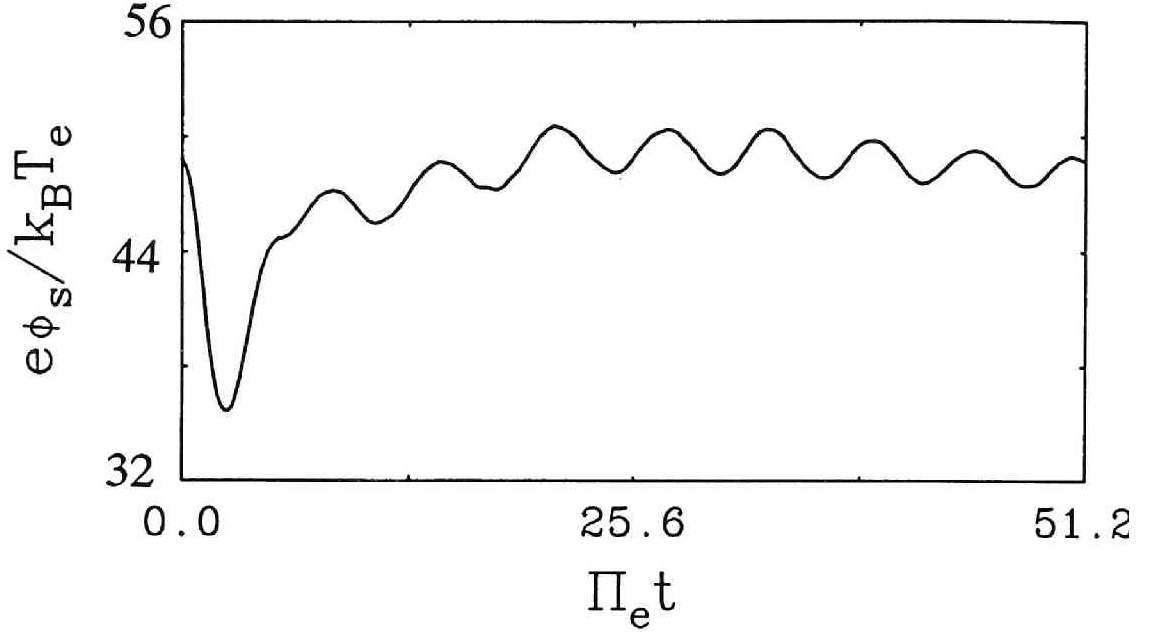
Figure 3.30: Time evolution of the satellite potential in the beam emission mode of three-dimensional space. The potential energy is normalized to the electron thermal energy.

Next, we examine the charging of the TSS in terms of potential. Figure 3.30 shows the time evolution of the potential energy of the satellite up to $\Pi_e t = 51.2$. The potential difference $\Delta\phi_s$ between the tether ends is kept constant. Namely, the orbiter potential is always lower than the satellite potential by $\Delta\phi_s$. As evidently shown in the figure, the satellite potential starts to oscillate in time after a potential drop due to the electron collection in an early phase. The frequency of the oscillation nearly corresponds to the electron plasma frequency. This is due to the electron attraction to the satellite along B_0. Although not displayed, the time evolution of the current flow to the TSS also shows the oscillation with the frequency of Π_e. According to the two-dimensional results, the potential oscillation with the frequency of ω_{UHR} and ω_{LHR} is observed in the model plane perpendicular to B_0. In the three-dimensional case, however, the oscillation with Π_e is dominant and the other frequencies are not detected or their amplitudes are too weak to be observed. Taking account of the high mobility of electrons along B_0, the electron collection of the satellite and the density modulation in its vicinity are mainly stressed along B_0. From the three-
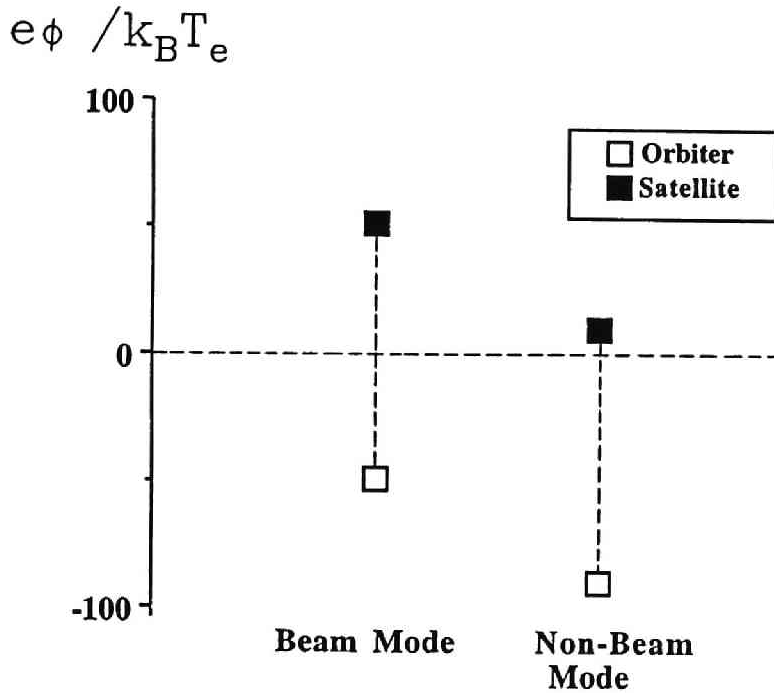
Figure 3.31: Potential values of the tether ends at the steady state for the beam mode and the non-beam mode in the three-dimensional cases.

dimensional point of view, the plasma oscillation with Π_e can be amplified more than that with the other frequencies.

Figure 3.31 shows the potential values of the tether ends in an equilibrium state. The potentials are plotted in terms of energy normalized to the electron thermal energy for the beam emission mode and the non-beam emission mode, respectively. As stated in the previous section, a space vehicle is normally charged negatively in the ionosphere because of the larger thermal velocity of electrons than that of ions. This situation is shown in the non-beam emission case in the figure. The net potential energy of the TSS, defined by taking the average value of the potential energy at the satellite and the orbiter, is approximately -40. On the other hand, due to the electron beam emission from the orbiter, the normalized potential recovers to a value close to the space potential in the beam emission case. The results stated above qualitatively agrees with the one obtained in the two-dimensional model.

3.3.4   Comparison With Two-Dimensional Results

We presented that basic physics associated with the plasma response to the TSS are qualitatively the same between for the two- and three-dimensional models. In the computer experiments performed in the previous sections, $e\Delta\phi/k_B T_e$ is 20 times higher than that adopted in the two-dimensional model to emphasize the plasma response to the TSS. We also performed three-dimensional computer experiments with the same potential difference $\Delta\phi_s$ as used in the two-dimensional cases; $e\Delta\phi_s/k_B T_e = 10$. However, as shown in Figure 3.28, no remarkable variation of the background plasma is observed as a response to the TSS. Regarding the electron beam dynamics, some differences are found in the cloud formation and the beam trajectories between the two-dimensional model and the three-dimensional model. The detail was described in the earlier section. The reasons for the differences in the beam dynamics can be accounted for as follows.

As for the beam cloud formation, it is closely related to the dimension of the model region adopted in computer experiment. In general, the electron dynamics depend on the direction of B_0. Along B_0 electrons are so mobile that they are easy to move while they are stuck to B_0 in the direction perpendicular to it unless cross-field drift effect such as $E \times B$ drift is taken into consideration. In the two-dimensional space, spatial variation of the physical quantities along the direction perpendicular to the model plane cannot be solved. Therefore, for example, in Model-2 where B_0 is perpendicular to the model plane, it is impossible to trace the beam dynamics such as diffusion or acceleration along B_0. Eventually the emitted electrons increase the density and form a beam cloud in the vicinity of the orbiter. In a real three-dimensional situation, however, electron transportation along B_0 is so dominant that the beam electrons are easily diffused and accelerated along B_0. We have clarified this process of the beam dynamic by the three-dimensional computer experiments in which all the physical quantities can be fully solved with electrostatic approximation.

As for the difference found in the structure of the beam trajectories, it is basically owing to the difference of Coulomb's force between the two- and three-dimensional spaces. Namely, the force between the charges is proportional to r^{-2} in the three-dimensional model while it is r^{-1} in the two-dimensional space where r denotes the distance between the charges. In both the two- and three-dimensional cases, the beam density has its maximum value at the gate of the beam emitter. Since electrons are rich in this region, the potential relative to the space potential becomes negative as well as the orbiter potential. Owing to this negative potential, electric field is induced inward the beam electrons which can accelerate them away from the cloud region. Taking account of the finite pitch angle of the electron beam, the beam electrons escaping from the

cloud region make a gyromotion as clearly observed in the two-dimensional case. However, in the three-dimensional model, the electric field induced by the beam electrons abruptly becomes weak as the distance from the cloud region becomes long because it is reduced according to r^{-2}. It turns out that the effect of the pitch angle modulation of the beam cloud, shown in the bending structure of the beam trajectory, is weakly observed in the three-dimensional space.

In conclusion, due to the difference in the function of Coulomb's force, the region where the electrostatic force induced by the TSS is effective is spatially limited much more in the three-dimensional space than that in the two-dimensional space.

3.4 Discussion and Conclusion

3.4.1 Comparison With Data Obtained in the TSS-1 Mission

The first mission of the TSS (TSS-1) was launched aboard the space shuttle Atlantis in July in 1992. Although the tether extension of 20km was not carried out due to several unexpected accidents, many interesting results were obtained [Banks et al., 1993; Thompson et al., 1993., Gilchrist et al., 1992; Aguero et al., 1992]. Out of them, one of our main concern is the current collection of the TSS. We review the result and compare it with the one obtained in the present computer experiments.

Figure 3.32 shows the time variation of the tether current and system resistance observed during one orbit of the deployed operations in the TSS-1 mission. During this orbit, the lowest valued resistor, called shunt, was used. Namely, the resistance of the tether R_{tether} itself, about 2040 Ω, was the main impedance between the tether ends. The FPEG beam was not emitted during this time. In the TSS, as stated earlier, the potential difference has magnitude $\Delta\phi = V_v \times B_0 \cdot L$, where V_v is the TSS velocity, B_0 is the geomagnetic field, and L is the tether length between the tether ends. Taking account of the extended tether length, 256m, the maximum $\Delta\phi_s$ reaches up to 60V. In Figure 3.32a, the upper curve, marked with + symbols, is the maximum current, $I_{max} = (V_v \times B_0 \cdot L)/R_{tether}$, that can be drawn through the tether with $\Delta\phi$. During the periods from 218/10:49 to 218/10:58 and from 218/12:15 at the end of the orbit, all the electrical potential available to the system is accounted for by the IR drop in the tether. However, during the larger part of the orbit the IR drop in the tether is not equal to the available potential. The amount of the current collection is much smaller than the maximum current. This implies that the net impedance in the current system is more than the tether impedance. As

shown in the schematic illustration in Figure 3.25, other factors such as plasma density of the sheath near the current collecting surfaces may control the amount of current collection. In comparison with Figure 3.32a, Figure 3.32b shows that the system resistance $R_{system} = (V_v \times B_0 \cdot L)/I_{tether}$ becomes extremely high during the period when the amount of the tether current is small around 0.005A. Although not displayed, the results of the TSS-1/SPREE experiment show that the strong correlation between the orbiter potential and that available after the tether IR drop is subtracted from the total $\Delta\phi$. Taking account of the small potential drop in the electron sheath around the satellite because of good mobility of electrons, nearly all the available voltage is in the ion sheath around the orbiter. This implies that the large resistance of R_{system} is mainly due to the ion sheath around the orbiter.

In Figure 3.32b, it should be also noted that the enhancement of the resistance occurs at night. In the ionosphere, generally, the ionization of the neutral particles becomes less active at night. Then the ion supply from the ionospheric plasma is not enough for the sheath formation around the orbiter. This means ions are not sufficiently collected by the orbiter. Then, the amount of the tether current becomes less than the maximum current.

As stated above, the current drop observed during the night in the TSS-1 may be accounted for by the decrease of the ion current at the orbiter. As for the observational fast that the ion current can control the total tether current in the non-beam emission mode, the results of the present computer experiments agree well. As shown in Figure 3.30, the TSS potential becomes negative with respect to the space potential in the non-beam emission mode due to the electron accumulation to the system. Once the satellite potential becomes low, comparable to the plasma potential, background electrons are not much attracted to the satellite compared to the beam emission case. This situation is shown in Figure 3.29. Rather, the ions are strongly attracted to the orbiter which is much negatively charged with respect to the plasma potential. Then the ion current becomes dominant at the orbiter. To balance the ion current, electrons are collected by the satellite with the same amount of ion charge at the orbiter.

In order to understand the effect of the density decrease of the background plasma on the tether current, computer experiments with different plasma density can provide helpful data. The main concern is the density dependence in the ion sheath formation about the orbiter. Ions are attracted to the orbiter and form a sheath. This ion sheath provides the ion current at the orbiter. In case of low density of the background plasma, however, the potential shielding effects by the ions may be insufficient. This can be examined by computer experiments with different density of the background plasma, which is left as a future work.

In the TSS-1 mission, the electron beam was emitted by the FPEG, Fast

TSS-1/SETS

(a)

$$I_{max} = (\underline{V} \times \underline{B} \bullet \underline{L})/R_{tether}$$

Tether Current (A)

0.025

0.02

0.015

0.01

0.005

0

218/10:45   218/11:00   218/11:15   218/11:30   218/11:45   218/12:00   218/12:15

(b)

Resistance (Ohms)

30000

20000

10000

0

218/10:45   218/11:00   218/11:15   218/11:30   218/11:45   218/12:00   218/12:15

Night
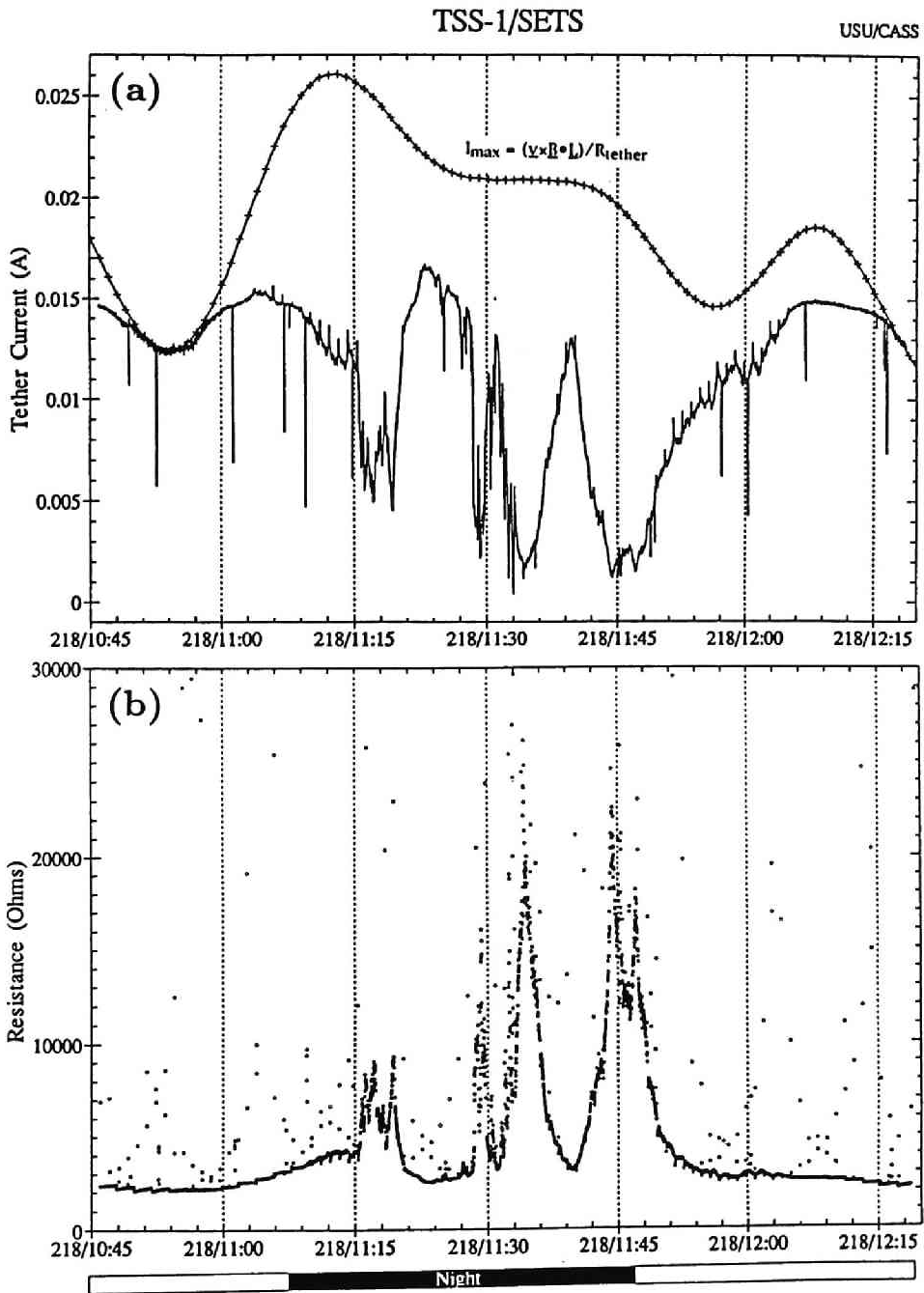
Figure 3.32: The results obtained during one orbit of the deployed operation in the TSS-1 mission. The time variation of (a) the tether current and (b) the system resistance. The lowest valued resistor, shunt, was used.
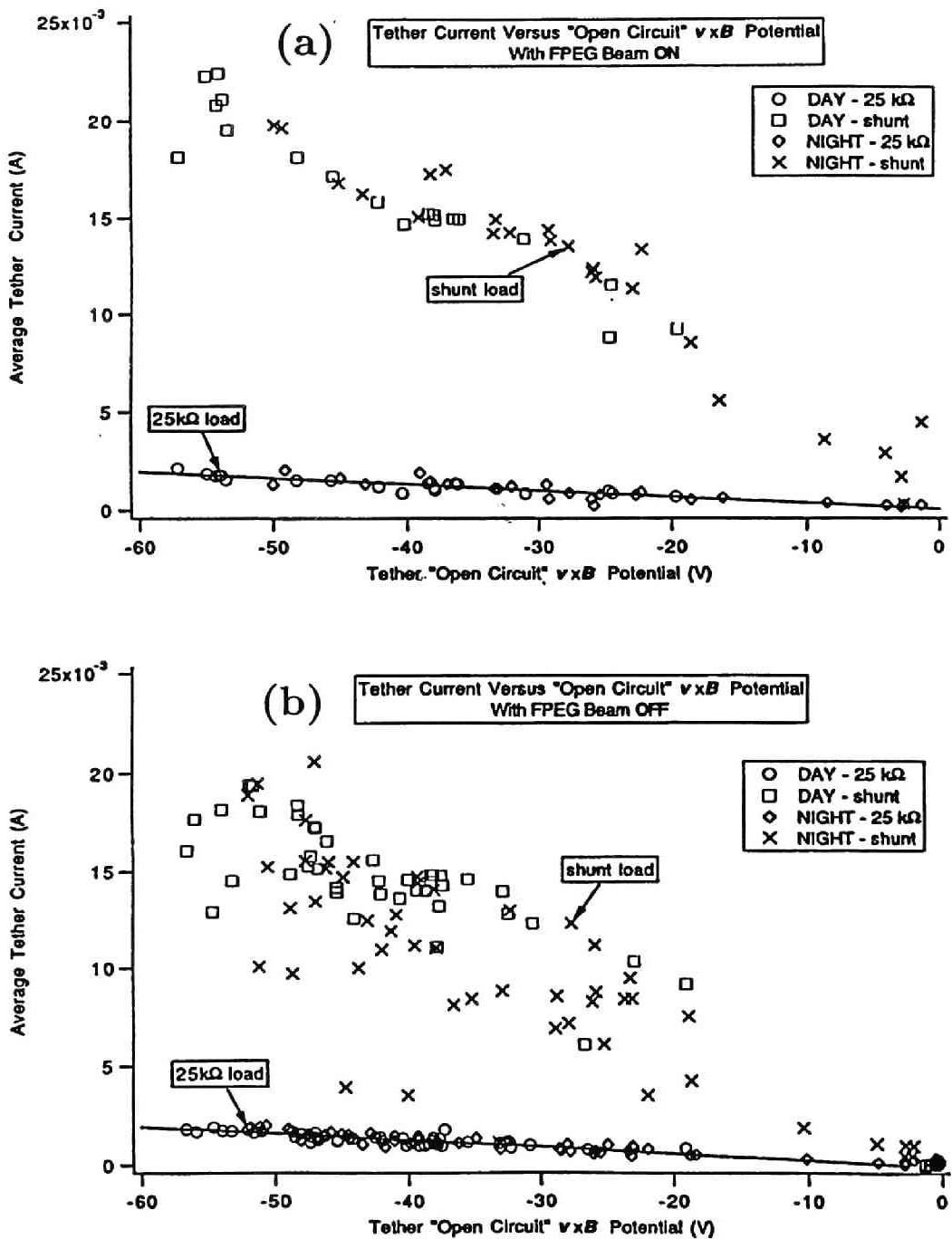
Figure 3.33: Tether current versus $\Delta\phi$ of the TSS for different modes (a) with FPEG Beam on and (b) with FPEG Beam off.

Pulse Electron Gun. During the period of the FPEG beam operation, the tether current was measured and compared to the current with the FPEG beam off. Figure 3.33 shows the tether current versus $\Delta\phi$ with various resistance in the tether system. Since the difference is found in the shunt mode in which the tether impedance is dominant, we just focus on the data marked with × and □. It is found that the variability of the tether current was dramatically reduced during the FPEG operation. In particular, at night, the variation in current intensity is obviously reduced by the FPEG beam emission. As stated above, in the non-beam mode, the tether current is controlled by the ion collection to the orbiter. As shown in Figure 3.32, the ion current depends on the local plasma density which is sometimes reduced at night due to the less ionization in the ionosphere. In this sense, the large variation of the current intensity in the non-beam mode can be accounted for by the density fluctuation in the ionosphere. With use of the electron beam emission, on the contrary, the total current can be controlled by the amount of the beam electrons, not the ion current. Therefore, primarily the current intensity is not affected by the ion density in the sheath. In the present computer experiments, we have shown this situation in Figure 3.8. When the electron beam is emitted from the orbiter, the electron current at the satellite is dominant and no ion current is observed at the orbiter. This implies that the density of the ion sheath around the orbiter is not important in the amount of the current collection of the TSS. The electron currents control the total tether current.

So far the electrostatic behaviors of the TSS such as the potential and current variation have been reported. As described above, the results concerning the tether current obtained in the present computer experiments qualitatively show a good agreement with those obtained in the TSS-1 mission. Although we could not obtain enough data concerning the electromagnetic field in the TSS-1 mission, next TSS experiment which is planned to be carried out in 1995 will provide us much more data and enable us to compare the results with those obtained in the computer experiments.

3.4.2 Conclusion

In the present paper, we have studied the electrodynamic interaction between the TSS and the ambient space plasma by the two- and three-dimensional computer experiments. In the model region, two conducting bodies, corresponding to a satellite and an orbiter, are placed in a vehicle frame of reference. They are connected electrically to each other. Taking account of electromotive force generated by the cross-field motion of the TSS, the potential difference between the tether ends $\Delta\phi$ is retained constant. In the computer experiments, the

plasma dynamics and field variation are obtained in self-consistent manner by solving the equation of motions and Maxwell's equation at each time step. In the three-dimensional electrostatic model, the field at each time step is solved with Poisson's equation. As performed in TSS-1, electron beam is emitted from the orbiter. In the interaction of the tether ends with their surrounding plasma, space charge effects play a significant roll. Therefore, we have utilized particle model in the computer experiments.

By performing the two-dimensional electromagnetic and three-dimensional electrostatic computer experiments, we have quantitatively examined some of the physics associated with the TSS such as the potential and current variation of the tether ends, density variation in the vicinity of the tether ends, electron beam dynamics, wave excitation due to the beam, and current path through the plasma. Since the satellite potential is elevated higher than the space potential at the initial time, electron attraction and ion repulsion are clearly observed. In the downstream region of the plasma flow, a rarefactional wake structure is found. As shown in three-dimensional space, high density region of electrons is formed around the satellite across B_0. Ions are spherically depleted by the satellite. At the orbiter which is negatively charged with respect to the ambient plasma, ions, which are assumed to be unmagnetized, are concentrated while electrons are depleted. When no electron is emitted from the orbiter, the tether system is negatively charged due to the accumulation of electrons by the satellite. Then, an ion sheath becomes large enough around the orbiter to control the potential and the current collection of the TSS. As for the beam dynamics, basically the beam electrons are accelerated away along B_0. As easily predicted, it is shown that the beam emissivity becomes low as the initial pitch angle of the beam becomes close to a right angle. This implies that the return current to the orbiter increases in a low emissivity case and the TSS becomes negatively charged. In the two-dimensional space, an electron beam cloud is clearly created in the downstream region in the direction perpendicular to B_0. The local electric field induced by the cloud modifies the beam pitch angle and accelerates some of the beam electrons along B_0. Moreover, due to the cross-field current by the electron $E \times B$ drift motion around the cloud, LHR mode waves are locally enhanced. The local LHR wave excitation is quantitatively interpreted by the theory of the lower-hybrid drift instability. In the three-dimensional computer experiments, however, the beam cloud structure in the downstream region is not observed. Instead, the beam cloud is located in the close vicinity of the gate of the beam emitter. In the three-dimensional case, beam electrons emitted from the orbiter can immediately escape along B_0 before they form a cloud in the plane perpendicular to B_0. In the two-dimensional case, however, they cannot escape along B_0 because B_0 is perpendicular to the model plane. Eventually,

a dense cloud is formed in the downstream region. Considering the real situation, the results obtained in the three-dimensional space is reasonable because electrons are generally so mobile along B_0 that they can escape along B_0. In any models, however, the beam-plasma interaction can occur such as local LHR mode excitation due to the presence of the density gradient of the beam edge and the cross-field current. In this sense, the discussion of the mechanism of LHR wave can be applicable in a real beam-plasma interaction.

The dimensional ratio of the tether ends to λ_D is considerably small compared to that in the actual situation although it is retained larger than unity. However, we believe that the results obtained in the computer experiments are quantitatively correct. For example, as long as a ratio of a vehicle size to λ_D is larger than unity, sheath width measured from the vehicle surface is a function of the vehicle potential and is independent of the vehicle size. The details will be examined in the next chapter.

In the present computer experiments, we adopted a simple manner for electron beam emission. The number of the beam electrons is the same as that of collected by the satellite at each time to avoid the excess charging of the system. In the actual situation of TSS-1, the beam emission is well controlled as follows. A Fast-Pulse Electron Gun (FPEG) emits electrons beams of 50 and 100 mA at 1 keV, stimulating wave activity over a wide range of frequencies. These beams discharge the orbiter and produce electrical changes in the system and can be a pulsed with on/off times ranging from 600 to 105 nanoseconds. In the present paper, we qualitatively studied the beam dynamics as well as the beam emissivity in the electrodynamic tether case. However, to quantitatively compare the results of the computer experiments to the real situation, we need to take account of the manner of the FPEG beam. To study the plasma response to each mode of the FPEG beam, we need to perform computer experiment for each case, which is left as a future work.

The importance of the present study is based on the fact that the multiple phenomena stated above are closely related to each other in the TSS, although each of them has been investigated independently in the past studies. Namely, the amount of the electron beam emission from the orbiter depends on the efficiency of the electron collection by the satellite. The density gradient of the beam electrons affects the intensity of the LHR mode waves. From this point of view, the knowledge obtained through the computer experiments and theoretical analyses described in the present chapter have significant meaning to understand the electrodynamic interaction of the TSS with the space plasma.

In the next chapter, based on the knowledge acquired in this chapter, we will focus on the electrodynamic interaction of the high potential tethered satellite with the ambient plasma.

Chapter 4

Plasma Response to High Potential Tethered Satellite

4.1 Introduction

As described in Chapter 3, the basic physics associated with the electrodynamic tether system have been revealed with the help of the computer experiments. Among the scientific objectives in the TSS experiments, the electrodynamic interaction with the high potential tethered satellite and the ambient space plasma is one of the most significant issues for the investigation. In order to study the detail of the plasma responses to the high potential satellite such as the density variation near the satellite and current collection, we have performed two- and three-dimensional computer experiments with a model region including the high potential satellite and a magnetized plasma flow. Theoretical interpretation of the obtained results associated with the current collection and current-voltage characteristics of the TSS are described in the present chapter. Before the description of the computer experiments, we provide a historical review concerning the previous works in conjunction with the electrical properties of a space vehicle in the ambient space plasma.

Since the 1960's, electrical properties of spacecraft in the ionosphere such as current-voltage characteristics and the sheath structure have been investigated [e.g., Garrett, 1981]. As for the current-voltage characteristics, the classical probe theory [Langmuir and Blodgett, 1924; Mott-Smith and Langmuir, 1926], is applicable for the satellite in the ionosphere at a potential up to 10 V. For higher voltages in the range $100 \sim 1000$ V, the plasma around the satellite is accelerated. The current-voltage characteristics are then modified by the resulting plasma waves, turbulent electron heating, and cross-field transport of electrons and ions. There have been several theoretical studies of the current-

voltage characteristics of such a high potential satellite in the ionosphere. Beard and Johnson [1961] estimated the maximum current to a satellite, neglecting the presence of a static magnetic field B_0. Parker and Murphy [1967] examined the maximum current in the presence of B_0 by assuming constants of motion of a single particle in the absence of time-varying electric and magnetic fields. Linson [1969] investigated the current-voltage characteristics of a spherical satellite of a large positive potential in an external magnetic field. His theory gives a value for current lying between the previous two theories assuming a constant plasma density in the vicinity of the satellite. Palmadesso and Ganguli [1992] modified Linson's method assuming nonuniform space charge around the satellite. They found reduced levels of current collection relative to Linson's model. In the present paper, the classical theories such as the Langmuir theory, the Parker-Murphy theory and the Linson theory are compared with the current-voltage characteristics obtained in the present computer experiments.

The Langmuir theory and the constant density theory deal with a case where the sheath effects around a body in a plasma dominate the current flow to the body. Therefore, Poisson's equation and space charge effects should be taken into consideration. For a case where a sheath is so thick that the space charge effects disappear, and the Debye length is assumed to be infinite, an orbit-limited current theory has been proposed [Whipple and Parker, 1969; Parker and Whipple, 1970; Laframboise and Parker, 1973; Prokopenko and Laframboise, 1980]. In this situation, the electrostatic field can be obtained by Laplace's equation. Then, the current flow to the body is maximized. In the present paper, however, we focus on the theories which include the sheath effects because the electron sheath around the satellite cannot be ignored in the present computer experiments.

In addition to the theoretical studies, active space experiments, such as the CHARGE 2 sounding rocket experiment, have been carried out. Most of them had a mother/daughter configuration connected by a tether to each other [Sasaki et al., 1988; Mandell et al., 1990; Myers et al., 1990; Gilchrist et al., 1990; Neubert et al., 1991]. Laboratory experiments have also been conducted by Stenzel and Urrutia [1990], simulating an electrodynamic tether model of the TSS-1. They examined the behavior of the current system. As for the numerical studies, a model with two bodies of the orbiter and the satellite, connected electrically to each other, has been examined by utilizing a two-dimensional electromagnetic particle code [Usui et al., 1991]. Concerning a one body problem, Martin [1974] studied the interaction of a conducting body through the ionospheric plasma by solving Poisson's and Vlasov's equations. Calder and Laframboise [1990], using a one-dimensional electrostatic code, and Ma and Schunk [1989], using a three-dimensional fluid code, have presented time-dependent behavior of a

plasma sheath surrounding a satellite body whose potential is abruptly changed from zero to a positive value. Using a two dimensional electrostatic code, Wang and Hastings [1992] have investigated dynamic interaction of a negatively biased plate in ionospheric plasma. They studied both the transient formation of the space-charge wake and its steady-state structure.

In many practical situations, transient phenomena associated by the onset of a high potential onto the electrical system are important. In the present study, we imposed a high potential on the satellite at $t = 0$, and observed transient responses in the surrounding magnetized plasma. Unless the electrical charge is released by the electron beam emitter, the satellite potential becomes negative [Neubert et al., 1990] because the thermal velocity of electrons is much higher than that of ions in the ionosphere. In the case of the tethered satellite, however, its potential can be kept positive with respect to the space potential by the dynamo cross-field motion of the tether system [Laframboise and Luo, 1989; Hastings and Chang, 1989], which makes the plasma response to the satellite different from that to an isolated single satellite. In the present study, we keep the satellite potential positive relative to the space potential throughout the computer runs.

Section 4.2 is devoted to a description of two-dimensional computer experiments using a full electromagnetic particle code. The model region and parameters used in the computer experiments are stated. The results of the computer experiments are then described in detail. We show the density variation in the vicinity of the satellite, the transient current to the satellite and the current flow pattern in the steady state. We also present an analysis of the current-voltage characteristics of the satellite, compare to existing theories and examine the transient current. In Section 4.3 we describe three-dimensional computer experiments using an electrostatic particle code.

4.2   Two-Dimensional Electromagnetic Particle Model

4.2.1   Models and Parameters

In the present computer experiments, we use a two-and-half dimensional full electromagnetic particle code called KEMPO [Matsumoto and Omura, 1985] which can deal with kinetic interactions of a space vehicle with its surrounding plasma. In KEMPO, we solve Maxwell's equations and equations of motion of electrons and ions. We use (x, y, z) coordinates but neglect a variation in one of the three dimensions which is perpendicular to the model plane. Three

velocity components v_x, v_y, v_z and all three components of electromagnetic fields are retained. The model configuration for the computer experiments is shown in Figure 4.1. We place a perfect conducting satellite in the center of the model box of our computer experiments. Through the computer runs, the satellite potential is fixed higher than the space potential. This is based on the assumption that the tethered satellite is driven to the high potential by the Lorentz electric field generated by the motion of the tether system across B_0. The static magnetic field B_0 is assumed to be along the y axis without loss of generality. Since the vehicle frame of reference is adopted, the ambient plasma has a cross-field flow in the x direction owing to the $E \times B$ effect.

We adopt three kinds of model for the two-dimensional computer experiments. The first one is Model-1 where both B_0 and the plasma flow lie in the model plane. The second one is Model-2 in which B_0 is perpendicular to the plane while the plasma flow lies in the plane. The third one is Model-3 in which B_0 lies in the plane while the plasma flow is perpendicular to the plane. Combining the three models, we may be able to understand, not all but most of, the three dimensional dynamics around the satellite. As for the boundary conditions of the outer edges of the model, we use an open-boundary. The open boundary is realized by adding wave-absorbing regions (numerical damping regions) to four surrounding boundaries of the physical region. The outer boundary of the wave-absorbing regions is fixed at zero potential [Press et al., 1987]. To obtain the equipotential solution of the satellite, we make use of the capacitance matrix method [Hockney and Eastwood, 1981]. To simplify the problem, no photoelectrons nor secondary electrons are emitted from our model satellite. The inclusion of these low energy electrons may change the situation to some extent. However, most essential results presented in the paper remain the same because their density is normally much less than the ambient plasma density. We neglect the effects of ionization and recombination, which itself is another interesting subject of study and is to be presented in future publications. We assume that the electrons which hit the satellite surface are all collected by the perfect conducting satellite.

The physical parameters used in the computer experiments are given below. Generally, there is no need to stick to a real unit system such as MKS unit system in computer experiments. The important rule we have to obey in selecting physical parameters is to retain the quantitative relations in the parameter group. Then each physical process involved in the evolution of the system can be correctly simulated in the computer experiment even if the absolute values of the physical quantities are different from those in the real situation. In selecting the relative mass ratio, we adopt $m_i/m_e = 100$ where m_e and m_i denote the electron and ion mass, respectively. At the low Earth orbit where the SETS ex-
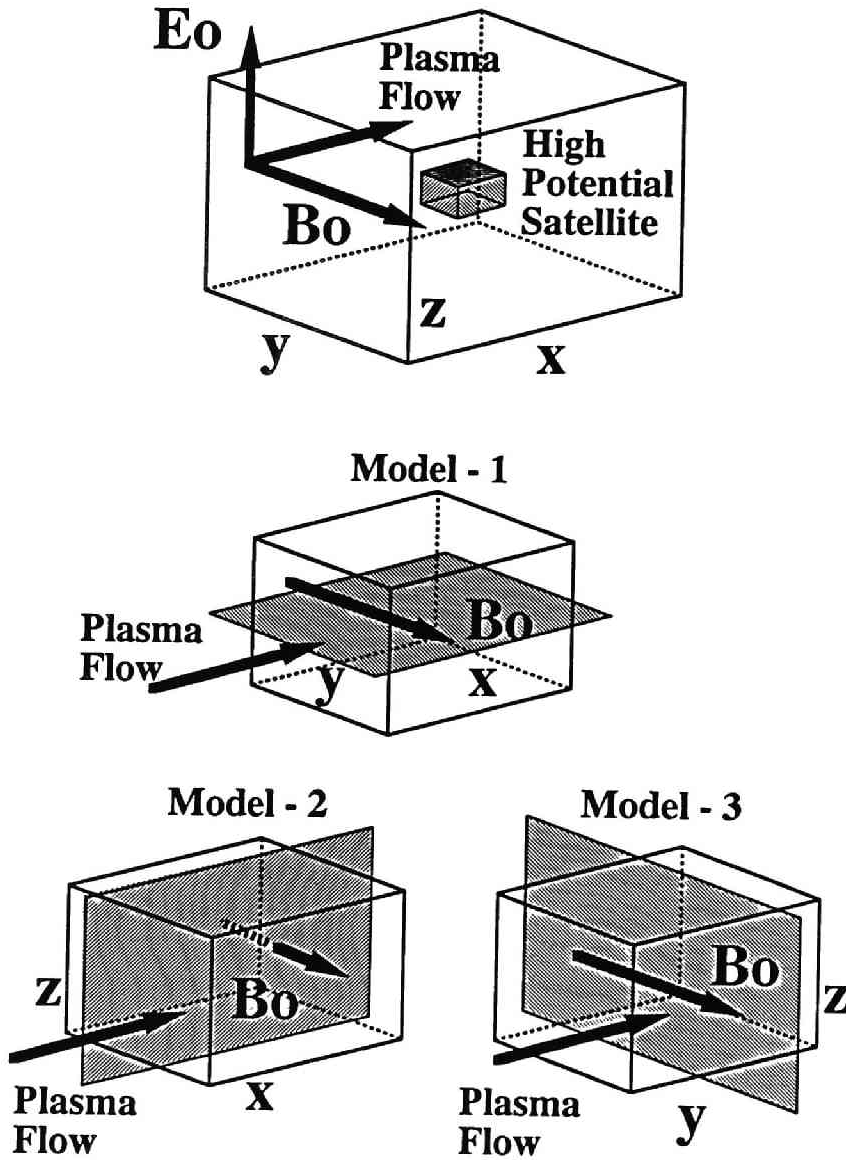
Figure 4.1: Model of computer experiments. Three kinds of plane are used for three models. The high potential satellite is located at the center in all cases.

periment will be performed, the ambient predominant ions are mostly Oxygens and have the mass of approximately 30,000 times heavier than the electrons. This implies that the time and spatial scales for the ion dynamics are much longer and larger than those for the electron dynamics, respectively. To examine both the electron and ion dynamics simultaneously within a reasonable running time of the computer experiments, we reduce the mass ratio as stated above. $m_i/m_e = 100$ is sufficiently large to discriminate ion contribution from that by electrons. In selecting the velocities, the relation $v_{te} \gg V_p > v_{ti}$ should be retained in computer experiments, where v_{te}, v_{ti} and V_p denote the electron and ion thermal velocities and the plasma flow velocity, respectively. At an altitude of 300 km, v_{te}/V_p and v_{ti}/V_p are approximately 30 and 0.5, respectively. In the computer experiments, we take each ratio of the velocity as 8.0 and 0.8, respectively; v_{te}/V_p is reduced for the same reason as in selecting the mass. This implies that plasma flow effects such as wake formation are more emphasized in the computer experiment than in the real situation. In selecting the frequencies, $\Pi_e > \Omega_e \gg \Pi_i > \omega_{LHR} > \Omega_i$ should be retained, where Π_e, Ω_e, Π_i, Ω_i, and ω_{LHR} denote the electron plasma frequency, gyrofrequency, the ion plasma frequency, gyrofrequency, and the Lower Hybrid Resonance frequency, respectively. In order to cover this wide range of frequency in the computer experiment, each ratio of the frequency is reduced: $\Pi_e/\Omega_e = 2, \Pi_i/\Omega_e = 0.2, \omega_{LHR}/\Omega_e = 0.1$, and $\Omega_i/\Omega_e = 0.01$. Thus, the ratios of the physical quantities are reduced to enable us to perform computer experiments within a reasonable running time. Even if the time and spatial scale of the system is reduced, the essential character of the problems is never changed in the computer experiment.

For Model-1 and Model-2, the grid spacing and the time step are $\Delta r = \lambda_D$ and $\Delta t = 0.032/\Omega_e$, respectively, where λ_D denotes the Debye length of the background plasma. The dimensions of the model plane in Model-1 and Model-2 are $128\Delta r \times 256\Delta r$ in the $x - y$ and $x - z$ planes, respectively. The numerical damping region with a length of $16\Delta r$ is added at each boundary. The number of the superparticles is 131,072 for each species (electrons and ions) of plasma particles at the initial state. To compensate the plasma particles outgoing from the downstream boundary, we feed the incoming particles at the upstream side of the boundary at a constant rate. In the model plane, the satellite shape is a square whose size is $4\Delta r \times 4\Delta r$. The potential energy of the satellite normalized to the background thermal energy, $e\phi_s/k_B T_e$, is fixed to be 100, where ϕ_s, e, T_e, and k_B denote the satellite potential, the electron charge, the electron temperature, and Boltzmann's constant, respectively. The satellite size relative to λ_D is much smaller than the actual ionospheric parameters. However, as long as the satellite size is kept larger than λ_D and the electron gyroradius, the essential character associated with the electrodynamic interaction of the

tether system is never changed in the computer experiments. We carried out the computer runs up to $\Pi_e t \simeq 2000$ which corresponds to approximately two times of the transient time of the plasma flow passing through the whole model region across B_0. This time step is sufficiently large to observe the steady state of the interaction of the satellite with the ambient plasma flow.

To obtain the current-voltage characteristics of the satellite, we perform twelve cases of computer experiments by using Model-3 with different satellite potential from $e\phi_s/k_B T_e = 10^0$ to 10^3. The grid spacing and the time step are $\Delta r = \lambda_D$ and $\Delta t = 0.005/\Omega_e$, respectively. The satellite shape is the same as that in Model-1 and Model-2. For the cases of $e\phi_s/k_B T_e \simeq 10^3$, we double the model region of the computer experiments, i.e., $512\Delta r \times 256\Delta r$ in the $y-z$ plane to cover the large expansion of the sheath region. In Model-3, the satellite and the surrounding plasma make a relative motion in the direction perpendicular to the model plane. Since the vehicle frame of reference is adopted, the ambient plasma flows perpendicular to the plane. In the two-dimensional model, however, no spatial variation is assumed in the direction perpendicular to the model plane. This implies that neither upstream nor downstream region exists in the model. Therefore, even if the plasma flow is taken into consideration in Model-3, the plasma flow has no influence on the plasma response to the satellite in the model plane. Model-3 is symmetric with respect to the magnetic field line which penetrates the satellite. To obtain a better spatial resolution, we calculated the plasma dynamics for only a quarter of the extended model region, i.e., $256\Delta r \times 128\Delta r$ area. The computer experiments are conducted up to $\Pi_e t \simeq 330$ (equivalent to $\omega_{LHR} t \simeq 17$).

4.2.2 Ambient Plasma Response

In the present study, the satellite potential is biased much higher than the space potential. This causes ion repulsion and electron attraction from and to the satellite. In the ionosphere, electrons are strongly magnetized while ions are much less because of their large mass, which leads to a substantial difference in the dynamics between the two species. In the present computer experiments, the plasma flow velocity V_p (or equivalently the velocity of the satellite) is taken to be slightly higher than v_{ti} and much lower than v_{te}. This implies that ions are affected by the plasma flow while electrons make random thermal motion without being restricted by the plasma flow. Thus, the B_0 effect, the velocity difference between v_{te} and v_{ti}, and the ambient plasma flow are significant factors for the plasma dynamics associated with the moving high potential satellite. In the present computer experiments, we place a high potential body representing the high potential satellite in the flowing ambient plasma at $t = 0$. To examine
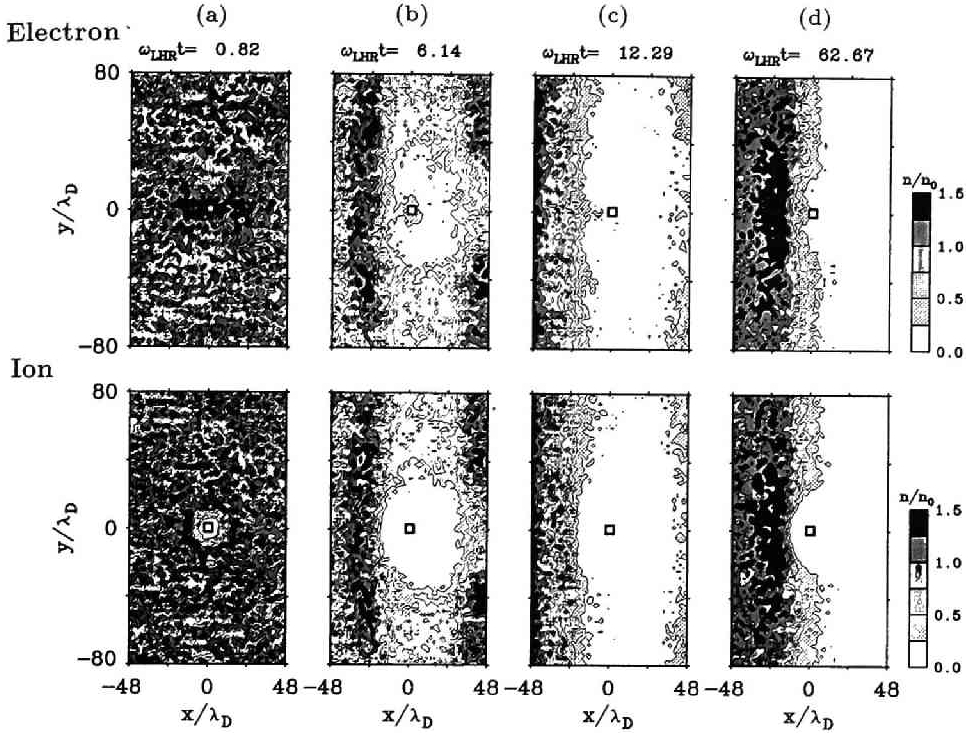
Figure 4.2: Contour maps of the number densities for the background electrons and ions in Model-1 where B_0 and the plasma flow are taken along the y and x directions, respectively.

the time evolution of the phenomena, we divide the whole chain of the plasma responses into three stages: initial, transient and steady stages.

The time history of the plasma number density for Model-1 is shown in Figure 4.2 which has four sets of density contour maps of the background electrons and ions. The number density is normalized to the ambient number density n_0. The small square located at the center of each panel indicates the high potential satellite. The initial plasma response to the high potential of the satellite occurs in a time scale of the period of the electron plasma oscillation. Figure 4.2a shows the density profiles at $\omega_{LHR} t = 0.82$ which corresponds to approximately two cycles of the electron plasma oscillation. Electrons within several Debye length of the satellite experience an intense attractive force, forming a dense electron sheath around the satellite. The sheath is thick in the x direction perpendicular to B_0. This is due to the B_0 effect which restricts the electron attraction of the satellite in the x direction transverse to B_0. The ions in the vicinity of the satellite are repelled away in the radial direction, forming an ion cavity.

At the transient stage, the electrons attracted toward the satellite in the

initial stage are absorbed by the perfect conducting surface of the satellite. This gradually reduces the electron number density in the electron sheath region. Figure 4.2b depicts a snapshot of the plasma number density at $\omega_{LHR}t = 6.1$. It is clearly seen that the plasma dynamics show the directional dependence on B_0. Due to repulsion from the satellite, the ion cavity continues to expand. In the transverse direction to B_0, the plasma density becomes high at both the upstream and downstream edges of the cavity. This is because of the snow-ploughing effect by the ions accelerated outward from the satellite. Along B_0, however, a low density region is created beyond the ion cavity region. The cavity is slightly shifted downstream by the plasma flow. The electrons in the ion cavity at this stage keep low density to maintain the quasi-neutrality of charge. Although the density is not as high as that in the initial stage, the electron sheath still remains around the satellite. Figure 4.2c shows the density profiles at $\omega_{LHR}t = 12.3$ which corresponds to approximately two cycles of the lower hybrid oscillation. The ion cavity is much extended along B_0 and downstream. At the upstream region, the high density plasma created by the snow-ploughing effect moves upstream against the plasma flow. The density profile of electrons is similar to that of ions except for the vicinity of the satellite. Although the density of the electron sheath becomes lower, the satellite draws electrons from the upstream region.

After the time in which the plasma flow passes through the simulation region, the plasma response reaches the steady state. Figure 4.2d shows the density profiles at $\omega_{LHR}t = 62.7$ which corresponds to approximately ten cycles of the lower hybrid oscillation. It is found that the dense plasma wall in the upstream region has moved downstream to a position where the force balance is reached between those by the gradient of the plasma pressure and the electric force by the high potential satellite. The ion cavity has expanded downstream forming a rarefaction. Electrons are attracted from the upstream side of the satellite to keep the electron sheath.

A time series of the density contour maps for Model-2 is depicted in Figure 4.3. The plasma dynamics around the satellite are basically the same as those in Model-1. At the initial stage, the electrons in the vicinity of the satellite are attracted by the high potential satellite, while the ions are repelled from it forming an ion cavity as shown in Figure 4.3a. Since B_0 is perpendicular to the plane, an electron sheath is uniformly created around the satellite with a radius of approximately $10\lambda_D$. Combining this result with the previous result in Model-1, we see that the electron sheath in the 3D situation has a donut form around the satellite at the initial stage. At the transient stage shown in Figure 4.3b, as the ion cavity expands, the electron density in the cavity becomes low keeping the charge neutrality. Since electrons are strongly magnetized, some of the elec-
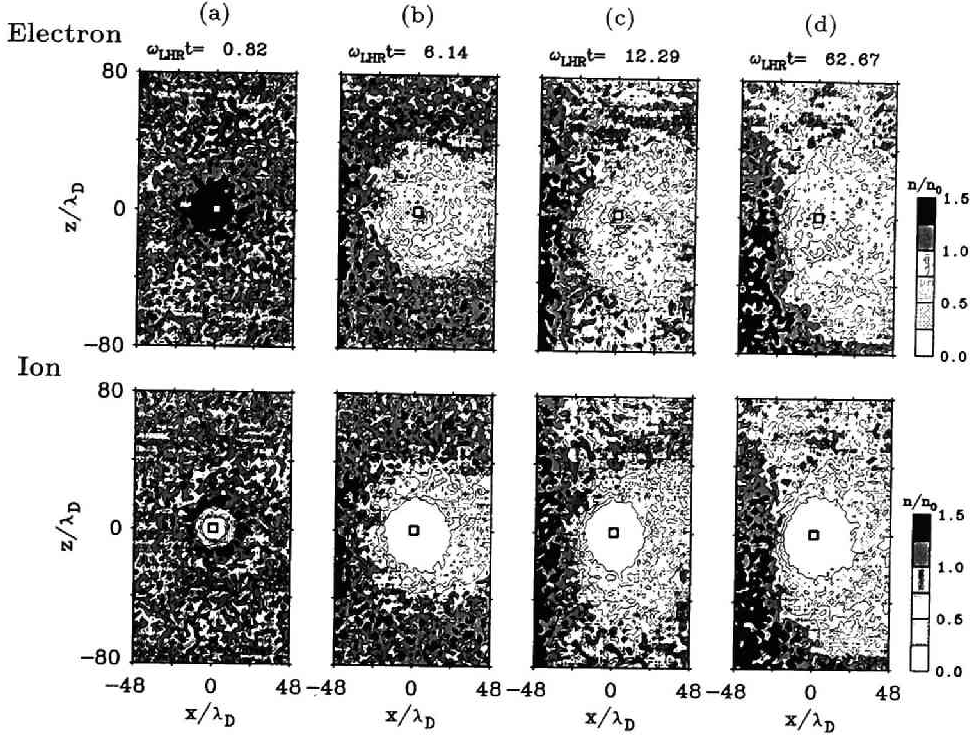
Figure 4.3: Contour maps of the number densities for the background electrons and ions in Model-2 where the plasma flow is taken along the x direction and B_0 perpendicular to the plane.

trons attracted by the high potential satellite remain unabsorbed forming the electron sheath. They suffer from the $E \times B$ drift in the direction perpendicular both to the radial electric field emerging from the satellite and the static magnetic field. The dynamics of those electrons will be discussed later in terms of current. Although the ion cavity is extended downstream in Model-1, the cavity continues to expand in the radial direction suffering little influence from the plasma flow in Model-2. This is because the $E \times B$ drift of the plasma is dominant around the satellite in the model plane. At the upstream region, the plasma density is high because of the compression effect caused by the ambient plasma flow.

Figure 4.3c shows the density profiles at $\omega_{LHR}t = 12.3$. The plasma density at the upstream edge of the ion cavity continues to increase owing to the continuous compression by the plasma flow. It should be noted that the profile of the rarefaction shows asymmetry which is extended to the lower side of the ion cavity. Associated with this asymmetry, the distribution of the high density plasma at the upstream region tends to be asymmetric.

(a) Model-1   (b) Model-2

Plasma Flow
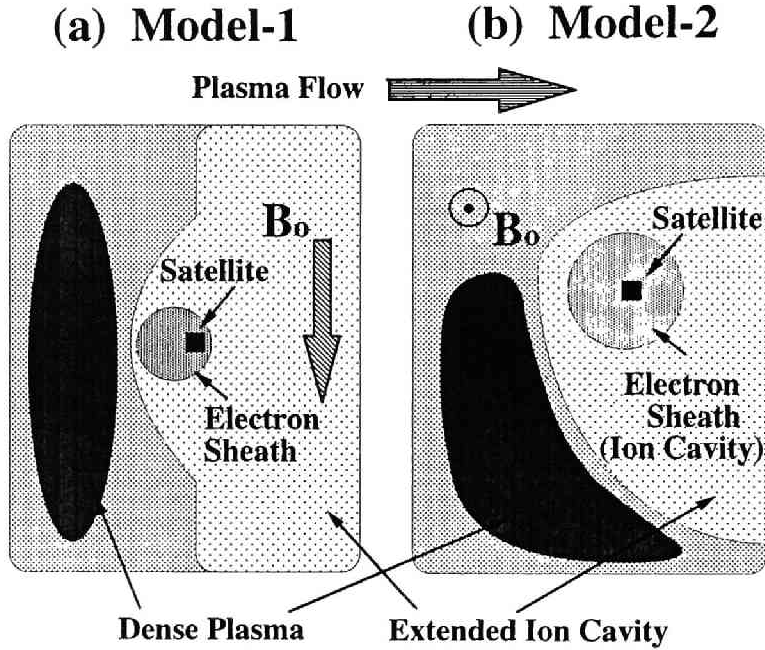
Figure 4.4: Schematic illustrations of the density profile in the steady state for Model-1 and Model-2.

At a later time in the steady state stage, the density asymmetry of the rarefaction becomes more evident with respect to a plasma stream line passing through the satellite. The density contour maps at $\omega_{LHR}t = 62.7$ are shown in Figure 4.3d. As well as the distortion of the ion rarefactional region, we see strong asymmetry in density at the upstream region. The density profile of electrons is almost the same as that of ions except for the electron sheath around the satellite.

Figure 4.4a and Figure 4.4b show a schematic illustration of the density profile in the steady state for Model-1 and Model-2, respectively. In the vicinity of the satellite, the electron sheath and the ion cavity are created. In the downstream and upstream regions with respect to the satellite position, the rarefactional region and the dense plasma wall are formed, respectively, which are extended along B_0 because of high plasma mobility in its direction. Although we supply no thermal electrons along B_0 at the boundary, the plasma depletion qualitatively makes sense because it is basically created by the ion repulsion from the satellite. If the thermal electrons were injected along B_0 at the edge of the model plane, the electron sheath around the satellite might become thick and

the resulting shielding effects would reduce the plasma depletion region along B_0. In estimating the current-voltage characteristics of the satellite, which will be described in a following section, the injection through this boundary is made properly. In 3D situation, the satellite will be more effectively shielded because of the effect of electron attraction from all the directions. This implies that the size of the plasma depletion region will be less than that observed in the present computer experiments. In the plane perpendicular to B_0, the ambient plasma shows the asymmetrical behavior. It is owing to the strong $E \times B$ effect on the plasma flow. In the next section, we will discuss the asymmetry of the density profiles in detail.

Note that the density value is different along $y/\lambda_D = z/\lambda_D = 0$ between Model-1 and Model-2. For example, at $x/\lambda_D = -48$, $y/\lambda_D = 0$, $z/\lambda_D = 0$ located at the upstream region in Figure 4.2 and Figure 4.3, the plasma density in Model-2 is higher than that in Model-1. This is due to the fact that these models hire different configuration in terms of direction of B_0 in two dimensional plane; B_0 is parallel and perpendicular to the model plane in Model-1 and Model-2, respectively. Generally, in a two dimensional plane, the spatial variation of quantities along the third dimension are not solved. Therefore, when the plasma is compressed at the upstream region in Model-2, the compressed plasma cannot escape along B_0 and eventually the thickness of the compressed region expands in time. In Model-1, however, some of the compressed plasma can escape along B_0. This makes the plasma compressed region thinner than that of Model-2 at the same position. At the downstream region, for example, at $x/\lambda_D = 48$, $y/\lambda_D = 0$, $z/\lambda_D = 0$, the plasma density in Model-2 is also higher than that in Model-1. This is also due to the fact that no plasma can escape along B_0 in Model-2. If we perform a three dimensional computer experiment, this confusion will be avoided.

4.2.3 Current Variation

The most significant factor dominating the plasma dynamics in the present computer experiment is the intense electrostatic field directed outward from the high potential satellite. In this section we present the plasma response in terms of the current due to this intense electric field. First, we examine the transient current which initially flows outward from the satellite. For simplicity, we use Model-3, in which the plasma flow is perpendicular to the model plane so that the plasma dynamics in the plane are independent of the flow effect. To see the current variation as a function of satellite potential, we performed three cases of computer experiment with different satellite potential: $e\phi_s/k_B T_e = 12.5, 125$, and 1000.
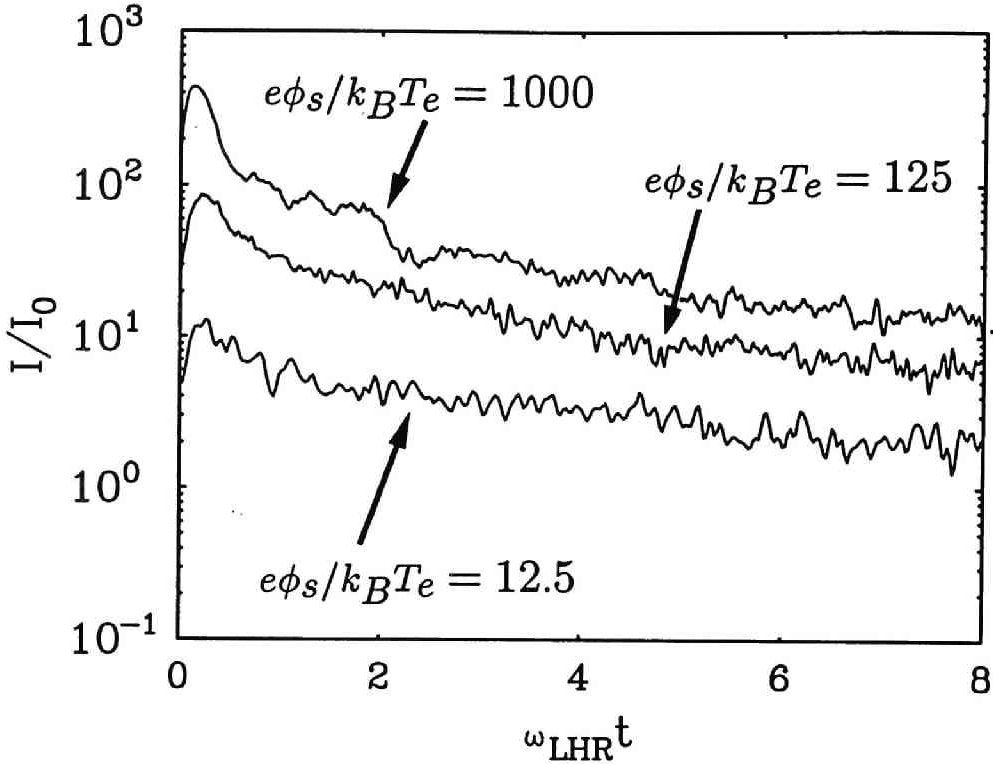
Figure 4.5: Time evolution of the transient current flowing out from the satellite for potentials $e\phi/k_BT_e = 12.5$, 125, and 1000.

Since the high potential satellite is placed in the unperturbed plasma at $t = 0$, the transient current flows outward from the satellite until it reaches the steady state. Figure 4.5 shows the time variation of the current from the satellite for the three different potential ϕ_s's. In the computer experiments, we measure the current by counting the number of particles which are trapped by the satellite for one time step Δt. To smooth the time series of the current values, we make use of a digital three-point-filter [Birdsall and Langdon, 1985]. The current is normalized to the ambient current I_0 which is defined as follows. When the satellite with a radius r_0 keeps its potential at the space potential, it will collect the current I_0 contributed by the thermal motion of the surrounding plasma, which is given by

$$I_0 = 2\pi r_0 j_0 \; ; \; j_0 = \frac{en_0}{2}\sqrt{\frac{2k_BT_e}{\pi m_e}} \quad . \tag{4.1}$$

where j_0 is the random thermal current density. In each case, the time scale for the initial rise of the current is the order of T_{pe} where T_{pe} denotes the period of the electron plasma oscillation. The peak value of the initial current increases as ϕ_s

increases. The peak initial current is approximately 10, 90, and 400 times I_0, for $e\phi_s/k_BT_e$ of 12.5, 125, and 1000, respectively. After this initial peak, the current decreases exponentially with respect to time up to around $\omega_{LHR}t = 12$. After this transient period, the current flowing out from the satellite is approximately constant.

In the steady state, the electrons attracted by the high potential satellite contribute to the current flow. In the present computer experiments, electrons are strongly magnetized. Therefore the current profile has to be analyzed in two directions; parallel and perpendicular to B_0. The general features are the followings. Initially, the electrons in the vicinity of the satellite are attracted toward the satellite from all directions. Later, however, the electron current flowing parallel to B_0 becomes dominant. In the direction perpendicular to B_0, the cross-field current flows only in the vicinity of the satellite owing to the local $E \times B$ drift motion of the plasma.

Figure 4.6a and Figure 4.6b show the vector plot of the current intensity in the steady state in Model-1 and Model-2, respectively. In Figure 4.6a, it is seen that the arrows are pointing outward from the satellite. The electron current flows along B_0 out from the satellite due to the electron attraction to the high potential. In the downstream region, the current is weak because of few number of electrons there. Figure 4.6b depicts the profile of the cross-field current in the $x - z$ plane for Model-2. In this case, the electron motion is along the $E \times B$ vector of the electric field out from the satellite and B_0 field. The area of the intense current corresponds to the electron sheath formed in the ion cavity. For $e\phi_s/k_BT_e = 100$, the intensity of this cross-field current is almost comparable to that of the field-aligned current observed in Model-1.

4.2.4 Current-Voltage Characteristics

Due to the large thermal velocity of electrons, the space vehicle is generally negatively-charged in the ionosphere. In the shuttle electrodynamic tether system, however, the satellite potential ϕ_s can be boosted up to $e\phi_s/k_BT_e \simeq 10^4$ which is much higher than the space potential. In this high potential, conventional models, e.g., the Langmuir theory, are inapplicable. One of the major aims of this paper is to study the current-voltage relation of such a high potential satellite.

When a dynamo is created in the space plasma owing to the cross-field motion of the electrodynamic tether, a current closure will be formed through the tether system and its surrounding plasma. To estimate the total current in the current closure, we have to take total resistance of the current loop into consideration. In addition to the impedance between the satellite and its surrounding plasma,

$\omega_{LHR}t= \ 62.26$
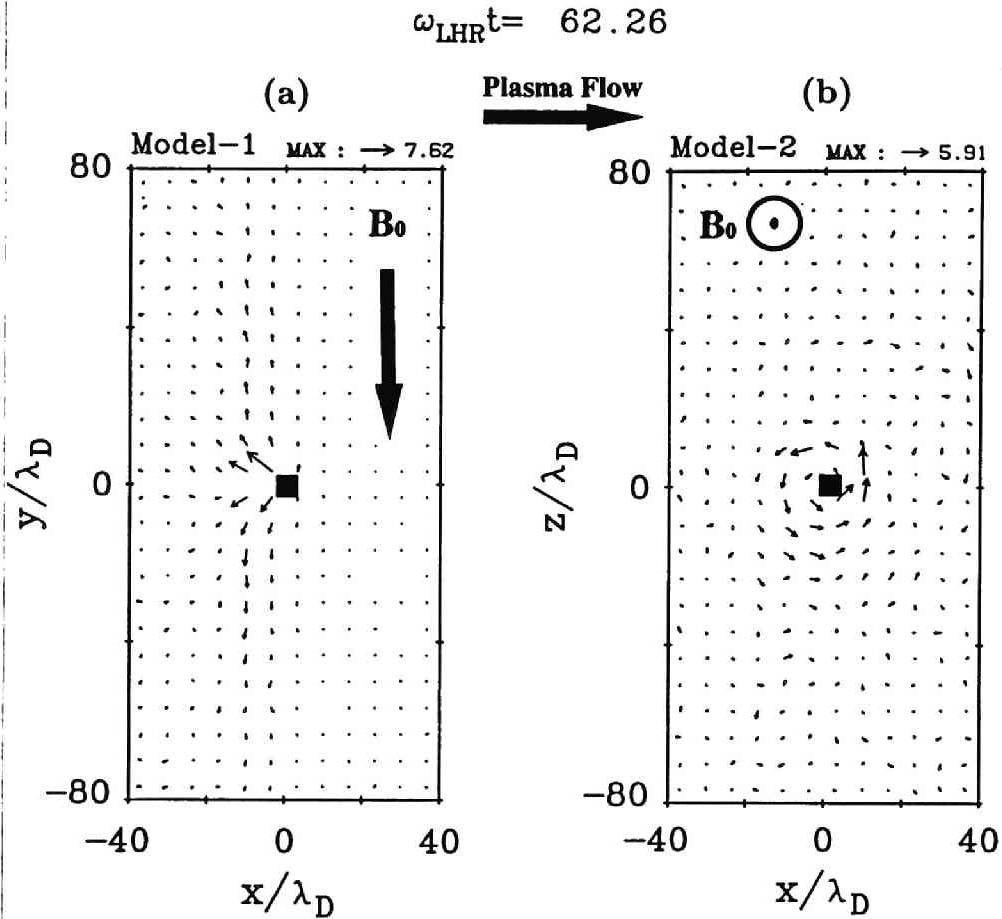
Figure 4.6: Snap shot of current density profile for (a)Model-1 and (b)Model-2. Current density is plotted as vectors on each grid point.

there exist the tether wire resistance, the impedance between the orbiter and the plasma controlled by the electron beam emission, and the impedance in the ambient plasma itself. In the present paper, however, we focus on the satellite-plasma interaction only. Although the total current in the current closure cannot be determined by the present model, the satellite-plasma impedance can be obtained by the current-voltage characteristics of the satellite, which is one of the essential factors in the current closure created by the electrodynamic tether system.

We approached to this problem by a series of computer experiments based on a particle model. To avoid plasma flow effects such as the plasma compression and the rarefactional wake formed in the upstream and downstream region, respectively, we use Model-3 in which the ambient plasma flows perpendicular to the model plane. As stated in the previous section, thermal electrons are

injected along B_0 at the edge of the model plane. Twelve cases of computer experiments are performed with different satellite potentials from $e\phi_s/k_BT_e = 10^0$ to 10^3. Since the steady-state current collection is of interest to us, we follow the plasma dynamics until the current reaches a steady state. To understand the current-voltage characteristics obtained by the computer experiments, we compare the results with existing theories of maximum electron current attainable to a cylindrical probe.

The first theory to be compared with is the well-known classical Langmuir theory for a co-axial cylindrical probe consisting of an outer cathode and an inner anode tube. This theory takes space charge effects into account [Langmuir and Blodgett, 1923]. Regarding the outer edge of the ion cavity as the outer cathode tube, we can apply the theory to the high potential satellite case. Equating the ratio of the cathode to the anode radii with that of the ion cavity and the satellite radii, the current-voltage relation is given by

$$I = \frac{8\epsilon_0\pi}{9}\sqrt{\frac{2e}{m_e}}\frac{\phi_s^{3/2}}{r_0\beta^2} \tag{4.2}$$

$$\beta = \ln\left(\frac{r_0}{r_{ic}}\right) - \frac{2}{5}\left[\ln\left(\frac{r_0}{r_{ic}}\right)\right]^2 + \frac{11}{120}\left[\ln\left(\frac{r_0}{r_{ic}}\right)\right]^3 - \frac{47}{3300}\left[\ln\left(\frac{r_0}{r_{ic}}\right)\right]^4 + \cdots \tag{4.3}$$

where I is the electron current to the satellite per unit length, r_{ic} is the ion cavity radius, and ϵ_0 is the electric permittivity. An unknown variable in the equation is the ratio of r_{ic} to r_0 which may vary as the satellite voltage changes. The ratio of r_{ic}/r_0 can be estimated as follows. Assuming that all of the electrons that enter the ion cavity region reach the high potential satellite, the current I flowing out from the satellite is simply estimated by

$$I = 2\pi r_{ic}j_0 = I_0\frac{r_{ic}}{r_0} \tag{4.4}$$

This gives the following relation between I and r_{ic}.

$$\frac{r_{ic}}{r_0} = \frac{I}{I_0} \tag{4.5}$$

Substitution of (4.5) into β in (4.3) yields the current-voltage relation

$$\phi_s^{3/2} = \frac{9r_0}{8\epsilon_0\pi}\sqrt{\frac{m_e}{2e}}I\left[\ln\left(\frac{I_0}{I}\right) - \frac{2}{5}\left[\ln\left(\frac{I_0}{I}\right)\right]^2 + \frac{11}{120}\left[\ln\left(\frac{I_0}{I}\right)\right]^3 - \frac{47}{3300}\left[\ln\left(\frac{I_0}{I}\right)\right]^4 + \cdots\right]^2. \tag{4.6}$$

It should be noted that the theory stated above includes no B_0 effects. The current I would be reduced if the B_0 effect was taken into consideration because

the B_0 effect may block some electrons which pass the surface of the cavity from reaching the surface of the satellite.

The second theory to be compared is the current-voltage relation derived by Parker and Murphy [1967]. They took account of B_0 effects using the conservation of energy and angular momentum of a single particle, neglecting the possible collective effects owing to the presence of the background plasma. Thus their theory gives a lower limit to the current. A brief description is given below.

Cylindrical coordinates r, θ, and z are chosen to represent the radial, azimuthal, and axial coordinates. The static magnetic field B_0 points along the z direction. Assuming that an electron is on a magnetic field line at infinite z with a radial distance r_{inf} from the z axis and its kinetic and potential energies are zero, the constants of the motion are given by

$$C_1 = r^2 \left(\frac{d\theta}{dt} + \frac{\Omega_e}{2} \right) \tag{4.7}$$

and

$$C_2 = \frac{m_e}{2} \left[\left(\frac{dr}{dt} \right)^2 + \left(\frac{dz}{dt} \right)^2 + r^2 \left(\frac{d\theta}{dt} \right)^2 \right] - e\phi_{rz} \tag{4.8}$$

which correspond to the conservation of canonical angular momentum and of energy, respectively, where ϕ_{rz} denotes the potential in the $r-z$ plane. C_1 and C_2 at infinite z, where all of $d\theta/dt$; dr/dt; dz/dt and ϕ_{rz} are set to be zero, are $r_{inf}^2 \Omega_e / 2$ and zero, respectively. By equating the constants of motion C_1 and C_2 at $z = \infty$ to (4.7) and (4.8), the particle trajectory in the $r-z$ plane is given by

$$\left(\frac{r}{r_{inf}} - \frac{r_{inf}}{r} \right)^2 = \frac{8}{m_e \Omega_e^2 r_{inf}^2} \left[e\phi_{rz} - \frac{m_e}{2} \left(\frac{dz}{dt} \right)^2 \right]. \tag{4.9}$$

The unknown variable is dz/dt. For simplicity, however, we set $dz/dt = 0$ which gives us the maximum value of r/r_{inf} in (4.9). In the case that the electron located at infinite z with r_{inf} is trapped by the satellite, $r = r_0$ and $\phi_{rz} = \phi_s$ can be substituted into (4.9) at the satellite surface. Assuming that all the electrons within a distance r_{inf} from the z axis can reach the satellite surface, the maximum current I attainable to the satellite along B_0 is given by

$$I = 2r_{inf} j_0 \cdot 2. \tag{4.10}$$

The normalization of I to I_0 by using (4.1) yields the following current-voltage relation.

$$\frac{I}{I_0} = \frac{2r_{inf}}{\pi r_0} = \frac{2}{\pi} \left(1 + \sqrt{\frac{8e\phi_s}{m_e \Omega_e^2 r_0^2}} \right)^{1/2}. \tag{4.11}$$

The third theory to be compared is a constant density model proposed by Linson [1969]. As the Boltzmann distribution can no more be descriptive for the electron density in the ion cavity region in case of $e\phi_s/k_BT_e \gg 1$, one can assume a constant density profile for electrons.

For Model-3, Poisson's equation is simply given by

$$\frac{\partial^2\phi}{\partial y^2} + \frac{\partial^2\phi}{\partial z^2} = \frac{en_e}{\epsilon_0} \tag{4.12}$$

where ϕ and n_e are the potential and the constant electron density in the ion cavity, respectively. As the electron mobility is very high along B_0 (i.e., along the y axis), we can assume the potential gradient along the y direction is zero. This assumption eliminates the first term on the left hand side of (4.12). Therefore (4.12) is easily integrated with respect to z under boundary condition such that the potential and the electric field at the edge of the cavity are equal to zero. The relation between the satellite potential ϕ_s and the ratio r_{ic}/r_0 is then given by

$$\phi_s = \frac{en_e r_0^2}{2\epsilon_0}\left(\frac{r_{ic}}{r_0} - 1\right)^2. \tag{4.13}$$

In a similar fashion, the maximum current I attainable to the satellite along B_0 is expressed as

$$I = 2r_{ic}j_0 \cdot 2. \tag{4.14}$$

The current ratio is then given by

$$\frac{I}{I_0} = \frac{2r_{ic}}{\pi r_0} = \frac{2}{\pi}\left(1 + \sqrt{\frac{2m\phi_s}{eq_c r_0^2 B_0^2}}\right), \tag{4.15}$$

where $q_c = \Pi_e^2/\Omega_e^2$ in the ion cavity region.

Estimation of q_c is not straightforward. q_c depends on the satellite potential and position relative to the satellite. The electron density observed in our computer experiments is actually not constant around the satellite and the electron density varies as the satellite potential changes. Figure 4.7 and Figure 4.8 show a series of contour maps of the electron and ion number densities for different satellite potentials from $e\phi_s/k_BT_e = 60$ to 2500. As the satellite potential increases, the ion cavity expands because of repulsion from the satellite. To maintain charge neutrality, the density profile of electrons is almost equal to that of ions except for the electron sheath in the ion cavity. The electron density used for q_c is averaged over the length from the satellite surface to the edge of the ion cavity in the direction transverse to B_0. As shown in Figure 4.7, the electron distribution in the ion cavity is rather uniform up to $e\phi_s/k_BT_e \simeq 1000$. The average density is approximately a quarter of the ambient density, this gives
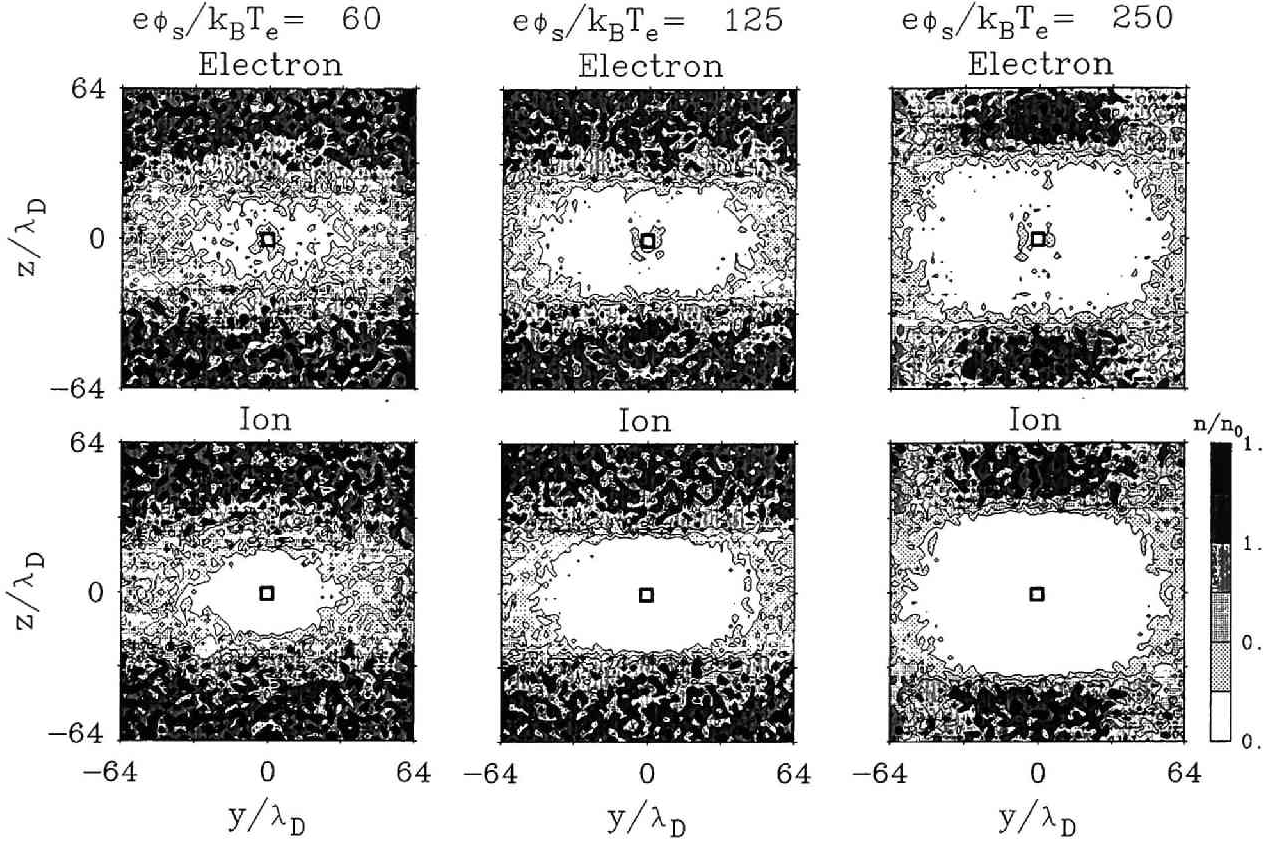
Figure 4.7: Contour maps of the number densities for the background electrons and ions in Model-3. The ratio of the satellite potential energy $e\phi/k_B T_e$ are 60, 125, and 250.

$q_c \simeq 1.0$. It is seen in Figure 4.8 that for $e\phi_s/k_B T_e > 1000$ electron distribution is nonuniform in the ion cavity. Electrons are highly concentrated around the satellite for $e\phi_s/K_B T_e = 2000$ and 2500. The maximum density is higher than the ambient plasma density. In addition, the ion cavity expands in the direction not only parallel but also perpendicular to B_0. The cavity size thus becomes comparable to the size of the model region of the computer experiments. As the thermal electrons are injected only along B_0 at the boundaries to compensate for the electrons collected by the satellite, the electron density in the ion cavity in these cases would be a little smaller than expected. However, we adopted the average values of the electron density in the ion cavity to estimate q_c. The average electron densities are 0.38 and 0.46 times the ambient density respectively for $e\phi_s/k_B T_e = 2000$ and 2500. The estimated q_c are thus approximately 1.5
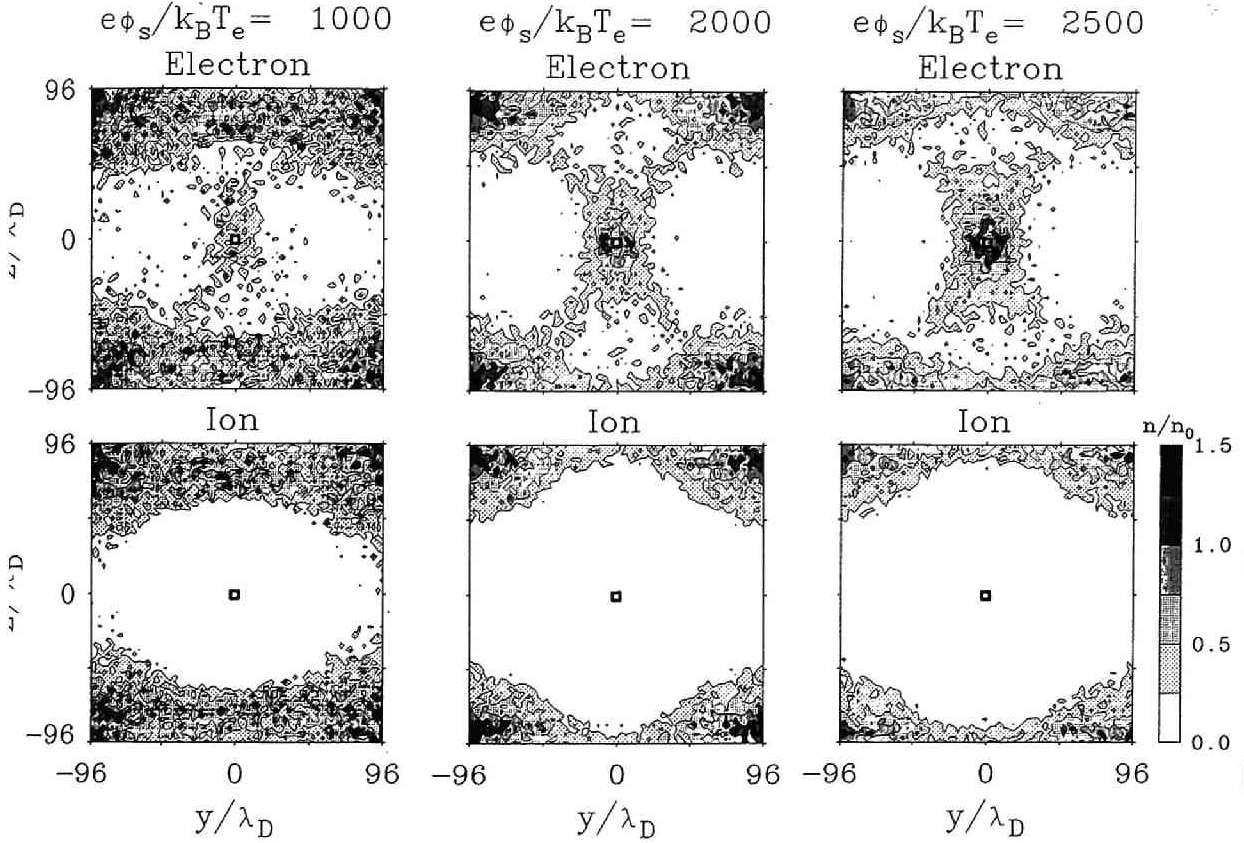
Figure 4.8: Contour maps of the number densities for the background electrons and ions in Model-3. The ratio of the satellite potential energy $e\phi/k_B T_e$ are 1000, 2000, and 2500. The square at the center represents the satellite.

and 1.8, respectively.

In Figure 4.9, the current values obtained by the computer experiments are plotted as a function of the satellite potential energy small squares with error bars. The each current value is averaged over a period of $\omega_{LHR} t = 12 \sim 17$. The maximum current values estimated by the three theories stated above are superimposed in Figure 4.9. The dotted curves (1) and (2) represent the current voltage relation of the Langmuir theory obtained from (4.6) and the single particle theory from (4.11), respectively. In addition, the current estimate from the constant density theory assisted by the result of the present computer experiments on the electron number density in the ion cavity is plotted cross marks.

The average current values obtained by the computer experiments lie be-
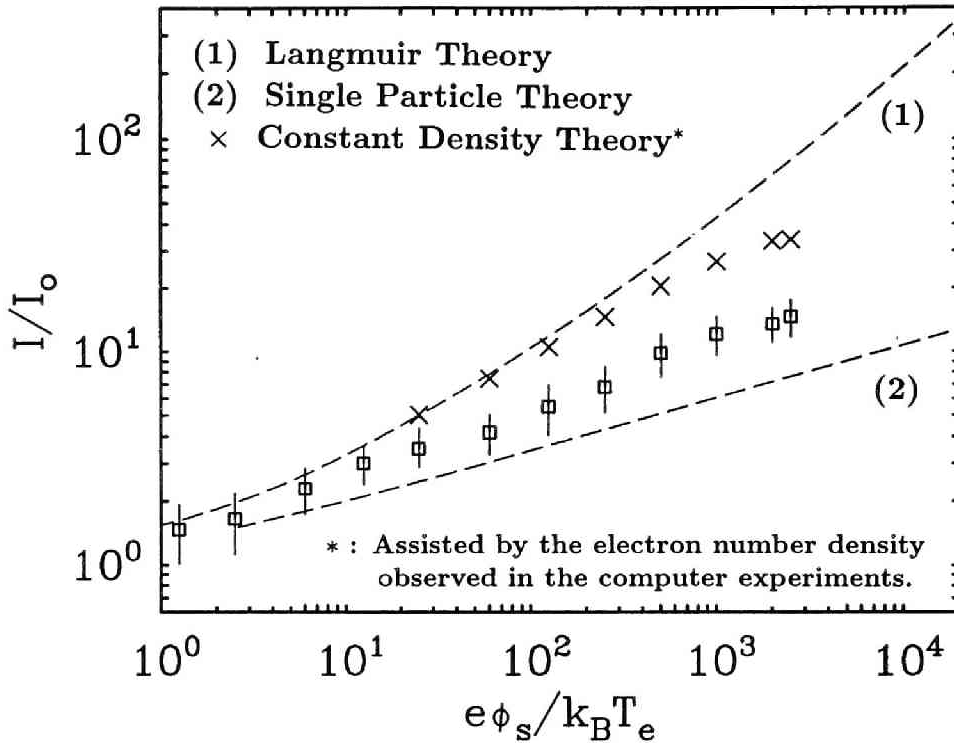
Figure 4.9: Current-voltage characteristics of the satellite. The dotted curves (1) and (2) correspond to the Langmuir theory and the single particle theory, respectively. The small squares with error bars indicate the average current in the steady state obtained by the computer experiments using Model-3. The cross marks correspond to the constant density theory assisted by the number density obtained by computer experiments.

tween the theoretical curves (1) and (2). The Langmuir theory, which gives the upper limit to the satellite current, can provide a good estimate of the average current for the satellite potential up to $e\phi_s/k_B T_e \sim 10$. For the higher potential, however, the current gap increases between the Langmuir theory and the average current by the computer experiments. The current by the Langmuir theory is approximately eight times higher than that by the computer experiments for $e\phi_s/k_B T_e = 2500$. Even though taking account of the boundary effects which may reduce the current collection of the satellite, this difference is essential because the Langmuir theory includes no B_0 effect.

In comparison with the single particle theory which includes the B_0 effect, the average current by the computer experiments is approximately twice as intense

as the theoretical estimate shown by curve (2). This gives a much better estimate of the average current from the satellite than the Langmuir theory. However, the electrons attracted by the satellite cannot strictly conserve the constants of motion as assumed in the single particle theory. This implies that the cross-field transportation of electrons occurs in spite of the magnetization of the plasma.

In terms of the upper bound of the current from the satellite in the steady state, the constant density theory represented by the cross marks in the figure provides the best estimate among the three theories discussed in the present study. In applying the constant density theory, we need to estimate the constant electron density in the ion cavity. However, it is difficult to obtain an analytic estimate of the density in the vicinity of the high potential body. In such cases, computer experiment can be a powerful method to estimate the density distribution in the ion cavity.

It is shown that the cavity size becomes as large as the model size of the computer experiments for the potential above $e\phi_s/k_BT_e \simeq 10^3$ in the present computer experiments. This might cause an error of the current estimate by the computer experiments. Basically, in the direction perpendicular to B_0, the cavity is hard to expand because the plasma tends to be frozen B_0. However, as the satellite potential is increased, the cavity grows and the edge of the cavity encounters the edge of the model plane. In such a case, the thermal electrons cannot be supplied fast enough to the ion cavity region across B_0. This will cause an erroneous reduction in the current collection of the satellite. To see the boundary effects on the electron collection to the satellite, we performed a computer experiment with a larger model region, i.e., $1024\Delta r \times 512\Delta r$. The satellite potential is $e\phi_s/k_BT_e = 2500$. Although not displayed, it is found that the model plane is large enough to cover the ion cavity in the steady state. Then the average of the steady-state current from the satellite is approximately 30% larger than that obtained with the present smaller model plane. This enhanced current value by the sufficiently large model, however, is still much smaller than the current estimated by the Langmuir theory. The constant density theory is still valid as a good estimate of the maximum current. Thus, in the limited potential range approximately up to $e\phi_s/k_BT_e \simeq 10^3$, the boundary gives little effects to the discussion of the current estimate described above. However, it is proved that, if the ion cavity becomes as large as the model plane, the current collection by the satellite is reduced by the undiserable interaction of the ion cavity with the boundary of the model plane. To avoid this boundary effect, we need a much larger model region for the computer experiment than that used here. This will be carried out when bigger computer becomes available.
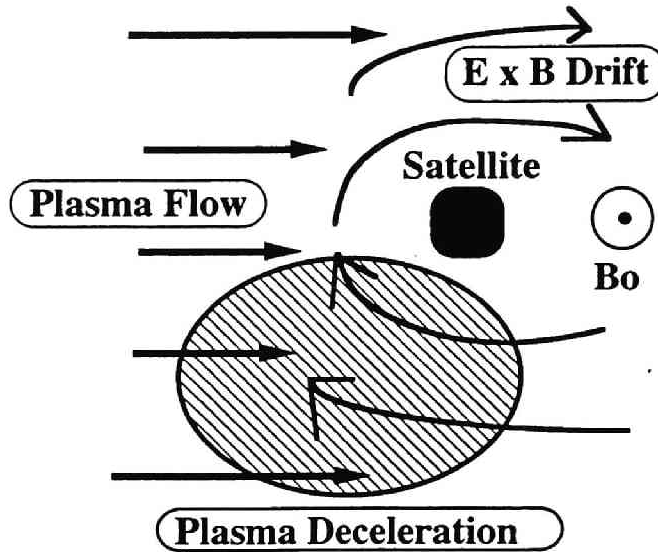
Figure 4.10: Schematic illustration showing the interaction between the ambient plasma flow and the $E \times B$ drift.

4.2.5   Discussion

Asymmetric Density Profile

In the theoretical study of the density distribution around a cylindrical structure, Grabowski and Fischer [1975] have shown an asymmetric rarefactional wake due to the combined action of a magnetic and electric field. In the present computer experiments, we also found an asymmetric profile of the ambient plasma density with respect to the satellite as shown in Figure 4.3. In the model plane to which B_0 is perpendicular, the asymmetric density structure is due to the local $E \times B$ effect on the plasma flow which is driven by the intense electric field caused by the high potential satellite passing through the static magnetic field. To interpret this effect, a schematic illustration is shown in Figure 4.10 in which the left side corresponds to the upstream region of the flow. The ambient plasma flowing toward the satellite experiences an $E \times B$ drift rotation of plasma in the clockwise direction. Without the plasma flow, the plasma around the satellite should rotate uniformly with respect to the satellite. In the presence of the plasma flow, however, the direction of the ambient plasma flow is opposite to the local $E \times B$ drift motion in the shaded region. Therefore, the ambient plasma flow is decelerated by the $E \times B$ effect and, thereby, the plasma is piled up leading to the high density region in the shaded region. In the upper side of the ion cavity region, the direction of the plasma flow is the same as that of the

$E \times B$ drift velocity. Therefore the plasma flow is accelerated downstream by the $E \times B$ effect. This relative difference of the plasma flow velocity can cause a distortion of the profile of the extended ion cavity as well.

We can roughly estimate the $E \times B$ drift velocity at the edge of the cavity as a function of the satellite potential neglecting the plasma flow effect. First of all, we need to know the intensity of the electric field at the edge of the cavity region. The potential ϕ and the electric field at a distance r from the satellite are generally written in terms of the local Debye length λ_D and the satellite potential ϕ_s as follows.

$$\phi = \phi_s \exp\left(-\frac{r}{\lambda_D}\right) \tag{4.16}$$

$$\frac{\partial \phi}{\partial r} = -\frac{\phi_s}{\lambda_D} \exp\left(-\frac{r}{\lambda_D}\right). \tag{4.17}$$

Assuming λ_D is equal to the radius of the ion cavity region r_{ic}, the electric field at the edge E_{ic} is,

$$|E_{ic}| = \left|\frac{\partial \phi}{\partial r}\right|_{r=r_{ic}} = \frac{\phi_s}{r_{ic}} \exp(-1). \tag{4.18}$$

Applying the constant density model, we can eliminate r_{ic} in (4.18) by using (4.13). Then the $E \times B$ drift velocity is roughly given by

$$V_{E\times B} = \left|\frac{E_{ic}}{B_0}\right| \simeq \phi_s \exp(-1) \left(B_0 r_0 + \sqrt{\frac{2m\phi_s}{eq_c}}\right)^{-1}. \tag{4.19}$$

To see the dependence of the asymmetry of the plasma density on the relative difference between V_p and $V_{E\times B}$, we conducted three computer experiments with different plasma flow velocities. The satellite potential energy is fixed to $e\phi_s/k_B T_e = 50$ in the three cases. Applying the parameters used in the computer experiments to (4.19), we obtain $V_{E\times B} \simeq 3.0$. Figure 4.11 shows the contour maps of the ion density for $V_p/V_{E\times B}$ approximately equal to; (a) 0.1, (b) 0.5, and (c) 2.0. When V_p is negligible compared to $V_{E\times B}$, the density profile is nearly symmetric as seen in Figure 4.11a. As V_p increases, the high density area is formed asymmetrically shown in Figure 4.11b. As stated above, this is due to the deceleration of the plasma flow by the $E \times B$ effect. As for the case (c), the high density region is located further downstream than in the case (b). Thus, it is concluded that the asymmetric region of the density profile depends on the ratio of V_p to $V_{E\times B}$.

Transient Current

In the SETS experiments, the burst emission of electrons will be undertaken
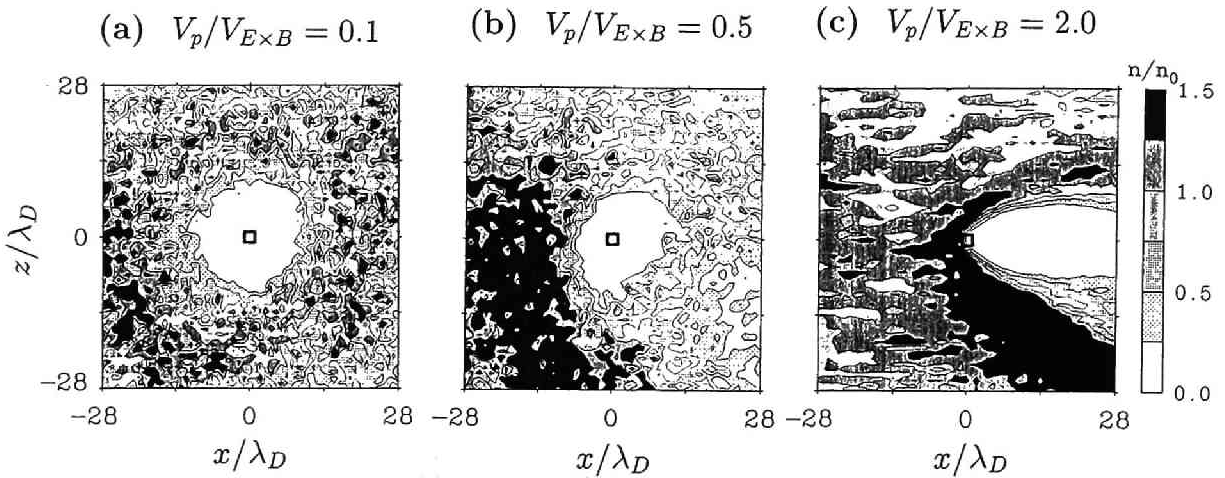
Figure 4.11: Contour maps for the number densities of the background ions. $V_p/V_{E\times B}$ are (a) 0.1, (b) 0.5, and (c) 2.0, respectively.

from the fast pulse electron gun called FPEG. The FPEG emissions can boost the satellite potential to higher than the space potential. This situation can give rise to the transient process examined earlier such as the current flowing out from the satellite and the plasma density in its vicinity.

It is demonstrated by the present computer experiments that the transient current flowing out from the high potential satellite consists of the intense initial current and the subsequent exponentially decreasing current. The initial current is due to the rapid attraction of electrons in the course of the formation of the electron sheath around the satellite. This implies that the time scale for the initial rise of the current is the order of the period of the electron plasma oscillation. Since the space charge effect to the satellite is not effective in this phase, the initial current is much more intense than in the steady state. We estimate the maximum current as a function of the satellite potential as follows.

The time scale for the satellite to obtain the maximum transient current is approximately $T_{pe}/4$. We estimate the maximum velocity of electron v_{max} accelerated by the satellite potential ϕ_s by using the energy conservation as follows.

$$\frac{1}{2}m_e v_{max}^2 = e\phi_s \tag{4.20}$$

Then v_{max} is given

$$v_{max} = \sqrt{\frac{2e\phi_s}{m_e}}. \tag{4.21}$$

In the actual case, all the electrons in the vicinity of the satellite cannot have the velocity v_{max}. The electron velocity oscillating at the frequency Π_e is taken to be

$$v(t) = v_{max} \sin(\Pi_e t). \tag{4.22}$$

The width of the electron layer Δl absorbed by the satellite is then given

$$\Delta l = \int_0^{T_{pe}/4} v_{max} \sin(\Pi_e t) dt = v_{max} \frac{T_{pe}}{2\pi} \tag{4.23}$$

The current I at the satellite for the time scale $T_{pe}/4$ is given by

$$I = e n_0 \pi ((\Delta l + r_0)^2 - r_0^2) \frac{4}{T_{pe}} \tag{4.24}$$

Substitution of (4.23) in (4.24) yields

$$I = e n_0 \left(v_{max}^2 \frac{T_{pe}}{\pi} + 4 r_0 v_{max} \right) = 2 e n_0 \left(\frac{e T_{pe}}{\pi m_e} \phi_s + 2 r_0 \sqrt{\frac{2e\phi_s}{m_e}} \right) \tag{4.25}$$

Figure 4.12 shows the comparison of the maximum current values between the theoretical estimate and the results by the computer experiments. The solid and dotted lines represent the theoretical estimate by (4.25) with T_{pe} for the plasma density n_0 and $4n_0$, respectively. The maximum transient current values obtained by the computer experiments are also plotted by small circles. They are located in between the theoretical lines. Thus (4.25) can provide a fairly good estimate of the maximum current. As the satellite potential increases, the dotted line can estimate the maximum current more accurate than the solid line. This implies that we need to take account of the increase of the electron sheath density owing to the electron concentration around the satellite. In the case of $e\phi_s/k_B T_e = 10^3$, the maximum density of the electron sheath is approximately four times the ambient plasma density. The dotted line shows this case.

After the rapid attraction of electrons to the satellite, the current intensity is exponentially reduced because of the space charge effect around the satellite. The time needed to reach the steady state is approximately $\omega_{LHR} t = 12$. In this stage, the formation of the ion cavity owing to the high potential is completed, which leads to the steady current.
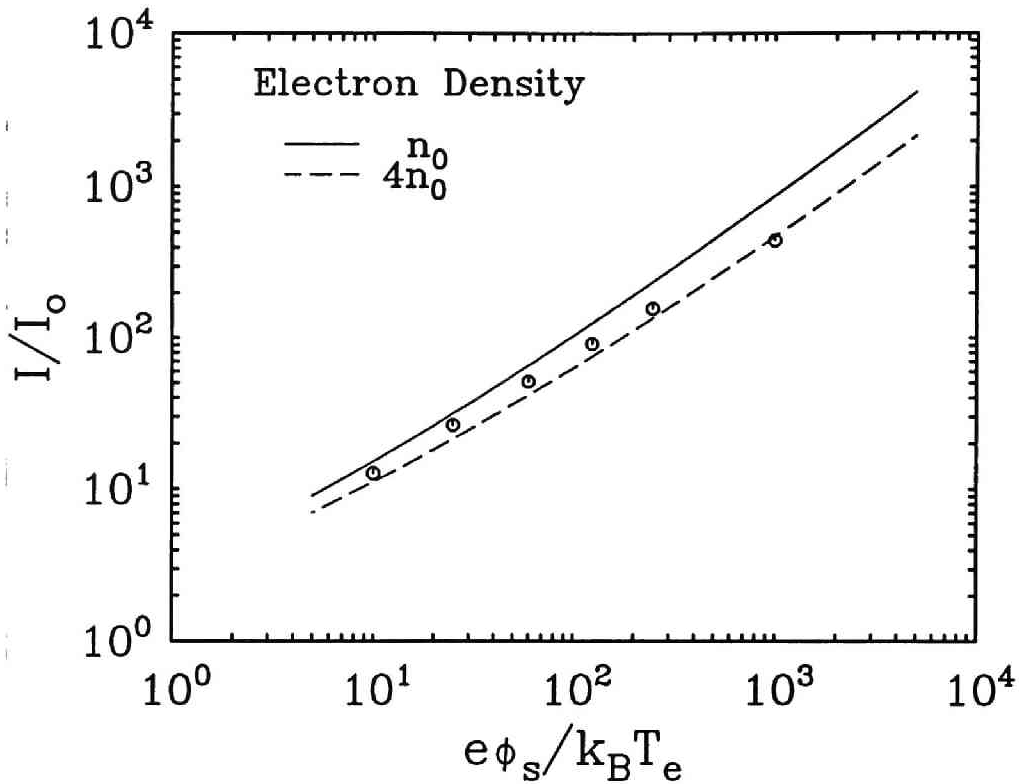
Figure 4.12: The maximum transient current as a function of the satellite potential. The solid and dotted lines represent the theoretical estimate by (4.25) with T_{pe} for n_0 and $4n_0$, respectively. The current values obtained by the computer experiments are plotted with the small circles.

4.2.6   Summary and Conclusion

Performing two-dimensional electromagnetic particle computer experiments, we have studied the plasma response to the high potential satellite in the electrodynamic tether system with the presence of the plasma flow and the static magnetic field. We focused on the spatial profiles of plasma density and of plasma current in the vicinity of the satellite. We also examined the transient process of the plasma response to the satellite. In the cases with B_0 and no plasma flow, the current-voltage characteristics of the satellite in the steady state are studied and compared with the classical theories. The density variations and the transient current are also analyzed in detail. A summary of the results is given below.

1. Plasma density and current profiles
Due to the high potential satellite, electron attraction and ion repulsion to and from the satellite are found. This causes the formation of an ion cavity and an electron sheath in the vicinity of the satellite in the steady state. Due to

the plasma flow, the ion cavity is extended to the downstream region as well as along B_0. The electron sheath created in the ion cavity is thicker in the direction transverse to B_0 than parallel to it [Ma and Schunk, 1989]. As the satellite potential becomes high, in particular, at $e\phi_s/k_B T_e \sim 10^3$, the electron sheath density in the ion cavity becomes larger than the ambient plasma density. In the perpendicular direction to B_0, the $E \times B$ effects cause an asymmetric distortion of the density profile of the ambient plasma at the upstream region. The plasma density is high in the region where the plasma flow is decelerated by the $E \times B$ effects.

The current flowing out from the satellite exhibits a transient process; intense initial transient current followed by exponentially decreasing current. The maximum transient current is successfully estimated as a function of the satellite potential. The steady state satellite current dominantly flows along B_0. In the vicinity of the satellite, the current owing to the $E \times B$ drift of the electron sheath is dominant in the direction transverse to B_0.

2. Current-Voltage characteristics

As far as the results of the present computer experiments are concerned, the current values indicate no saturation in association with the increase of the satellite potential up to $e\phi_s/k_B T_e \simeq 10^3$. Basically, B_0 regulates the electron flow to the satellite. Therefore the average current values can be approximately estimated by the theory derived from the conservation of a single particle constants of motion in B_0 [Parker and Murphy, 1967]. The results of the computer experiments, however, show that the average current values are approximately twice as large as the estimate of the single particle theory. This implies the cross-field transportation of electrons should be considered. Still, the current values are much below the estimate by the Langmuir theory which includes no B_0 effects. In terms of the upper bound of the current flowing from the satellite in the steady state, the constant density theory by Linson [1969] provides a good estimate for the satellite potential above $e\phi_s/k_B T_e \simeq 10^1$. In solving Poisson's equation, analytic plasma distribution such as the Boltzmann distribution cannot be used because it diverges in the vicinity of the satellite at the high potential $e\phi_s/k_B T_e \gg 1$. Therefore, to estimate the density value which is needed in the constant density theory, we needed to perform computer experiments for each potential of the satellite.

The theories we applied in the present paper neglect the finite gyroradius on the assumption that it is much smaller than the satellite size. Therefore the significant value r_{ic}/r_0 which determines the maximum current to the satellite takes no account of the electron gyroradius ρ_e. In the present computer experiments, however, ρ_e is finite and approximately a half of the satellite radius. In the cases of low potential approximately up to $e\phi_s/k_B T_e = 10$, ρ_e is comparable

to r_{ic}. Then we definitely need to include ρ_e to the theories. As the satellite potential is increased, however, r_{ic} becomes much larger than ρ_e and it can be negligible as in the theories of Parker and Murphy [1967] and Linson [1969]. We focused on the current values for the potential above $e\phi_s/k_B T_e \simeq 100$ in comparing with the theories. As shown in Figure 4.8, r_{ic} is much larger than ρ_e for the high potential cases. Then we can neglect the gyroradius effects.

The dimensions of the conducting body relative to the Debye length adopted to the present study are much smaller than those of the real tethered satellite. However, the size of the ion cavity measured from the satellite surface $r_{ic} - r_0$, is calculated from (4.13) and expressed in the form of

$$r_{ic} - r_0 = \sqrt{\frac{2\epsilon_0 \phi_s}{e n_e}} \qquad (4.26)$$

which is a function of the satellite potential, independent of r_0. Assuming that the size of the electron sheath is equivalent to that of the ion cavity, the dimensions of the ion cavity measured from the satellite surface described in this paper can be applicable to those of the electron sheath around the ionospheric satellite. Actually (4.26) indicates that the sheath size of the high potential satellite is larger than the Debye length by a factor of a ratio of the accelerated mean velocity of electrons to the electron thermal velocity of the background plasma. According to this, the actual size of the electron sheath of the high potential satellite of the order of several kV is from several centimeters to a few tens of centimeters. Thus the plasma dynamics in the vicinity of the satellite are greatly modified, which can change the electrostatic and electromagnetic environment around the satellite. A good example is the current-voltage characteristics of the satellite. We found that the amount of the current collection by the satellite depends on the electron density in the ion cavity region where microphysics in the order of Debye length plays a significant role.

In the present study, the plasma response to the high potential satellite was studied with two-dimensional model. In the more realistic case of a three-dimensional spherical the satellite, most of the basic physics described in the present paper will be qualitatively retained. However, their physical quantities such as the amount of the current collection by the satellite will be different from those obtained in the two-dimensional model because the third dimension is added for the plasma dynamics. To investigate and compare the physical quantities with the real situation, the computer experiments with three dimensional model are needed and are currently being performed.

Calder and Laframboise [1990] examined electrostatic oscillations owing to an abrupt change of electrode potential. Since they treated the cases which had no static magnetic field, the oscillation with the electron plasma frequency

was dominant in the vicinity of the electrode. In the present study in which the B_0 effect is considered, we confirmed the electrostatic oscillation with the local electron plasma and the upper hybrid frequencies along and across B_0, respectively.

Electromagnetic wave radiation from the satellite is also an interesting subject. The intense cross-field current driven by the local $E \times B$ effect can cause perturbations in the magnetic field as shown in Chapter 3. In the present computer experiments, the ratio of the perturbation to the ambient magnetic field B_1/B_0 is about -60 dB on the average in the vicinity of the satellite. Because the model region in the present computer experiments is too small to cover the long wave length of Alfvén waves, we cannot treat the perturbation of the magnetic field such as Alfvén wings [Drell et al., 1965]. The plasma wave generated in the vicinity of the high potential satellite will be studied in Chapter 5.

4.3 Three-Dimensional Electrostatic Particle Model

4.3.1 Model and Parameters

In this section, we examine the plasma response to the high potential tethered satellite by using a three-dimensional electrostatic model. Qualitatively, the plasma behavior may be the same as observed in the two-dimensional case. As discussed in Chapter 3, however, the Coulomb force in the three-dimensional space differs from that in the two-dimensional space. This implies that the electrical properties of the TSS such as current-voltage characteristics can be modified to some extent in the three-dimensional case. The following is the description of the three-dimensional computer experiments by using the electrostatic code.

The model space for the computer experiment is the same as shown in the upper panel of Figure 4.1. Since we adopt a vehicle frame of reference as well as in the two-dimensional case, the direction of the plasma flow with velocity of V_p points along the x axis. The external magnetic field B_0 lies in $-y$ direction. The potential values at the outer boundaries are set to be zero. At the center of the model space, we have one conducting body representing a high potential satellite whose dimensions are $6\lambda_D \times 6\lambda_D$. The satellite potential ϕ_s is fixed high compared with the space potential throughout the simulation run.

We adopt two models for the computer experiments. One is Model-1 where the ambient plasma flows in self-consistent manner in the model box along the x direction. The other is Model-2 in which the plasma flow is neglected. In the

two-dimensional case, the current-voltage characteristics of the satellite were obtained in the model region which is independent of the plasma flow effects. In the three-dimensional case, therefore, to match the conditions under which the current-voltage characteristics are obtained, we use Model-2 which suffers from no plasma flow effects. In the real situation, the satellite potential cannot be elevated without a relative motion between the satellite and B_0. However, we artificially fix a high potential to the satellite in Model-2.

The physical parameters used in the computer experiments are the same as we used in the two-dimensional cases stated in the previous section. For ambient electrons, $\Pi_e/\Omega_e = 2$, and $v_{te}/V_p = 8$. For ambient ions, $\Pi_i/\Omega_e = 0.2, \Omega_i/\Omega_e = 0.01$, and $v_{ti}/V_p = 0.8$. Because of the limitation to the speed and memories of the computer, we reduced the size of the model box in the present computer experiments. The dimensions are $64 \times 64 \times 64$ in the x, y, and z directions, respectively. The grid spacing is $\Delta r = \lambda_D$. The time step is $\Delta t = 0.1/\Omega_e$ which is much larger than that of the two-dimensional electromagnetic model, but still small enough for us to trace the plasma dynamics correctly. The number of the superparticles is 1,048,576 for each species of plasma particles at the initial state. The outgoing particles which have crossed the boundary planes are no more traced. To compensate the particles in the model box, the thermal plasma is injected from the $y - z$ planes at $x = 0$ in Model-1. In Model-2, the thermal electrons are injected along B_0 to compensate the electron depletion due to the electron collection by the satellite. We carried out the simulation run up to $\Omega_e t = 327$.

4.3.2   Ambient Plasma Response

In terms of number density of the electrons and ions around the satellite, we investigate the plasma response to the satellite in the three-dimensional space. A series of contour map shows the time evolution of the electron and ion density variation in the vicinity of the satellite. To see the three-dimensional profile of the density, We cut three planes out of the model box; $x - z$, $y - z$, and $x - y$ planes which correspond to Figure 4.13, Figure 4.14, and Figure 4.15, respectively. Each plane cuts the cross-section of the satellite. In each figure, panel (a), (b), and (c) correspond to the density profile at $\Omega_e t = 6.4$, 19.2, and 160, equivalent to T_{pe}, $3T_{pe}$, and $25T_{pe}$ where T_{pe} denotes one period of the electron plasma oscillation, respectively.

First, we examine the plasma dynamics in the $x - z$ plane as shown in Figure 4.13. B_0 is perpendicular to the plane and the plasma flow points along the x direction from the left to right side. Approximately within T_{pe} as shown in the panel(a), the electrons in the vicinity of the satellite are strongly attracted

(a)

Electron   Ion

(b)

(c)

n/n_0
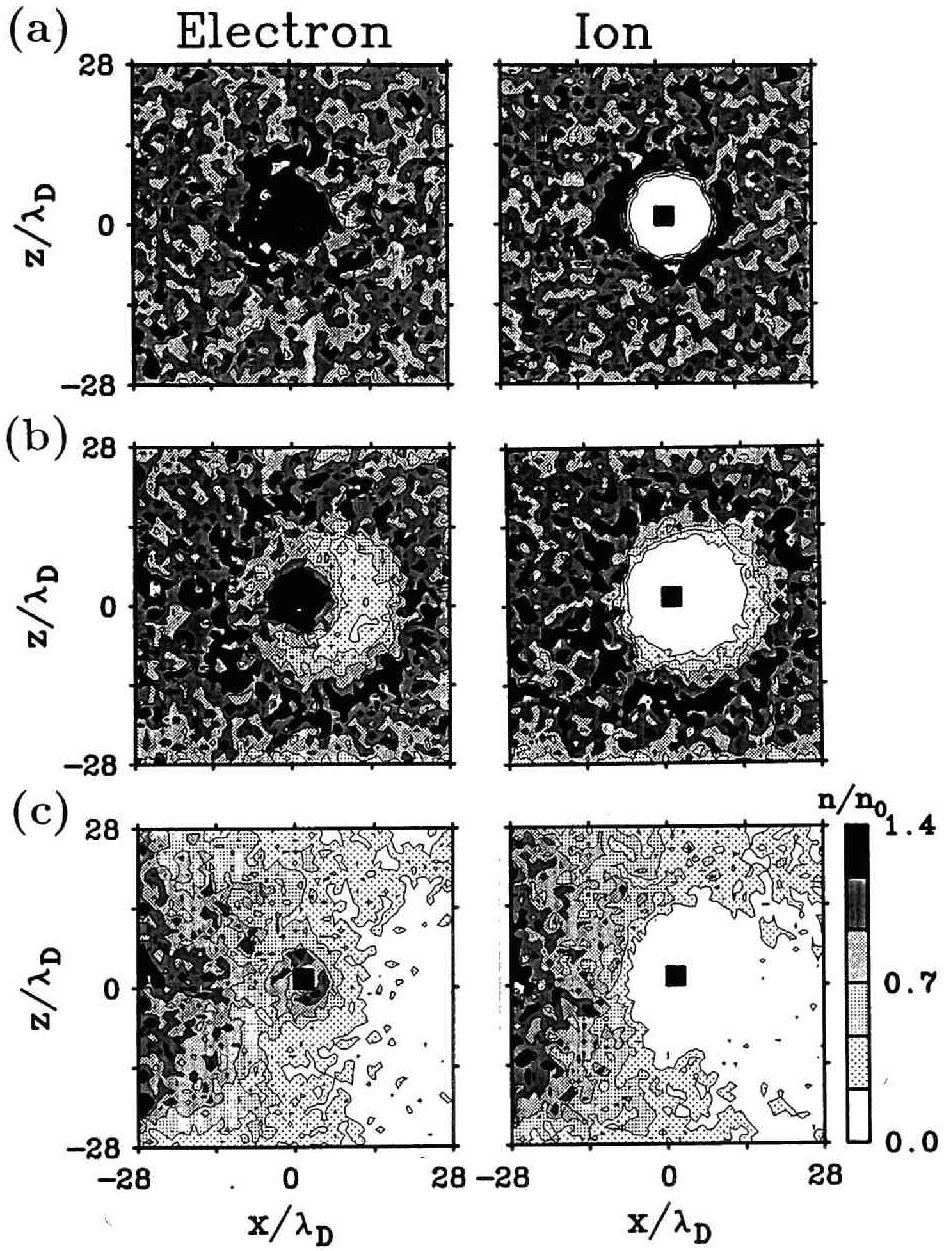
Figure 4.13: Contour maps of the number density for the background electrons and ions in the $x - z$ plane at different times.
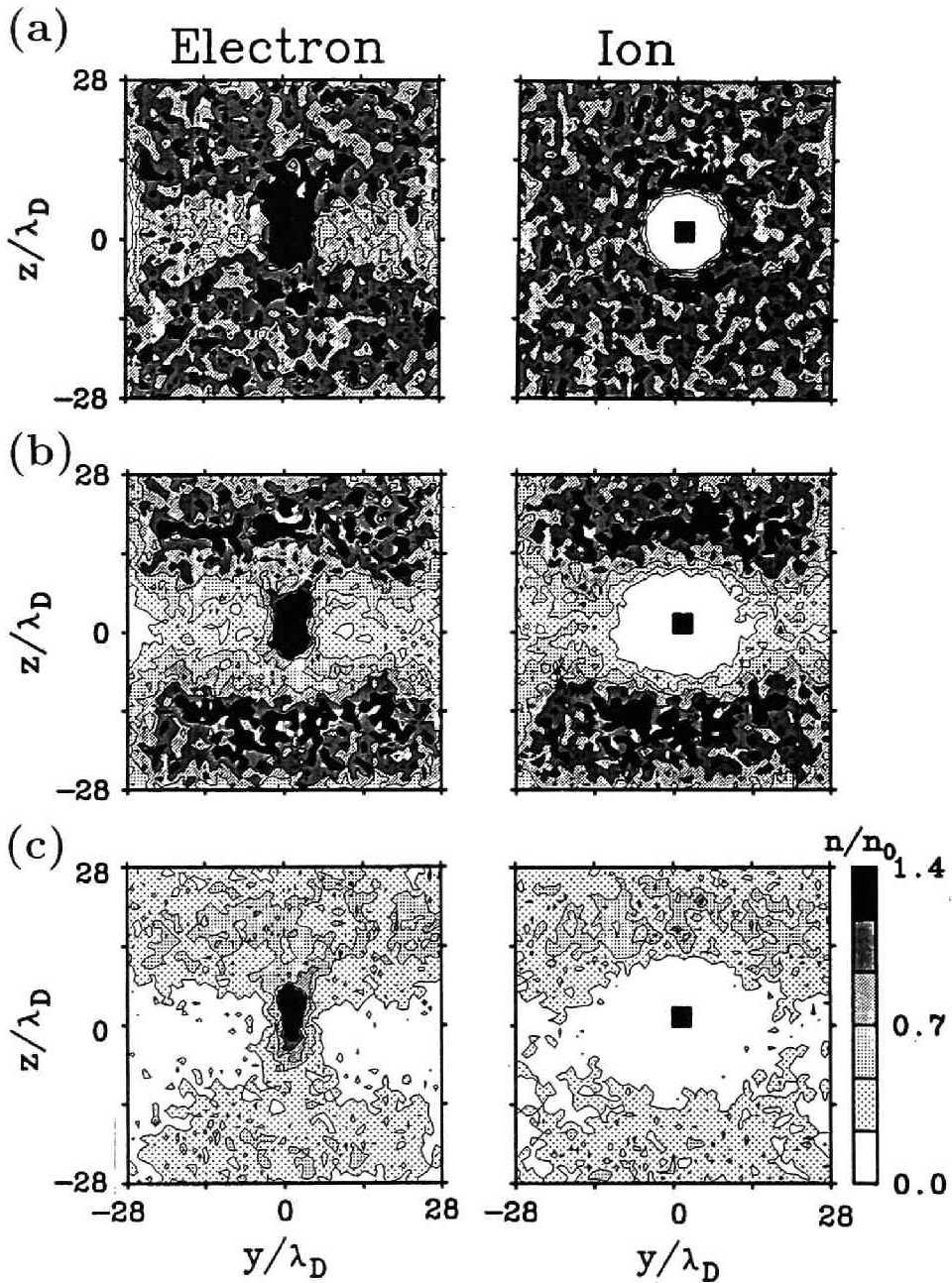
Figure 4.14: Contour maps of the number density for the background electrons and ions in the $y - z$ plane at different times.
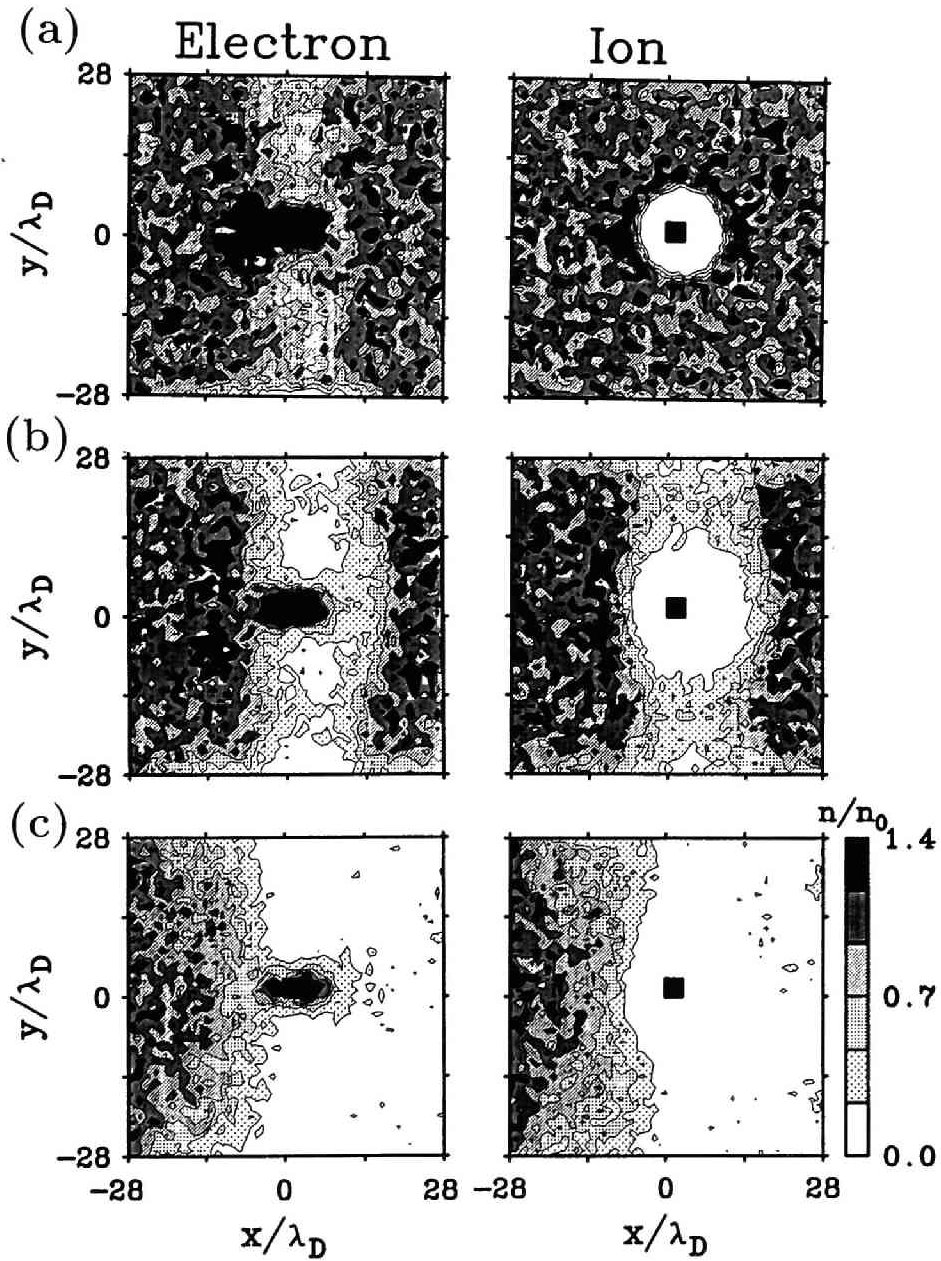
Figure 4.15: Contour maps of the number density for the background electrons and ions in the $x - y$ plane at different times.

to the satellite and a dense sheath is created around it. Ions are expelled in the radial direction from the satellite as shown in the two-dimensional case. Ion density is high at the ion cavity boundary due to the snow-ploughing effects between the ions accelerated outward by the satellite and the ambient rest ions. The ion cavity is a little shifted to the right hand side because of the plasma flow effect. At $3T_{pe}$, the size of the electron sheath shrank owing to the electron collection of the satellite. At the outer region of the sheath, a ring distribution of dense electrons is observed. This structure is also found in the ion distribution. The ion cavity becomes large and the density at its boundary is kept dense as observed at T_{pe}. Electron ring distribution at the cavity boundary is formed in order to maintain the local charge neutrality. Between the sheath structure around the satellite and the ring distribution at the edge of the ion cavity, the electron density is lower than the one of the ambient plasma. In the steady state around $25T_{pe}$, the ion cavity has expanded and due to the plasma flow effect, a wake structure with a rarefactional region is created in the downstream region. In the upstream region, owing to the snow ploughing effects, the ion density becomes higher than the ambient plasma density. The profile of the electron density is similar to that of the ion density except for the vicinity of the satellite. Although the density is reduced, the electron sheath remains around the satellite.

Figure 4.14 shows the density profile in the $y - z$ plane which includes B_0 along the y direction. In the initial stage, electrons and ions are attractive to and repulsive from the satellite, respectively as shown in the panel (a). Electrons are dilute along B_0 because they are quickly collected by the high potential satellite. On the contrary, electron density is high across B_0 because electrons are so strongly magnetized that they are hard to move across the magnetic field. As time elapses, the ion cavity continues to expand due to the repulsion to the satellite. A dense ion wall due to the snow-ploughing effects is created at the boundary of the cavity. At the ion wall, the electron density also becomes high to maintain the local charge neutrality. Along B_0, the ion density is low because ions as well as electrons are mobile in this direction so that they are accelerated away from the satellite region. In the vicinity of the satellite, electrons are still concentrated in the direction perpendicular to B_0. In the steady state shown in the panel (c), the ion cavity has expanded and the ion wall structure at the cavity boundary has disappeared from the model region. It is noted that the ion cavity structure is asymmetry with respect to the magnetic field line penetrating the satellite along the y direction. The density profile distorted downward in the figure. The same profile can be seen in the electron structure. In the vicinity of the satellite, the electron sheath remains across B_0.

Figure 4.15 shows the density contour map in the $x - y$ plane. The ambient
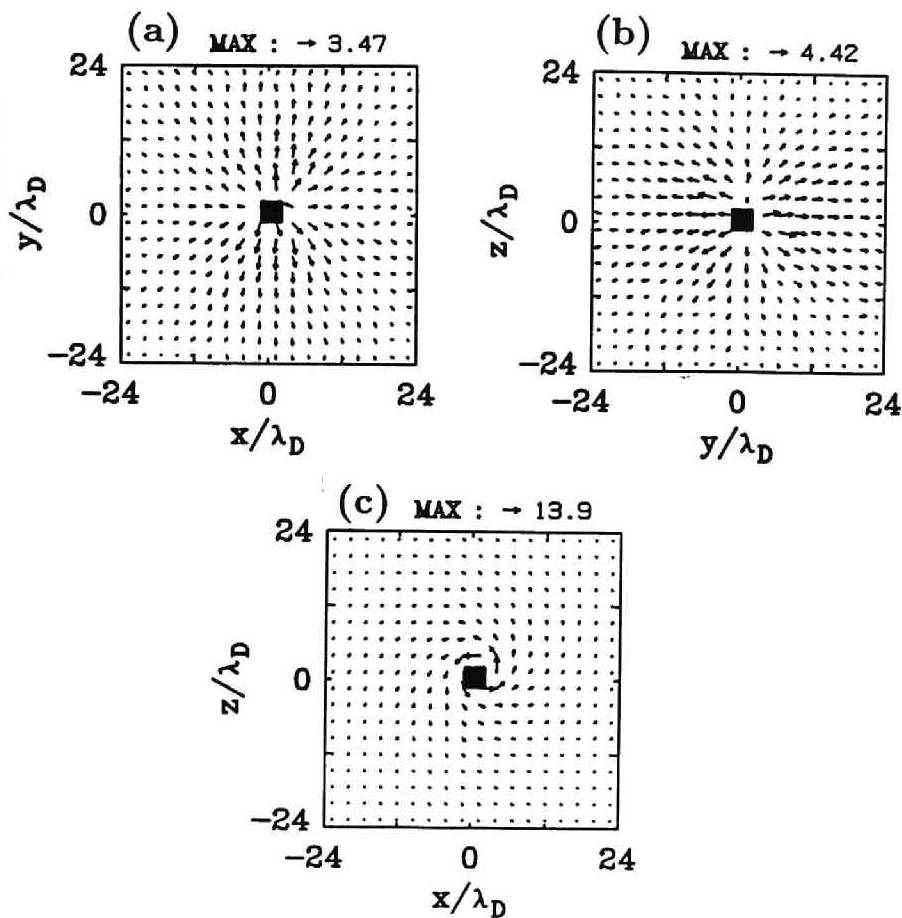
Figure 4.16: Vector plots of current density at each grid point at the initial stage.

plasma flows along the x direction and B_0 lies in the y direction. In the initial stage, the density profiles are almost the same as obtained in Figure 4.14. The electron density at the upstream side of the satellite is approximately twice as high as the average one because electrons are more supplied to the satellite due to the plasma flow. Along B_0, electrons are dilute due to the electron attraction to the satellite. The profile of the ion density is almost the same as obtained in Figure 4.14. At this stage, an ion cavity is created almost symmetrically with respect to the satellite position. As time elapses, as shown in both the electron and ion profiles, low density region expands along B_0 which is caused by the electron collection to the satellite and the ion evacuation. Due to the plasma flow effects, the ion density is reduced in the downstream region at the steady state. To maintain the charge neutrality, electrons form a similar profile to ions' except for the vicinity of the satellite. As observed in Figure 4.14, the electron sheath remains thick in the direction across B_0.

In order to see the plasma dynamics responding to the high potential satellite, we show the current flow profiles at the initial stage in Figure 4.16. The panel (a), (b), and (c) show the plots in the $x - y$, $y - z$, and $x - z$ planes. Each plane includes the cross section of the satellite. Each arrow from each grid point corresponds to the current density vector. As seen in the panel (a) and (b), the current flow is dominant along the y direction. Owing to good mobility of electrons along B_0, this current flow is mainly due to the electron acceleration toward the satellite by the intense electric field. Although not displayed, however, the current flow along B_0 becomes weak as time elapses. As the ion cavity expands and the electron sheath is formed, the influence of the intense electric field from the satellite becomes weak on the ambient electrons which are located beyond the sheath. Eventually, the current collection of the satellite reaches to the steady state. In the panel (c), the rotational current around the satellite is dominant. As examined in the two-dimensional case, it is due to the electron $E \times B$ drift motion. Contrary to the field-aligned current shown in the panel (a) and (b), the cross-field current is strongly maintained even at the steady state because this current essentially represents the sheath dynamics themselves. The qualitative analysis of the current flow at the satellite will be performed in the next section.

4.3.3   Transient Current to High Potential Satellite

As described in Section 4.2, the current collection of the satellite was quantitatively examined by a two-dimensional space. In this section, with a three-dimensional model, we will also analyze the process of the current collection. Qualitatively, the process of the current collection to the satellite should be the same no matter how the dimension of the model space differs. However, the absolute value of the current depends on the dimensions of the model region. In principal, the data obtained in the three-dimensional model are more realistic than those in the two-dimensional model. In this aspect, the current variation in the transient stage is estimated again in the three-dimensional model.

As well as the results in the two-dimensional computer experiments, we can observe the transient phase in the current collection of the high potential satellite. To avoid the complexity of the plasma flow effects, we adopted Model-2 for the computer experiments, which hires no relative motion between the ambient plasma and the satellite.

Figure 4.17 shows the time variation of the transient current collected by the satellite for the cases of $e\phi_s/k_B T_e = 50, 125$, and 500. As observed in the previous section, the electron current is dominant, which implies that the current variation is almost equivalent to the variation of the electron collection of the
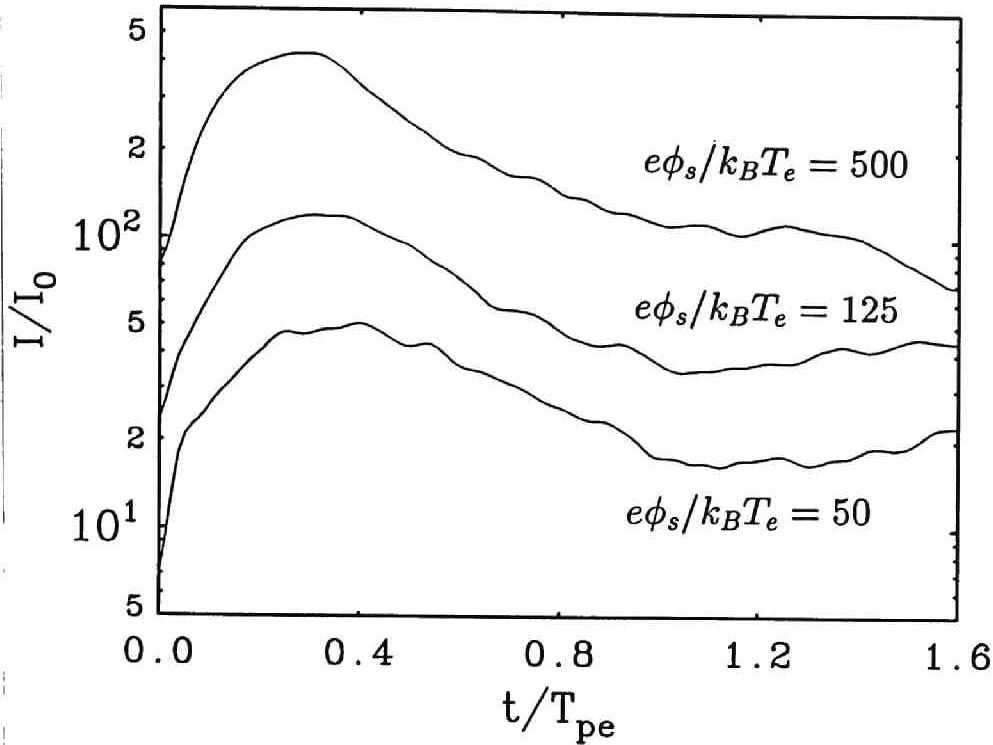
Figure 4.17: Time evolution of the electron current flowing from the satellite due to the electron collection for the different satellite potential.

satellite. The current values in the figure are normalized to the ambient current I_0 given by

$$I_0 = 4\pi r_0^2 j_0 \qquad j_0 = \frac{en_0}{2}\sqrt{\frac{2k_BT_e}{\pi m_e}}. \qquad (4.27)$$

As shown in Figure 4.17, the time scale for the initial rise of the current is approximately $T_{pe}/4$. The peak values of the transient current are approximately 5, 100, and 400 times I_0 for $e\phi_s/k_BT_e$ of 50, 125, and 500, respectively.

Here we estimate the peak value of the current. Since the maximum current is obtained due to rapid attraction of electrons to the satellite, the same formulation of the current evaluation as used in the two-dimensional case can be basically applied to the present three-dimensional case.

Assuming that electron layer with a width of Δl around the satellite are all absorbed to the satellite within $T_{pe}/4$, the average current I at the satellite can be given by

$$I = \frac{4\pi en_0}{3}\left((\Delta l + r_0)^3 - r_0^3\right) \cdot \frac{4}{T_{pe}}. \qquad (4.28)$$

The unknown parameter in the above equation is Δl, which is evaluated in the following way.

The maximum velocity of electrons v_{max} accelerated by the satellite potential ϕ_s is approximately given by using the energy conservation as follows.

$$\frac{1}{2}m_e v_{max}^2 = e\phi_s \tag{4.29}$$

$$v_{max} = \sqrt{\frac{2e\phi_s}{m_e}} \tag{4.30}$$

Assuming the velocity oscillates at the plasma frequency, i.e., $v(t) = v_{max}\sin(\Pi_e t)$, the electron velocity $\tilde{v}$ averaged over $T_{pe}/4$ is given by

$$\tilde{v} = \frac{4}{T_{pe}}\int_0^{T_{pe}/4} v_{max}\sin(\Pi_e t)dt = \frac{2}{\pi}v_{max}. \tag{4.31}$$

Then the width of the electron layer Δl is approximately estimated as

$$\Delta l = \tilde{v}\frac{T_{pe}}{4} = \frac{v_{max}}{\Pi_e} \tag{4.32}$$

Substitution of (4.32) in (4.28) yields

$$I = \frac{8en_0}{3}\left(\frac{\tilde{v}}{\Pi_e}^3 + 3r_0\frac{\tilde{v}}{\Pi_e}^2 + 3r_0^2\tilde{v}\right) \tag{4.33}$$

Figure 4.18 shows the plots of initial peak current versus the satellite potential energy. The current values are normalized to I_0 which is defined in (4.27). The small circles and the solid line represent the results obtained in the computer experiments and the theoretical estimate according to (4.33), respectively. For comparison, the dashed line indicated below the solid line represents the estimate derived by substitution of $0.5\Delta l$ in (4.33). Up to $e\phi_s/k_B T_e \sim 10^2$, it is seen that the solid line approximates the current values represented by the small circles. However, the difference between the experimental and theoretical results increases as the satellite potential becomes large. The main reason for the difference is the collection rate of electrons within the layer of Δl of (4.32). In a realistic case, all the electrons within the layer of Δl cannot be collected to the satellite due to the repulsion to their own charges during the concentration toward the satellite. Consequently the collection rate of electrons at the satellite becomes low and the large gap arises between the results of the computer experiments and the estimate of (4.33). With this point of view, we reduce the width of the electron layer of (4.32) by half as one example, and estimate the current
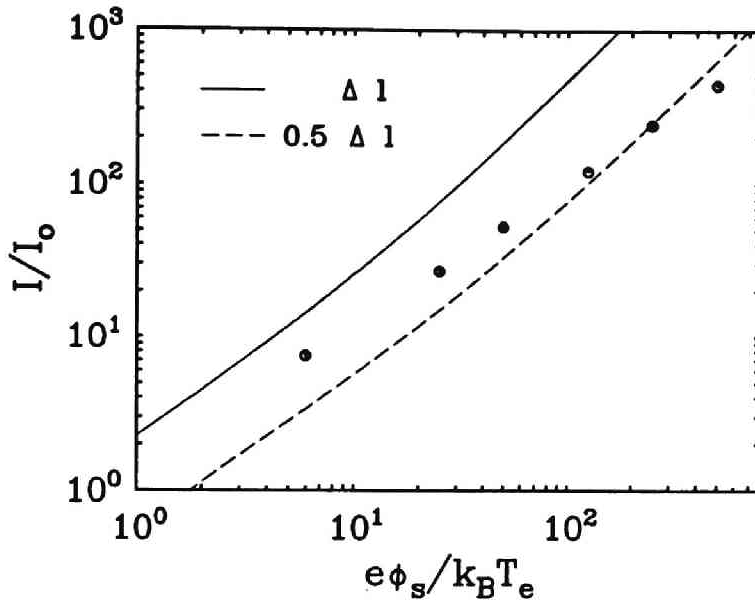
Figure 4.18: The maximum transient current as a function of the satellite potential. The solid line represents the theoretical estimate. The dashed line indicates the estimate for $0.5\Delta l$ for comparison. The current values obtained by the computer experiments are plotted with the small circles.

collection by (4.33). The corresponding dashed line can account for the current values at potential region higher than $e\phi_s/k_BT_e$ obtained in computer experiments. The gap in the current estimation can also comes from the assumption of constant electron density n_0. In the real situation, the sheath density increases as the satellite potential becomes large owing to the electron attraction to the satellite region. To obtain more accurate estimate of the peak current at higher potential range, we need to take into consideration of the density increase in the sheath as a function of the satellite potential. As stated earlier section, the electron density can be expressed as the Boltzmann distribution for the case where the potential energy of the satellite is comparable to the thermal energy. However, at the high potential case such as $e\phi_s/k_BT_e > 10^2$, the estimate of the sheath density is difficult. The Boltzmann distribution can no more be descriptive for the sheath density because the density values diverse in the vicinity of the satellite at such high potential. Since the searching for the sheath density as a function of the satellite potential is beyond the scope of the present study, we simply hired the constant sheath density in the evaluation of the peak current as stated above.

A minor reason for the difference between the experimental and theoretical results is due to the difference in the model of the satellite shape. In the theory stated above, the satellite is taken as a sphere while it is a cubic in the computer experiments. Then the derivation stated above needs some modification because the electric field distribution near the satellite differs in the cubic satellite case.

As well as the results of the two-dimensional case, the current intensity is exponentially reduced in time after the initial peak as shown in Figure 4.17. Around $\omega_{LHR} \sim 6$ which corresponds to one period of the lower-hybrid resonance oscillation, the current variation in time is hardly seen, which implies the system has reached to the steady state. In the next section, we examine the current-voltage characteristics of the satellite in the steady state.

4.3.4   Current-Voltage Characteristics

In Section 4.2.4, we described the detail of the current-voltage characteristics of tethered satellite in two-dimensional model. Here, using a three-dimensional electrostatic model, we study the relation between the satellite potential and the current collection of the satellite in the steady state. As stated in the two-dimensional case, the current collection of the satellite is basically determined by space charge effects in the vicinity of the satellite. However, as shown in the density variation, the space charge effect in the three-dimensional case quantitatively differs from that of the two-dimensional case. This may cause some modification in the current collection of the satellite in the three-dimensional case.

We performed five cases of computer experiments with different satellite potentials up to $e\phi_s/k_B T_e = 10^3$. We adopted Model-2 where we include no effects of the plasma flow to avoid the complexity in evaluating the current collection. Since the steady-state current collection is of our interest, we follow the plasma dynamics long enough until the current reaches the steady state and shows little variation in time in each simulation run. To quantitatively understand the current-voltage characteristics obtained in the computer experiments, we compare the results with the existing theories on the maximum electron current attainable to a spherical probe.

The first theory to be compared is the well-known classical Langmuir theory for a spherical probe consisting of outer cathode and inner anode. The theory takes the space charge effects into account [Langmuir and Blodgett, 1924]. Regarding the outer edge of the ion cavity as the outer cathode, we can apply the theory to the high potential satellite case as done in the two-dimensional case. By equating the ratio of the cathode to the anode radii with that of the ion

cavity and the satellite radii, the current-voltage relation is given by

$$I = \frac{16\epsilon_0\pi}{9}\sqrt{\frac{2e}{m_e}}\frac{\phi_s^{3/2}}{\alpha^2} \tag{4.34}$$

$$\alpha = \ln\left(\frac{r_0}{r_{ic}}\right) - 0.3\left[\ln\left(\frac{r_0}{r_{ic}}\right)\right]^2 + 0.075\left[\ln\left(\frac{r_0}{r_{ic}}\right)\right]^3 - 0.0143182\left[\ln\left(\frac{r_0}{r_{ic}}\right)\right]^4 + \cdots \tag{4.35}$$

where I is the electron current to the satellite per unit area of its surface, r_{ic} is the ion cavity radius, and ϵ_0 is the electric permittivity. Unknown variable in the equation is the ratio of r_0 to r_{ic} which may vary as the satellite voltage changes. The ratio of r_0/r_{ic} can be estimated as follows. Assuming that all of the electrons that enter the ion cavity region reach the high potential satellite, the current I owing to the electron collection to the satellite is simply estimated by

$$I = 4\pi r_{ic}^2 j_0 = I_0\left(\frac{r_{ic}}{r_0}\right)^2 \tag{4.36}$$

This gives the following relation between I and r_{ic}.

$$\frac{r_0}{r_{ic}} = \left(\frac{I_0}{I}\right)^{1/2} \tag{4.37}$$

Substitution of (4.37) into α in (4.35) yields the current-voltage relation in a form of

$$\phi_s^{3/2} = \frac{9}{16\epsilon_0\pi}\sqrt{\frac{m_e}{2e}}I\left[\frac{1}{2}\ln\left(\frac{I_0}{I}\right) - 0.3\left[\frac{1}{2}\ln\left(\frac{I_0}{I}\right)\right]^2 + 0.075\left[\frac{1}{2}\ln\left(\frac{I_0}{I}\right)\right]^3 + \cdots\right]^2. \tag{4.38}$$

It should be noted that the theory stated above includes no B_0 effects.

The single particle theory by Parker and Murphy [1967] is also used for theoretical estimate of maximum current to a sphere. As in the two-dimensional case, cylindrical coordinates are adopted in the theory. (4.9) is valid in the three-dimensional case. To obtain a maximum current collection, $r = r_0$ and $\phi_{rz} = \phi_s$ are substituted in (4.9). Assuming that all the electrons within a distance r_{inf} from the z axis can reach the satellite surface, the maximum current I attainable to the satellite along B_0 is given by

$$I = r_{inf}^2\pi j_0 \cdot 2 \tag{4.39}$$

The normalization of I to I_0 by using (4.27) gives

$$\frac{I}{I_0} = \frac{1}{2}\left(\frac{r_{inf}}{r_0}\right)^2 = \frac{1}{2}\left(1 + \sqrt{\frac{8e\phi_s}{m_e\Omega_e^2 r_0^2}}\right) \tag{4.40}$$

The theory by Linson [1969] is also adopted to be compared with the results obtained in the computer experiments. As stated in Section 4.2.4, we assume that the electron density in the ion cavity region is constant. The brief derivation of the characteristics is stated below.

As the electron mobility is very high along B_0 (i.e., along the y axis), we can assume the potential gradient along the y direction is zero. Moreover the potential profile is symmetric in the azimuthal direction. Then Poisson's equation involves only the radial variable which is simply given by

$$\frac{1}{r}\frac{\partial}{\partial r}\left(r\frac{\partial \phi}{\partial r}\right) = \frac{en_e}{\epsilon_0} \tag{4.41}$$

where ϕ and n_e are the potential and the constant electron density in the ion cavity, respectively. (4.41) is easily integrated with respect to r under such boundary condition that the potential and the electric field at the edge of the cavity are equal to zero. The relation between the satellite potential ϕ_s and the ratio r_{ic}/r_0 is then obtained to give

$$\phi_s = \frac{eq_c r_0^2 B_0^2}{2m_e}\left(\left(\frac{r_{ic}}{r_0}\right)^2\left(\ln\left(\frac{r_{ic}}{r_0}\right)^2 - 1\right) + 1\right) \tag{4.42}$$

where $q_c = \Pi_e^2/\Omega_e^2$ in the ion cavity. The maximum current I attainable to the satellite along B_0 is expressed as

$$I = r_{ic}^2 \pi j_0 \cdot 2 \tag{4.43}$$

The current ratio is then given by

$$\frac{I}{I_0} = \frac{1}{2}\left(\frac{r_{ic}}{r_0}\right)^2 . \tag{4.44}$$

Substitution of the ratio $(r_{ic}/r_0)^2$ into (4.42) gives the current-voltage relation.

$$\phi_s = \frac{eq_c r_0^2 B_0^2}{2m_e}\left[\left(\frac{2I}{I_0}\right)\left(\ln\left(\frac{2I}{I_0}\right) - 1\right) + 1\right] \tag{4.45}$$

where $q_c = \Pi_e^2/\Omega_e^2$ in the ion cavity reion.

As done in the two-dimensional cases, we estimate q_c with results of the computer experiments on the electron number density in the ion cavity. Figure 4.19 shows a series of contour maps of electron and ion number density for $e\phi_s/k_B T_e = 50$, 125, and 200 in the $x - z$ plain which includes B_0 along the x direction, respectively. It is seen that ion cavity around the satellite expands as the satellite potential increases. Electrons are attracted to the satellite and a
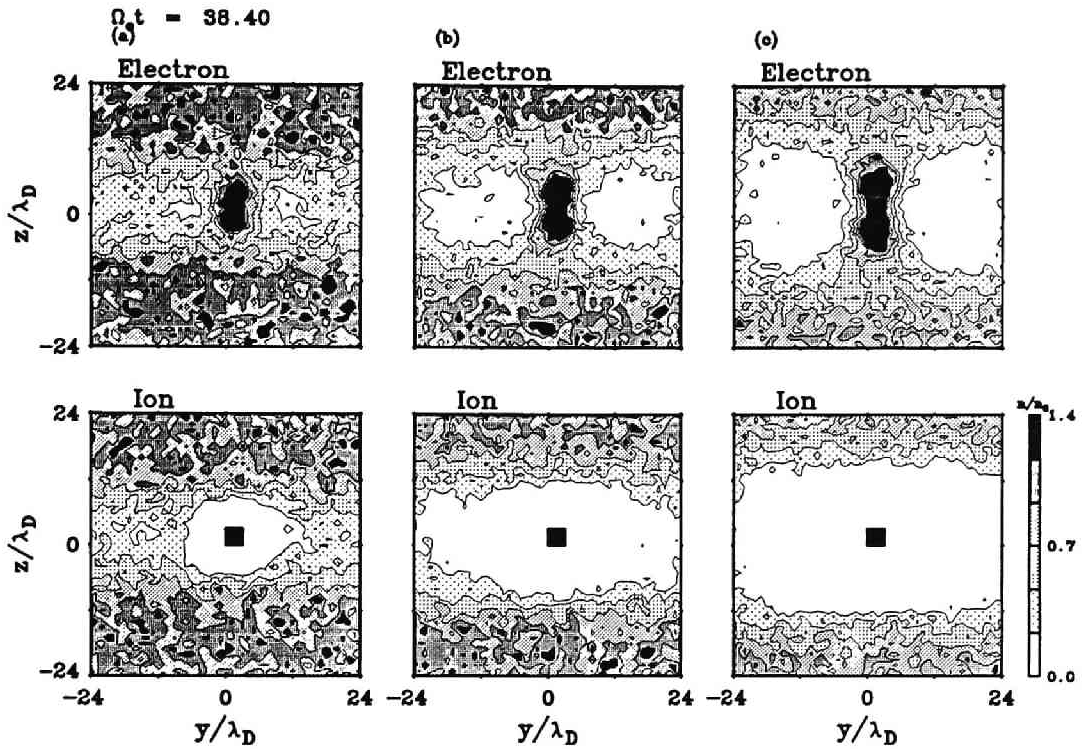
Figure 4.19: Contour maps of the number densities for the background electrons and ions in Model-2. The ratio of the satellite potential energy $e\phi/k_BT_e$ are (a) 50, (b) 125, and (c) 200.

donut-like structure of electron sheath is clearly observed while the sheath is thin along B_0. To obtain the values of q_c, we make use of density values of electrons averaged over the length from the satellite surface to the edge of the ion cavity in the direction transverse to B_0. In the close vicinity of the satellite, electrons are highly condensed around the satellite and the number density is beyond the average one. The high density region is, however, not so thick enough to reach the edge of the ion cavity. Consequently, up to $e\phi_s/k_BT_e \sim 100$, the average density in the ion cavity is approximately the same as the unperturbed electron density, which gives $q_c \simeq 4$.

We compare the current values obtained by the computer experiments with those estimated by the theories stated above. Figure 4.20 shows the current-voltage characteristics. Small squares represent the current values obtained in the computer experiments. The dotted curves (1) and (2) indicate the current voltage relation of the Langmuir theory obtained from (4.38) and the single par-
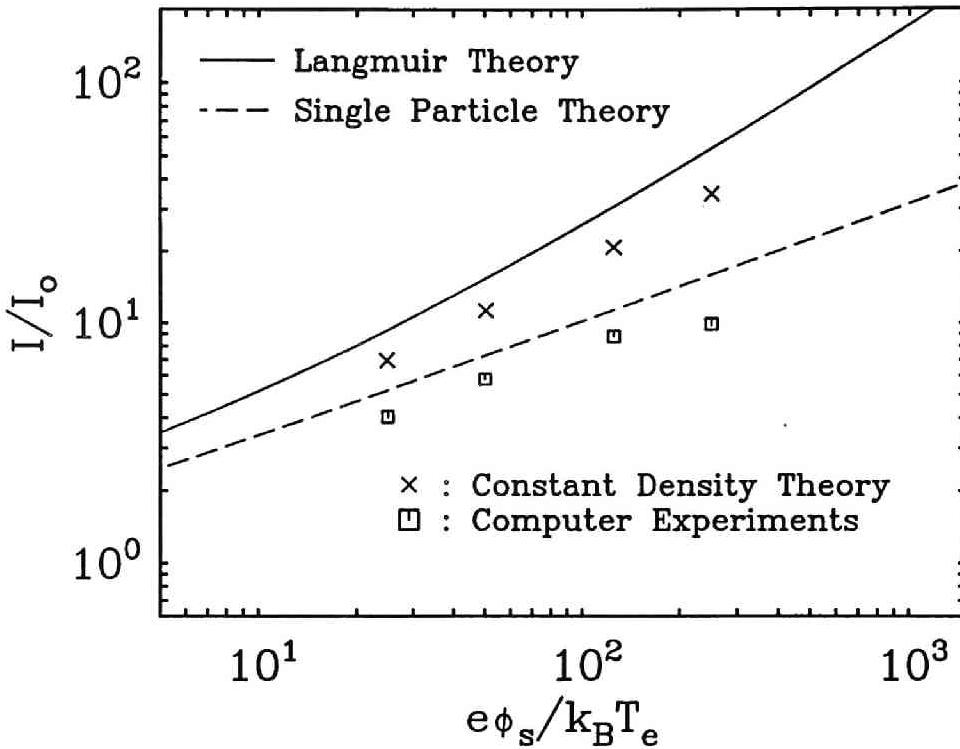
Figure 4.20: Current-voltage characteristics of the satellite. The dotted curves (1) and (2) correspond to the Langmuir theory and the single particle theory, respectively. The small squares indicate the average current in the steady state obtained by the computer experiments using Model-2. The cross marks correspond to the constant density theory assisted by the number density obtained by computer experiments.

ticle theory from (4.40), respectively. In addition, the current estimate from the constant density theory assisted by the result of the present computer experiments on the electron number density in the ion cavity is plotted as cross marks in the figure.

As the satellite potential becomes large, the current values obtained by the computer experiments is monotonously increased. Contrary to the characteristics obtained in the two-dimensional model, the steady-state currents obtained in the experiments are below the current estimate by the single particle theory for all the cases up to $e\phi_s/k_BT_e = 250$. The Langmuir theory which provides the upper bound of the current flowing from the satellite in no B_0 case shows much larger current values than those observed in the computer experiments. From the quantitative point of view, the single particle theory shows a good estimate of the current values obtained in the experiments. Around up to $e\phi_s/k_BT_e \sim 10^2$,

the current estimate by the constant density model, which is slightly larger than the current by the single particle theory, also well predicts the maximum current values attainable to the satellite. It should be noted that the current characteristics obtained in the computer experiments tend to be saturating for the region of $e\phi_s/k_B T_e > 10^2$ as shown in Figure 4.20. In the present computer experiments, the current collection in the cases where $e\phi_s/k_B T_e > 10^2$ can be influenced by the boundary conditions of the model region. To compensate the absorbed electrons by the satellite, we inject thermal electron flux along B_0 at the boundaries as we did in the two-dimensional case. When the ion cavity expands to a size as large as the model region, however, erroneous reduction in the current collection of the satellite can occur because thermal electrons cannot be supplied enough into the ion cavity. In a case of such a large ion cavity, the electron distribution in the vicinity of the boundary are affected by the satellite potential and eventually the electron collection to the satellite is limited to the thermal flux at the boundary. One way to avoid the situation stated above is use a larger model region. However, because of the limited memory on the computer hard ware, it is difficult to enlarge the model region as much as we need. To solve this technical problem, we need to control the injection of the electron flux at the boundary by monitoring the variation of the plasma number density. For a case of large ion cavity, we need to inject electron flux more than that of thermal electrons. Then the current reduction due to the boundary effects will be avoided and the current values will be increased more than that obtained in the present computer experiments for $e\phi_s/k_B T_e > 10^2$. We will leave this modification of the electron injection as a future work.

4.3.5 Conclusion

In the present section, we have examined the plasma response to the high potential tethered satellite in the three-dimensional space. For the analyses, we performed computer experiments using a newly developed three-dimensional electrostatic particle code. As done in the two-dimensional model, one body representing a satellite is introduced in the model region filled with a magnetized plasma. The satellite potential is abruptly elevated up to a fixed high potential at the initial stage. First, we examined the transient response of the plasma to the high potential satellite in terms of density and current variation. With a qualitative point of view, the plasma responses observed in the three-dimensional space are the same as those in the two-dimensional space. Electrons and ions near the satellite are attracted and excluded by the intense electric force from the satellite. In the present model, the directional dependence of the electron sheath is clearly seen. Along B_0, the charged particles are highly mobile

that ions are mostly evacuated in this direction. Electrons, which has large thermal velocity compared to ions', form a low density region along B_0 to maintain the local charge neutrality. In the direction perpendicular to B_0, however, the density profile obtained by the three-dimensional computer experiments shows a donut-like electron sheath created around the satellite. This is due to the strong magnetizing of electrons. The profile of the current flow shows that the field-aligned current is primarily dominant as observed in the two-dimensional computer experiments. Associated with the sheath, cross-field current due to the sheath drift motion with $E \times B$ drift is intense around the high potential satellite. As for the current collection of the satellite, an intense transient current is collected as a response to the abrupt change of the satellite potential. As done in Section 4.2.5, the initial peak of the current is theoretically estimated by a simple model. In the steady state, the current-voltage characteristics of the satellite are examined by performing computer experiments with different satellite potentials and comparing them to some of the classical theories. In the three-dimensional case, because of the unexpected boundary effects due to the expansion of the ion cavity region, we obtained the current-voltage characteristics up to $e\phi_s/k_B T_e \simeq 10^2$. the current flowing out from the satellite can be roughly approximated by the single particle theory derived by Parker and Murphy, [1967]. For the higher potential, the current can be increased and the constant density model be a good estimate of the maximum current at the satellite as examined in the two-dimensional cases, which is left as a future work.

Chapter 5

Field Response to Electrodynamic Tethered Satellite System

5.1 Introduction

As a result of the interaction with the space plasma, a space vehicle disturbs the electrostatic and electromagnetic fields in its vicinity. The source of its perturbation can be such as potential difference between the vehicle and space plasma and the field-aligned/cross-field current induced near the vehicle. When the space vehicle moves faster than the characteristic velocity in the plasma media, Cherenkov type wave is radiated from the vehicle. In this respect, space vehicle can be called as a plasma wave radiator. The TSS is none of its exception. Taking an advantage of its unique configuration of the system such as a long conductive tether wire, it can be either used passively, for receiving radio waves from other sources, or actively, as a transmitting antenna. Up to the previous chapters, we have mostly focused on the electrostatic response of the ambient plasma to the TSS in terms of plasma density, current, and potential variations. In this chapter, we regard the TSS as a wave radiator and examine its feature by performing computer experiments.

Since 1960's, theoretical works on the plasma wave radiation from a moving vehicle in a magnetized plasma have been intensively studied. The first work concerning this was done by Drell el al. [1966]. Owing to the charge separation in a space vehicle caused by the $V \times B$ effects, the vehicle can draw a current from the ambient plasma, which causes perturbation along the static magnetic field B_0. The perturbation is believed to be Alfvén mode wave. Since the vehicle moves across B_0, the perturbation is left behind the vehicle, which

forms like wing-like profile named 'Alfvén Wings'. By assuming various kinds
of current source in a magnetized plasma, many scientists [e.g. Barnett and
Olbert, 1986; Estes, 1988; Hastings et al.,1987; Rasmussen et al., 1985, 1990].
have intensively investigated the linear dispersion relation for Alfvén wings with
fluid approximation. In the laboratory experiment, field perturbation caused by
a moving current source has been studied by Stenzel and Urrutia, [1989, 1990].
They showed the current profile and whistler mode propagation along B_0 named
'whistler wings'.

In electrodynamic tether system, there are several candidates for possible
energy sources of wave excitation. First of all, as described in Chapter 3, the
beam-plasma interaction due to electron emission at the orbiter can be responsi-
ble for the wave excitation such as LHR mode and whistler mode waves. As also
stated in Chapter 3, the tether ends, which have direct contact to the ambient
plasma, can cause field perturbation in their vicinity. Electrostatic perturbation
with the electron plasma, upper hybrid, and lower hybrid frequencies are driven
by the potential difference between the tether ends and its surrounding plasma.
In terms of electromagnetic, Alfvén wave can be excited and radiated from the
tether ends as first proposed by Drell et al. [1966]. The third candidate for
wave source is the current flow in the tether wire. Owing to the electromotive
force generated by the cross-field motion of the TSS, a current closure is created
through the TSS and the ambient plasma. As the current-voltage character-
istics show, the satellite, whose potential energy $e\phi_s/k_B T_e$ can become several
thousand, can collect electron current of about 10 times as much as the average
current of the ambient plasma. Assuming that the emissivity of electron beam
is high enough and the return current is little collected by the orbiter, the total
impedance in the current closure can be negligible except for that between the
satellite and the ambient plasma. Then the tether current equivalent to the
electron current at the satellite can stimulate the electromagnetic environment
near the tether wire and cause plasma wave radiation. In the TSS-1, the tether
current is capable of being modulated from 0.1Hz to 30kH, which makes the
tether an effective transmitter of wave in this frequency range.

The problems concerning the beam-plasma interaction have been intensively
studied by many scientists by theories, observation data, and numerical anal-
ysis. With the tethered satellite model, field perturbation associated with the
electron beam emitted from the orbiter has already been investigated in Chapter
3. In this chapter, therefore, we will focus on the remaining problems such as
the field modulation by the tether current and the tether ends. In Section 5.2,
field perturbation induced by the tether current is examined by the one- and
two-dimensional computer experiments. Since our interest is transient response
of the electromagnetic environment, we adopt time varying tether current as a

wave sourcer. In Section 5.3, we will describe the analysis concerning the field perturbation associated with the plasma interaction between the high potential satellite and its surrounding plasma. Possible interactions such as plasma instability arising near the satellite region are intensively investigated via computer experiments.

5.2 Wave Radiation by Transient Tether Current

5.2.1 Two-Dimensional Model

Basic concept of the interaction between the current flow in the tether wire and a magnetized plasma is illustrated in Figure 5.1 in the plasma rest frame of reference. Each stationary magnetic field line encounters a moving cross-field tether current at frequency of $\omega_{crs} = 2\pi V_b/d_t$ where V_b and d_t denote the TSS velocity and the diameter of the tether cross section, respectively [Wang and Hastings, 1992]. The tether current can be modulated with arbitrary frequency ω_m. In such a situation, waves at either ω_{crs} or ω_m are naturally radiated. If they match the wave modes existing in the ambient plasma, they will be able to propagate away from the TSS. At the low Earth orbit, typical intensity of
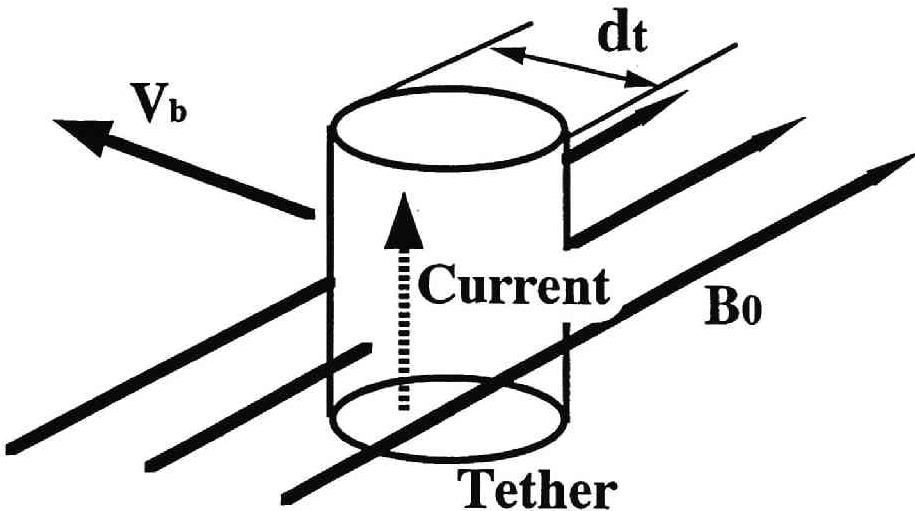
Figure 5.1: Basic concept of interaction of tether current with the ambient plasma.

the magnetic field $|B_0|$ is about $3.3 \times 10^{-5}T$. The ion and electron densities are

almost the same and $n_i = n_e = 2 \times 10^5 cm^{-3}$, respectively. In this situation, $\Omega_e = 9 \times 10^6 s^{-1}$, $\omega_{LHR} = 3 \times 10^4 s^{-1}$ and $\Omega_i = 2 \times 10^2 s^{-1}$. Taking into account that d_t is 2.4 mm and V_b is 7.3 km/s in the real TSS model, ω_{crs} is $1.9 \times 10^7 s^{-1}$ which is slightly higher than Ω_e. Since the plasma parameters stated above depends on the altitude of the flight, whistler mode can be enhanced by the moving tether current when ω_{crs} becomes less than Ω_e. In the TSS-1 mission, the tether current is artificially modulated with the frequency ω_m from 0.1Hz to 30kHz. In terms of angular frequency, those are approximately $0.6s^{-1}$ and $1.8 \times 10^5 s^{-1}$ corresponding to the frequency range of Alfvén and whistler mode waves, respectively.

In the computer experiments, we adopt the vehicle frame of reference, which implies that ω_{crs} is zero. Then the frequency of our interest is ω_m in the present case. As obviously predicted, at the steady state, field will be kept perturbed at a frequency of the current modulation in the tether. Our concern here is rather the initial field response to the abrupt change of the TSS potential. The drastic change of the tether current in the initial phase can mainly determine the characteristics of the field perturbation near the TSS. To study the field
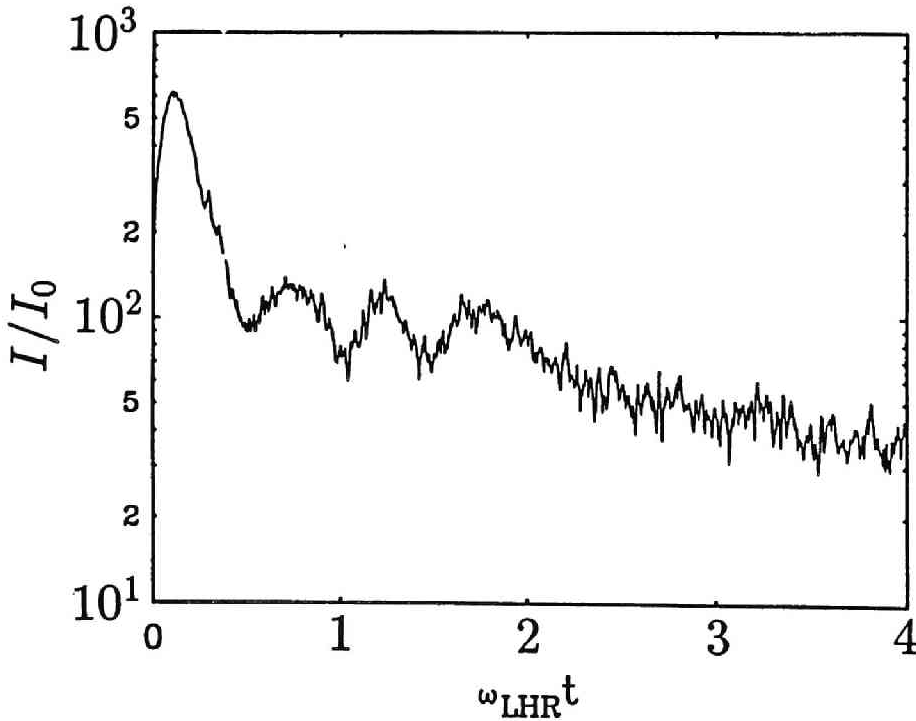
Figure 5.2: Time evolution of the satellite current in the transient stage.

characteristics, we pay our attention to the case of the electron emission from

the orbiter. As discussed in Chapter 4, a current loop is created through the TSS and the ambient plasma and the current in the loop is controlled by the electron dynamics such as the acceleration along B_0 and the electrons collection and emission at the tether ends. Assuming that the main impedance in the current loop is due to the electron collection of the satellite, the current in the loop is almost equivalent to the satellite current. Therefore, as the tether current, we adopt the data of the satellite current which is obtained previously in the computer experiments in Chapter 4. In the present computer experiments, we utilize the data of the satellite current in the case of $e\phi_s/k_B T_e = 10^3$. The time variation of the tether current is plotted in Figure 5.2. Since we imposed a high potential on the tethered satellite at $t = 0$, the current collected by the satellite shows drastic increase in time at the transient stage. The current value is maximized approximately within one period of the electron plasma oscillation. The maximum current value can be several hundred times as large as the thermal current to the satellite at $e\phi_s/k_B T_e > 10^3$. This initial peak current will be able to excite plasma wave, which will be shown in the next section.

Figure 5.3 shows a schematic illustration of the model region for the computer experiments in two-dimensional space. The dimensions of the model plane are $1024\lambda_D \times 512\lambda_D$. To avoid the boundary effects on the field propagation, we put the current source at the center of the model plane, i.e., $x/\lambda_D = 512, y/\lambda_D = 256$, where we flow the current along the z direction according to the time variation of the current shown in Figure 5.2. To avoid unexpected reflection of outgoing waves at the boundaries of the model region, the field quantities are attenuated in damping regions whose size is $64\lambda_D$ from each boundary. The static magnetic field B_0 lies along the x direction. The physical parameters in the computer experiments are basically the same as those used in the previous chapters. The grid spacing and the time step are taken as $\Delta r = \lambda_D$ and $\Delta t = 0.014/\Omega_e$, respectively. We performed the computer experiments up to the time where a wave packet generated by the current source reaches to the boundary of the model plane. In the following, we describe the results of the computer experiments.

First we examine the spatial distribution of the field intensity in the model plane. Figure 5.4 displays a series of contour map of the field distribution of B_z component. Since B_0 lies along the x direction, B_z component is one of the electromagnetic component. The field intensity is plotted as energy and is normalized to B_0^2. As clearly seen, a packet of intense electromagnetic field is induced from the current source at $(x/\lambda_D, y/\lambda_D) = (512, 256)$. The most part of the wave packet propagates away in the x direction, i.e., along B_0, as time elapses. Taking account of the current variation shown in Figure 5.2, the wave packet is induced by the initial maximum current which has its peak at the time
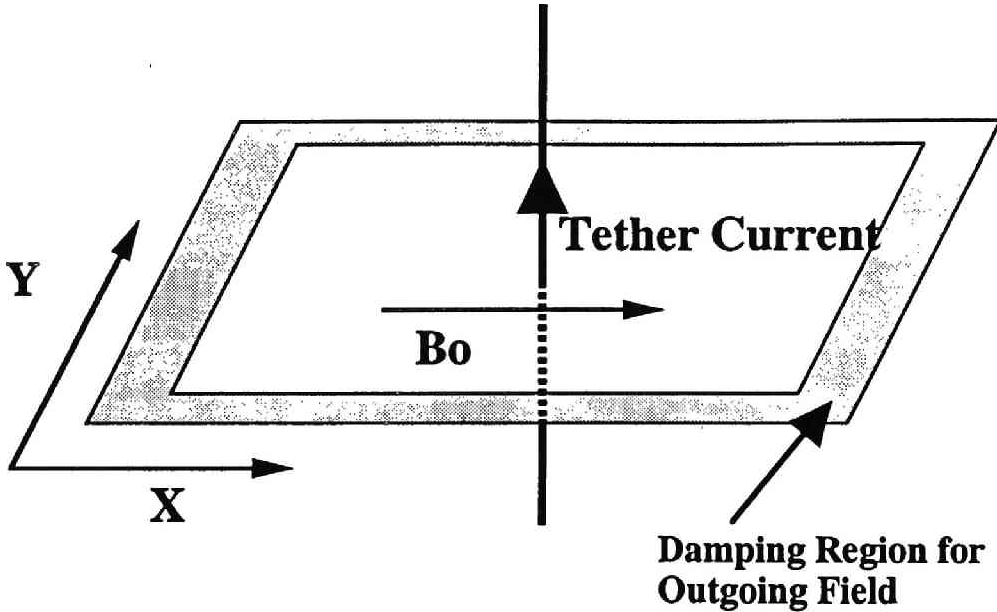
Figure 5.3: Schematic illustration of the model region for the computer experiment.

around $T_{pe}/4$. Later, we will discuss the relation between the current variation and the characteristics of the induced wave packet.

Next, to obtain the propagation velocity of the wave packet, we examine the time evolution of the wave form of B_z along the x direction. In Figure 5.5, we show the wave forms of each time step by superimposing along the vertical axis. The field intensity is measured at $y = 256\lambda_D$. The current source is located at the left edge of the figure, i.e., at $x/\lambda_D = 512$. As examined in Figure 5.4, it is shown that a wave packet propagates away from the current source. By tracing the peak position of the packet, we can estimate the propagation speed of the wave packet. According to Figure 5.5, the ratio of the propagation velocity to the speed of light V_w/c_v is approximately 0.1.

To obtain the characteristics of the wave packet, we next analyzed the polarization of the wave field. Figure 5.6 depicts a hodogram of the magnetic field components in the $y - z$ plane at a fixed time $\Omega_e t = 10.75$. In the figure, field amplitudes at each grid point along the x axis at $y/\lambda_D = 256$ are plotted. The amplitude of the magnetic field is normalized to $|B_0|$. Since the electromagnetic wave packet propagates along the x direction, the hodogram should show the polarization of the wave packet. As examined in the contour map of the field
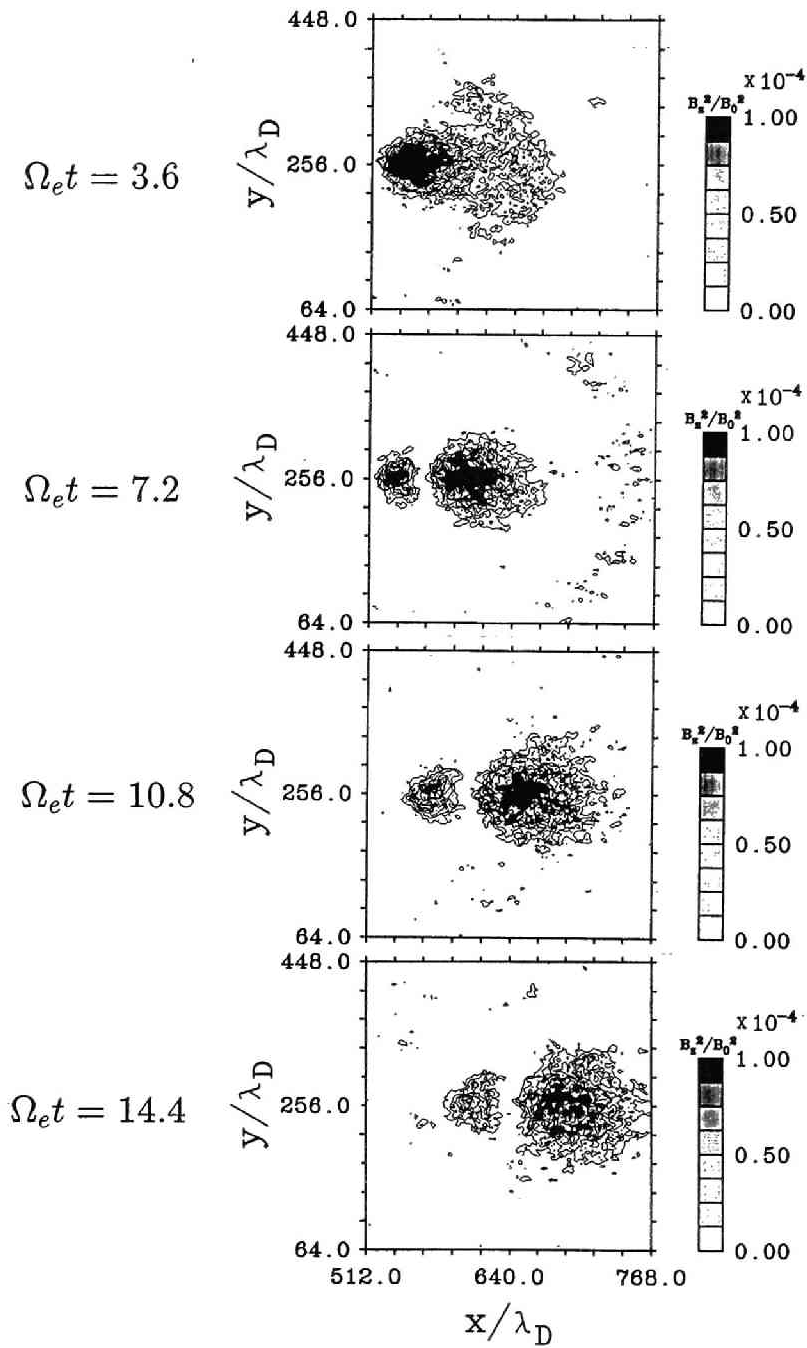
Figure 5.4: Time series of contour map of electromagnetic field perturbation induced by the tether current
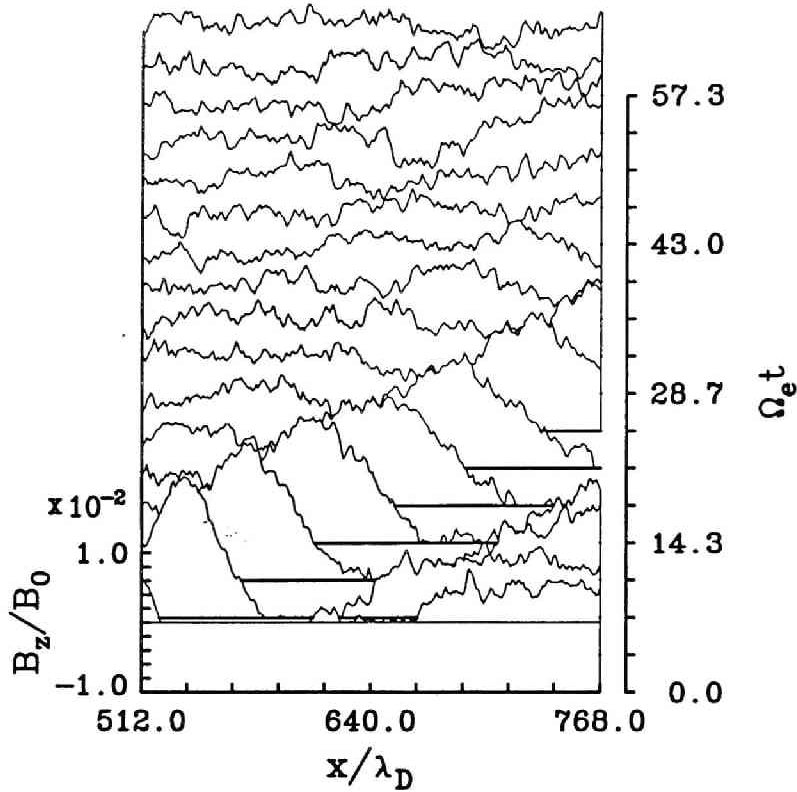
Figure 5.5: Spatial profiles of the B_z field and its time evolutions.

intensity, B_z is enhanced from $x/\lambda_D \sim 550$ to 700 at $\Omega_e t = 10.75$. In Figure 5.6, the field intensity is also amplified in this region owing to the presence of the wave packet. The wave form indicates left-hand circularly polarization with respect to the x direction at the fixed time. This implies, at the fixed position, right-hand circularly polarization with respect to time. Judging from the above analysis, it can be concluded that the wave packet propagating along B_0 is whistler mode wave.

To examine the detail of the whistler wave packet, we review whistler mode by using the dispersion relation with cold plasma approximation. The dispersion relation is given as

$$\left(\frac{c_v}{V_w}\right)^2 = 1 + \frac{\Pi_e^2}{\omega(\Omega_e \cos\theta - \omega)} \tag{5.1}$$

where c_v, V_w, and θ denote the speed of light, the velocity of the wave packet, and the angle between B_0 and k vector of the wave, respectively. Since we know

Spatial Hodogram
$\Omega_e t \; = \; 10.75$

A : 550 x/λ_D
B : 566 x/λ_D
C : 582 x/λ_D
D : 598 x/λ_D
E : 614 x/λ_D
F : 630 x/λ_D
G : 646 x/λ_D
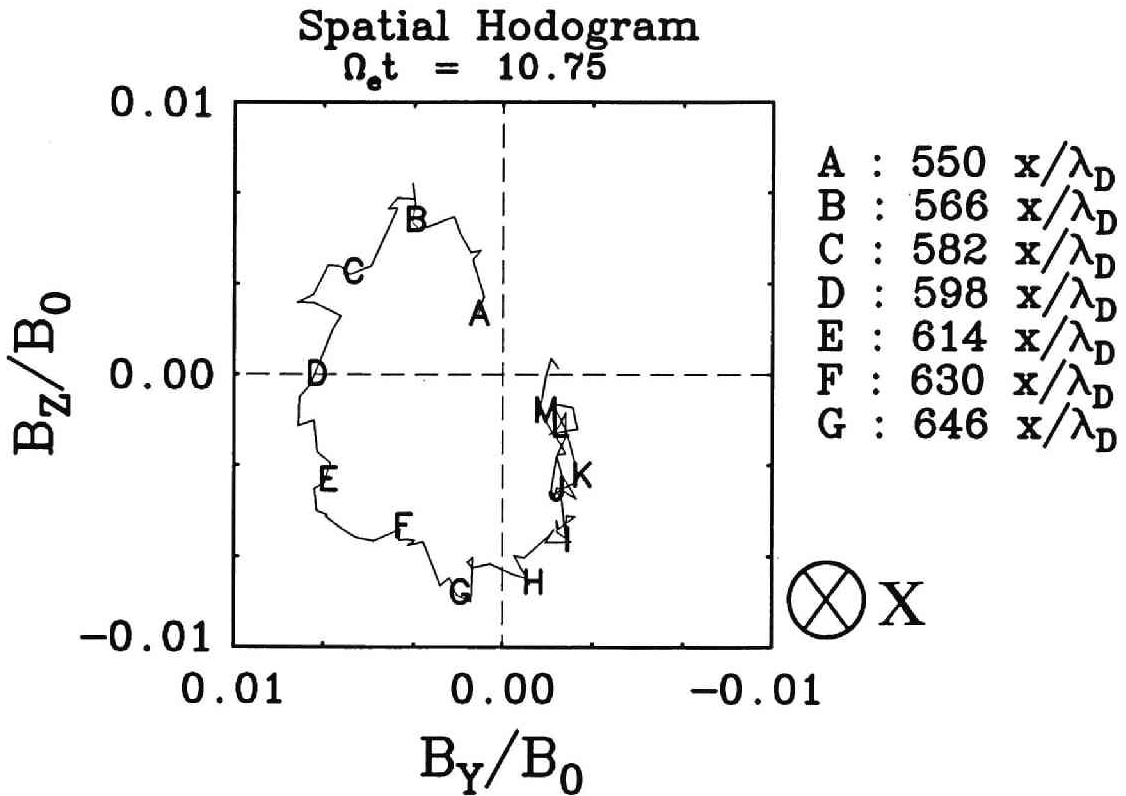
Figure 5.6: Hodogram of the magnetic field in the $y - z$ plane

the propagation velocity of the wave, we can estimate its frequency with the help of (5.1). According to the experimental results shown in Figure 5.5, V_w/c_v is approximately estimated as 0.1. Since V_w is measured along the line parallel to B_0, we can substitute zero for θ in (5.1). Taking account of $\Pi_e/\Omega_e = 2$ used in the computer experiment, (5.1) yields $\omega/\Omega_e = 0.21$. Assuming infinite refractive index, the resonance angle of the whistler mode is estimated. In the present case, $\theta \simeq 78°$. From Figure 5.4, it is seen that the wave packet propagates within this resonance angle.

5.2.2   One-Dimensional Model

In the previous computer experiment, we utilized the data of the satellite current as the tether current which is obtained in the case that the satellite potential is abruptly elevated up to $e\phi_s/k_B T_e = 10^3$. In terms of wave enhancement, the tether current in the transient stage around $\sim T_{pe}$ plays an important role because it drastically varies from the thermal fluctuation level to a maximum peak level which is relevant to several hundred times as large as the ambient current. Then the results show that a whistler wave packet at frequency $\sim 0.2\Omega_e$

is induced and propagates along B_0.

First, let us discuss qualitatively the relation between the time variation of the tether current and the induced wave mode. Since we take a vehicle frame of reference, we just focus on the effect of tether current variation on the characteristics of induced wave in the present case. The effect due to cross-field motion of the tether wire will be discussed from a plasma rest frame of reference later. In general, time variation of current can cause electromagenetic field perturbation. The way of current oscillation determines the characteristics of enhanced field such as frequency and amplitude. In the previous computer experiments, the tether current model can be chosen rather arbitrarily. Intensity and frequency ω_m of the current flow in tether are variable and controllable by changing the impedance of the TSS and the way of the electron beam emission from the orbiter. In this aspect, the current model used in the previous computer experiment seems to be too specific. As far as the initial field response is concerned, however, it is clarified that the frequency of the perturbed field depends on the time variation of initial maximum current. According to the results and discussion in the previous chapter, the initial variation of the satellite current depends on both the satellite potential and the local density of electron sheath at the satellite region. As easily predicted, a large potential change of the satellite in the transient stage leads to a large satellite current and eventually causes the amplification of induced wave field. Simultaneously, the increase of the satellite potential gives rise to concentration of electrons in the vicinity of the satellite. When the sheath density around the satellite becomes high, the time for the satellite current to reach its peak becomes short because T_{pe} becomes small. In this situation, it can be expected that the frequency of the induced wave packet is shifted to high frequency. However, taking account of that the time period of the initial maximum current is approximately within a quarter of T_{pe} in any cases, the frequency of the transient field perturbation falls into the whistler range in the present parameters of the computer experiments. In this sense, the characteristics of field perturbation due to the transient tether current are determined by the satellite potential variation.

In the steady state, ω_m may become effective in field perturbation. Considering a situation that we select ω_m in the whistler range, we will examine the detail of the relation between current variation and field perturbation. For this purpose we perform one-dimensional computer experiments. We also study the propagation of induced wave packet with respect to the direction of B_0. The model for the computer experiments is illustrated in Figure 5.7. The system length is $2048\lambda_D$ along B_0. The outgoing waves from the model region are attenuated in damping regions $0 \sim 256\lambda_D$ and $1792\lambda_D \sim 2048\lambda_D$. We fix a location of a sheet current source J_z at $256\lambda_D$. Instead of applying the satellite
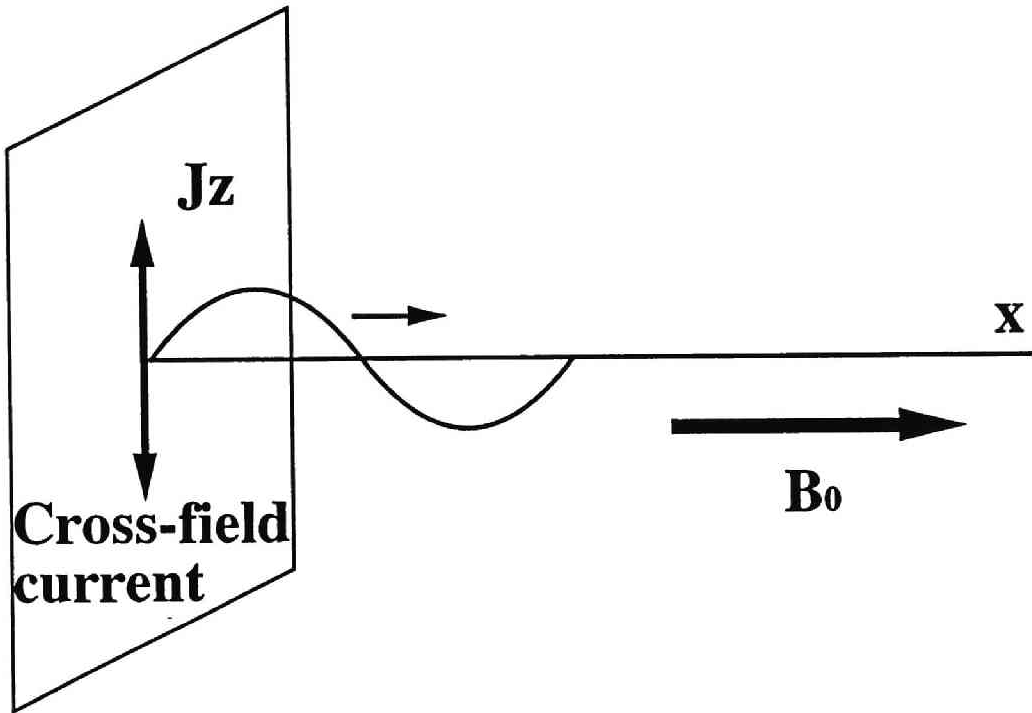
Figure 5.7: Schematic illustration of the model region for the one-dimensional computer experiment.

current observed in the computer experiment, we provide a current which varies in sinusoidal way in time to J_z. To see the propagation of induced wave packet clearly, we oscillate the current for one period only. The physical parameters are the same as those used in the two-dimensional experiments.

First, we focus on a case of parallel propagation, i.e., $k \parallel B_0$. The frequency of the current oscillation ω_m is $0.5\Omega_e$ which is within the whistler range. Figure 5.8 displays the time evolution of one of the electromagnetic field component B_y along the system. The wave form at each time step is normalized to the magnitude of B_0 and superimposed along the vertical direction up to $\Omega_e t = 122.88$. The J_z current source is located at the left edge of the figure. As clearly seen, a wave packet is induced at the current source and is propagating away. Since the horizontal and vertical axes respectively represent space and time in the figure, their ratio provides the propagation speed of the wave packet. For comparison, the propagation of the light mode is drawn with a solid line in the figure. It is seen that the packet propagation shown by a series of ripple has much slow velocity compared with c_v. The ratio of the velocity of the induced wave V_w to c_v is approximately 0.2. We also analyzed the polarization of the wave packet.
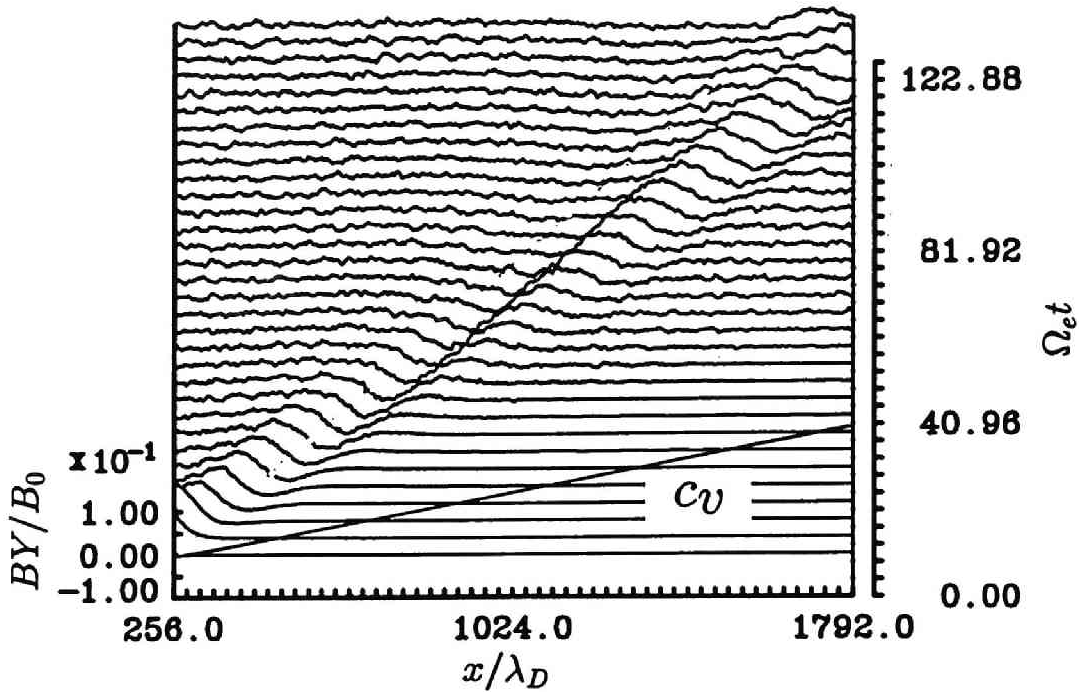
Figure 5.8: Spatial profiles of the B_y field and its time evolutions.

Figure 5.9 depicts a hodogram of the magnetic field components in the $y - z$ plane which are perpendicular to k vector at a fixed position $x/\lambda_D = 1024$. The amplitude of the magnetic field is normalized to $|B_0|$. Up to the time before the wave front reaches to the observation point, the field intensity is in order of fluctuation level. When the wave front encounters the observation point, the amplitude is drastically enlarged and the hodogram shows the right-handed circularly polarization. As well as the results of the two-dimensional computer experiments, this implies that the wave packet propagating along B_0 is a whistler mode wave. As time elapses, the wave packet has passed the observation point and the amplitude decreases in time. We obtain $\omega - k$ diagram in Figure 5.10 by Fourier transforming B_y data with respect to time and space. Dispersion line of whistler mode for cold plasma is superimposed in the figure. The simulation results show a good agreement with the line of whistler mode. Since one wave packet, not a continuous sinusoidal function, is Fourier transformed over the whole duration time of the simulation run, the spectra obtained in the ω domain spread down to $\omega \sim 0$ along the whistler dispersion curve.

As described above, it is confirmed that the generation and propagation of whistler wave packet is artificially reproduced by current oscillation for one pe-

Hodogram
$x/\lambda_D = 1024.0$

$$D : 56.32 \ \Omega_e t$$
$$E : 61.44 \ \Omega_e t$$
$$F : 66.56 \ \Omega_e t$$
$$G : 71.68 \ \Omega_e t$$
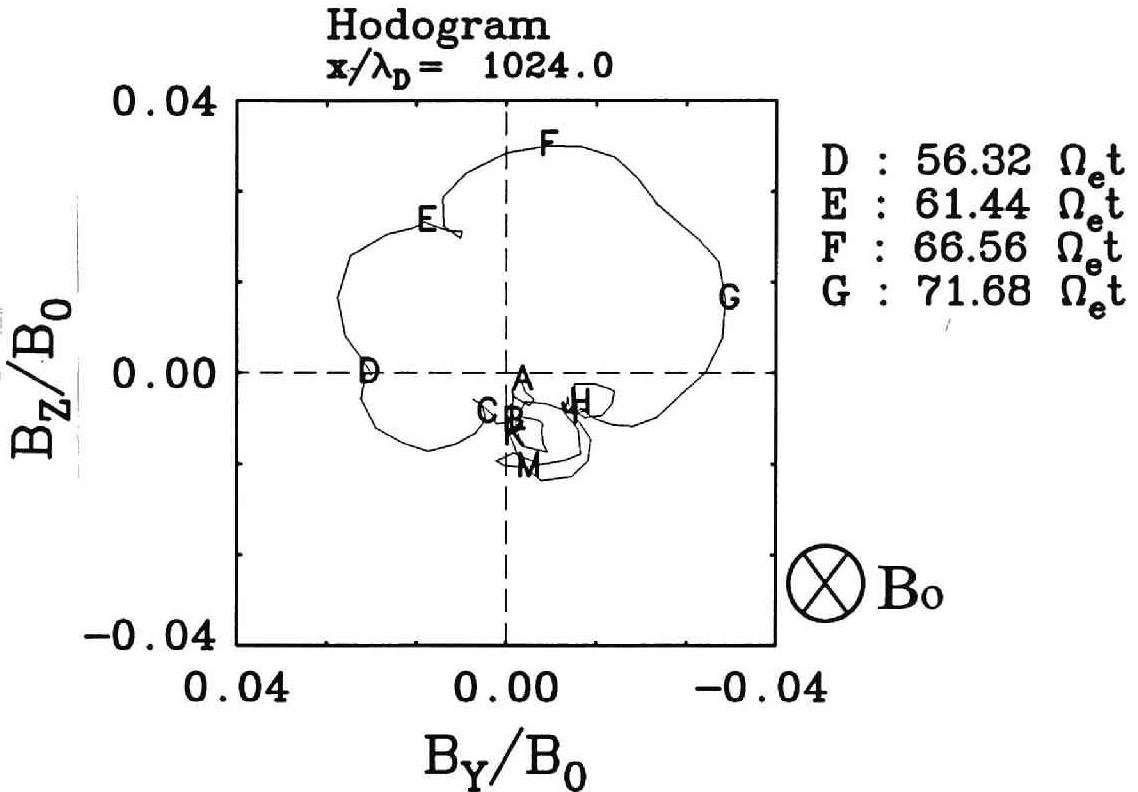
Figure 5.9: Hodogram of the magnetic field in the $y - z$ plane obtained in the one-dimensional computer experiment.

riod which represents the initial current variation observed in the tether current. To see the details of the whistler wave propagation with respect to the angle θ between k vector and B_0, we examine the oblique propagation of the whistler mode with the same model of the computer experiments as used in the previous experiments. Figure 5.11 shows the time evolution of the B_y field form for each case in the same manner as in Figure 5.8. Figure 5.11-(a), (b), (c), and (d) correspond to the case of $\theta = 0°, 30°, 60°$, and $90°$, respectively. According to Figure 5.11, the propagation speed of the wave packet V_w decreases as θ becomes large and approaches to a right angle. As shown in the panel (d), eventually the wave propagation cannot be observed in the direction perpendicular to B_0. As θ approaches to a right angle, in general, the resonance frequency of the whistler mode decreases and the mode cannot exist at $\theta = 90°$. This implies the reduction of the velocity of the whistler mode for oblique propagation. The results shown in the Figure 5.11 are consistent to the characteristics of the whistler mode stated above and can assist the fact the wave packet observed in the two-dimensional model mainly propagates along B_0 within the resonance angle.
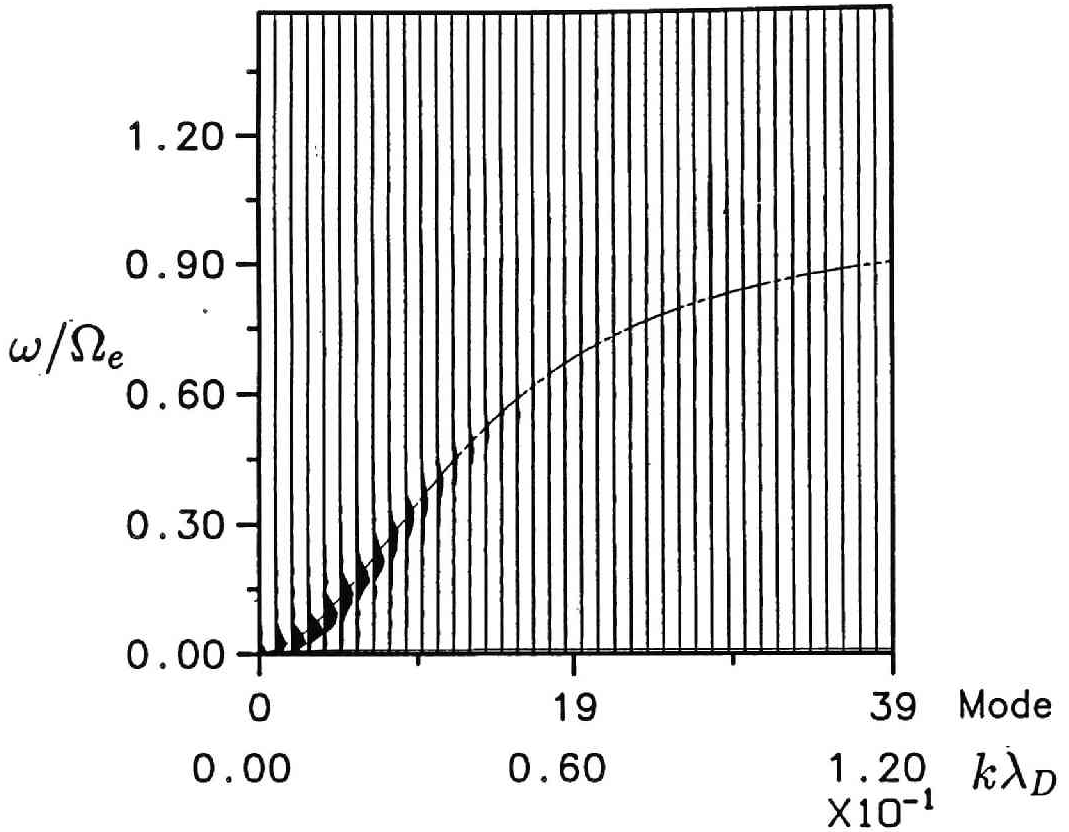
Figure 5.10: The $\omega - k$ diagram of the B_y component.

To examine the characteristics of wave packet induced by a current source which oscillates at higher frequency than Ω_e, we performed another set of one-dimensional computer experiments. We focused on the parallel case, i.e., $k \parallel B_0$. For the frequencies of the current oscillation, we choose $1.5\Omega_e$ and $3.0\Omega_e$. The other parameters used in the computer experiments are the same as those used in the previous one-dimensional computer experiments. Figure 5.12 shows the time evolution of the B_y field form for the cases of $1.5\Omega_e$ and $3.0\Omega_e$ in the same manner as in Figure 5.11. We plotted the wave form up to $\Omega_e t \sim 30$. The solid line represents the propagation of the light wave. The characteristics of the wave propagation are basically the same as those observed in the case of the tether current at frequency of $0.5\Omega_e$; a wave packet is induced at the current source and propagates along B_0 in the x direction. However, the whistler propagation is no more evident because the frequency of the current oscillation is beyond Ω_e. The difference between the panel (a) and (b) is found in the amplitude of the

$$\omega/\Omega_e = 0.5$$

(a) $\theta = 0^o$

(b) $\theta = 30^o$

(c) $\theta = 60^o$

(d) $\theta = 90^o$
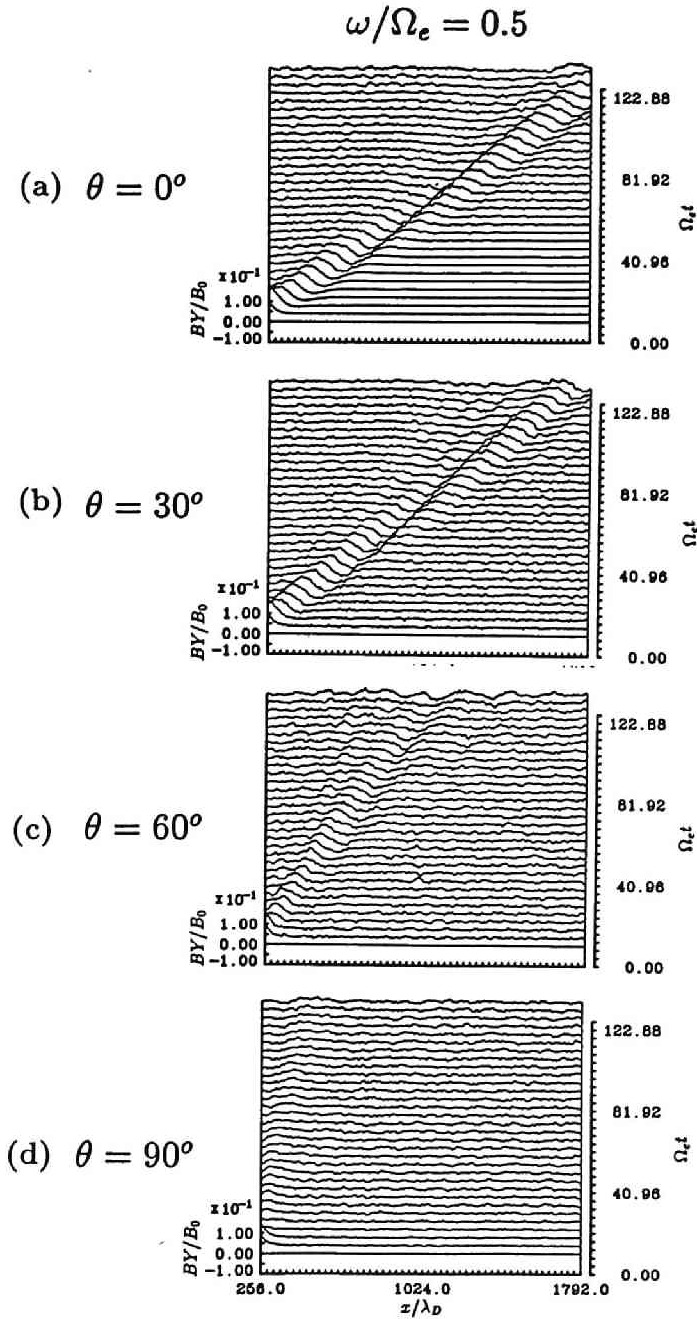
Figure 5.11: Spatial profiles of the B_y field and its time evolutions at different angle with respect to B_0
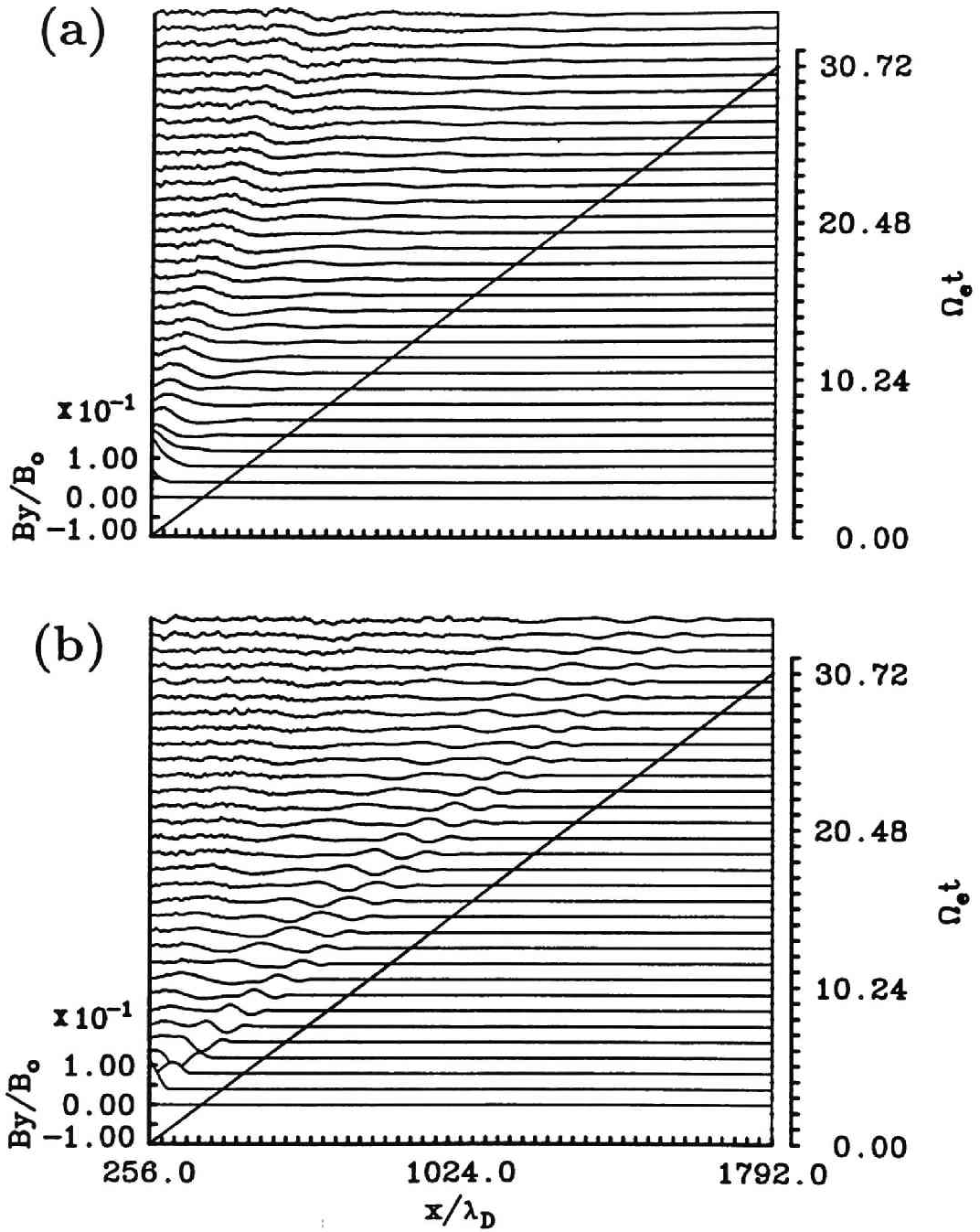
Figure 5.12: Spatial profiles of the B_y field and its time evolutions for the cases of tether current oscillation at frequency (a) $1.5\Omega_e$ and (b) $3.0\Omega_e$

wave packet. Although not clearly shown, the wave form in the panel (a) shows two modes propagation; one is the slower propagating mode which travels up to $x/\lambda \sim 250$ at $\Omega_e t = 30$ and the other is the faster propagating mode which approaches to the light mode. In the panel (b), however, the propagation of the faster propagating mode becomes evident. In the present situation of the parallel propagation, the frequency range from Ω_e to the lower cutoff frequency $\omega_L = \Omega_e/2 + \sqrt{\Pi_e{}^2 + (\Omega_e^2/4)}$ corresponds to so called stop-band where no plasma mode can support the radiated waves. Since $\omega_L \sim 2.5\Omega_e$ in the present case, one of the frequencies used in the present computer experiments, $1.5\Omega_e$, is in the stop band. In such a situation, the radiated field is forced to be converted to the whistler mode and the high frequency light mode which is left-hand polarized. In this aspect, the slower and faster modes observed in the panel (a) and (b) of Figure 5.12 correspond to the whistler and light modes, respectively. When $\omega_m = 3.0\Omega_e$, the light mode can support the radiated field, which is clearly observed in the panel (b).

It is now confirmed that the wave mode which is radiated from the tether current is determined by its time variation. Namely, the ratio of how much energy out of the total emitted by the tether current can be transferred to the whistler mode depends on the current variation in time. As discussed above, current oscillation at a higher frequency than Ω_e can induce the light mode wave rather than the whistler wave.

5.2.3 Discussion and Conclusion

In the previous sections we have shown the plasma wave excitation and propagation due to time variation of the tether current by performing one- and two-dimensional computer experiments. In the computer experiments, we took a vehicle frame of reference. Namely, the time variation of the enhanced field is only associated with the current modulation at frequency ω_m. The results obtained in the computer experiments show that a wave packet of whistler mode is excited and propagates away from the current source along B_0. To the oblique direction with respect to B_0, the radiated waves tend to be damped and no propagation is seen to the direction perpendicular to B_0.

In the present model, we considered no effect of the plasma flow on the propagation of the whistler wave packet. According to the parameters used in Chapter 3, the ratio of the propagation velocity of the whistler mode to the TSS moving velocity is approximately 40. This implies that the angle of the whistler propagation measured from B_0 is 1.43 degrees which is negligibly small enough. Namely, the wave packet can propagate almost along B_0 even in the presence of the relative motion between the TSS and the ambient plasma.

Although not considered in the present computer experiments, initial tether current should be treated as a traveling current pulse along the tether. Since we flow the tether current perpendicular to the model region, no spatial variation of the tether current is taken into consideration. Namely, an infinite wave length is assumed along the tether wire. According to the results obtained in the previous computer experiments, the initial current pulse due to the abrupt change of satellite potential has a time period approximately corresponding to the electron plasma oscillation. This period is equivalent to around 4 MHz in terms of frequency according to the parameters in the ionospheric plasma. If we assume that the traveling speed of the current pulse in the tether is c_v for simplicity, the wave length of the current pulse can be estimated as approximately 75m. In actual tether system, this is much less than the tether length, which has to be taken into consideration for the tether current.

To estimate the radiation due to this current pulse, we need to include the spatial variation of the current intensity along the tether as well as the time variation. Assuming that the current pulse is composed of a half period of sinusoidal function with frequency of Π_e and it travels at c_v in the tether wire, the current pulse is expressed as a function of space z and time t as follows.

$$J(z,t) = j_{zmax} \exp\left(j(\Pi_e t - k_0 z)\right) \left(u(\Pi_e t - k_0 z) - u(\Pi_e t - k_0 z - \frac{\pi}{2})\right) \quad (5.2)$$

where j_{zmax}, k_0 and u are the maximum amplitude of the tether current density, the wavenumber equivalent to Π_e/C_v and the Heaviside function with which we can cut a half period out of the sinusoidal function.

The main reason that we included no spatial variation of the current flow along the tether is that the width of the current pulse becomes much longer than the tether length according to the parameters used in the present computer experiments. To estimate the intensity of radiation field in realistic situation of the TSS, basically we need to solve the wave equation including an external current source such as (5.2). The radiated wave electric field E at a frequency of ω (with the term $\exp(j\omega t)$) satisfies the following wave equation.

$$\nabla \times \nabla \times E - k_0[\kappa]E = -j\omega\mu_0 J_s \quad (5.3)$$

where J_s, k_0 and μ_0 are the external current source, the wavenumber and the magnetic permeability in free space, respectively, and the tensor $[\kappa]$ is the so-called plasma dielectric tensor.

Stimulated by the pioneering work by Drell et al. [1965], many scientists have worked on the problems of the wave radiation from a moving current source by solving (5.3) [Rasmussen et al., 1985,; Barnett and Olbert, 1986,; Estes, 1988,; Hastings et al., 1988,; Stein and Neubauer, 1992]. As a current source J_s,

various kinds of model have been proposed so far such as a cylindrical shape and a dumbbell shape. The major difficulty arises in performing the inverse Fourier transformation of the wave equation linearized in $\omega - k$ space. For a complex model of current configuration, it will be difficult to analytically solve the equation correctly.

To obtain the field intensities at an arbitrary position, a numerical technique, so called full wave method, is a powerful tool [Yagitani et al., 1993]. The wave radiated from a current source is divided into a large number of elementary plane waves, for each of which the propagation in the media such as homogeneous plasma or horizontally stratified model consisting of the ionosphere, the free space and the ground is calculated by the full wave technique. Then the plane waves are summed up to give a horizontal distribution of the radiated wave intensities at any altitudes. This method is particularly useful to estimate the field intensities on the ground. Since we model the tether current as in (5.2), we can investigate the propagation characteristics of the wave radiation with the full wave method, which is left as a future work.

When we move to the plasma rest frame of reference, we need to take account of ω_{crs} which corresponds to the cross-field motion of the tether as well as ω_m. As stated earlier, the waves naturally radiated from a tether are at either ω_{crs} or ω_m. Meanwhile the ambient plasma naturally supports the waves at $\omega < \Omega_i$ and $\omega_{LHR} < \omega < \Omega_e$ [Bernett and Olbert, 1986]. Therefore, the characteristics of the wave radiation from the tether can be determined by the matching of the two groups of the frequency stated above [Wang and Hastings, 1991]. In the transient period when the tether current varies drastically at frequency of ω_m, a wave packet of whistler mode is induced and propagates along B_0. However, after the transient period, no intense waves is excited from the moving current source because the tether current approaches to the steady state. In the steady state, field perturbation at frequency of ω_{crs} owing to the cross-field motion of the vehicle will become dominant.

Regarding the tethered satellite which has a diameter around $\sim 1m$, ω_{crs} is estimated as $8 \times 10^3 s^{-1}$, which is close to ω_{LHR} and in the whistler range. When the space vehicle becomes larger, ω_{crs} decreases and eventually it falls into the Alfvén mode range. This is called 'Alfvén wings' which has been intensively studied by many scientists theoretically and analytically. As explained in Chapter 2, it is difficult to perform computer experiment in a plasma rest frame of reference because the capacity matrix for equipotential solution of a space vehicle has to be calculated at each time step in the model plane. However, ω_{crs} can be estimated with the field profiles obtained at the steady state in the vehicle frame. In the plasma rest frame, the steady field profile attached to the vehicle seems to be moving with the vehicle speed V_b. Then, Doppler

shifted frequency $\omega_{crs} = \omega_b - k \cdot V_b$ can be observed where ω_{crs} and ω_b denote the frequency observed in the frame of the vehicle and the ambient plasma, respectively. Since ω_b is almost zero at the steady state, $\omega_{crs} \sim |k \cdot V_b|$. In the presence of vehicle, dominant k is $2\pi/d_b$ where d_t denotes the diameter of the vehicle. Then $\omega_{crs} \sim 2\pi V_b/d_b$ is obtained.

5.3   Plasma Instability Near High Potential Tethered Satellite

5.3.1   Introduction

In this section we investigate the field perturbation associated with the abrupt change of the satellite potential. Primarily the ambient plasma distribution and dynamics are modulated due to the electrodynamic interaction with space vehicle. In the case of the TSS, as described in the chapter 4, the ambient plasma is non-uniformly distributed near the satellite as observed in the formation of electron sheath and ion cavity. In terms of dynamics, the electron field-aligned current and the $E \times B$ drift motion around the satellite are induced by the intense electric field from the satellite. It should be noted that the plasma distribution and dynamics stated above are not steady but vary in time as a result of the transient responses to the potential change of the satellite. Associated with the variation of plasma response, it is speculated that the electrostatic/electromagnetic fields in the vicinity of the tether ends can be greatly perturbed. In this section, we will focus on the field variation near the high potential satellite via computer experiments.

For the last decade, field environment in the vicinity of a space vehicle, particularly Space Shuttle, has been intensively studied via onboard observation, active experiment, and theory. In the ionospheric plasma, floating potential of a space vehicle becomes negative with respect to the space potential because of larger thermal velocity of electron than that of ion. Due to the negative potential, ion population becomes large near the vehicle. Therefore, wave generation associated with ion interaction is expected to be dominant. It has been reported that various kinds of wave were observed by the detectors of the shuttle. In particular, broadband VLF electrostatic waves are often detected. Hanson and Cragin [1981] and Papadopoulos [1984] suggested that they are lower hybrid waves generated by the modified two-stream instability between the ambient oxygen ions and ions reflected from the vehicle surface. According to Cairns and Gurrett [1991 a, b], those broadband waves are due to the interaction between the ambient plasma and pickup water ions which are outgassed from the

shuttle tiles and ionized near the surface.

In the case of high potential satellite, contrary to the situation near the shuttle, electrons may play important roles for wave excitation near the satellite because the electron population becomes large as shown in the formation of electron sheath. To examine the field variation in such a situation, electron kinetic effect should be taken into account. Moreover, considering that our concern is the transient response to the potential change of space structure, the analysis using the computer experiment is the most appropriate.

As described in Chapter 3, it was found that the field perturbation at the characteristic frequencies such as Π_{pe}, ω_{UHR}, and ω_{LHR} are dominant at the tether ends. This fact is reasonable because the plasma itself near the tether ends is stimulated to oscillate by the strong electric field from the conducting parts of the TSS. In this aspect, these oscillations can be considered as an initial response to the abrupt change of the potential difference between the TSS and the space plasma.

From the electromagnetic point of view, the perturbation with ω_{LHR} is dominantly observed at the tether ends, in particular at the satellite region. This is also because of the abrupt enhancement of cross-field current flow around the satellite. Figure 5.13 shows the spatial distribution of the electromagnetic perturbation induced on B_0 for the frequency range of ω_{LHR}. Since a high potential satellite is initially placed in the ambient magnetized plasma, the electrons in the vicinity of the satellite experience intense electrostatic force to be attracted to the satellite along B_0. Simultaneously, across B_0, they rotate around the satellite due to the intense $E \times B$ drift effect. Ions which have much heavy mass, however, can be assumed as unmagnetized and are accelerated along the direction of the electric field from the satellite. This situation implies the sudden switch-on of cross-field current around the satellite, which leads to perturbation of the magnetic field.

The field perturbation stated above are mostly initial response to the abrupt potential change of the TSS. This topic has been studied and published in several papers. Calder and Laframboise [1990] investigated the time-dependent sheath response to abrupt electrode voltage change. They showed that the potential oscillation at frequency of Π_{pe} was dominant in the electron sheath, which they called 'Plasma Ringing'. It should be noted that they also found that the plasma oscillation can be amplified by the ion-electron two-stream instability in a case with large relative motion of electrons and ions. They examined the dependence of the instability on the temperature ratio T_i/T_e and the threshold drift speed of electrons. Ma and Schunk [1989] has also observed spontaneous plasma-frequency oscillations in a two-fluid simulation of stepped-potential spherical electrode in an unmagnetized plasma, and attributed the oscillations to the ion-
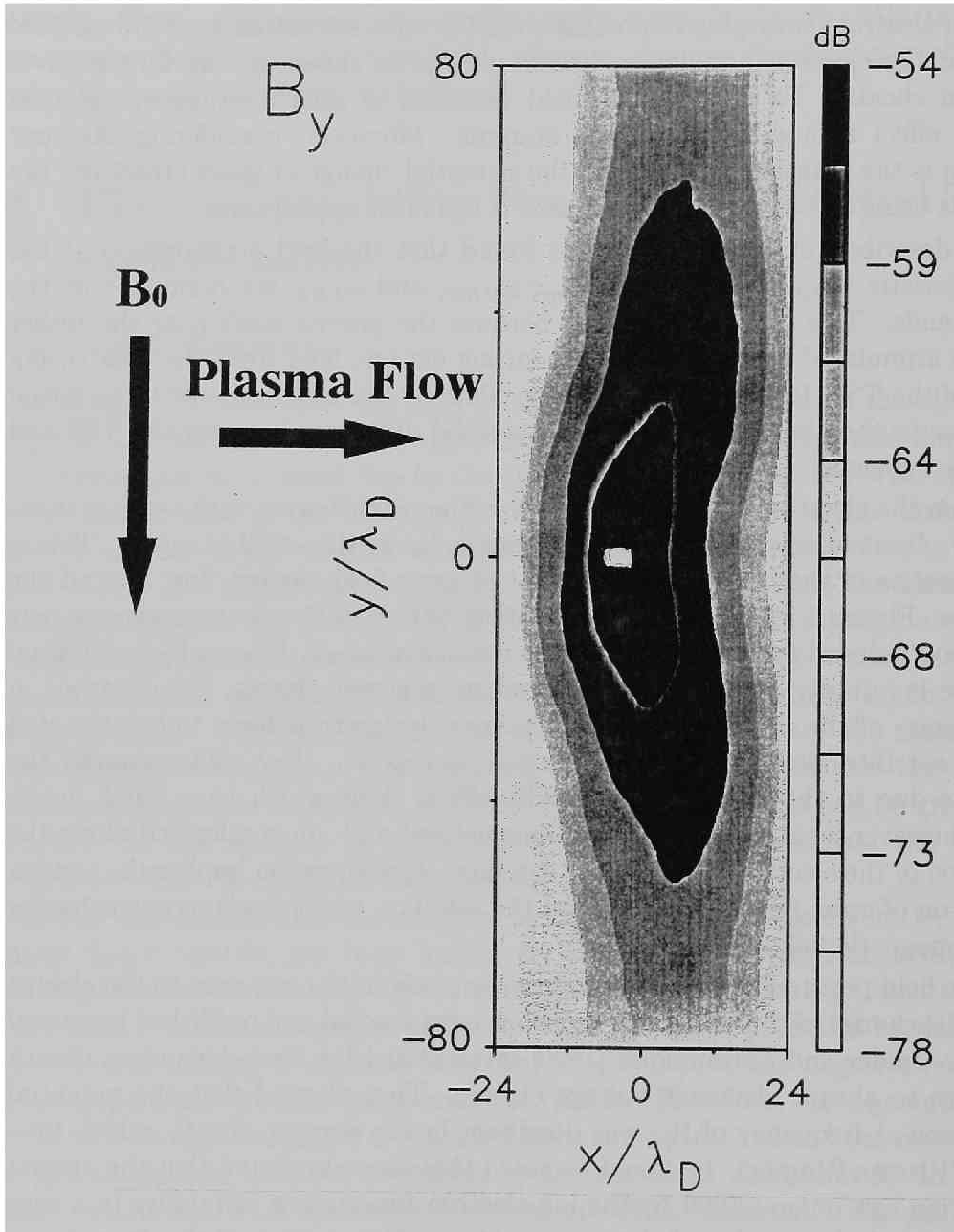
$$\omega/\Omega_e = \quad 0.3 \quad \sim 0.4$$

Figure 5.13: Spatial distribution of the B_y component at the frequency around ω_{LHR}.

electron two-stream instability.

The main aim of this section is that we seek the possibility of plasma instability in the case of the TSS due to the relative motion of the electrons which are attractive to the satellite and the ions evacuated from the satellite region. We will also discuss whether the instability will affect the current collection to the satellite. In the previous studies, no static magnetic field is taken into account for the instability. In the present situation, however, B_0 exists and we can have the directional dependence of the plasma instability. Along B_0, as well known, the ion acoustic and the Buneman type instabilities can occur. In the direction perpendicular to B_0, the beam cyclotron instability such as the upper hybrid two-stream and modified two-stream instabilities can take place. The process of the growth of those instabilities is also of our interest. We will examine the possibility of those plasma instabilities using numerical analysis of the dispersion relation and performing computer experiments.

5.3.2 Buneman Instability Near the Tethered Satellite

In this section, we will examine the possibility of the Buneman instability along B_0 enhanced by the electron acceleration by the electric field from the high potential satellite. Primarily, no ion-electron interaction can occur in the ion cavity region around the satellite because only electron sheath exists there. Due to the oscillation of the sheath itself, electrostatic perturbation can be observed, which is called plasma ringing by Calder and Laframboise [1990]. Beyond the ion cavity region, however, electrons and ions are forced to move in the opposite direction to each other by the intense electric field of the satellite. In result, the ion-electron two-stream instability can grow. One of the significant factors which determine the threshold of the instability is the relative velocity of the electrons and ions in the presheath region which is low density region beyond the ion cavity. As well known, in the presence of the relative motion of electrons and ions, the ion acoustic instability and the Buneman type instability can occur. In the ionospheric plasma in which the ion temperature is almost equivalent to the electron temperature, the ion acoustic mode wave is easily damped by the Landau resonance. In this section for the field perturbation near the TSS, therefore, the ion acoustic mode is not taken into account. The possibility of the enhancement of the ion acoustic mode will be examined later.

Prior to the performance of the computer experiments, we briefly review the dispersion relation of the Buneman instability with cold plasma approximation as follows.

$$1 - \frac{\Pi_{pe}^2}{(\omega - k \cdot V_d)^2} - \frac{\Pi_{pi}^2}{\omega^2} = 0 \qquad (5.4)$$

where V_d denotes the drift velocity of the electrons. The maximum growth rate and its corresponding frequency in cold plasma approximation is well known [Mikhailovskii, 1974]:

$$\gamma = \Pi_{pe} \frac{\sqrt{3}}{2} \left(\frac{m_e}{2m_i} \right)^{1/3}, \omega_r = \Pi_{pe} \frac{1}{2} \left(\frac{m_e}{2m_i} \right)^{1/3} \qquad (5.5)$$

With a thermal plasma, the Buneman instability can also take place provided that the relative velocity is larger than the thermal velocity. To confirm this quantitatively, we solve the dispersion relation numerically by the dispersion solver which has been developed in the Space Plasma Study Group at Radio Atmospheric Science Center of Kyoto University. The physical parameters used in the dispersion solver are the same as those in the computer experiments. To see the dependence of the relative velocity on the growth rate of the instability, we examined the cases of $v_d/v_{te} = 4, 3, 2$ and 1. Figure 5.14 shows the results. The upper and lower panels depict the real and imaginary parts of the frequency versus k value, respectively. As v_d/v_{te} decreases, the frequency ω_r at which the growth rate or ω_i is positive also decreases. In the case of $v_d/v_{te} = 4$, we find that the maximum growth rate is obtained around $\omega_r/\Omega_e \sim 0.3$ at $k \sim 0.25$. These are close to the results obtained in the cold plasma approximations given in (5.4). As the relative velocity approaches to the electron thermal velocity, the growth rate, i.e., ω_i decreases and becomes almost zero when v_d/v_{te} is unity. In conclusion, it is confirmed that the buneman instability can occur in a condition that the relative velocity is larger than the electron thermal velocity in a thermal plasma.

In the following, to clarify the discussion stated above, we will study the Buneman instability by performing a computer experiment with the TSS model. The parameters and model configuration used in the computer experiments are stated below. As a simulation code, we will utilize the two-dimensional KEMPO. The mass ratio of ion to electron m_i/m_e is 100. At an altitude of 300 km, v_{te}/V_p and v_{ti}/V_p are approximately 30 and 0.5, respectively. In the computer experiments, we reduce the ratios and take each ratio of the velocity as 8.0 and 0.8, respectively. The parameters of frequency are the followings: $\Pi_e/\Omega_e = 2, \Pi_i/\Omega_e = 0.2, \omega_{LHR}/\Omega_e = 0.1$, and $\Omega_i/\Omega_e = 0.01$. Even if the time and spatial scale of the system is reduced, the essential character of the problems is never changed in the computer experiment. Since our interest is the initial field response to the abrupt change of the satellite potential, the time period of our concern is around up to one period of the lower hybrid oscillation. Since the TSS moves approximately $10\lambda_D$ from the original position with respect to the ambient plasma in such a period of time, the field environment as well as the plasma dynamics won't be affected very much by the plasma flow effect. In
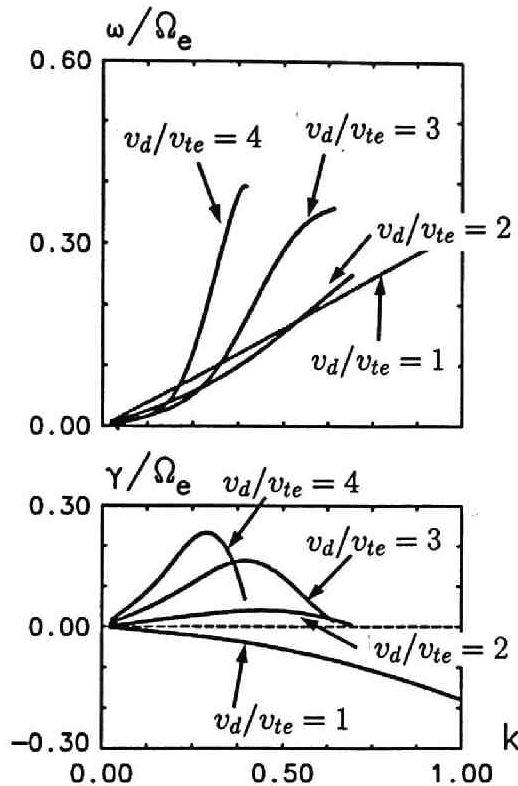
Figure 5.14: The $\omega - k$ diagram obtained by the dispersion solver for the Buneman instability with thermal plasma. The variable parameter is the ratio of the electron drift velocity to the thermal velocity v_d/v_{te}.

this aspect, then, we use a model region which introduces no relative motion of the TSS and the ambient plasma in the computer experiments. The model region of Case 3 used in the Chapter 4 is an appropriate one and we will use it for the present computer experiments. The dimensions of the model plane are $256\Delta r \times 128\Delta r$ in the $y - z$ plane. The grid spacing and the time step are $\Delta r = \lambda_D$ and $\Delta t = 0.005/\Omega_e$, respectively. The numerical damping region with a length of $16\Delta r$ is added at each boundary. The number of the superparticles is 131,072 for each species (electrons and ions) of plasma particles at the initial state. We supply the thermal electrons from the both edges of the the y direction to compensate the electrons captured by the high potential satellite. In the $y - z$ plane, B_0 lies along the y direction. The satellite is located at the center of the model plane. We abruptly change the potential energy of the satellite $e\phi_s/k_B T_e$ from zero to 100 at $\Omega_e t = 0$.

In the followings, we will describe the results obtained in the computer ex-

periments. First of all, we show the density modulation in the transient stage
as a response to the abrupt change of the satellite potential. Figure 5.15 and
Figure 5.16 show contour maps of the number density of electrons and ions at
different times. The square located at the center in each panel indicates the
satellite position. As discussed in the previous chapter, electrons and ions
are primarily attractive and repulsive to and from the satellite, respectively.
Since the charged particles are so mobile along B_0, namely the y direction, that
the presheath region which is low density region beyond the ion cavity spreads
along B_0. On the contrary, along the z direction near the satellite, high den-
sity plasma wall is created by the snow ploughing effect owing to the strong
magnetized electrons. The details of the formation of electron sheath and ion
cavity were described in the previous chapter. The most important thing to
be mentioned here is the density modulation with some spatial interval in the
presheath region along B_0. The structure becomes obvious in the third panel
from the top. This feature is observed in the both species of plasma. In com-
parison with Figure 5.15 and Figure 5.16, the panel for $\omega_{LHR}t = 2.82$ shows
the modulation pattern for the electrons becomes indistinct while the pattern
in the ion contour map is still clearly seen. The density contour maps at the
steady state around $\omega_{LHR}t = 8.19$ is plotted for electrons and ions in Figure 5.17
for comparison. The ion cavity has spread and the density modulation in the
presheath has disappeared in both panels.

From a view point of velocity space, we will examine the plasma modulation
observed in the density plots. In Figure 5.18 and Figure 5.19 the snapshots
of phase diagram of the $v_y - y$ space at different times are depicted for the
electrons and ions. The sampling region of the plasma particle for the phase
diagrams is $-128 < y/\lambda_D < 128$ and $-12 < z/\lambda_D < 12$ assuming the satellite
position is located at the origin indicated by the dashed lines in each panel.
The velocity and the position are normalized to v_{te} and λ_D, respectively. In
the transient stage up to the completion of the sheath formation, the electrons
near the satellite are strongly accelerated by the intense electric field from the
satellite. In particular, the sheath region where no ions exist near the satellite,
the electrons are enormously accelerated up to $v_y/v_{te} \sim 15$ maximum. In the
presheath region, though the acceleration is much lower than that in the sheath
region, the drift velocity of the electrons toward the satellite is larger than
v_{te}. For instance, at $\omega/\omega_{LHR} = 0.51$, the average drift velocity of electrons is
approximately three times as fast as v_{te} at the presheath region $|y/\lambda_D| > 32$.
Although the ions which are much heavier than electrons are slow to respond
to the intense field, they are also accelerated away from the satellite region to
form an ion cavity as shown in Figure 5.19. Particularly, as shown in the panel
(c), some ions located at the edge of the cavity is accelerated up to v_{te}. In such
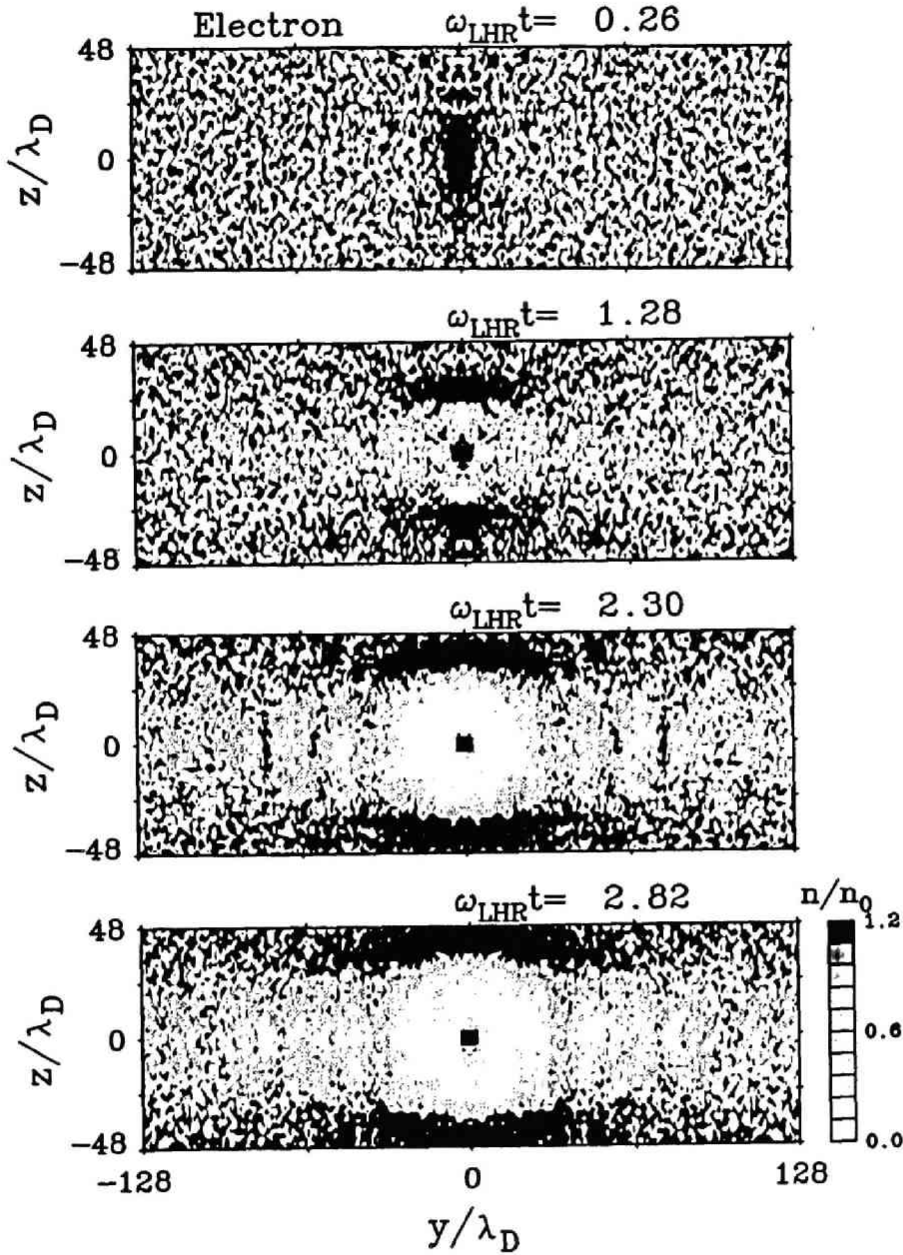
Figure 5.15: Time series of the contour maps for the electron number density. The square located at the center in each panel indicates the satellite position.
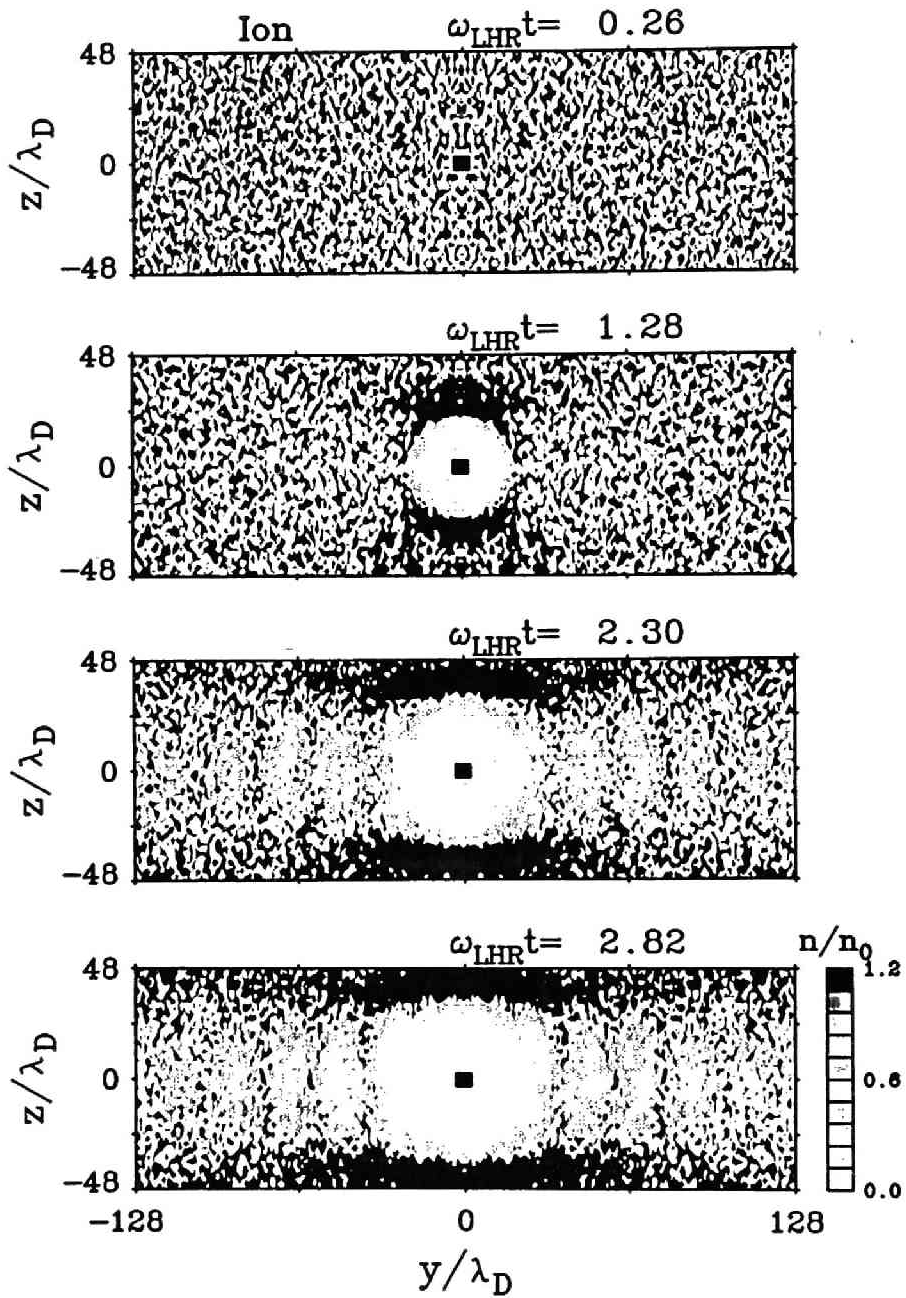
Figure 5.16: Time series of the contour maps for the ion number density. The square located at the center in each panel indicates the satellite position.
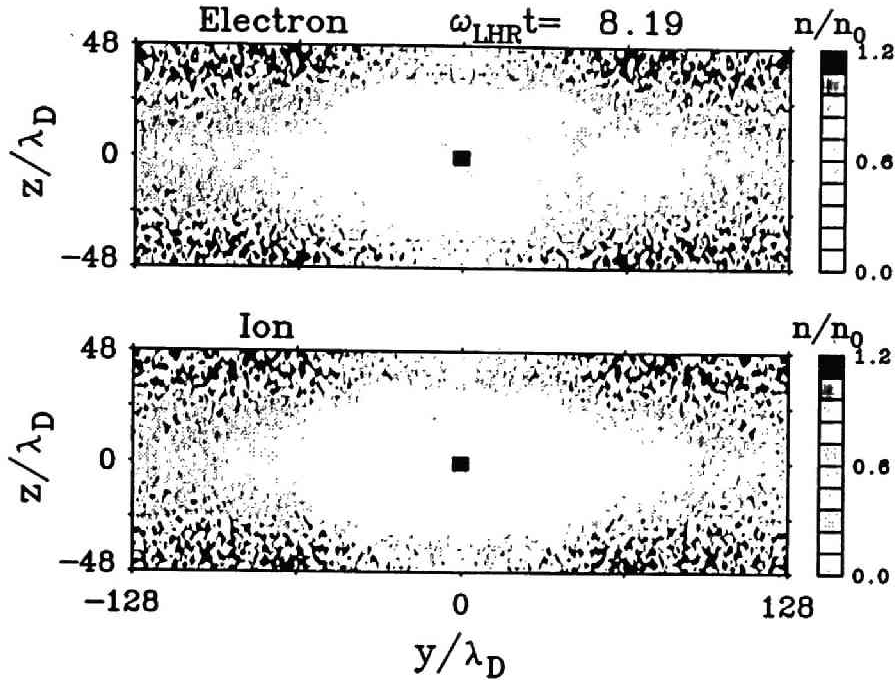
Figure 5.17: Contour maps for the electron and the ion number densities measured at the steady state.

a transient process, the relative velocity between the electrons and ions in the presheath becomes more than v_{te}. Hence, in such a situation, the ion-electron two-stream instability will be able to grow. As shown in Figure 5.18, plasma interaction takes place and phase-space vortices start to form and grow in time at the both sides of the satellite position. As time elapses, the ion velocity is also modulated in position by the instability. Since the ion cavity expands as time elapses, the interaction region also moves away from the satellite. Speculated from the above analysis concerning the velocity modulation of electrons and ions, the density modulation observed in Figure 5.15 and Figure 5.16 can be interpreted as the spatial bunching of the particle due to the plasma instability in the presheath region.

The plasma instability in the presheath region should perturb the electrostatic field. To clarify this, we will analyze the field data. First, to seek the dominant frequency of the field perturbation, we examine the field spectra by performing the Fourier transformation of the time series of the electrostatic potential at the plasma interaction region. Figure 5.20 shows frequency spectra of the perturbations in electrostatic potential. The electrostatic fields are measured along the z axis fixed at $y/\lambda_D = 30$ which crosses the presheath region. The potential values and frequency are normalized to the electron thermal energy
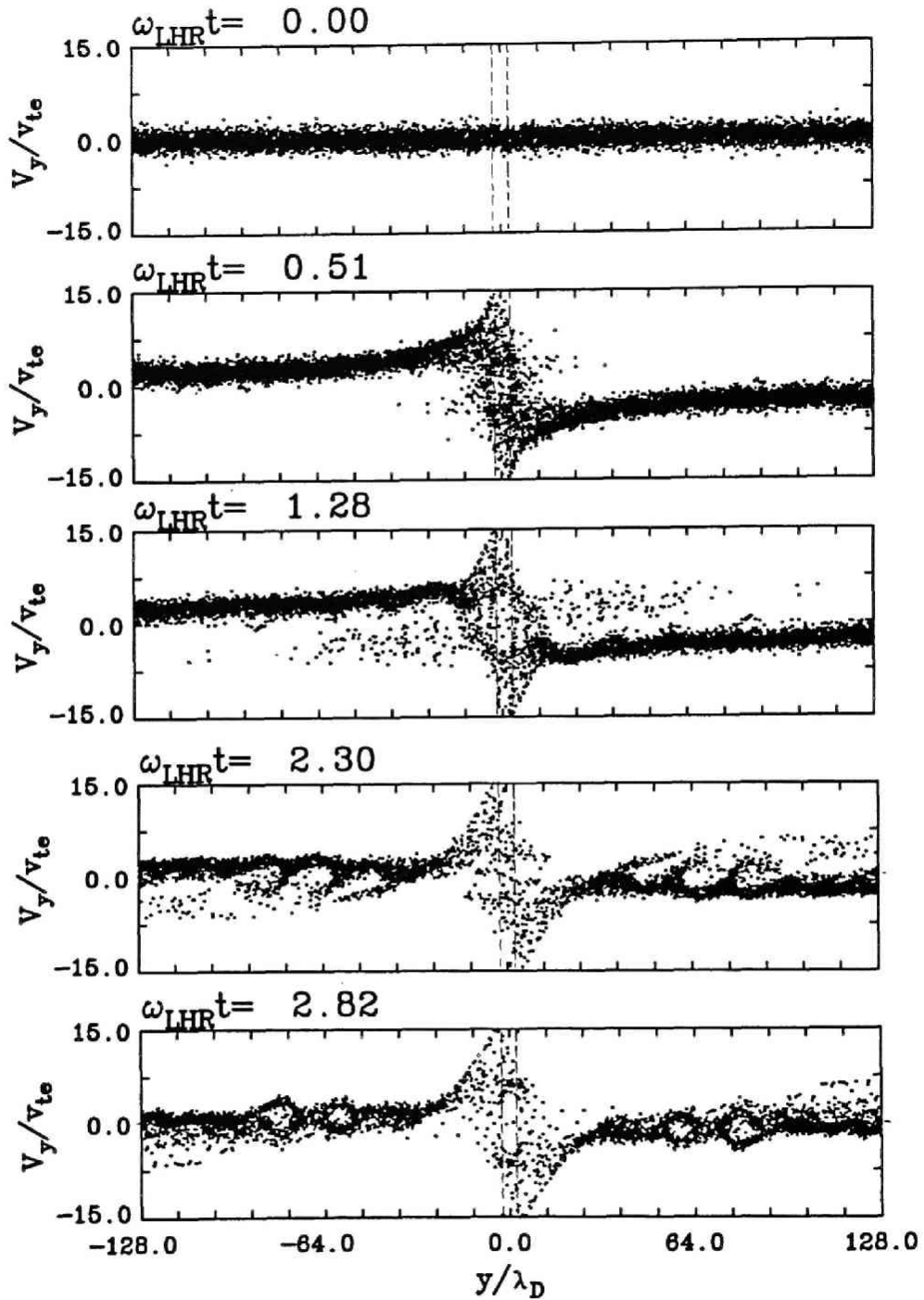
Figure 5.18: Phase space plots for electrons at different times. B_0 lies along the y direction.
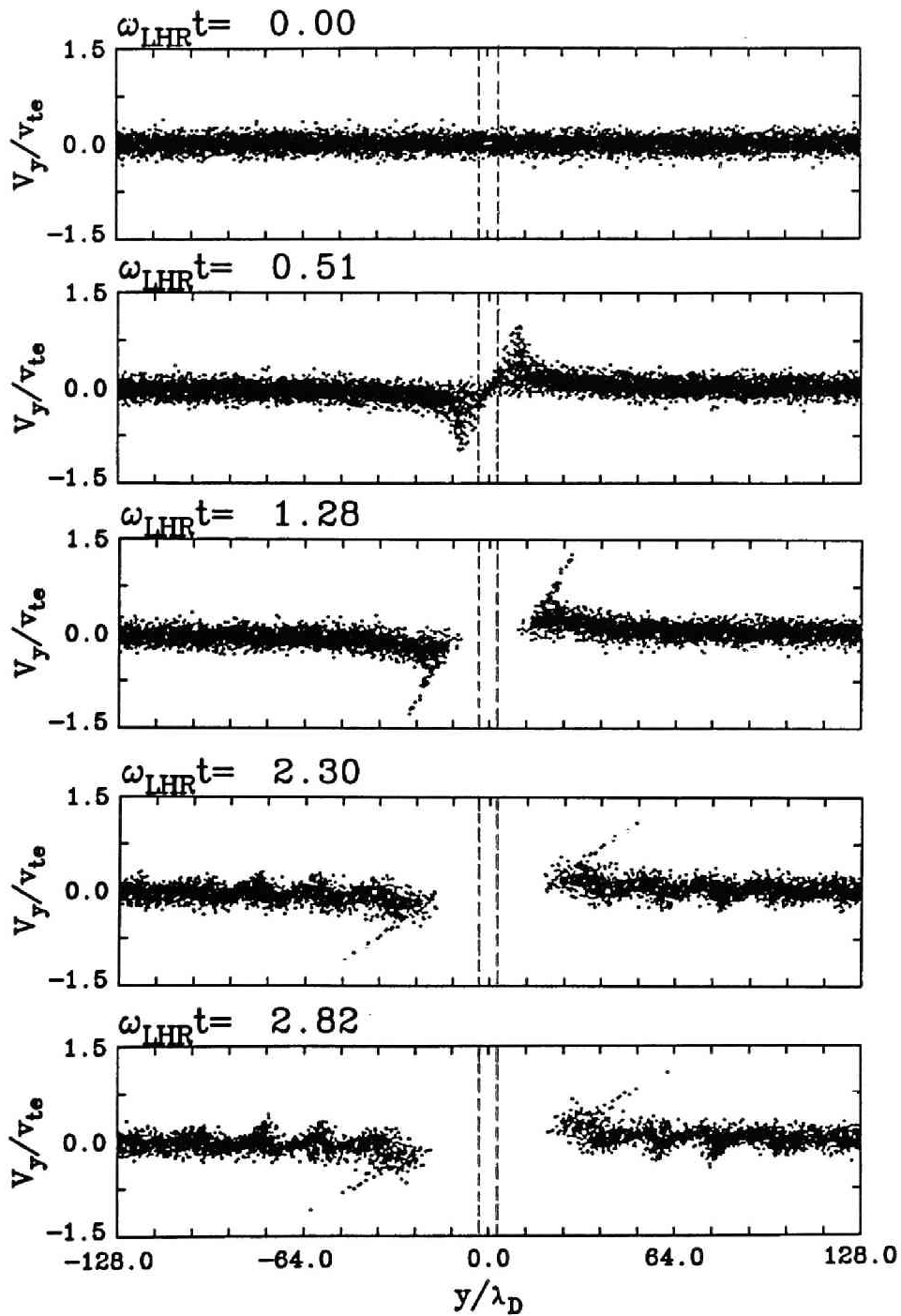
Figure 5.19: Phase space plots for ions at different times. B_0 lies along the y direction.
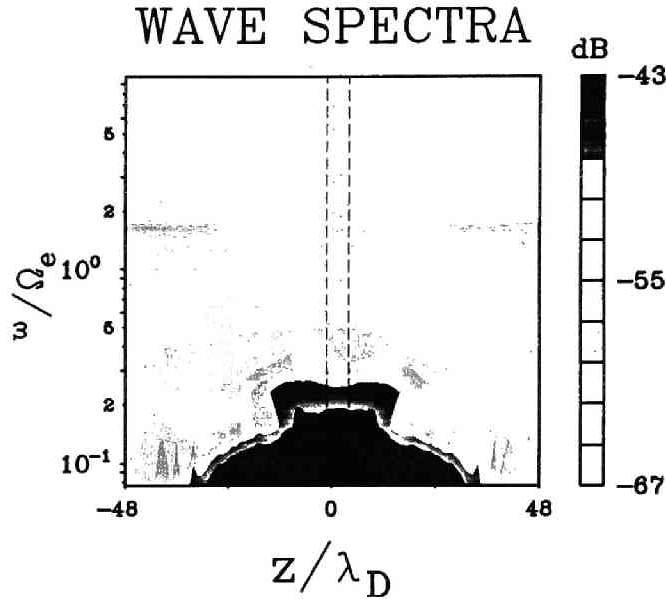
Figure 5.20: Wave spectra of the electrostatic potential.

and ω_{LHR}, respectively. The dashed lines represent the satellite region. Taking account of the fact that the potential near the satellite is decreased in time due to the potential shielding by the electron sheath, low frequency perturbation of the potential can be stressed in the Fourier components. However, in comparison with the potential intensity at $z/\lambda_D = 0$ and $z/\lambda_D = 40$, it is obviously seen that the perturbation at low frequency up to $0.3\Omega_e$, i.e., $\sim 3\omega_{LHR}$ is dominant around $z/\lambda_D = 0$ in the presheath region. From this point of view, we can conclude the low frequency field can be attributed to the results of the plasma instability. In the analysis of the dispersion relation of the Buneman instability, it is examined that the instability occurs when the relative velocity between electrons and ions exceeds the thermal velocity. In the present computer experiments, as shown in the phase diagrams, the relative velocity becomes approximately three times as much as the thermal velocity. According to the dispersion curve for $v_d/v_{te} = 3$ in Figure 5.14, a wave can grow at the frequency range around $\omega/\omega_{LHR} \sim 3$. This frequency range shows good agreement with the results of the computer experiments shown in Figure 5.20.

We next examine the spatial region of the intense field perturbation. Since we found the dominant frequency range stated above, we extract the Fourier components of the potential field in this frequency range and plot them in the
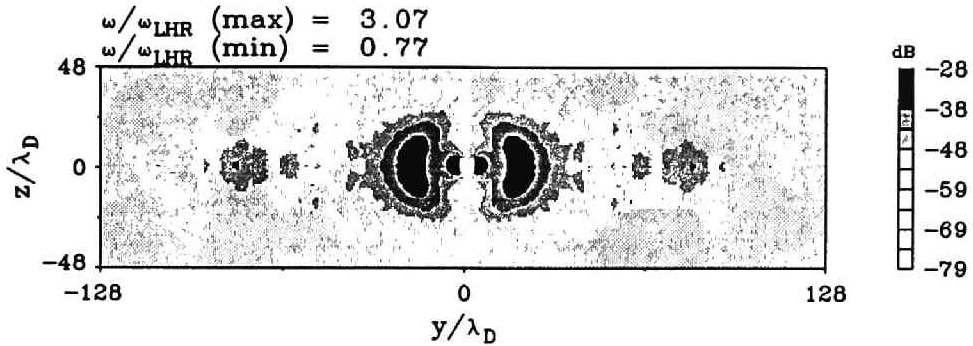
Figure 5.21: Field profile of the electrostatic potential in the model plane for the low frequency up to $\sim 3\omega_{LHR}$.

$y - z$ plane as a contour map shown in Figure 5.21. The square at the center of the plane indicates the satellite. In comparison with the contour map of the number density shown in Figure 5.15, it is found that the region where the electrostatic field is the most intense corresponds to the boundary of the ion cavity region in the y direction. This is because that the relative velocity between the electrons and ions is the largest at the ion cavity boundary as shown in the previous phase diagrams. Taking account of the analysis described above, it is straightforward to conclude that the electrostatic field is perturbed owning to the Buneman instability beyond the ion cavity region in the direction parallel to B_0. As well known, the threshold of the instability depends on the relative velocity of electrons and ions. In the TSS, it is primarily determined by the satellite potential which accelerates the electrons toward the satellite. To estimate the relation of the satellite potential and the electron acceleration, we made a rough analysis on this as follows.

The potential at a distance r from the satellite is generally written in terms of the local Debye length λ_D and the satellite potential ϕ_s as follows.

$$\phi = \phi_s \exp\left(-\frac{r}{\lambda_D}\right) \tag{5.6}$$

Our concern is the average velocity of the electrons in the presheath region. To obtain it, for simplicity, we estimate the velocity at the edge of the ion cavity region. Assuming λ_D is equal to the radius of the ion cavity r_{ic}, the potential at the edge of the cavity ϕ_{ic} is

$$\phi_{ic} = \phi_s \exp\left(-1\right) \tag{5.7}$$
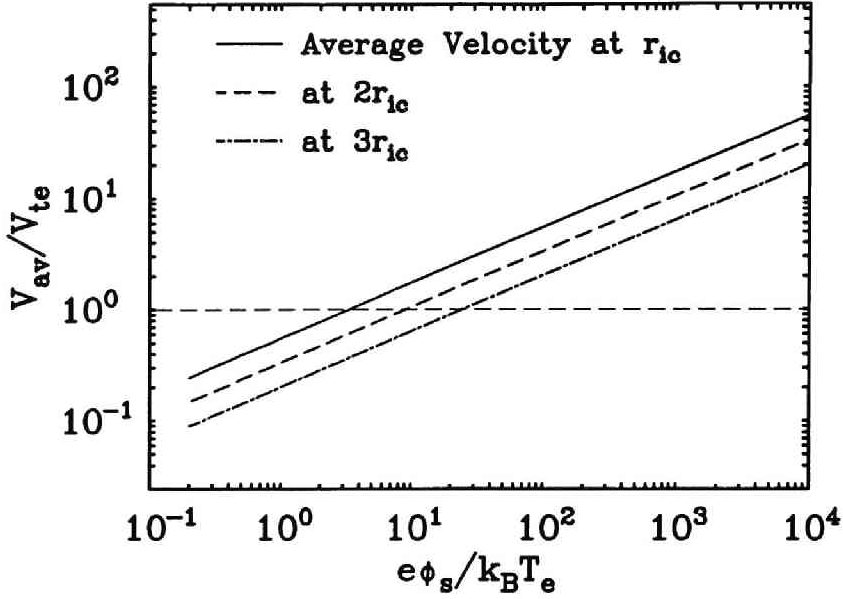
Figure 5.22: Estimation of electron velocity accelerated by the satellite potential in the presheath region.

The maximum velocity accelerated by ϕ_{ic} is estimated by the using the energy conservation as follows.

$$\frac{1}{2}m_e v^2_{max} = e\phi_{ic} \tag{5.8}$$

Then v_{max} is given

$$v_{max} = \sqrt{\frac{2e\phi_{ic}}{m_e}} \tag{5.9}$$

Since our concern is the transient phenomena as response to the potential change of the satellite, the time scale for the electron acceleration by the high potential satellite can be roughly determined as follows. As discussed in Chapter 4, the time scale for the satellite to obtain the maximum transient current is approximately $T_{pe}/4$. Taking account of the velocity oscillation at the frequency Π_{pe}, the averaged velocity obtained in the transient period, namely $T_{pe}/4$, is given

$$v_{av} = \int_0^{T_{pe}/4} v_{max}\sin(\Pi_e t)dt = \frac{2v_{max}}{\pi} = \frac{2}{\pi}\sqrt{\frac{2e\phi_s \exp{(-1)}}{m_e}} \tag{5.10}$$

Figure 5.22 shows the relation between ϕ_s and v_{av} obtained in (5.10). As examined with the dispersion solver stated earlier, the Buneman instability can

grow when the drift velocity of the presheath electrons exceeds v_{te}. According to Figure 5.22, the satellite potential which satisfies this criteria is approximately above $e\phi_s/k_B T_e = 5$.

In the discussion above, we just considered the threshold of the relative velocity of electrons and ions in the condition that the distribution and acceleration of the electrons in the presheath region are spatially uniform. In a realistic case, however, the acceleration of the electrons in the presheath is not constant in space but becomes weak at far distance from the satellite because the electric force by which electrons are attracted becomes weak. In this sense, (5.10) just provides us the rough criteria for the instability. Actually, for a certain mode to be unstable, the electron drift velocity which exceeds the threshold needs to be maintained spatially for a region of at least several wavelengths of excited wave. Taking account of this, the satellite potential which is required for the instability to occur in the presheath region can be more or less larger than that obtained from (5.10). For example, we can assume that the threshold velocity for the instability to occur should be obtained at $2\lambda_{ic}$ or $3\lambda_{ic}$, not at the ion cavity boundary λ_{ic}. In such cases, the average drift velocities at $2\lambda_{ic}$ or $3\lambda_{ic}$ are indicated by the dashed lines respectively in Figure 5.22. As shown in the figure, $e\phi_s/k_B T_e$ which provides the threshold $v_{av}/v_{te} = 1$ becomes high as the distance from the satellite surface becomes large. For the case of $3\lambda_{ic}$, $e\phi_s/k_B T_e \sim 20$ provides the threshold velocity for the electron drift. Since the detailed modification of the estimate (5.10) including the density variation of the electron sheath is beyond our scope in the present study, we will leave it for a future work.

5.3.3 Beam Cyclotron Instability Near the Tethered Satellite

With a view point of plasma interaction, it was shown in the previous section that the Buneman type instability can grow due to the relative motion of electrons and ions in the presheath region. In the Buneman instability the electron acceleration along B_0 toward the satellite plays an important role. Meanwhile, in the direction perpendicular to B_0, the electrons near the satellite surface make a drift motion with $E \times B$ velocity where E is the electric field from the satellite. Particularly, in the transient stage of the sheath formation, ions start to be accelerated by the satellite electric field in the radial direction while electrons make a cross-field drift motion with $E \times B$ velocity. In such a situation, the electron beam cyclotron instability is able to grow due to the relative motion of electrons and ions across B_0. In the direction perpendicular to B_0 the cavity expansion of ion is restricted by the effect of the finite Larmor radius. In
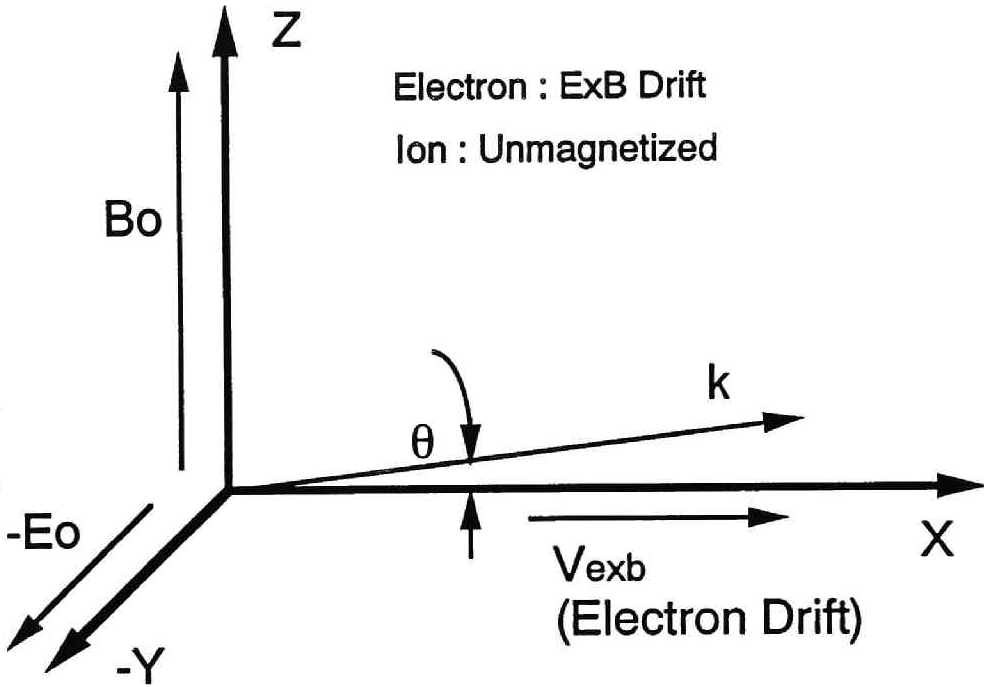
Figure 5.23: Schematic illustration of the coordinates used in the dispersion equation for the electron beam cyclotron instability.

this sense, the region of field perturbation due to the electron beam cyclotron instability can be near the satellite surface. Here we microscopically focus on the plasma interaction, mainly electron beam cyclotron instability, due to the relative motion of the electrons drifting with $E \times B$ velocity and the stationary ions.

As have been done in the previous section, we will study the field perturbation by performing computer experiments. Prior to the experiments, we will first examine the linear dispersion relation under cold plasma approximation for the electron beam cyclotron instability. Since our concern is the perturbation due to the relative motion of plasma in the perpendicular to B_0, we need to take account of $v \times B$ term in the equation of motion. The coordinates used in the dispersion equation for the instability is illustrated in Figure 5.23. Since our interest is the plasma interaction between drifting electrons and stationary ions, we will take an ion rest frame of reference in which electrons drift with $E \times B$ velocity. The static magnetic field B_0 is along the y direction. The intense electric field owing to the high potential of the satellite points toward the $-z$ direction. Then the electrons move along the x direction with the $E \times B$

velocity $V_{e\times b}$. The interaction takes place in the $x - y$ plane. In the cold plasma approximation, the plasma oscillations are described by the dispersion equation

$$1 - \frac{\Pi_{pe}^2 \cos^2 \theta}{(\omega - k \cdot V_{e\times b})^2 - \Omega_e^2} - \frac{\Pi_{pe}^2 \sin^2 \theta}{(\omega - k \cdot V_{e\times b})^2} - \frac{\Pi_{pi}^2}{\omega^2} = 0 \qquad (5.11)$$

where ω, k and θ denote the wave frequency, wavenumber, and the angle between the directions of k vector and the electron drift, respectively. The second term represents the dynamics perpendicular to B_0. The third term is due to the electron motion along B_0.

This type of the dispersion equation has been studied by many scientists. It has been reported that two types of electrostatic instabilities can grow nearly perpendicular to B_0. One is the upper-hybrid-two-stream instability studied by Buneman [1962]. The other is the modified-two-stream instability [Krall and Liewer 1971; Lemons and Gary 1977]. This instability causes the field growth which has the characteristic frequency and growth rate comparable to ω_{LHR}. They examined the dispersion relation in an electron rest frame of reference. The frequency range for the former and later instabilities approximately corresponds to ω_{UHR} and ω_{LHR}, respectively. The dispersion relation of the two regimes were discussed in detail by Chen and Birdsall [1973]. The dispersion equation with thermal plasma effect was presented and examined by McBride, et al. [1972]. To apply the cold dispersion equation (5.11) to the analysis of a thermal plasma, $|\omega - k \cdot V_\alpha| \gg k v_{t\alpha}$ should be satisfied where α denote plasma species. This condition implies that the mean thermal displacement of the particles during an oscillation period measured in a coordinate system moving with the drift velocity of the particle must not exceed the wavelength of the oscillation. They focused on the modified-two-stream instability and examined the parametric dependence of the unstable roots on T_e/T_i, V_0/v_{ti}, m_e/m_i and Π_{pe}/Ω_e. They also discussed the electromagnetic effects on the stabilization. According to the dispersion equation, the plasma interaction generally tends to occur when the second and third terms becomes comparable. Namely, $\Pi_{pe}^2 \sin^2 \theta \sim \Pi_{pi}^2$ is satisfied in (5.11). Then the effective electron mass $\tilde{m}_e = m_e/\sin^2 \theta$ can be comparable to m_i, which gives us the unstable roots of the dispersion equation.

Next we will examine the dispersion relation by substituting the parameters used in the present computer experiments in (5.11). In the ionospheric parameters we focus on, the magnetic field strength is characterized by

$$\Omega_i \ll \Pi_{pi} \ll \Pi_{pe} \sim \Omega_e \qquad (5.12)$$

In fact, $\Omega_i/\Omega_e = 0.01$, $\Pi_{pi}/\Omega_e = 0.2$, and $\Pi_{pe}/\Omega_e = 2.0$ are used in the computer experiments. To compare the dispersion relation with the results obtained in

the computer experiments, we use the same values of frequencies as those stated above. Then, in the dispersion relation (5.11), the parameters which remain variable are $V_{e \times b}$ and θ. Concerning $V_{e \times b}$, it absolutely depends on the intensity of the local electric field which is increased as the satellite potential becomes large. For the instability to grow in the thermal plasma, $V_{e \times b} > v_{te}$ should also be satisfied. Taking the results in computer experiments of $e\phi_s/k_B T_e \sim 10^2$ as one example, it is found that $V_{e \times b}$ near the satellite is larger than v_{te}. This assures that the cold dispersion can be valid at least in the linear stage. According to the result of the computer experiments, we fix $V_{e \times b}$ as 10 while v_{te} is 2 in solving the dispersion equation (5.11) analytically.

Figure 5.24 shows the dispersion lines in $\omega - k$ plane obtained by solving the equation (5.11). The panel (a), (b) and (c) correspond to the cases of $\theta = 0$, 10, and 20 degrees, respectively. The solid and dotted lines indicate the real and imaginary roots of ω. The frequency ω and wavenumber k are respectively normalized to ω_{LHR} and $\omega_{LHR}/V_{e \times b}$. Basically, two modes arise with positive growth rate. One is found in all the three panels around $kV_{e \times b}/\omega_{LHR} = 20 \sim 30$. The real part of the frequency ω_r covers approximately from $0.1\omega_{LHR}$ to $3\omega_{LHR}$. This branch corresponds to the wave mode due to the upper hybrid two-stream instability. Because of the effect due to the Doppler shift, the backward propagating UHR mode in the electron beam frame of reference can be observed at the lower frequency than ω_{UHR} in the ion frame of reference. Although not in the panel (a) which shows the case for $\theta = 90$ degrees, the other mode branch is shown in the panel (b) and (c) at a frequency range almost up to ω_{LHR} at lower k value around $kV_{e \times b}/\omega_{LHR} \sim 5$. This corresponds to the wave mode induced by the modified two-stream instability. In terms of k value, it is shown that the wavenumber which provides positive growth rate becomes large as the direction of the k vector approaches to B_0. In a real situation of thermal plasma. however, the Landau damping will play a roll to restrict the growth of the instability. Since the dispersion relation plotted in the figure is derived with cold plasma approximation, no Landau damping is concerned. The dispersion equation including the thermal effects was examined and presented in detail by McBride, et al.[1972].

As examined above, it is confirmed that the electron beam cyclotron instability generates two branches of wave mode and gives rise to the field perturbation in the low frequency range around ω_{LHR} in the ion stationary frame of reference. In order to confirm those instabilities, we will perform a computer experiment with the same parameters used in the analysis of the dispersion relation. The detail of the computer experiment is described below.

Our concern is the microscopic interaction between the electrons and ions at the sheath edge, it is not necessary to include a conducting body such as
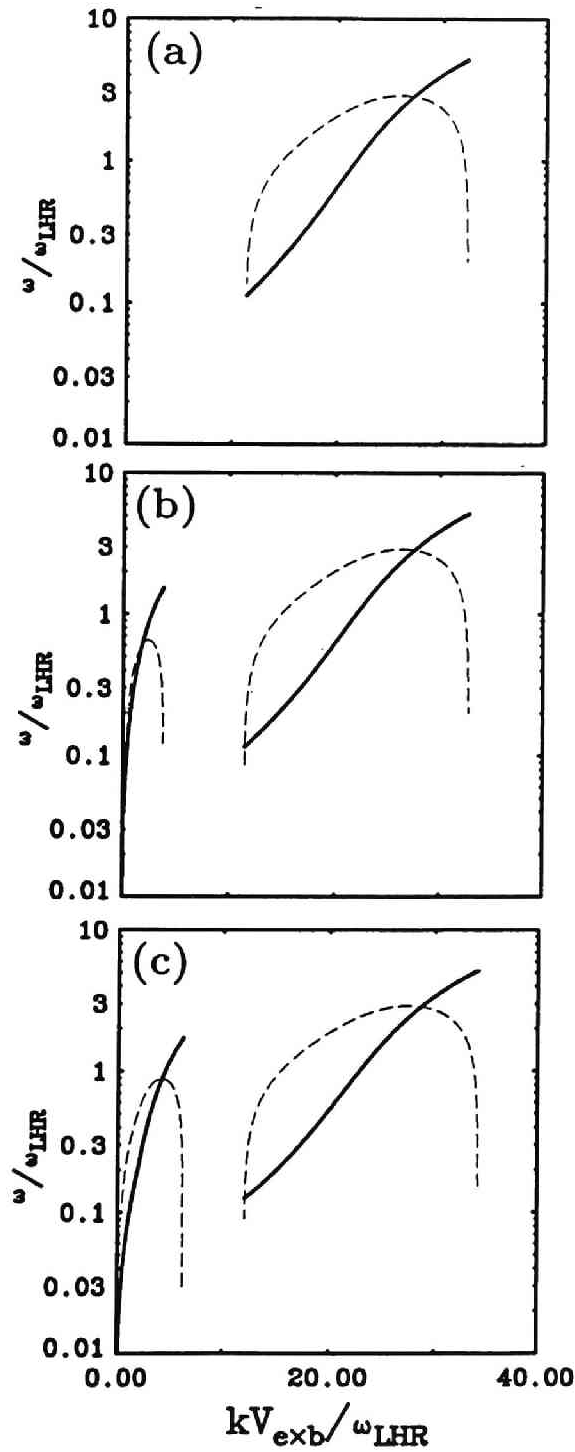
Figure 5.24: The $\omega - k$ diagram obtained by the cold dispersion relation at different angle between the direction of k and B_0. The panel (a), (b) and (c) correspond to the cases of $\theta = 0$, 10, and 20, respectively.
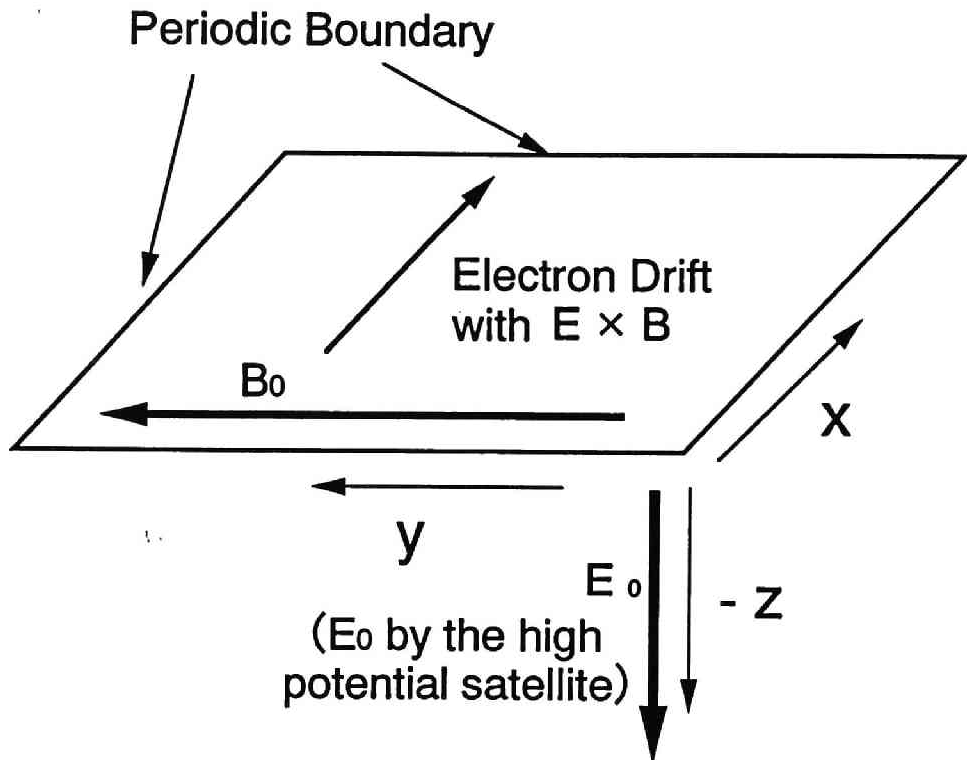
Figure 5.25: Schematic illustration of the two-dimensional model plane used in the computer experiments for the beam cyclotron instability. The periodic boundary condition is adopted.

the tethered satellite in the model region. We hire a two-dimensional model plane with periodic boundary conditions. The model configuration is illustrated in Figure 5.25. The dimensions of the model region are $256\Delta r \times 256\Delta r$. The model plane is filled with electrons and ions which have the same temperature. The static magnetic field B_0 lies along the y direction. The intense electric field E_{sat} induced by the high potential satellite is put in the $-z$ direction. Owing to this field configuration, the charged particles make a drift motion with $E_{sat} \times B$ velocity along the x direction. In the initial stage, particularly, only electrons, which are much lighter than ions, move along the x direction while the ions start to be accelerated by E_{sat} along the $-z$ direction. This is the situation of our concern and we can expect the beam cyclotron instability due to the electron-ion relative motion along the x direction.

First, we present the time series of the density variation in the model plane. Figure 5.26 shows the contour maps of the number density of electrons and ions. The panel (a), (b), and (c) corresponds to the maps at $\omega_{LHR}t = 1.02$, 2.05, and 3.07, respectively. In each panel, the number density is normalized to the average

one. As easily found, along the x direction, i.e., in the direction of $E_{sat} \times B_0$, ripple-like density modulation is enhanced as time elapses. As shown in the panel (a), electron profile starts to be modulated and later around $\omega_{LHR}t = 2$, the density modulation is also seen for ions. The spatial interval of the density modulation is approximately $25\lambda_D$ which is equivalent to $kV_{e\times b}/\omega_{LHR} \sim 25.1$. As time elapses shown in the panel (c), the regular modulation pattern seen in the electron profile becomes weak while the pattern is still clearly seen in the ion profile.

We next examine the variation of the particle dynamics in phase diagrams. Figure 5.27 and Figure 5.28 depict the time series of electron plots in the $v_x - x$ phase space. The panel (a), (b), and (c) correspond to the diagram at $\omega_{LHR}t = 1.28$, 2.30, and 3.33, respectively. In each figure, the vertical and horizontal axes are normalized to the electron thermal velocity v_{te} and the Debye length λ_D, respectively. As well as the density modulation shown in Figure 5.26, the electron velocity starts to be modulated regularly along the x direction as shown in the panel (b). Around $\omega_{LHR}t = 2.3$, the velocity of ions also starts to be modulated. The spatial interval of the velocity modulation is the same as that observed in the density modulation. After $\omega_{LHR}t \simeq 3$, the electrons are smeared out in the phase space while the ions keep the modulation with a regular structure and some ions are accelerated up to the ten times as high as the ion thermal velocity.

According to the above analysis in the phase diagrams, it is speculated that a plasma instability is induced across B_0 by the relative motion between electrons with $E \times B$ drift and stationary ions. In the followings, we will examine the field data to confirm the possibility of instability. We first analyze the direction of the k vector of the excited wave mode. In Figure 5.29 we present contour plots of the E_x field intensity in the $k_x - k_y$ plane at different times. The field intensity in the k space is obtained by performing the Fourier transformation of the field data with respect to the two-dimensional space. As obviously shown in Figure 5.29, the k values of the dominant waves vary as time elapses. Around $\omega_{LHR}t \sim 3$ as shown in the panel (a), the dominant wave is intense in the region approximately from $k_x V_{e\times b}/\omega_{LHR} \sim 15$ to 30. The field intense region also spreads in the k_y direction, approximately from zero to $k_x V_{e\times b}/\omega_{LHR} \sim 20$ at most. At $\omega_{LHR}t = 5.15$ as shown in the panel (b), however, the intense wave component shown in the panel (a) has been damped and the field component with $k_x V_{e\times b}/\omega_{LHR} \sim 15$ only survives. The k_y component has shifted to the lower value. It should be noted that another unstable mode has appeared around $(k_x V_{e\times b}/\omega_{LHR}, k_y V_{e\times b}/\omega_{LHR}) \sim (4, 3)$. This mode keeps growing as time elapses, which is shown in the panel (c).

By evaluating k_y/k_x value, we can estimate the direction of the k vector for the induced wave mode. At $\omega_{LHR}t = 3.1$ the excited wave mode propagates
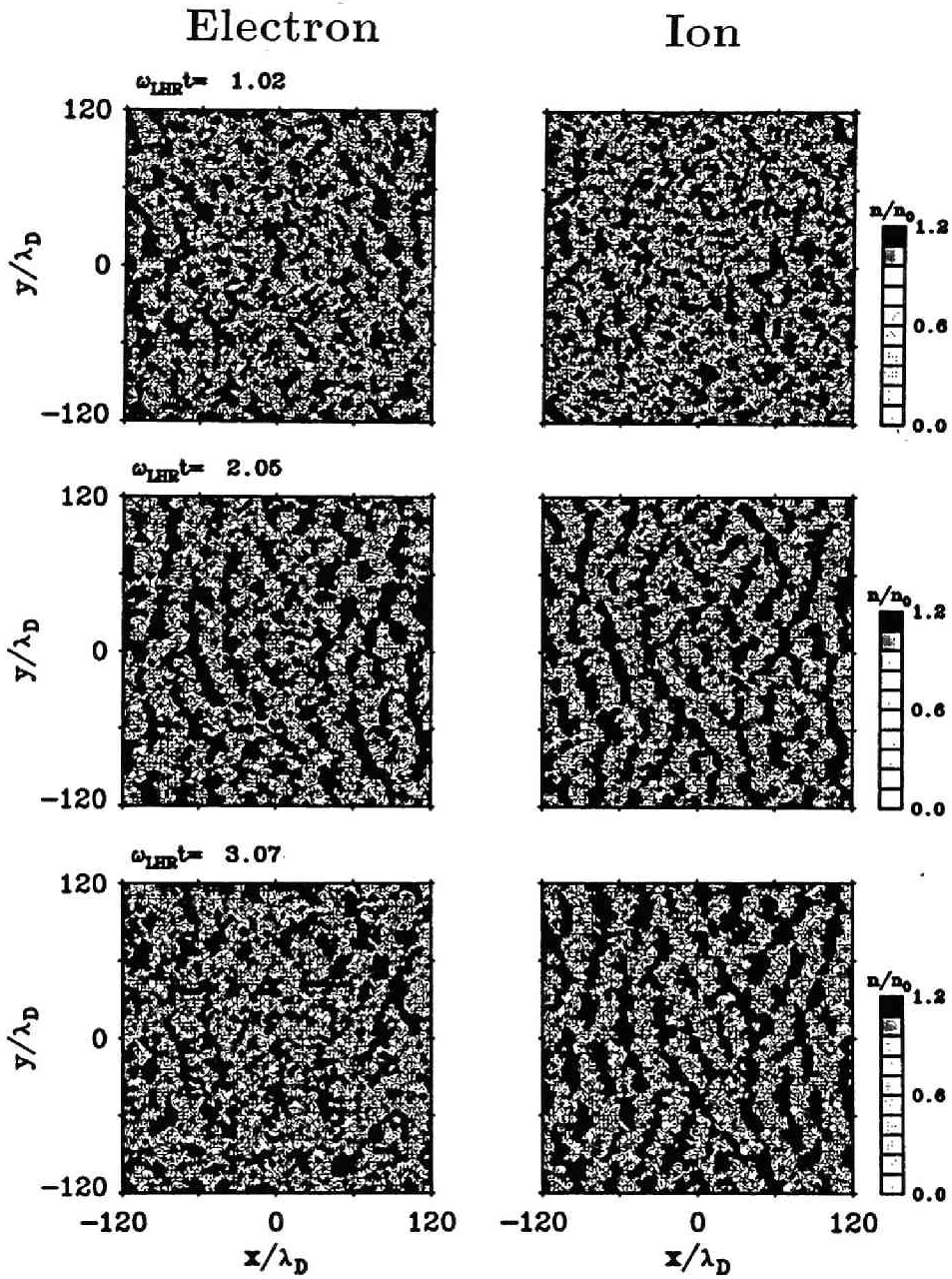
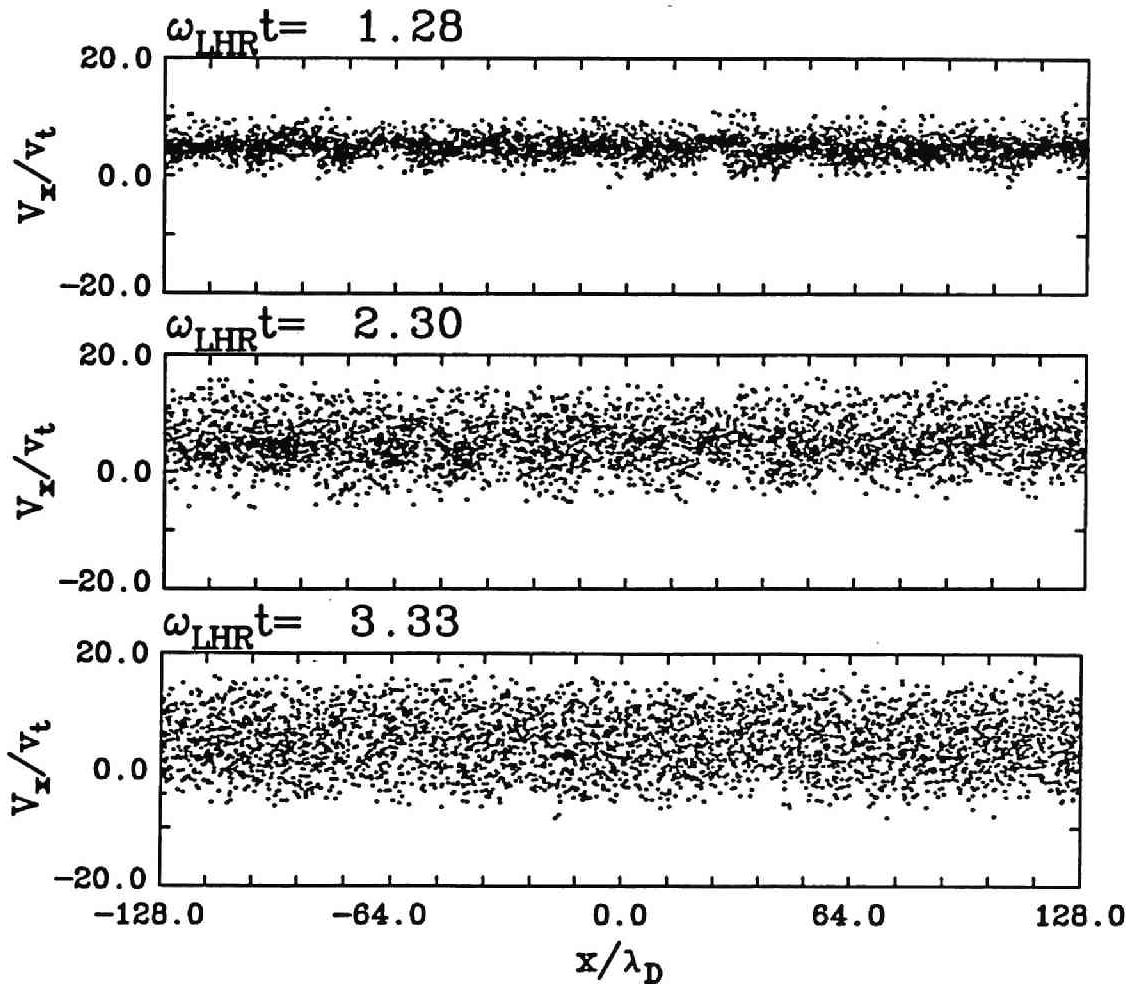Figure 5.26: Time series of contour maps for the number density of electrons and ions.

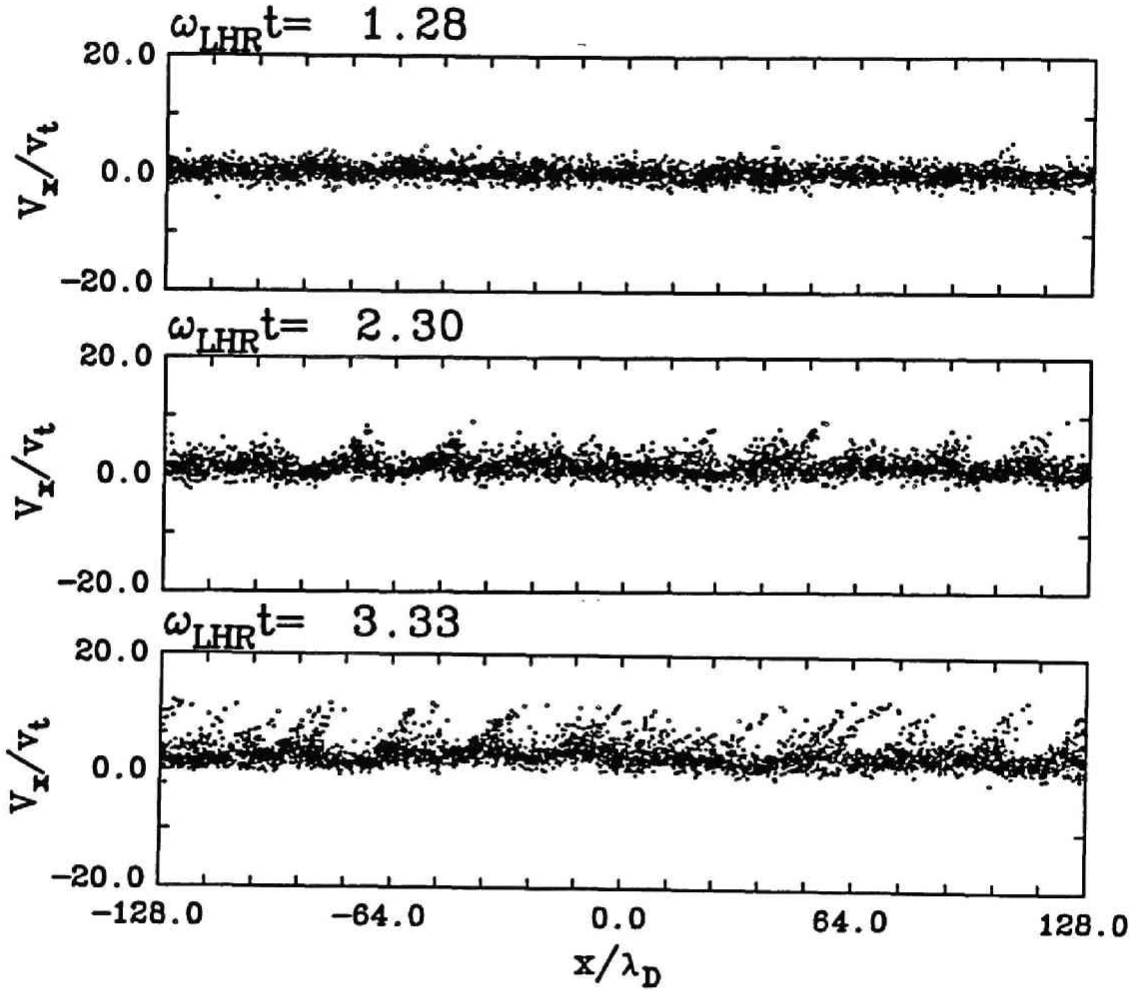Figure 5.27: Phase diagram of electrons in the $v_x - x$ space at different time.

Figure 5.28: Phase diagram of ions in the $v_x - x$ space at different time.
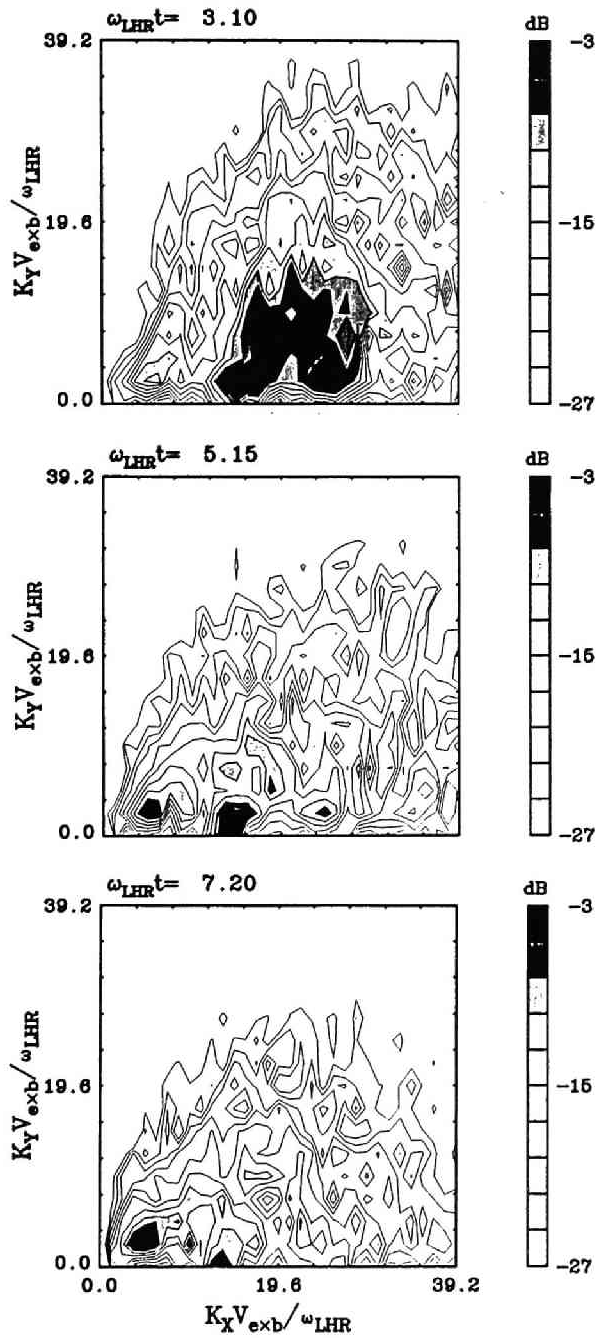
Figure 5.29: Contour maps of k-spectra for the E_x field component at different times.

approximately within an angle of 33 degrees measured from the x axis or the $E \times B$ flow direction. Particularly, for the most intense fields found around $(k_x V_{e \times b}/\omega_{LHR}, k_y V_{e \times b}/\omega_{LHR}) \sim (15, 2)$ and $(25,4)$, their k vectors point toward the direction with approximately $8 \sim 9$ degrees from the flow direction. This implies that the excited wave mode propagates almost, not exactly, along the electron $E \times B$ flow direction, namely perpendicular to B_0. The parallel component of the electrostatic field is more or less enhanced simultaneously in the y direction. The plasma heating due to this induced electrostatic field will be examined later.

The dominant wavenumber $k_x V_{e \times b}/\omega_{LHR} \simeq 25$ observed in the panel (a) of Figure 5.29 shows a good agreement with the wavenumber of the plasma modulation as shown in Figure 5.26 and Figure 5.27. The ripples of the plasma density are mainly observed along the x direction. Although weakly observed, the density is also irregular along the y direction. This is due to the interaction with the y component of the oblique propagating electrostatic wave with respect to the x direction.

Regarding the wave excited at $(k_x V_{e \times b}/\omega_{LHR}, k_y V_{e \times b}/\omega_{LHR}) \sim (4, 3)$, which is shown in the panel (b) and (c), the propagating direction is approximately 30 to 40 degrees away from the electron $E \times B$ drift direction.

We also compared the wavenumber of the excited waves in the computer experiments with the results of the linear dispersion equation shown in Figure 5.24. Two instabilities, the upper-hybrid two-stream instability and the modified two-stream instability, are respectively found at the higher and lower wavenumbers in the presence of the cross-field relative motion between electrons and ions. As shown in the panel (a) of Figure 5.24, the upper-hybrid two-stream instability can grow in the direction perpendicular to B_0, i.e., the x direction in the present computer experiments. It also has growth rate even for the oblique direction with respect to the x direction as shown in the panel (b) and (c) of Figure 5.24. In fact, it is shown in Figure 5.24 that the k region for the unstable mode observed in the panel (a) of Figure 5.29 approximately agrees with the region which provides the positive growth rate for the upper-hybrid two-stream instability. As the angle between the k vector and the x direction increases, the modified two-stream instability becomes dominant according to Figure 5.24. The unstable mode at the lower k values shown in Figure 5.29 corresponds to the waves excited by the modified two-stream instability. In the computer experiments, this wave starts to appear at later time as shown in the panel (b) and (c) of Figure 5.29. This implies that the growth rate is smaller than that of the upper-hybrid two-stream instability. According to Figure 5.24, the growth rates for the modified two-stream instability is actually lower than those for the upper-hybrid two-stream instability, which accounts for the results obtained in

the computer experiments.

As a consequence of the interaction with the excited electrostatic waves, the plasma heating will be expected. The time histories of each species of plasma and the temperature ratio of electron to ion are plotted in Figure 5.30. The temperature is spatially averaged over the system region of the computer experiment. In the panel (a) and (b), the solid and dashed lines represent the temperature of perpendicular and parallel component with respect to B_0, respectively. According to the field analyses described above, the excited electrostatic wave mainly propagates perpendicular to B_0. This can account for the plasma heating perpendicular to B_0 as shown in the panel (a) and (b). As for the electrons, T_e at $\omega_{LHR}t \sim 4$ becomes approximately 30 times as high as the initial temperature T_0. Contrary to the variation in the electron temperature, the variation of the ion temperature indicates no drastic heating. At $\omega_{LHR}t \sim 4$, T_i/T_0 becomes more or less 3. It should be noted that parallel heating of electrons, which is indicated by a dashed line in the panel (a), also becomes obvious as time elapses. It occurs due to the electrostatic component parallel to B_0 induced by the beam cyclotron instability.

As for the threshold value of the relative velocity v_d between electrons and ions, the upper-hybrid two-stream instability requires $v_d > v_{te}$, while the modified two-stream instability only requires $v_d > v_{ti}$ [Chen and Birdsall, 1973]. According to the results of the plasma heating, the electrons are heated more than ten times as much as the initial temperature. This gives rise to the increase of v_{te} and it eventually becomes comparable to v_d. In such a situation, the upper-hybrid two-stream instability is no more strongly enhanced. The background ions, on the contrary, are much less heated by the instabilities, which little affects the growth of the modified two-stream instability. Consequently the enhancement of the electrostatic field due to the modified two-stream instability becomes dominant mostly in the oblique direction, which is responsible for the parallel electron heating.

In the panel (c), the time history of the temperature ratio of electron to ion is plotted. According to the ionospheric plasma, we adopted isothermal plasma, i.e., $T_e/T_i = 1$ as the initial values in the present computer experiments. As time elapses, T_e/T_i increases in time and shows saturation around $\omega_{LHR}t \sim 3$. The maximum value of T_e/T_i is approximately 8. When T_e/T_i becomes more than the unity, the ion acoustic instability can grow in general. The temperature dependence of the ion acoustic instability will be examined in the next section.

According to the analyses stated above, we can conclude that the upper-hybrid two-stream instability and the modified two-stream instability are responsible for the field perturbation and plasma heating near the high potential satellite in the direction mostly perpendicular to B_0.
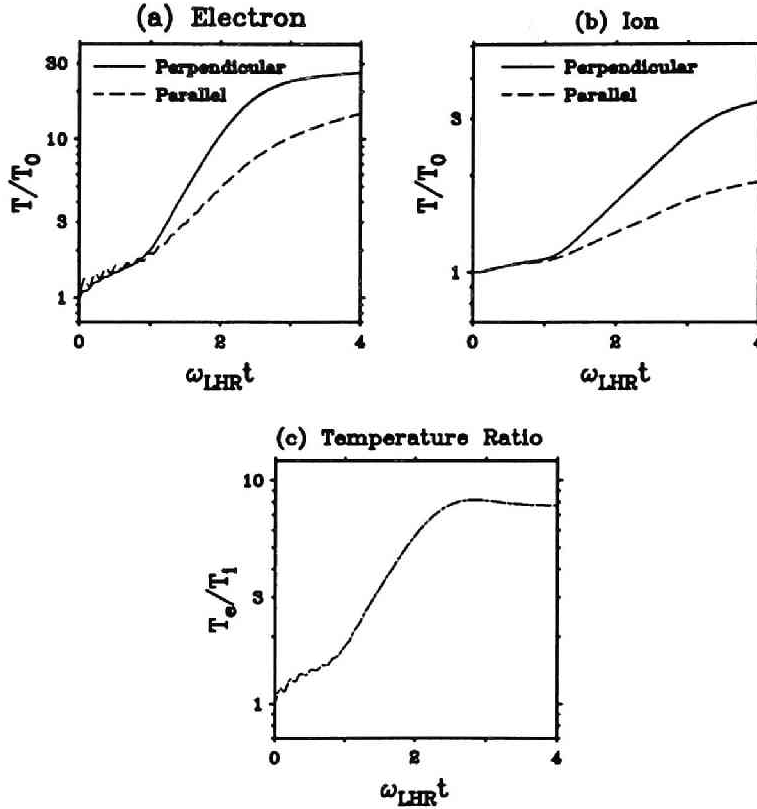
Figure 5.30: Time history of the plasma heating due to the interaction with the beam cyclotron instability. The panels (a), (b), and (c) show the variation of the electron temperature, the ion temperature, and the temperature ratio, respectively.

5.3.4   Discussion and Conclusion

In the previous sections we independently analyzed the field perturbation in the direction parallel and perpendicular to B_0 due to the Buneman instability and the beam cyclotron instability, respectively. In the real three-dimensional space, however, those two types of instability can coexist simultaneously. In a general situation in which the electric field from the satellite E_{sat} and the geomagnetic field B_0 intersect to each other with a certain angle, electrons are accelerated by the parallel component of E_{sat} along B_0 and simultaneously they make an $E \times B$ drift in the direction perpendicular to B_0. Particularly, in the transient process of the electron sheath formation near the satellite, this dynamics of electrons
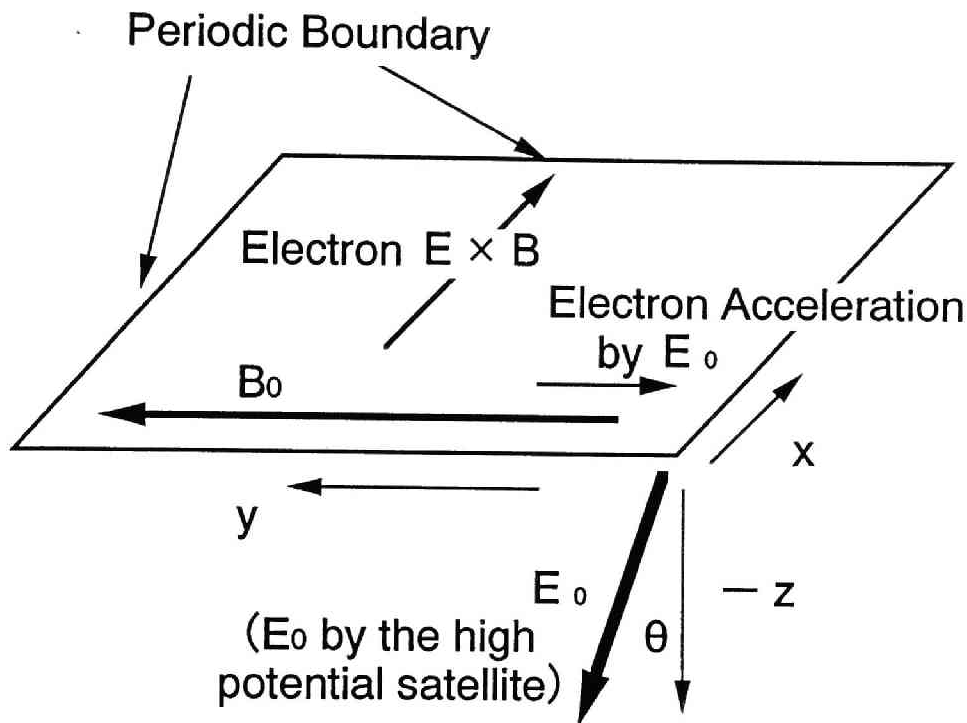
Figure 5.31: Schematic illustration of the model plane for the computer experiments of plasma instability around the sheath edge. The static electric field from the satellite has an angle of 80 degrees with respect to B_0.

is apparently observed as described in Chapter 4. Here, based on the electron motion in a general situation stated above, the process of the field perturbation in the coexistence of the two types of plasma instability will be demonstrated via computer experiment.

The model configuration is illustrated in Figure 5.31. The difference from the model used in the previous section is the direction of E_{sat} from the high potential satellite. To realize a general situation, E_{sat} is set along the $-z$ direction declining 10 degrees toward B_0 direction as shown in Figure 5.31. Owing to this field configuration, electrons, which are much lighter than ions, make a drift motion with $E \times B$ velocity along the x direction and are simultaneously accelerated along $-y$ direction by the y component of E_{sat}. The dimensions of the model plane and the physical parameters used in the present computer experiments are the same as those in the previous section.

First, we present the time series of the density variation in the model plane. Figure 5.32 shows the contour maps of the number density of electrons and ions

Electron   Ion

$\omega_{LHR}t$= 2.05

$\omega_{LHR}t$= 3.07
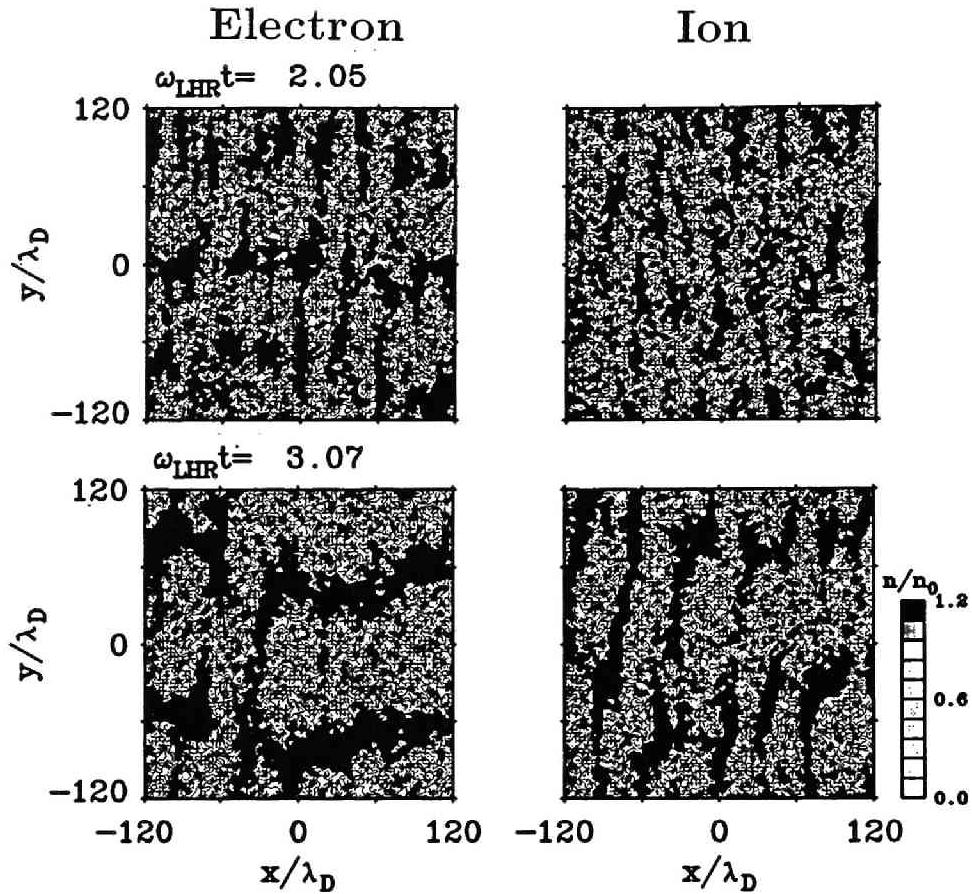
Figure 5.32: Time series of contour maps for the number density of electrons and ions.

with the same fashion as in Figure 5.26. The panel (a) and (b) corresponds to the maps at $\omega_{LHR}t = 2.05$ and 3.07, respectively. At $\omega_{LHR}t = 2.05$, as shown in the panel (a), the density modulation along the x direction is apparently seen in the both species, which is similar to the one observed in the case of the beam cyclotron instability shown in Figure 5.26. According to the discussion in the previous section, this density modulation is because of the upper-hybrid two-stream instability. It should be also noted that the density modulation in the y direction is also seen particularly in the electron plot. Taking account of the continuous acceleration of electrons in the y direction, the density variation is owing to the Buneman instability. The spatial interval of the density modulation is approximately $\lambda_{dns} \sim 80\lambda_D$. At the later time around $\omega_{LHR}t = 3.07$, the density ripple becomes more obvious as particularly seen in the electron panel. The spatial interval is elongated as time elapses. The panel (b) shows $\lambda_{dns} \sim 120\lambda_D$. Along the x direction, the density modulation also remains although it becomes faint. In the panel for ions, the density ripple along the x direction

grows and the structure becomes evident as time elapses.

We next examine the variation of the particle dynamics with phase diagrams. Figure 5.33 and Figure 5.34 depict the time series of electron plot in the $v_y - y$ space and $v_x - x$ space, respectively. The panel (a), (b) and (c) correspond to the diagram at $\omega_{LHR}t = 2.05, 2.82$, and 3.84, respectively. In the $v_y - y$ space, electrons are accelerated to the $-y$ direction by the parallel component of E_{sat}. At early time around $\omega_{LHR}t = 2.05$, as shown in Figure 5.33, the modulation in velocity domain is also observed and the spatial interval λ_{vel} is approximately $80\lambda_D$ which is the same as λ_{dns} in the density variation. According to the discussion in the previous section, the Buneman instability is responsible for the modulation along B_0. Some of the electrons are trapped in the potential well created by the instability and accelerated back to the positive y direction against the force by E_{sat}. At the later time shown in the panel (b) and (c), the net velocity increases in the $-y$ direction and reaches more than $v_y/v_{te} \sim 25$. λ_{vel} of the velocity modulation becomes long around $120\lambda_D$ and the mode 2 seems dominant. This results is also consistent with λ_{dns} in the density modulation. As shown in the panel, the electron thermalization becomes apparent although the net velocity is still suffered from the modulation by the potential of mode 2 induced by the instability. In the present model of computer experiments, E_{sat} is kept constant during the simulation run. In a real situation, however, the electron sheath can shield the satellite potential so that the intense E_{sat} becomes weak in the presheath region. In this sense, the electron acceleration up to $v_y/v_{te} \sim 25$ observed in the computer experiments may be exaggerated although the modulation of the plasma environment due to the Buneman instability can be qualitatively examined.

Along the x direction shown in the $v_x - x$ space, the upper-hybrid two-stream instability can be mainly responsible for the plasma modulation. Although not so obviously shown, the velocity modulation is observed in the panel (a). Some of the electrons which drift with the $E \times B$ velocity are decelerated to the opposite direction in the x direction. As time elapses, the velocity modulation becomes more evident. This situation is shown in the panel (b). At the later time around $\omega_{LHR}t = 3.84$, the regular modulation in the phase space disappears and eventually the electrons are almost thermalized in the direction of the $E \times B$ direction.

Judging from the analysis of the plasma dynamics, we can conclude that two types of instability, the Buneman instability along B_0 and the beam cyclotron instability across B_0, simultaneously take place owing to the relative motion of electrons and ions induced by the high potential satellite. Since the two instabilities enhances waves in different directions, it is rather easy to distinguish each other. To do so, we conduct the spatial analysis of the electrostatic field
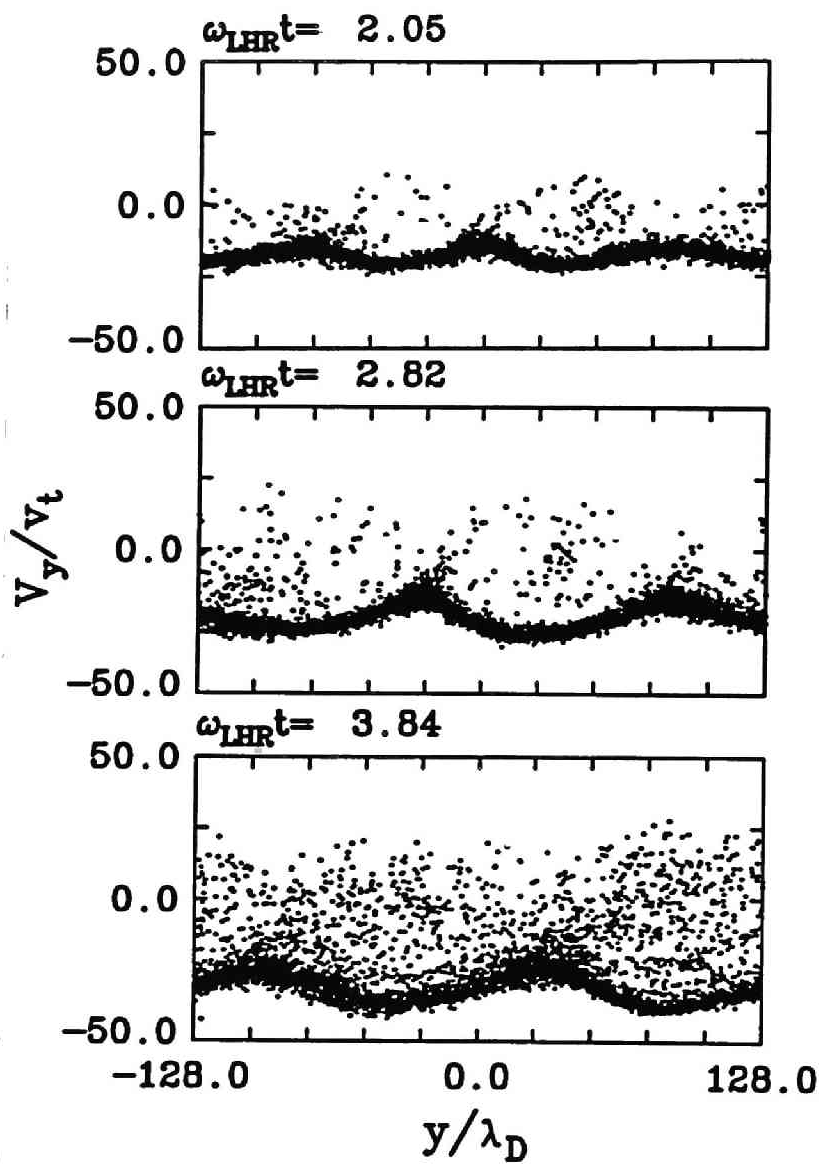
Figure 5.33: Phase diagram of the $v_y - y$ space for the electrons at different times.
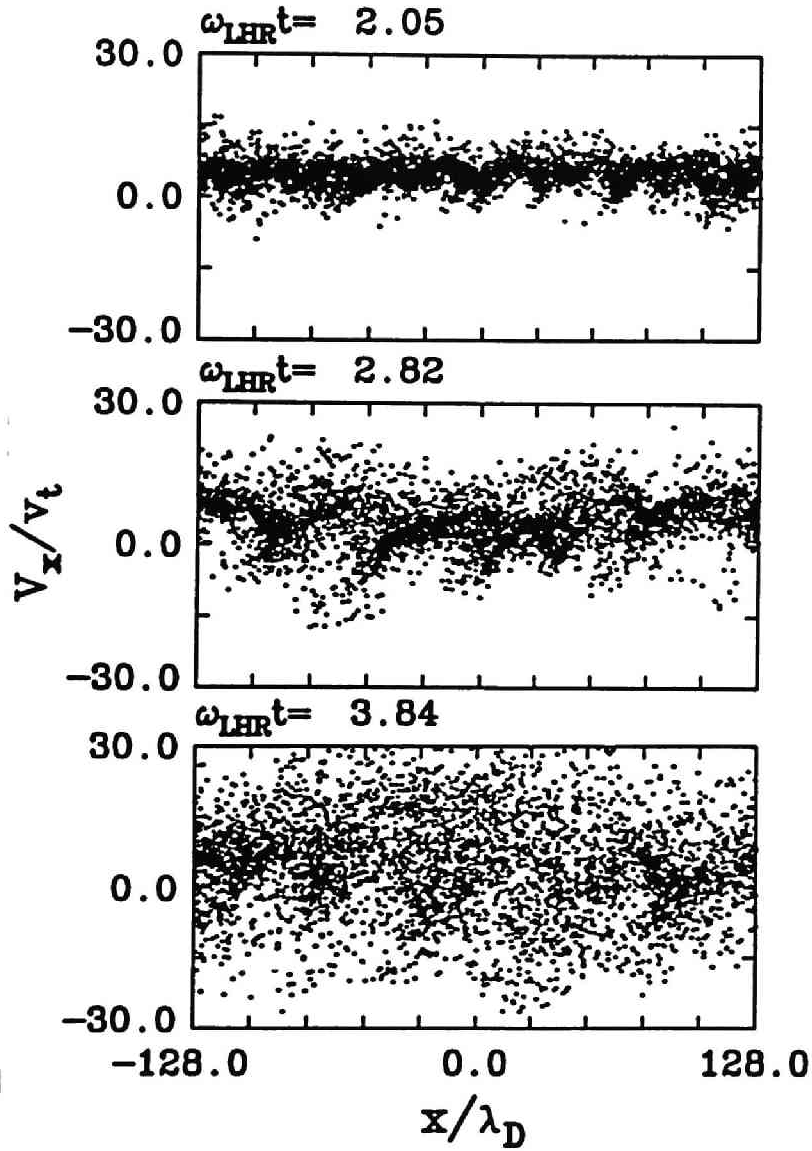
Figure 5.34: Phase diagram of the $v_x - x$ space for the electrons at different times.

in terms of k vectors of the excited wave mode. In Figure 5.35 we present the time series of contour plots of the intensity of the E_x and E_y field in $k_x - k_y$ plane. The panel (a), (b), and (c) correspond to the plots at $\omega_{LHR} = 1.12$, 1.63, and 2.66, respectively. The field intensity in k space is obtained by performing the Fourier transformation of field data with respect to the two-dimensional space. Regarding the E_x field, as examined above, the upper-hybrid two-stream instability is the major source for the perturbation. At early time shown in the panel (a), the field perturbation is rather monochromatic with the mode number 8 although the intensity is weak. As speculated from the analysis of the plasma dynamics, the modulation of the field with a regular structure tends to become random as time elapses. It turns out that the field spectra in the k domain also spreads to the lower value, which implies that the perturbation with longer wave length is induced as the result of the cascading. This process is shown in the panel (b) and (c). The spectra spreads approximately from $k_x V_{e \times b}/\omega_{LHR} \sim 2.5$ to 25. Contrary to the E_x case, the E_y perturbation in the k space shows rather monochromatic which lasts even at the later time. This agrees with the phase plots shown in Figure 5.33 indicating that the mode 2 is intense even at the later time. The dominant mode in the k space also varies in time. In the panel (a), the dominant mode is found at approximately $k_y V_{e \times b}/\omega_{LHR} = 15$. As time elapses the peak position moves to the lower k value $k_y V_{e \times b}/\omega_{LHR} \sim 8$ and 5 in the panel (b) and (c), respectively. This is all due to the continuous increase of the relative motion between electrons and ions along B_0. As examined in the linear analysis of the Buneman instability, the higher relative velocity provides the larger growth rate for unstable mode at the smaller k number. This tendency agrees with the analysis of the k spectra described above.

So far, we have examined the electrostatic field perturbation due to the Buneman instability and the beam cyclotron instability. Another candidate for the electrostatic perturbation is the ion acoustic instability. At the altitude around 300 km where the TSS experiment is carried out, the plasma is almost isothermal so that the ion acoustic wave is hard to grow due the strong Landau damping. Instead, as described, the Buneman instability is driven by the relative velocity of electrons and ions larger than the electron thermal velocity. In the nonlinear process of the Buneman instability, the electrons are smeared out in the phase space and consequently become heated. In the present computer experiments, some of the electrons are trapped and heated by the electrostatic potential as shown in the panel (c) of Figure 5.18. At the presheath where the Buneman instability occurs, the temperature ration of electrons to ions becomes approximately $T_e/T_i \sim 3$ in the nonlinear stage while it was unity in the initial stage. As described earlier, not only the Buneman instability, but also the beam cyclotron instabilities are responsible for the plasma heating around the
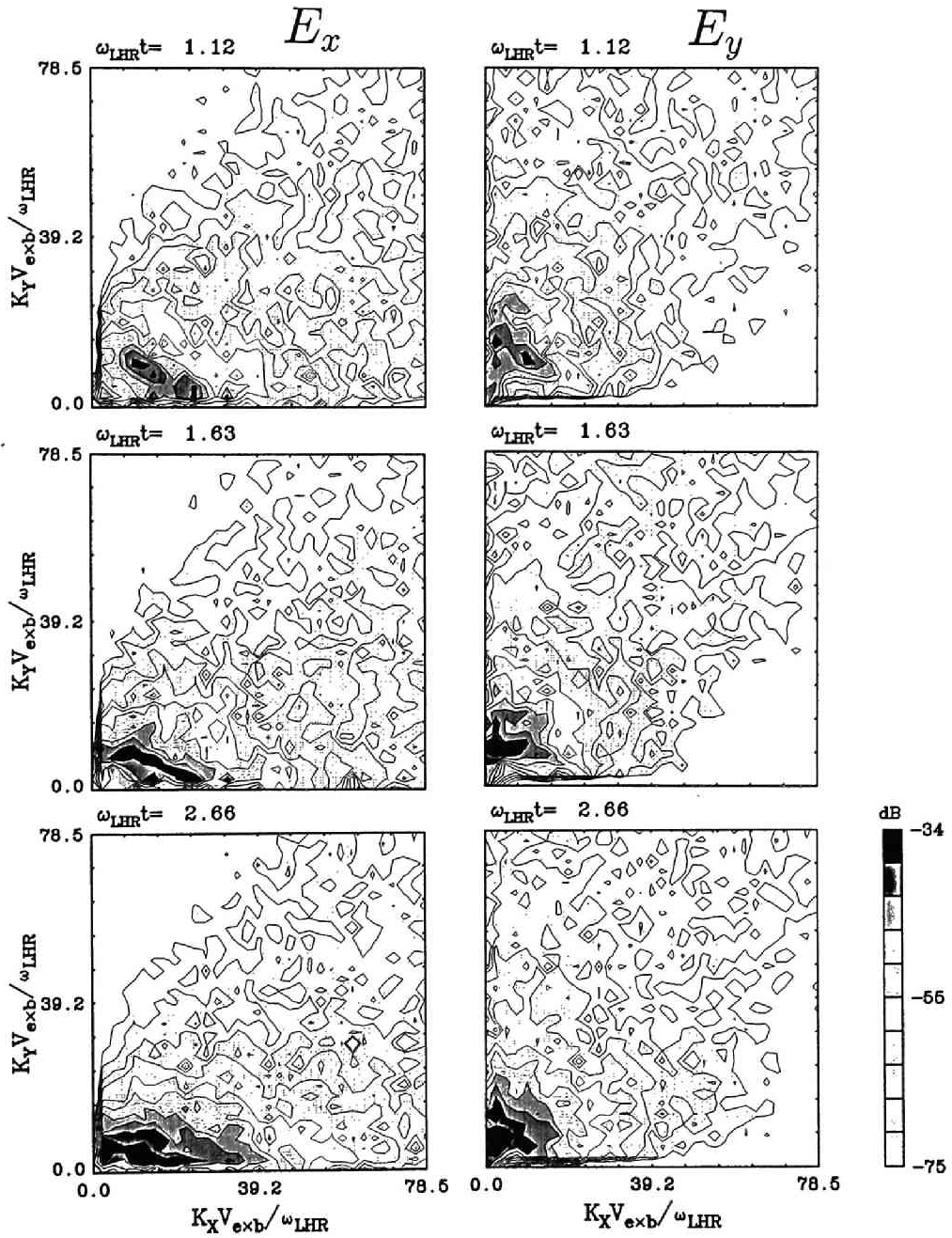
Figure 5.35: Contour map of k-spectra for the E_x and E_y field component.
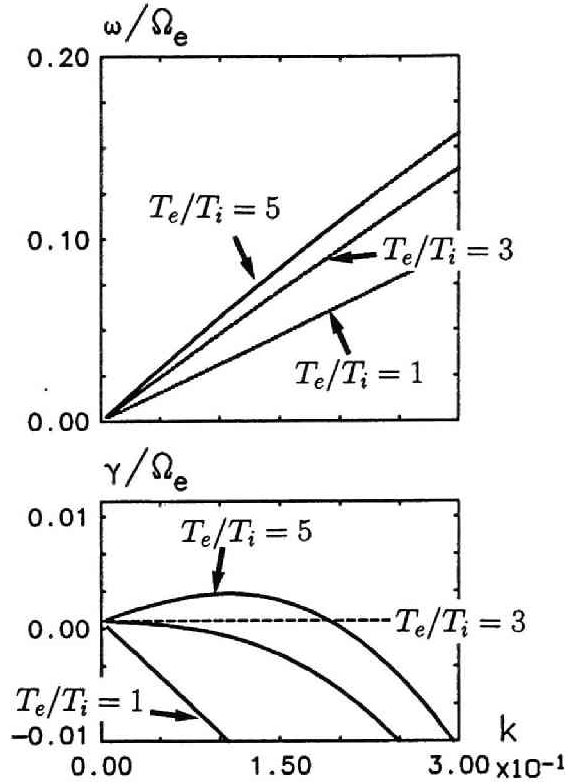
Figure 5.36: The $\omega - k$ diagram obtained by the dispersion solver for the ion acoustic instability for different temperature ratios.

satellite. As shown in Figure 5.30, T_e/T_i becomes approximately 8 due to the beam cyclotron instability. At the steady state, $T_e/T_i > 1$ can be natural at the ion cavity boundary near the satellite due to the continuous plasma heating. In such a situation, the ion acoustic wave can exist without suffering from strong damping. To quantitatively evaluate the growth of the ion acoustic wave, we solved the dispersion relation and the obtained curves for the ion acoustic mode are plotted in Figure 5.36 in the same fashion as in Figure 5.14. To see the dependence of the wave growth on T_e/T_i, we have different cases of T_e/T_i. By taking account of the situation of the relative motion of electrons and ions along B_0, we assume electron drift equal to v_{te} in the ion rest frame of reference. As easily predicted, the ion acoustic wave starts to have positive growth rate as the temperature ratio becomes large. In the isothermal case, no growth rate can be found. Even for the case of $T_e/T_i = 3$, the growth rate of the ion acoustic wave is negative. For the case of $T_e/T_i = 5$, the imaginary part of frequency appears in the k region up to 0.2, which is $0.003\Omega_e$ and fairly low compared with

the one for the Buneman instability. In the present computer experiments in which the electrons are heated up to $T_e/T_i = 3 \sim 8$, it is concluded that the ion acoustic wave can be excited but hardly observed because of its small growth rate even if the electrons are heated by the electrostatic perturbation due to the Buneman instability. Moreover, as time elapses, the electron acceleration toward the satellite becomes weak because of the electrostatic shielding by the electron sheath formation. This implies that the relative velocity between electrons and ions decreases and the possibility for the ion acoustic instability to occur becomes low.

In terms of electromagnetic, wave enhancement due to a specific instability cannot be expected in the present situation where the isothermal background electrons and ions have a relative velocity. When a beam component of electrons exists in the background electrons, various kinds of unstable modes are excited mostly oblique direction to B_0 [Zhang et al., 1993], which does not corresponds to the situation around the high potential satellite. The plasma heating due to the beam cyclotron instability may lead to anisotropic electrons which can enhance the whistler mode wave. As shown in Figure 5.30, however, $T_\perp/T_\parallel$ of electrons is at most around 2 at the wave saturation, which weakly enhances the whistler mode. Rather, as shown in Figure 5.13, transient field response to the abrupt change of the TSS potential becomes dominant in the vicinity of the TSS. In fact, the potential is changed actively during the various experiments carried out in the TSS mission. In this aspect, the transient response of the field will play an important role for the electromagnetic field perturbation [Wang and Hastings, 1991].

In conclusion, we have examined the electrostatic instability driven by the relative motion between electrons and ions near the satellite region. In the process of the sheath formation, electrons are easily accelerated by the intense field of the satellite along B_0 in the presence of the ions which are slowly expanding away from the satellite. When the beam velocity of the electrons exceeds the the electron thermal velocity, the electrostatic field is perturbed by the Buneman instability. Due to the field enhancement, charged particles are heated in the interaction region. Across B_0, the electrons near the satellite make a drift motion with $E \times B$ velocity owing to the intense electric field from the satellite. Assuming the ions are unmagnetized in the initial phase, the electron drift becomes an electron beam across B_0, which drives the beam cyclotron instability in electrostatic domain. From the ion rest frame of reference, the frequency of the excited field is near the lower-hybrid frequency. In a realistic case, the two instabilities stated above can grow at low frequency around ω_{LHR}. The competing process of them depends of the direction with respect to B_0. Along B_0, as described in the early section, the Buneman type instability becomes dominant.

As the direction of our concern becomes oblique to B_0, then, the beam component with $E \times B$ velocity becomes important for the plasma interaction and the beam cyclotron instability can dominantly occur and heat the plasma.

Chapter 6

Summary and Conclusions

In this thesis we have studied the electrodynamic interaction between a tethered satellite system (TSS) and space plasma through computer experiments and theoretical analysis. Since our main concern is the kinetic effects which play an important role in determining the plasma and field environments in the vicinity of the TSS, we have utilized a full particle model for the computer experiments. Contrary to the uniform plasma models of one or two-dimensional geometry which are typically used in computer experiments, we first introduced two conducting bodies which represented the two tether ends into our model. To characterize the electrodynamic interaction from a three-dimensional point of view, we have developed a three-dimensional electrostatic particle code and have utilized it in the computer experiments for the TSS.

In Chapter 1, we presented a brief introduction of the present study and provided a historical overview regarding the electrodynamic tether system. We also described the experiment of Shuttle Electrodynamic Tether System (SETS) which was carried out during the TSS-1 mission in 1992.

In Chapter 2, we described the numerical techniques of the simulation codes used in the present study. We briefly reviewed the 2-1/2 dimensional electromagnetic particle code called KEMPO. In order to accurately model an isolated system in the computer experiments carried out herein, we have modified the boundary treatment of the model region to avoid the unexpected reflection of outward propagating perturbations in the field. For simplicity, we have regarded the TSS as two conducting bodies which are electrically connected to each other via the tether in the computer experiments. To control the TSS potential in a self-consistent manner, we have applied a capacitance matrix method. This numerical technique has been well described in detail in this chapter. The basic physics associated with the interactions of the TSS with the ambient space plasma can be well-studied by performing two-dimensional computer experi-

ments. However, to understand the three-dimensional structure of phenomena observed in two-dimensional computer experiments, we definitely need to perform the same analysis in three-dimensional space. For this purpose we have developed a three-dimensional electrostatic particle code and its numerical treatment is also stated in Chapter 2.

In Chapter 3, we have investigated the electrodynamic interaction of the TSS with the ambient space plasma. In our model, we have considered two conducting bodies in a magnetized plasma which represent an orbiter and a tethered satellite. In order to avoid excess charging of the system, an electron beam is emitted from the orbiter. We have used two types of simulation codes. One is 2-1/2 dimensional electromagnetic particle code, and the other is three-dimensional electrostatic code. The electromagnetic code is used to ascertain the basic physics associated with the plasma and field responses to the TSS as well as the electric properties of the TSS. Since the electrodynamic interaction is driven by the electrical potential difference between the TSS and the ambient plasma, an electrostatic approximation is adequate in such a situation. In order to examine phenomena observed in the two-dimensional computer experiments in a three-dimensional aspect, we have also performed three-dimensional computer experiments.

Contrary to the case of a single space vehicle, the TSS, which has a long dimension in one direction, is unique in terms of potential distribution. Owing to the $V \times B$ effect of the cross-field motion of this system, a potential energy difference which is much larger than the thermal energy of the ambient space plasma can be generated between the tether ends. The electrical properties such as current collection and the potential variation at the tether ends are examined in detail by the computer experiments. The plasma response to the TSS is also investigated in terms of density variation and current path. In principle, electrons are attractive to while ions are repulsive from the high potential satellite and vice versa for the negative potential orbiter. In particular, in the vicinity of the satellite, an electron sheath is created from which ions are evacuated due to the high potential. Since the ambient plasma flows toward the TSS in the vehicle frame of reference, an ion cavity tends to be formed downstream, thereby generating a rarefactional wake region. In a three-dimensional aspect, the electron sheath is much thicker in the transverse direction as opposed to the parallel direction with response to B_0 owing to the difference in mobility of the electrons along B_0. A donut-like structure of the electron sheath is clearly observed in the results of the three-dimensional computer experiments. The dynamics of the electron beam emitted from the orbiter are one of the significant issues which are investigated in the present study. We have considered various pitch angles for the beam electrons. Basically, the electrons emitted from the orbiter are

accelerated away along B_0 by the electric field force induced by the negatively charged orbiter as well as the dense beam itself. In two-dimensional case, a plasma cloud is created in the plane perpendicular to B_0 in the vicinity of the orbiter. This effect is due to the concentration of the beam electrons rotating with an $E \times B$ drift velocity. In the plasma cloud, intense field perturbation in the LHR mode range is enhanced. This field enhancement is interpreted by linear theory to be due to the lower-hybrid drift instability. The detailed discussion of this relationship is described in Chapter 3. In the three-dimensional computer experiments, however, the plasma cloud formation is rarely observed. This is because a majority of the beam electrons can escape along B_0. Now, a beam-plasma interaction can take place along B_0 which may excite whistler mode waves. This phenomena has been addressed by a number of studies to date. The field response at the tether ends due to the change in the TSS potential was examined for various cases. The results obtained in these computer experiments show that the field is strongly perturbed at the tether ends at the characteristic frequencies of the plasma such as Π_e, ω_{UHR}, and ω_{LHR}. However, we point out that the low frequency perturbation is reduced by the electron beam emission which is used to avoid an abrupt drop of potential due to the charge accumulation in the TSS.

In Chapter 4, we have considered the plasma response to the high potential satellite in the TSS. In the model used in our computer experiments we introduce one conducting body representing a satellite whose potential is abruptly elevated to a fixed high potential. As was done in the previous chapter, we used both the two-dimensional electromagnetic and the three-dimensional electrostatic codes for the computer experiments. First, we examined the transient response of the plasma to the high potential satellite in terms of density variation and current collection of the satellite. As for the density variation, electrons are attracted by the satellite uniformly during the initial stage which corresponds approximately to the electron plasma oscillation period. Ions are excluded by the high potential of the satellite. After the initial stage, a directional dependence for the plasma distribution is clearly seen. Along B_0 the charged particles are highly mobile so that ions are mostly evacuated in this direction. Electrons, which have large thermal velocities compared to ions, form a low density region along B_0 to maintain the local charge neutrality. As discussed in the previous chapter, the density profile obtained by the three-dimensional computer experiments shows that an electron sheath with a donut-like structure is created around the satellite. A rarefactional wake region is also formed in the downstream region for both electrons and ions. The wake structure becomes asymmetric with respect to the direction of the plasma flow vector. This is due to the intense $E \times B$ drift effects on the ambient plasma. A detailed discussion of these effects is provided

in this chapter. As for the current collection of the satellite, an intense transient current is observed initially followed by an exponentially decreasing current. The initial peak of the current can be theoretically estimated successfully using a simple model. Under steady state conditions, the current-voltage characteristics of the satellite are examined by performing computer experiments with different satellite potential up to $e\phi_s/k_B T_e \simeq 10^3$ and comparing our results to classical theories. For the two-dimensional cases, it can be concluded that the theory based on the constant density model by Linson, [1969] provides a good estimate for the upper bound of the current flowing from the satellite. In the three-dimensional case, because of the unexpected boundary effects due to the expansion of the ion cavity region, we obtained the current-voltage characteristics up to $e\phi_s/k_B T_e \simeq 10^2$. In this limited range, the current from the satellite can be roughly approximated by the single particle theory derived by Parker and Murphy, [1967]. For higher potentials, the current can be increased and the constant density model may provide a good estimate of the maximum current at the satellite as examined in the two-dimensional cases. However, this is left for a future work.

In Chapter 5, we have investigated the field perturbation by the TSS, The sources for the field perturbation of our concern are the transient tether current and the plasma instability driven the relative motion of electrons and ions near the high potential satellite. Regarding the tether current model in the computer experiments, we introduced a cross-field current source which varies in the same manner in time as the transient current flowing out from the satellite to the ambient plasma. The results show that a wave packet of whistler mode emission is induced by the current flow and propagates along B_0. To examine the characteristics of the whistler wave packet, we have also performed one-dimensional computer experiments using different frequencies of current modulation and different angles with respect to the direction of B_0. Meanwhile, in the process of the sheath formation around the satellite, the acceleration of electrons and ions at the satellite region is observed toward and away, respectively, due to the intense electric field therein. This relative motion of the electrons and ions can cause two-stream type of plasma instability. To clarify the possibility of an instability, we have performed two-dimensional computer experiments. At the presheath region beyond the sheath where the plasma density is low, a Buneman instability occurs along B_0 and an electrostatic perturbation at low frequencies around ω_{LHR} is also observed. Across B_0 the beam cyclotron instability represents the dominant enhancement at low frequencies around ω_{LHR}. This is due to the relative motion of unmagnetized ions and electrons drifting with an $E \times B$ velocity induced by the intense electric field from the satellite.

In conclusion, we have studied the electrodynamic interaction between a teth-

ered satellite system and space plasma by performing computer experiments. The theoretical analyses associated with the current-voltage characteristics and current collection of the TSS have also been done. Particularly, as described in Chapter 4, it turns out that computer experiment of particle model is a powerful and important method to determine the current-voltage characteristics of high potential satellite which cannot be interpreted by the classical Langmuir theory. Through the present study, we can quantitatively examine and understand the plasma and field response to a space structure whose potential energy is much larger than the thermal energy of the underlying ambient plasma. We hope that this body of work will contribute to a further understanding of the electrodynamic interaction between future space structures and the ambient space plasma in which they must reside.

Appendix

Free Boundary Treatment for Electrostatic Model

In Chapter 2, we have described the sine transform method for solving Poisson's equation with the Dirichlet condition $\phi = 0$ at boundaries. However, in such a situation that a model region cannot be taken large enough to shield the energy source electrostatically, the boundary with Dirichlet condition $\phi = 0$ causes unphysical profile and reflection of electrostatic field. To avoid such a situation, we need to realize an isolated system in which the potential values at the boundaries are not fixed at a certain value.

As one of the method to realize the isolated system in terms of electrostatic field, Poisson's equation can be solved with the Green function [*Eastwood and Brownrigg*, 1979]. The basic concept is stated as follows. In the isolated system, the boundary condition for the potential ϕ is given as

$$\Phi \to 0 \ (\ |x| \to \infty) \tag{6.1}$$

The potential value Φ is obtained as

$$\Phi(\boldsymbol{x}) = \int G(\boldsymbol{x} - \boldsymbol{x}')\rho(\boldsymbol{x}')d^3x' \tag{6.2}$$

where

$$G(\boldsymbol{x} - \boldsymbol{x}') = \frac{1}{4\pi\epsilon|\boldsymbol{x} - \boldsymbol{x}'|} \tag{6.3}$$

with the boundary conditions of (A.1).

To simplify the formulation, one-dimensional model is considered here. In discrete space,

$$\Phi(x_i) = \Delta r \sum_{n=0}^{N_x-1} G(x_i - n\Delta r)\rho(n\Delta r) \tag{6.4}$$

where N_x and Δr denote the total grid number and the grid space, respectively. ($i = 0 \sim N_x$)

The convolution of (6.2) gives

$$\hat{\Phi}(k) = \hat{G}(k)\hat{\rho}(k) \tag{6.5}$$

This can be readily solved using FFT, which is described by [Hockney, 1970] giving the correct potential at the grid points within the simulation region.

References

Aguero, V. M., P. M. Banks, B. E. Gilchrist, T. Neubert, W. J. Raitt and D. C. Thompson, Observations of shuttle vehicle charging in the ionosphere using the TSS-1 SETS experiment, *EOS Trans., AGU, 73,* 1992.

Arnold, D. A., and M. Dobrowolny, Transmission line model of the interaction of a long metal wire with the ionosphere, *Radio Sci., 15,* 1149, 1980.

Banks, P. M., B. E. Gilchrist, I. Linscott, W. J. Raitt, D. Thompson, S. Williams, P. R. Williamson, V. Aguero, V. Tolat, and A. B. White, The shuttle electrodynamic tether system (SETS) on TSS-1, Submitted to *Il Nuovo Cimento,* 1993.

Banks, P. M., Review of electrodynamic tethers for space plasma science, *J. Spacecr. Rockets, 26,* 234, 1989.

Banks, P. M., and P. Byers, SETS development phase proposal, Stanford University, 1986. Banks, P. M., P. R. Williamson, and K. I. Oyama, Electrical behavior of a shuttle electrodynamic tether system(SETS), *Planet. Space Sci., 29,* 139, 1981.

Barnett, A. and S. Olbert, Radiation of plasma waves by a conducting body moving through a magnetized plasma, *J. Geophys. Res., 91,* 10117, 1986.

Birdsall, C. K., and A. B. Langdon, *Plasma Physics via Computer Simulation,* McGraw-Hill, New York, 1985.

Beard, D. B., and F. S. Johnson, Ionospheric limitation on attainable satellite potential, *J. Geophys. Res., 66,* 4113, 1961.

Buneman, O., Instability of electrons drifting through ions across a magnetic field, *J. Nucl. Energy, PartC (Plasma Physics), 4,* 111, 1962

Bush, R. I., G. D. Reeves, P. M. Banks, T. Neubert, and P. R. Williamson, Electromagnetic fields from pulsed electron beam experiments in space: spacelab-2 results, *Geophys. Res. Lett., 14,* 1015, 1987.

Calder, A. C., and J. G. Laframboise, Time-dependent sheath response to abrupt electrode voltage changes, *Phys. Fluids B, 2,* 655, 1990.

Chen, L., and C. K. Birdsall, Heating of magnetized plasmas by a large-amplitude low-frequency electric field, *Phys. Fluids 16,* 2229, 1973.

Chen, L., and C. K. Birdsall, Lower-hybrid drift instability saturation mechanism in one-dimensional simulations, *Phys. Fluids 26,* 180, 1983.

Colombo, G., E. M. Gaposchkin, M. D. Grossi and G. C. Weiffenbach, Proposal by smithsonian institution astrophysical observatory, September, 1974.

Davidson, R. C., N. T. Gladd, and C. S. Wu, Effects of finite plasma beta on the lower-hybrid-drift instability, *Phys. Fluids, 20,* 301, 1977.

Dobrowolny, M., Electrodynamics of long metallic tethers in the ionospheric plasma, *Radio Sci., 13,* 417, 1978.

Drell, S. D., H. M. Foley, and M. A. Ruderman Drag and propulsion of large satellites in the ionosphere: An Alfvén propulsion engine in space, *J. Geophys. Res., 70,* 3131, 1965.

Eastwood, J. W., and D. R. K. Brownrigg, Remarks on the Solution of Poisson's Equation for Isolated Systems, *J. Comp. Phys.,* 32, 24, 1979.

Estes, R. D., Alfvén waves from an electrodynamic tethered satellite system, *J. Geophys. Res., 93,* 945, 1988.

Garrett, H. B., The Charging of spacecraft surfaces, *Reviews of Geophysics and Space Physics, 19,* 577, 1981.

Gilchrist, B. E., P. M. Banks, T.Neubert, V. M. Aguero, S. G. Bilen, S. D. Williams, I. Linscott, D. C. Thompson and W. J. Raitt, Measurements of TSS-1 voltage-current characteristics using the SETS experiment, *EOS Trans., AGU, 73,* 1992.

Gilchrist, B. E., SETS Functional Objectives, TSS-1 O & IA-01, Revision: Basic, April, 1990.

Gilchrist, B. E., P. M. Banks, T. Neubert, P. R. Williamson, N. B. Myers, W. J. Raitt, and S. Sasaki, Electron collection enhancement arising from neutral gas jets on a charged vehicle in the ionosphere, *J. Geophys. Res., 95,* 2469, 1990.

Godard, R., and J. G. Laframboise, Total current to cylindrical collectors in collisionless plasma flow, *Planet. space Sci., 31*, 275, 1983.

Grabowski, R., and T. Fischer, Theoretical density distribution of plasma streaming around a cylinder, *Planet. Space Sci., 23*, 287, 1975.

Gurnett, D. A., W. S. Kurth, J. T. Steinberg, P. M. Banks, R. I. Bush, and W. J. Raitt, Whistler-mode radiation from the spacelab-2 electron beam, *Geophys. Res. Lett., 13*, 225, 1986.

Hastings, D. E., and J. Wang, The radiation impedance of an electrodynamic tether with end connectors, *Geophys. Res. Lett., 14*, 519, 1987.

Hastings, D. E., A. Barnett, and S. Olbert, Radiation from large space structures in low earth orbit with induced alternating currents *J. Geophys. Res., 93*, 1945, 1988.

Hastings D. E., and P. Chang, The physics of positively biased conductors surrounded by dielectrics in contact with a plasma, *Phys. Fluids., 1*, 1123, 1989.

Hockney, R. W., The potential calculation and some applications, *Methods in Computational Physics, 9*, 135, 1970.

Hockney, R. W., and J. W. Eastwood, *Computer simulation using particles*, McGraw-Hill, New York, 1981.

Kiel, R. E., Electrostatic probe theory for free molecular cylinders, *AIAA Journal, 6*, 708, 1967.

Krall, N. A., and P. C. Liewer, Low-frequency instabilities in magnetic pulses, *Phys. Rev., 4*, 2094, 1971.

Kroll, K. R., Tether implications on space station gravity level, *AAS 86-236*, Int. Conf. 1986.

Lampe, M., W. M. Manheimer, J. B. McBridge, J. H. Orens, K. Papadopoulos, R. Shanny, and R. N. Sudan, Theory and Simulation of the Beam Cyclotron Instability, *Phys. Fluids., 15*, 662, 1972.

Laframboise, J. G., and J. Luo, High-voltage polar-orbit and beam induced charging of a dielectric spacecraft: a wake-induced barrier effect mechanism, *J. Geophys. Res., 94*, 9033, 1989.

Langmuir, I. and K. Blodgett, Currents limited by space charge between coaxial cylinders, *Phys. Rev., 22,* 347, 1923.

Langmuir, I., and K. Blodgett, Currents limited by space charge between concentric spheres, *Phys. Rev., 24,* 49, 1924.

Lemons, D. S., and S. P. Gary, Electromagnetic Effects on the Modified Two-Stream Instability, *J. Geophys. Res., 82,* 2337, 1977.

Linson, L. M., Charge neutralization as studied experimentally and theoretically, *Artificial Particle Beams in Space Plasma Studies,* edited by G. Grandal, 573, Plenum, New York, 1982.

Linson, L. M., Current-voltage characteristics of an electron-emitting satellite in the ionosphere, *J. Geophys. Res., 74,* 2368, 1969.

Ma, T.-Z., and R. W. Schunk, A Fluid model of high voltage spheres in the ionosphere, *Planet. Space Sci., 37,* 21, 1989.

Mandell, M. J., J. R. Lilly, Jr., I. Katz, T. Neubert, and N. B. Myers, Computer modeling of current collection by the CHARGE 2 mother payload, *Geophys. Res. Lett., 17,* 135, 1990.

Martin, A. R., Numerical solutions to the problem of charged particle flow around an ionospheric spacecraft, *Planet. Space Sci., 22,* 121, 1974.

Matsumoto, H., and Y. Omura, Particle simulation of electromagnetic waves and its application to space plasmas, *Computer Simulation of Space Plasma,* ed. by H. Matsumoto and T. Sato, Terra Sci. Pub., 43, 1985.

McBride, J. B., E. Ott, J. P. Boris, and J. H. Orens, Theory and simulation of turbulent heating by the modified two-stream instability, *Phys. Fluids., 15,* 2367, 1972.

Merlina, P., W., Bogo, S. Ciardo, Tethered elevator and pointing platform demonstrations: a shuttle flight test of scaled engineering models, *AAS 86-213,* Int. Conf., 1986.

Myers, N. B., W. J. Raitt, B. E. Gilchrist, P. M. Banks, T. Neubert, and P. R. Williamson, A comparison of current-voltage relationships of collectors in the earth's ionosphere with and without electron beam emission, *Geophys. Res. Lett., 16,* 365,1989.

Neubert, T., S. Sasaki, B. E. Gilchrist, P. M. Banks, P. R. Williamson, A. C. Fraser-Smith, and W. J. Raitt, Observations of plasma wave turbulence generated around large ionospheric spacecraft: effects of motionally induced EMF and of electron beam emission, *J. Geophys. Res.*, *96*, 9639, 1991.

Neubert, T., M. J. Mandell, S. Sasaki, B. E. Gilchrist, P. M. Banks, P. R. Williamson, W. J. Raitt, N. B., Meyers, K. I. Oyama, and I. Katz, The sheath structure around a negatively charged rocket payload, *J. Geophys. Res.*, *95*, 6155, 1990.

Neubert, T., W. W. L. Taylor, L. R. O. Storey, N. Kawashima, W. T. Roberts, D. L. Reasoner, P. M. Banks, D. A. Gurnett, R. L. Williams, and J. L. Burch, Waves generated during electron beam emissions from the space shuttle, *J. Geophys. Res.*, *91*, 11321, 1986.

Okuda, H., and J. R. Kan, Injection of an electron beam into a plasma and spacecraft charging, *Phys. Fluids.*, *30*, 209, 1987.

Okuda, H., and J. Berchem, Injection and propagation of a nonrelativistic electron beam and spacecraft charging, *J. Geophys. Res.*, *93*, 175, 1988.

Omura, Y., and H. Matsumoto, Computer experiments on whistler and plasma wave emissions for spacelab-2 electron beam, *Geophys. Res. Lett.*, *15*, 319, 1988.

Omura, Y., Study on nonlinear wave-particle interactions in space plasmas via computer simulations, Ph.D. thesis, Dep. of Electr. Eng., Kyoto Univ., Kyoto, Japan, 1985.

Palmadesso, P. J., and G. Ganguli, Effects of plasma turbulence on electron collection by a high-voltage spherical probe in a magnetized plasma, *J. Geophys. Res.*, *97*, 6493, 1992.

Parker, L. W. and B. L. Murphy, Potential buildup on an electron-emitting ionospheric satellite, *J. Geophys. Res.*, *72*, 1631, 1967.

Parker, L. W., and E. C. Whipple, Jr., Theory of spacecraft sheath structure, potential, and velocity effects on ion measurements by traps and mass spectrometers, *J. Geophys. Res.*, *75*, 4720, 1970.

Press, H. W., B. P. Flannery, S. A. Teukolsky, and W. T. Vetterling, *Numerical Recipes*, Cambridge University Press, New York, 1987.

Pritchett, P. L., and R. M. Winglee, The plasma environment during particle beam injected into space plasmas 1. Electron Beams, *J. Geophys. Res.*, *92*, 7673, 1988.

Prokopenko, S. M. L., and J. G. Laframboise, High-voltage differential charging of geostationary spacecraft, *J. Geophys. Res.*, *85*, 4125, 1980.

Rasmussen, C. E., P. M. Banks, and K. J. Harker, The excitation of plasma waves by a current source moving in a magnetized plasma: The MHD approximation, *J. Geophys. Res.*, *90*, 505, 1985.

Rasmussen, C. E., P. M. Banks, and K. J. Harker, The excitation of plasma waves by a current source moving in a magnetized plasma: Two-dimensional propagation, *J. Geophys. Res.*, *95*, 10459, 1990.

Reeves, G. D., P. M. Banks, A. C. Fraser-Smith, T. Neubert, R. I. Bush, D. A. Gurnett, and W. J. Raitt, VLF wave stimulation by pulsed electron beams injected from the space shuttle, *J. Geophys. Res.*, *93*, 162, 1988.

Reeves, G. D., P. M. Banks, T. Neubert, R. I. Bush, P. R. Williamson, A. C. Fraser-Smith, D. A. Gurnett, and W. J. Raitt. VLF wave stimulation by pulsed and DC electron beams in space. 1. spacelab 2 observations, *J. Geophys. Res.*, *93*, 14699, 1988.

Sasaki, S., K. I. Oyama, N. Kawashima, and T. Obayashi, K. Hirao, W. J. Raitt, N. B. Myers, P. R. Williamsom, P. M. Banks, W. F. Sharp, Tethered rocket experiment (CHARGE-2): Initial results on electrodynamics, *Radio Sci.*, 1988.

Savich, N. A., Electrodynamics of Tethered Satellite System: Two concepts, *40th Congress of the International Astronautical Federation*, 1989

Stein, R. V., and F. M. Neubauer, Plasma Wave Field Generation by the Tethered Satellite System, *J. Geophys. Res.*, *97*, 10849, 1992.

Stenzel, R. L., and J. M. Urrutia, Laboratory model of a tethered balloon-electron beam current system, *Geophys. Res. Lett.*, *13*, 797, 1986.

Stenzel, R. L., and J. M. Urrutia, Whistler wings from moving electrons in a magnetized laboratory plasma, *Geophys. Res. Lett.*, *16*, 361,1989.

Stenzel, R. L., and J. M. Urrutia, Currents between tethered electrodes in a magnetized laboratory plasma, *J. Geophys. Res.*, *95*, 6209, 1990.

Thompson, W. B., Passive Current Collection, *Tethers in Space Toward Flight*, 88, 1989.

Thompson, D. C., W. J. Raitt, C. Bonifazi, S. D. Willams, V. M. Aguero, B. E., Gilchrist, P. M. Banks, TSS-1 : Orbiter Current and Voltage Experiments, *AIAA conference paper at 31st Aerospace Sciences Meeting & Exhibit*, January, 1993.

Usui, H., Computer Experiments of Shuttle Electrodynamic Tether System, Master thesis, Dep. of Electr. Eng., Kyoto Univ., Kyoto, Japan, 1989.

Usui, H., H. Matsumoto, and Y. Omura, Electron beam injection and associated LHR wave excitation: Computer experiments of electrodynamic tether system, *Geophys. Res. Lett.*, *18*, 821, 1991.

Usui, H., H. Matsumoto, and Y. Omura, Plasma response to high potential satellite in electrodynamic tether system, *J. Geophys. Res.*, *98*, 1531, 1993.

Wang, J., and D. E. Hastings, A dynamic analysis of the radiation excitation from activation of a current collecting system in space, *J. Geophys. Res.*, *96*, 3611, 1991.

Wang, J., D. E. Hastings, and M. Martinez-Sanchez, Electrodynamic interactions between a space station and the ionospheric plasma environment, *J. Spacecr. Rockets, in press*, 1992.

Wang, J., and D. E. Hastings, Ionospheric plasma flow over large high-voltage space platforms, I; Ion-plasma-time scale interactions of a plate at zero angle of attack, *Phys. Fluids B, 4*, 1597, 1992a.

Wang, J., and D. E. Hastings, Ionospheric plasma flow over large high-voltage space platforms, II; The formation and structure of plasma wake, *Phys. Fluids B, 4*, 1615, 1992b.

Whipple, E. C., Jr., and L. W. Parker, The theory of an electron trap on a charged spacecraft, *J. Geophys. Res.*, *74*, 2962, 1969.

Winglee, R. M., and P. L. Pritchett, Space charging effects during the injection of dense electron beams into space plasmas, *J. Geophys. Res.*, *92*, 6114, 1987.

Winglee, R. M., and P. L. Pritchett, Comparative study of cross-field and field-aligned electron beams in active experiments, *J. Geophys. Res.*, *93*, 5823, 1988.

Winglee, R. M., and P. J. Kellogg, Electron beam injection during active experiments, 1, Electromagnetic wave emissions, *J. Geophys. Res.*, *95*, 6167, 1990.

Winske, D., Short-wavelength modes on expanding plasma clouds, *J. Geophys. Res.*, *93*, 2539, 1988.

Woodies, W. R., and J. M. VanPelt, Benefits of tether momentum transfer to space station operations, *AAS 86-235*, Int. Conf. 1986.

Yagitani, S., I. Nagano, K. Miyamura, and I. Kimura, Full wave calculation of ELF/VLF propagation from a dipole source located in the lower ionosphere, *Radio Science.,* in press, 1993.

Zhang, Y. L., H. Matsumoto and Y. Omura, Linear and nonlinear interactions of an electron beam with oblique whistler and electrostatic waves in the magnetosphere, *J. Geophys. Res.*, *98*, 21353, 1993.